THE UNIVERSITY OF QUEENSLAND

AUSTRALIA

Automated Segmentation and Quantitative Analysis of the Hip Joint from Magnetic Resonance Images

Ying Xia

A thesis submitted for the degree of Doctor of Philosophy at

The University of Queensland in 2014

School of Information Technology and Electrical Engineering

ABSTRACT

The aim of this thesis is to develop a novel computer-aided system with advanced medical image processing approaches. This will allow automatic segmentation and quantification of the osteochondral elements (i.e. the articulating bones and cartilages) from high-resolution three-dimensional (3D) magnetic resonance (MR) images of the hip joint.

This research is motivated by the importance of early detection of structural changes and degeneration of the bones and articular cartilages for good patient outcomes, particularly for early and pre-osteoarthritic conditions such as cam-type femoroacetabular impingement (FAI). MR imaging provides an optimal tool for *in vivo* assessment of the hip joint structure, including the bones and cartilages. This has generated extensive interest in the development of MR technologies to analyse cartilage morphology and assess biochemical compositions of the hyaline cartilage to facilitate early diagnostic and treatment for hip osteoarthritis (OA) and FAI.

Quantitative analyses can provide useful morphometric data from complex MR data. In the hip joint, the segmentation of bones and cartilages is an essential prerequisite, which must be accurate, reliable and reproducible, for quantitative measurements. However, this is difficult and is traditionally performed using time- and expert-intensive manual or semi-automatic methods.

The hypothesis behind this research is that accurate and reproducible quantitative data can be automatically obtained from high-resolution 3D MR images of the hip joint, through the use of advanced image processing techniques. To this end, this research focuses on two specific aims: **Aim 1** - to develop and evaluate a fully automated segmentation approach to deliver accurate and reproducible bone and cartilage segmentations from high-resolution 3D MR images of the hip joint and **Aim 2** - to automatically extract reliable and reproducible morphometric data based on the segmented subchondral bones and articular cartilages.

The development of an automatic segmentation scheme for the bones and cartilages with high precision and reproducibility is firstly needed in order to provide a basis for subsequent quantitative measurements, which deliver reliable morphometric data of the segmented bones and cartilages for the use in early OA and FAI studies. To attain these aims, images were acquired using different MR sequences from a mixed demographic (male or female and young adult to elderly) of participants with a variety of femoral head-neck junction presentations but no apparent hip OA. Different sequence scans were used to image the same participant for the associated reproducibility experiments.

Two state-of-the-art methods (multi-atlas-based and active shape model (ASM) based algorithms)

were developed and evaluated for automatic segmentation of proximal femurs and innominate bones from large field of view (FOV) MR images (water-excitation dual echo steady state (DESS) and multi echo data image combination (MEDIC)). The validation results have indicated accurate and robust segmentation performance of both methods for potential use to generate data on the bone morphology as well as provide a basis for subsequent cartilage segmentation; notably, the ASM-based method is significantly more time-efficient, which is favourable for clinical utility.

Quantitative assessment of 3D bone morphology at the femoral head-neck junction was automatically performed in terms of alpha angle measures for potential use in the detection and quantification of cam-type lesions. Strong correlations were achieved between manual and automatic measures at anterosuperior and anterior regions of the femoral head-neck junction, in evaluation of large FOV DESS images from 30 subjects (including 18 high-performance athletes). The reproducibility experiment, based on the subset of 18 athletes, revealed a high consistency in alpha angles obtained between bilateral DESS and unilateral True Fast Imaging with Steady-state Precession (TrueFISP) images.

A hybrid cartilage segmentation scheme was developed, based on bone pre-segmentation, and utilized an improved graph search framework with an arc-weighted graph representation and varying surface feasibility constraints. This is the first method capable of automatic and reliable delineation of the femoral and acetabular cartilages from MR images despite the indistinct separation between the two apposed cartilage plates. The validation study, based on 46 high-resolution TrueFISP images, indicated an overall high level of validity and reliability of automated cartilage segmentations in comparison with benchmark manual segmentations.

Quantitative measurements (i.e. volume and thickness) of the femoral and acetabular cartilages were automatically obtained from cartilage segmentations, which had a good agreement with the results from manual segmentation volumes. Subregional analyses of the cartilage morphology were performed to learn a pattern of morphological variation across different subregions of each cartilage plate, which is significant in detecting small cartilage changes, e.g. focal cartilage lesions. A preliminary evaluation of reproducibility has demonstrated promising results in the volume and thickness measurements obtained from MR scans using three imaging sequences, including high-resolution TrueFISP, low-resolution DESS and low-resolution 3D turbo spin echo with variable flip angle (SPACE).

In summary, this thesis has developed and validated a computer-aided system involving several novel technologies for reliable and repeatable automatic segmentation and quantification of the bones and cartilages from high-resolution 3D MR images of the hip joint. These technical developments show great potential for dedicated use in prospective large-scale research and clinical studies on morphometric evaluation of the hip joint in pathoanatomical conditions such as early OA and cam FAI.

Declaration by author

This thesis is composed of my original work, and contains no material previously published or written by another person except where due reference has been made in the text. I have clearly stated the contribution by others to jointly-authored works that I have included in my thesis.

I have clearly stated the contribution of others to my thesis as a whole, including statistical assistance, survey design, data analysis, significant technical procedures, professional editorial advice, and any other original research work used or reported in my thesis. The content of my thesis is the result of work I have carried out since the commencement of my research higher degree candidature and does not include a substantial part of work that has been submitted to qualify for the award of any other degree or diploma in any university or other tertiary institution. I have clearly stated which parts of my thesis, if any, have been submitted to qualify for another award.

I acknowledge that an electronic copy of my thesis must be lodged with the University Library and, subject to the General Award Rules of The University of Queensland, immediately made available for research and study in accordance with the *Copyright Act 1968*.

I acknowledge that copyright of all material contained in my thesis resides with the copyright holder(s) of that material. Where appropriate I have obtained copyright permission from the copyright holder to reproduce material in this thesis.

Publication during candidature

Peer-reviewed journal articles

Chandra, S. S., Surowiec, R., Ho, C., Xia, Y., Engstrom, C., Crozier, S., and Fripp, J. (2015b). Automated analysis of hip joint cartilage combining MR T2 and three-dimensional fast-spin-echo images. *Magnetic Resonance in Medicine*, DOI:10.1002/mrm.25598. http://dx.doi.org/10.1002/mrm.25598 (Chandra et al. 2015b)

Yang, Z., Fripp, J., Chandra, S. S., Neubert, A., Xia, Y., Strudwick, M. W., Paproki, A., Engstrom, C., and Crozier, S. (2015). Automatic bone segmentation and bone-cartilage interface extraction for the shoulder joint from magnetic resonance images. *Physics in Medicine and Biology*, 60(4):1441. http://stacks.iop.org/0031-9155/60/i=4/a=1441 (Yang et al. 2015)

Xia, Y., Chandra, S. S., Engstrom, C., Strudwick, M. W., Crozier, S., and Fripp, J. (2014). Automatic hip cartilage segmentation from 3D MR images using arc-weighted graph searching. *Physics in Medicine and Biology*, 59(23):7245. http://stacks.iop.org/0031-9155/59/i=23/a=7245 (Xia et al. 2014)

Chandra, S. S., Xia, Y., Engstrom, C., Crozier, S., Schwarz, R., and Fripp, J. (2014). Focused shape models for hip joint segmentation in 3D magnetic resonance images. *Medical Image Analysis*, 18(3):567--578, DOI:10.1016/j.media.2014.02.002. http://dx.doi.org/10.1016/j.media.2014.02.002 (Chandra et al. 2014)

Xia, Y., Fripp, J., Chandra, S. S., Schwarz, R., Engstrom, C., and Crozier, S. (2013). Automated bone segmentation from large field of view 3D MR images of the hip joint. *Physics in Medicine and Biology*, 58(20):7375. http://iopscience.iop.org/0031-9155/58/20/7375/ (Xia et al. 2013)

Journal manuscripts under review

Xia, Y., Fripp, J., Chandra, S. S., Walker, D., Crozier, S., and Engstrom, C. (2015). Automated 3D quantitative assessment and measurement of alpha angles from the femoral head-neck junction using MR imaging. *Physics in Medicine and Biology*. (Submitted) (Xia et al. 2015)

Peer-reviewed conference proceedings

Yang, Z., Crozier, S., Engstrom, C., Xia, Y., Neubert, A., Brancato, T., Schwarz, R., Lauer, L., Fripp, J., Chandra, S. S., and Salvado, O. (2012). Morphology-based interslice interpolation on manual segmentations of joint bones and muscles in MRI. In *Digital Image Computing Techniques and Applications (DICTA), 2012 International Conference on*, pages 1--8. http://dx.doi.org/10.1109/DICTA.2012.6411678 (Yang et al. 2012)

Chandra, S. S., Xia, Y., Engstrom, C., Schwarz, R., Lauer, L., Crozier, S., Salvado, O., and Fripp, J. (2012b). Unilateral hip joint segmentation with shape priors learned from missing data. In *Biomedical Imaging (ISBI), 2012 9th IEEE International Symposium on*, pages 1711--1714. http://dx.doi.org/10.1109/ISBI.2012.6235909 (Chandra et al. 2012b)

Xia, Y., Chandra, S., Salvado, O., Fripp, J., Schwartz, R., Lauer, L., Engstrom, C., and Crozier, S. (2012). Automated bone segmentation and bone-cartilage interface extraction from MR images of the hip. In *International Society for Magnetic Resonance in Medicine (ISMRM) 20th Annual Meeting & Exhibition: Adapting MRI in a Changing World* (Xia et al. 2012)

Xia, Y., Chandra, S. S., Salvado, O., Fripp, J., Schwarz, R., Lauer, L., Engstrom, C., and Crozier, S. (2011). Automated MR hip bone segmentation. In *Digital Image Computing Techniques and Applications (DICTA), 2011 International Conference on*, pages 25--30. http://dx.doi.org/10.1109/DICTA.2011.13 (Xia et al. 2011)

Publication included in this thesis

The following publications were included in this thesis, of which significant portions were used in parts of different chapters (Chapter 3, 4, 5 and 6).

- **Chapter 3** - (Xia et al. 2012; 2011; 2013)
- **Chapter 4** - (Xia et al. 2015)
- **Chapter 5** - (Xia et al. 2014)
- **Chapter 6** - (Xia et al. 2014)

For all these publications, individual contributions of all the authors are listed here.

Xia, Y., Fripp, J., Chandra, S. S., Schwarz, R., Engstrom, C., and Crozier, S. (2013). Automated bone segmentation from large field of view 3D MR images of the hip joint. *Physics in Medicine and Biology*, 58(20):7375. http://iopscience.iop.org/0031-9155/58/20/7375/ (Xia et al. 2013) - **incorporated in Chapter 3.**

Contributor	**Statement of contribution**
Ying Xia	Experiment design (20%), data collection (20%), code implementation (70%), execution of experiments (100%), analysis and interpretation (60%), manuscript preparation (100%)
Jurgen Fripp	Experiment design (20%), data collection (30%), code implementation (10%), analysis and interpretation (10%), manuscript review (30%)
Shekhar S Chandra	Experiment design (10%), data collection (10%), code implementation (20%), analysis and interpretation (10%), manuscript review (20%)
Raphael Schwarz	Experiment design (10%), data collection (10%), manuscript review (10%)
Craig Engstrom	Experiment design (20%), data collection (30%), analysis and interpretation (10%), manuscript review (30%)
Stuart Crozier	Experiment design (20%), analysis and interpretation (10%), manuscript review (10%)

Xia, Y., Chandra, S., Salvado, O., Fripp, J., Schwartz, R., Lauer, L., Engstrom, C., and Crozier, S. (2012). Automated bone segmentation and bone-cartilage interface extraction from MR images of the hip. In *International Society for Magnetic Resonance in Medicine (ISMRM) 20th Annual Meeting &*

Exhibition: Adapting MRI in a Changing World (Xia et al. 2012) **- incorporated in Chapter 3.**

Contributor	**Statement of contribution**
Ying Xia	Experiment design (20%), data collection (10%), code implementation (70%), execution of experiments (100%), analysis and interpretation (50%), manuscript preparation (100%)
Shekhar S Chandra	Experiment design (10%), data collection (10%), code implementation (20%), analysis and interpretation (10%), manuscript review (20%)
Olivier Salvado	Experiment design (10%), analysis and interpretation (10%)
Raphael Schwarz	Experiment design (10%), data collection (10%)
Lars Lauer	Experiment design (10%), data collection (10%)
Craig Engstrom	Experiment design (10%), data collection (20%), analysis and interpretation (10%), manuscript review (20%)
Jurgen Fripp	Experiment design (20%), data collection (30%), code implementation (10%), analysis and interpretation (10%), manuscript review (40%)
Stuart Crozier	Experiment design (10%), analysis and interpretation (10%), manuscript review (20%)

Xia, Y., Chandra, S. S., Salvado, O., Fripp, J., Schwarz, R., Lauer, L., Engstrom, C., and Crozier, S. (2011). Automated MR hip bone segmentation. In *Digital Image Computing Techniques and Applications (DICTA), 2011 International Conference on*, pages 25--30. http://dx.doi.org/10.1109/DICTA.2011.13 (Xia et al. 2011) **- incorporated in Chapter 3.**

Contributor	**Statement of contribution**
Ying Xia	Experiment design (20%), data collection (10%), code implementation (70%), execution of experiments (100%), analysis and interpretation (50%), manuscript preparation (90%)
Shekhar S Chandra	Experiment design (10%), data collection (10%), code implementation (20%), analysis and interpretation (10%), manuscript preparation (10%), manuscript review (30%)
Olivier Salvado	Experiment design (10%), analysis and interpretation (10%)
Raphael Schwarz	Experiment design (10%), data collection (10%)
Lars Lauer	Experiment design (10%), data collection (10%)
Craig Engstrom	Experiment design (10%), data collection (20%), analysis and interpretation (10%), manuscript review (30%)
Jurgen Fripp	Experiment design (20%), data collection (30%), code implementation (10%), analysis and interpretation (10%),

	manuscript review (30%)
Stuart Crozier	Experiment design (10%), analysis and interpretation (10%), manuscript review (10%)

Xia, Y., Fripp, J., Chandra, S. S., Walker, D., Crozier, S., and Engstrom, C. (2015). Automated 3D quantitative assessment and measurement of alpha angles from the femoral head-neck junction using MR imaging. *Physics in Medicine and Biology*. (Submitted) (Xia et al. 2015) **- incorporated as Chapter 4.**

Contributor	**Statement of contribution**
Ying Xia	Experiment design (30%), data collection (10%), code implementation (80%), execution of experiments (100%), analysis and interpretation (50%), manuscript preparation (100%)
Jurgen Fripp	Experiment design (20%), data collection (30%), code implementation (10%), analysis and interpretation (10%), manuscript review (20%)
Shekhar S Chandra	Experiment design (10%), code implementation (10%), manuscript review (20%)
Duncan Walker	data collection (20%), analysis and interpretation (10%)
Stuart Crozier	Experiment design (10%), analysis and interpretation (10%), manuscript review (10%)
Craig Engstrom	Experiment design (30%), data collection (40%), analysis and interpretation (20%), manuscript review (50%)

Xia, Y., Chandra, S. S., Engstrom, C., Strudwick, M. W., Crozier, S., and Fripp, J. (2014). Automatic hip cartilage segmentation from 3D MR images using arc-weighted graph searching. *Physics in Medicine and Biology*, 59(23):7245. http://stacks.iop.org/0031-9155/59/i=23/a=7245 (Xia et al. 2014) **- incorporated in Chapter 5 and 6.**

Contributor	**Statement of contribution**
Ying Xia	Experiment design (20%), data collection (10%), code implementation (80%), execution of experiments (100%), analysis and interpretation (50%), manuscript preparation (100%)
Shekhar S Chandra	Experiment design (10%), code implementation (10%), analysis and interpretation (10%), manuscript review (20%)
Craig Engstrom	Experiment design (20%), data collection (30%), analysis and interpretation (10%), manuscript review (30%)
Mark W Strudwick	Data collection (30%), analysis and interpretation (10%), manuscript review (10%)

Stuart Crozier	Experiment design (20%), analysis and interpretation (10%), manuscript review (10%)
Jurgen Fripp	Experiment design (20%), data collection (30%), code implementation (10%), analysis and interpretation (10%), manuscript review (30%)

Contributions by others to the thesis

Professor Stuart Crozier (primary supervisor): obtaining funding, conception and design of the project, analysis and interpretation of research data and critical revision of the thesis;
Dr. Jurgen Fripp (associate supervisor): obtaining funding, conception and design of the project, data collection, development of computer algorithms, analysis and interpretation of research data and critical revision of the thesis;
Dr. Craig Engstrom (associate supervisor): obtaining funding, conception and design of the project, data collection, manual delineation of the imaging data for the study in Chapter 5, analysis and interpretation of research data and critical revision of the thesis;
Dr. Shekhar S Chandra: analysis and interpretation of research data and critical revision of the thesis;
Dr. Mark W Strudwick: assistance with manual delineation of imaging data for the study in Chapter 3, 5 and 6;
Dr. Duncan Walker: radiological assessment of imaging data for the study in Chapter 4;
Kimberley Nunes: critical revision of the thesis;
Dr. Raphael Schwarz: conception and design of the study in Chapter 3, data collection;
Aiman Al-Najjar: assistance with magnetic resonance data acquisition.

Statement of parts of the thesis submitted to qualify for the award of another degree

None.

Acknowledgement

It will not be possible to get to this point without the kind help and support of the people around me.

First and foremost, I would like to thank my PhD supervisors, Prof. Stuart Crozier, Dr. Jurgen Fripp and Dr. Craig Engstrom, for their generous support and sound advice throughout my PhD period. I am fortunate to have such a great supervisory team with the professional guidance in comprehensive ways. Thanks to Prof. Stuart Crozier for the insightful suggestions and discussions as well as the regular meetings to keep my PhD candidature on track. Thanks to Dr. Jurgen Fripp who is always there to listen and to give advice and inspires me with brilliant ideas in my research. Thanks to Dr. Craig Engstrom for his invaluable advice from a clinical point of view, patiently explaining about anatomical and clinical knowledge and the meticulous editing to my manuscripts.

Thanks to Dr. Shekhar S. Chandra and Dr. Aleš Neubert for their experience sharing, encouragement and tremendous help offered. Thanks to Dr. Jason Dowling for allowing me to use his dataset and reviewing my manuscripts. Thanks to Dr. Mark W. Strudwick, Dr. Duncan Walker and Mr. Phillip Melville for their great patience and support for provision of time-consuming manual analyses in this research. Thanks to Kimberly Nunes and Anthony Paproki for reading chapters of this thesis and providing useful comments.

I also would like to thank Rachel Surowiec and Dr. Charles Ho from Steadman Philippon Research Institute (Vail, Colorado, USA) who kindly provided the access to their clinical hip MR data with professional manual analyses.

Last but not least, I would like to extend a special thanks to my parents, my little brother, all my close relatives and friends, who have been supportive throughout all my studies in every way imaginable.

The research in this thesis was funded by a UQ International scholarship and a CSIRO top-up scholarship.

Keywords

Bone, Cartilage, Femoroacetabular Impingement, Graph Search, Hip Joint, Magnetic Resonance Imaging, Quantitative Measurement, Segmentation, Statistical Shape Modelling

Australian and New Zealand Standard Research Classifications (ANZSRC)

ANZSRC code: 080106, Image Processing, 50%
ANZSRC code: 090399, Biomedical Engineering not elsewhere classified, 50%

Fields of Research (FoR) Classification

FoR code: 0801, Artificial Intelligence and Image Processing, 50%
FoR code: 0903, Biomedical Engineering, 50%

TABLE OF CONTENTS

Abstract i

Table of Contents xiii

List of Figures xvii

List of Tables xxiii

List of Abbreviations xxv

1 Introduction 1

1.1 Scope of the Research . . . 1

1.2 Motivation . . . 1

1.2.1 Clinical context . . . 1

1.2.2 Technical motivation . . . 2

1.3 Research Aims and Challenges . . . 3

1.4 Expected Contributions of the Thesis . . . 6

1.5 Organization of the Thesis . . . 7

2 Background and Methodological Overview 9

2.1 Basic Anatomy of the Hip Joint . . . 9

2.1.1 Bone structure . . . 9

2.1.2 Articular cartilage . . . 10

2.1.3 Labrum, capsular and ligamentous structures . . . 13

2.2 Hip Osteoarthritis and Femoroacetabular Impingement . . . 14

2.2.1 Osteoarthritis (OA) of the hip joint . . . 14

2.2.2 Femoroacetabular impingement (FAI) . . . 16
2.3 Imaging of the Hip Joint . . . 19
2.3.1 Plain radiography . . . 19
2.3.2 Computed tomography (CT) . . . 19
2.3.3 Magnetic resonance (MR) imaging . . . 20
2.4 Medical Image Segmentation . . . 26
2.4.1 Classical image analysis techniques . . . 27
2.4.2 Atlas-based segmentation . . . 27
2.4.3 Model-based segmentation . . . 28
2.4.4 Graph-based segmentation . . . 30
2.5 Methodological Overview . . . 31
2.5.1 MR data acquisition . . . 31
2.5.2 Segmentation methods . . . 32

3 Bone segmentation from large field of view 3D MR images of the hip joint 35
3.1 Introduction . . . 36
3.2 Materials and Methods . . . 37
3.2.1 Image dataset and MR acquisition protocol . . . 37
3.2.2 Training process: shape modelling and atlas creation . . . 38
3.2.3 Segmentation algorithms . . . 40
3.2.4 Validation method . . . 42
3.3 Results . . . 44
3.3.1 Inter- and intra-rater reliability . . . 44
3.3.2 Segmentation accuracy . . . 45
3.3.3 Hausdorff distance maps . . . 47
3.3.4 Computational time . . . 49
3.4 Discussion . . . 49
3.5 Conclusion . . . 53

4 Automated MR-based 3D quantitative assessment of the femoral head-neck junction 55
4.1 Introduction . . . 56
4.2 Materials and Methods . . . 57
4.2.1 Image datasets and MR acquisition protocols . . . 57

4.2.2 Manual bone segmentation and alpha angle measurements . . . 57
4.2.3 Automated MR-based 3D bone reconstruction and alpha angle measurements 58
4.2.4 Validation method and statistical analyses . . . 61
4.3 Results . . . 62
4.3.1 Intra- and inter-rater reliability of manual alpha angle measures from auto-extracted slices . . . 62
4.3.2 Comparisons between manual (ground truth) and automatic measures . . . 62
4.3.3 Comparisons between automatic measures of alpha angles from DESS and TrueFISP images . . . 64
4.4 Discussion . . . 66
4.5 Conclusion . . . 68

5 Automatic Cartilage segmentation from high-resolution 3D MR images of the hip joint 73
5.1 Introduction . . . 74
5.2 Previous work . . . 75
5.2.1 Manual and semi-automatic segmentation of hip joint cartilage . . . 75
5.2.2 Automatic segmentation of hip joint cartilage . . . 75
5.2.3 Optimal 3D graph search framework . . . 76
5.3 Materials and Methods . . . 77
5.3.1 MR image acquisition . . . 77
5.3.2 Multi-atlas based cartilage segmentation . . . 78
5.3.3 Our approach: model generation and graph-based cartilage segmentation . . . 78
5.3.4 Validation method . . . 87
5.4 Results . . . 88
5.4.1 Inter- and intra-rater reliability . . . 88
5.4.2 Segmentation accuracy . . . 88
5.4.3 Comparison with the multi-atlas-based method . . . 89
5.5 Discussion . . . 90
5.6 Conclusion . . . 91

6 Quantitative Analyses of the Cartilages and Its Reproducibility 97
6.1 Introduction . . . 98
6.2 Materials and Methods . . . 99

6.2.1 Data acquisition . . . 99
6.2.2 Quantitative analyses . . . 101
6.3 Results . . . 104
6.3.1 Quantitative analyses on TrueFISP images . . . 104
6.3.2 Reproducibility: DESS and SPACE images . . . 107
6.4 Discussion . . . 108
6.5 Conclusion . . . 111

7 General Discussion and Conclusion **119**
7.1 Key Contributions and Findings . . . 119
7.2 Implications of Findings . . . 121
7.3 Limitations of the Study . . . 122
7.4 Opportunities and Future Directions . . . 123
7.4.1 Bone and cartilage segmentation . . . 123
7.4.2 Quantitative analysis . . . 124
7.5 Conclusion . . . 124

Bibliography **125**

LIST OF FIGURES

1.1 Computer-aided system for MR images of the hip joint. 4

2.1 Articular surfaces of the hip joint (anterior view) (Used without permission from (Drake et al. 2009)). 10

2.2 Thickness variation of articular cartilage of the femoral head (left) and the acetabular lunate surface (right). A and B are designated reference grids, where the distance and angular direction of sampling points (black dots in C and D) are measured from the center of the femoral head and the acetabulum center. C and D show average contours of the thickness ranges indicated by the shaded codes below the diagrams (Used without permission from (Fagerson 1998)). 11

2.3 Cross-sectional diagram of healthy articular cartilage: A, cellular organization in the zones of articular cartilage; B, collagen fiber architecture. (Used without permission from (Sophia Fox et al. 2009)). 12

2.4 Ventral view of the intra-articular structure of the (right-side) hip joint after opening of the capsule and partial (top left) or complete (bottom right) exarticulation of the femoral head (Used without permission from (Paulsen and Waschke 2013)). 13

2.5 Illustration of (left) normal and (right) osteoarthritis hip joint (Used without permission from `http://www.everettboneandjoint.com/birmingham-hip-resurfacing/diseases.htm`) 15

2.6 Cross-section of a hip joint displaying (a) the normal femoral and acetabular anatomy, (b) cam FAI (bony excrescence causing reduced head-neck offset), (c) pincer FAI (acetabular over-coverage of the femoral head) and (d) mixed FAI. (Used without permission from (Lavigne et al. 2004)) 17

2.7 Bony bump (arrow) in cam-type FAI observed on (left) the AP pelvic view and (right) Dunn view at 45° of hip flexion. The alpha angle measurement (α) is illustrated in the latter view. (Used without permission from (Aliprandi et al. 2014)). 18

2.8 (a) Anteroposterior (AP) and (b) lateral radiographs of the hip joint (Used without permission from (Skripkus and Gentili 2006)); (c) demonstrates medial OA features observed on plain radiographs including joint space narrowing (balck arrow), osteophyte formation (white arrow) and abnormal head-neck offset (open arrow) (Used without permission from (Karachalios et al. 2007). 20

2.9 High-resolution large field-of-view MR images within the hip region acquired at 3.0 T from the same subject: (a) water-excitation DESS ($0.67 \times 0.67 \times 0.61$ mm^3), (b) MEDIC ($0.65 \times 0.65 \times 0.70$ mm^3) and (c) 3D proton density-weighted fat suppression SPACE ($0.77 \times 0.77 \times 0.70$ mm^3). 21

2.10 High-resolution MR imaging of hip joint cartilage at 7 T: (a) 3D water-excitation FLASH and (b) 3D frequency-selective fat suppressed VIBE sequences at a resolution of $0.23 \times 0.23 \times 1.5$ mm^3 (Used without permission from (Chang et al. 2014)). 24

2.11 MR artifacts observed in the image of the hip joint: (a) bias field in water-excitation DESS image with a large field-of-view of bilateral hip joints and (b) partial volume averaging in water-excitation DESS image with a small field-of-view of the right-side hip joint. . . . 25

2.12 Different shapes of the proximal femur with varying shape parameters b_1 and b_2 for (a) first and (b) second mode of variation of the SSM, respectively. 29

3.1 Example (top) coronal and (bottom) axial slices of MR images with multiple sequences as well as an example of manual segmentations of the proximal femur (blue, green) and innominate (brown, red) bone elements: (a) MEDIC; (b) DESS; (c) manual labels overlaying on a DESS image. 38

3.2 Illustrative shape model creation process. 39

3.3 Hip bone shape models with the colour map illustrating normalized variation of the primary mode: (a) the bilateral hip SSM; (b) the unilateral hip SSM; (c) innominate bone SSM; (d) femur SSM. 41

3.4 The compactness of (a) the bilateral hip SSM, (b) the unilateral hip SSM and (c) SSMs of the proximal femur and innominate bone. 41

3.5 Flow diagram of the multi-atlas-based and ASM-based segmentation pipelines. 43

3.6 Illustrative ASM segmentation process using an example SSM of the innominate bone. . 44

3.7 Example coronal slices of bone segmentation results with DSC values for the multi-atlas method (left) and ASM-based method (right): (a) below the mean DSC showing over/under-segmentation occurred (arrows); (b) around the mean DSC; (c) above the mean DSC. . . 45

3.8 Histograms of DSC values for the (left) proximal femur and (right) innominate bone segmentations using (a) multi-atlas-based method and (b) ASM-based method (light blue: left-side cases and blue: right-side cases). 46

3.9 DSC scores for automatic segmentations of the proximal femur (green) and innominate bone (yellow) obtained at (left) initialization, (middle) ASM-based segmentation and (right) bone surface relaxation stage in the ASM-based segmentation pipeline. 46

3.10 Statistical analyses of automated segmentation results: (a) scatter plots plus the regression lines for automated and manual segmentation: $R^2_{\text{Multi-atlas}} \simeq 0.948$, $R^2_{\text{ASM}} \simeq 0.975$ for the proximal femur and $R^2_{\text{Multi-atlas}} \simeq 0.974$, $R^2_{\text{ASM}} \simeq 0.981$ for the innominate bone; (b) Bland-Altman plots showing the relative volume differences against the logarithm of the average of automated and manual volumes. (The colored regions indicate the confidence intervals of ± 1.96 standard deviation (SD) limits for each automated segmentation method.) 48

3.11 Comparison of mean and SD Hausdorff distance maps computed from the validation results of both sides using the multi-atlas-based method (left) and ASM-based approach (right) focusing on the femoral head (dashed circle 1) with fovea (dashed circle 2) and acetabulum (dashed circle 3) and inferiolateral lunate (dashed circle 4) regions. 50

3.12 Example manual (top), automated multi-atlas (middle) and automated ASM (bottom)) segmentations of the head-neck region (dashed circle) of the femur including the directed Hausdorff distance maps with: (a) normal geometry of the head-neck junction (no cam-type abnormality), (b) moderate cam-type abnormality (arrows) and (c) large cam-type abnormality (arrows). 51

3.13 Segmentation accuracy for various ϕ used in the multi-atlas-based segmentation pipeline from 0, i.e., using all the atlases, to 0.99, i.e., using the most similar atlas: (a) average DSC values with regions of 95% confidence interval for segmentations of the proximal femur and innominate bone against ϕ; (b) the histogram of failed segmentations (DSC $<$ 0.8) for both the proximal femur and innominate bone with various ϕ values. 54

3.14 Example multi-atlas-based bone segmentations for MR images with: (a) different FOV and (b) varied anatomical structure (i.e., the female subject). 54

4.1 Example coronal slices of MR images acquired from the same subject using (a) bilateral DESS and (b) unilateral TrueFISP sequences. (Red dash line in (a) the DESS image slice (a) indicates a small FOV used in (b) the paired TrueFISP examination.) 57

4.2 Examples of manual alpha angle measurements for the (a) anterosuperior and (b) anterior positions of the FHN junction from auto-extracted 2D radial planes reformatted from bilateral DESS images. 58

4.3 Workflow diagram of automated alpha angle measurement scheme for assessment of cam lesions from MR images of the hip joint. 59

4.4 Statistical analyses of manual alpha angle measures at the (a, c) anterosuperior and (b, d) anterior positions between Rater 1 and Rater 2 based on automatic image reformation process in the dataset of 30 bilateral DESS images for hip joints of both sides: (a-b) are the scatter plots with the regression lines (r is the Pearson's correlation coefficient), (c-d) are the Bland-Altman plots. 63

4.5 (a) Mean and (b) standard deviation maps of directed Hausdorff distances computed from validation results of the bilateral DESS (N = 30) and unilateral TrueFISP (N = 18) examinations. 64

4.6 Statistical analyses of alpha angles at the positions of (a,c) 45° and (b,d) 90° of the FHN junction measured between the manual method based on automatic image reformation process and the proposed automated assessment scheme from 30 bilateral DESS images: (a-b) are the scatter plots with the regression lines (r is the Pearson's correlation coefficient), (c-d) are the Bland-Altman plots. 65
4.7 Representative auto-extracted 2D radial slices at five different positions in the upper anterior quadrant of the FHN junction (from left to right, 0°, 30°, 45°, 60°, 90°) from (top) DESS and (bottom) TrueFISP examinations of the right hip joints with (a) big and (b) small alpha angles (Red arrows indicating the perceptible cam-type lesion). 69
4.8 (a) Average alpha angle curves with regions of 95% CI across all positions 0° - 180° of the FHN junction and (b) linear correlation plots and boxplots of alpha angles at four preselected positions (30°, 45°, 60°, 90°) in the upper anterior quadrant of the FHN junction in the reproducibility test between paired DESS and TrueFISP scans from 18 subjects. . . 70
4.9 Example assessment results for hip joints having (a) smaller anterosuperior and anterior alpha angles, (b) a larger anterosuperior alpha angle, (c) larger anterosuperior and anterior alpha angles: (from left to right) diagrams of alpha angles (blue dots) around the FHN junction (The red line indicates the average alpha angle contour computed from the bilateral DESS images (i.e., 60 hips).), anterosuperior radila slices, anterior radial slices and 3D visualization of the segmented femur surfaces. 71
4.10 Comparisons of manual and automatic alpha angle measures in cases having varying presence of osteophytes at the anterosuperior position of the FHN junction. 72

5.1 Example (a) sagittal and (b) oblique coronal reformatted MR slice (top right, in-plane resolution: 0.234 mm, slice thickness: 0.490 mm) with manual labels (bottom right, red: femoral cartilage, purple: acetabular cartilage) overlaid on the zoomed region of the hip joint (left), with weak to non-existent boundaries between the femoral and acetabular cartilage plates (arrows show the bright signal of synovial fluid). 76
5.2 Automatic segmentation scheme for the articular cartilage from MR images of the hip joint. 79
5.3 Cartilage probability and thickness measures of the acetabular (left) and the femoral head (right) cartilage models of the hip joint based on manual segmentations from the training dataset of 46 subjects: (a) probability of segmented cartilage tissue being present (valued 0 to 1), (b) average and (c) standard deviation of cartilage thickness (in mm) mapped to the atlas bone surfaces of the acetabulum and femoral head. 80
5.4 Articular interacting regions on the femoral head and acetabulum with the projection from the average thickness map of the (a) acetabular and (b) femoral cartilage plates using one-to-one correspondences built from BCI surface coupling. Dashed circles show the corresponding regions between (left) the articular interacting regions and (right) reference average cartilage thickness maps in the articular cartilage model. 81
5.5 Examples showing the construction of the multi-object graph with inter-object arcs at the interacting regions within the hip joint. G_F is the dual-surface graph constructed from the femoral BCI and G_A is the dual-surface graph constructed from the acetabular BCI. . . . 83

5.6 The construction of an arc-weighted graph for example showing (a) surface smoothness constraints between the neighboring column $N_i(v_p)$ and $N_i(v_q)$, $\overline{\Delta}_{p,q} = 1$, $\sigma_{p,q} = 2$, $\alpha_1 = 1$; (b) inter-surface distance constraints between two columns $N_0(v_p)$ and $N_1(v_p)$ at the vertex v_p, $\overline{\Lambda}_p = 2$, $\phi_p = 1$, $\alpha_2 = 1$. 84

5.7 Boxplots of validation results with example slices for maximum, median, minimum DSC values for the combined, femoral and acetabular cartilage volumes (red - region in common, yellow - only in manual segmentations, blue - only in automatic segmentations). . . 93

5.8 (a) 2D MR slices (top) with overlaid cartilage segmentations (bottom) (green - femoral cartilage, red - acetabular cartilage) and (b) 3D visualization of smoothed cartilage volumes (green - femoral cartilage, orange - acetabular cartilage) with the reference of (proximal femur, acetabulum) bone surfaces obtained from an example automatic segmentation results around the mean DSC of (0.79, 0.76, 0.74) for the (combined, femoral, acetabular) cartilage. 94

5.9 DSC results for segmentation of the (a) combined, (b) femoral and (c) acetabular cartilages obtained using the multi-atlas-based method (dashed line) and our proposed method. The results are sorted based on DSC scores of the combined cartilage segmentations from our approach (Asterisk symbols indicate cases with an evident drop of the DSC value using the multi-atlas-based method). 95

5.10 Overlaid segmentations for (a) case 18, (b) case 11 and (c) case 45 obtained using (top) the multi-atlas-based method and (bottom) our proposed method. 96

6.1 Example coronal slices of MR images acquired from the right-side hip joint of the same subject with three different sequences: (a) TrueFISP, (b) DESS and (c) SPACE. 100

6.2 (a) Partitioned regions with associated regional descriptors for the (top) acetabular and (bottom) femoral cartilages of the hip joint based on manual landmarks (red dots), which were illustrated using a 3D innominate bone volume from the left-side hip joint and a bone volume of proximal femur from the right-side hip joint, respectively; (b) Example manual cartilage segmentation overlaid on both the (left) 3D SPACE and (right) T2 echo as slices of the 3D image volume. (Used with permission from (Chandra et al. 2015b; Ho et al. 2014)) 102

6.3 Cartilage thickness measurement illustrated on an example 2D slice overlaid with manual cartilage contours. The example slice is assumed to go through the estimated center of the femoral head. Point A, B and C are the intersection points on the dashed line from the femoral head center with the inner acetabular cartilage interface, the outer acetabular cartilage interface (or outer femoral cartilage interface) and the inner femoral cartilage interface, respectively. The cartilage thickness is measured as the distance between A and B for the acetabular cartilage plate, between B and C for the femoral cartilage plate. . . . 103

6.4 Comparative analyses between automatic and manual cartilage volume data:(left) scatter plots with linear regression lines and (right) Bland-Altman plots of volume segmentations for the (a, b) combined, (c, d) femoral and (e, f) acetabular cartilages. Segmentations of the combined and individual femoral and acetabular cartilage volumes were from all TrueFISP images of 46 subjects. 105
6.5 Cartilage thickness maps:(a) average thickness with color scale (0 - 2.5 mm) for automatic segmentations and (b) absolute thickness difference against manual segmentations from the set of 46 TrueFISP images with color scale (0 - 1.0 mm) for the femoral and acetabular cartilage. 107
6.6 Example 3D visualization of the segmented cartilage volumes with the partitioned regions (see Figure 6.2a) for the individual (a) acetabular and (b) femoral cartilage plates obtained from a 3D high-resolution TrueFISP image. 109
6.7 Boxplots display the average thickness in each partitioned subregion of the individual (a) acetabular and (b) femoral cartilage plates calculated from automatic segmentations of 46 TrueFISP images. Asterisks indicate significant differences between the partitioned subregions. 113
6.8 Example 2D axial MR slices with overlayed cartilage segmentation contours obtained from MR examinations of case 11 using three different acquisition sequences: (a) TrueFISP, (b) DESS and (c) SPACE. 114
6.9 3D visualizations of the (a) acetabular and (b) femoral cartilage volumes automatically segmented from three different MR examinations of case 11: (from *left* to *right*) TrueFISP, DESS, SPACE. 115
6.10 Volume measurements of the (a) combined, (b) femoral and (c) acetabular cartilages for each case obtained from automatic segmentations of TrueFISP, DESS and SPACE scans as well as manual segmentations from TrueFISP images in the dataset of 18 subjects. . . 116
6.11 Average thickness maps with color scale (0 - 2.5 mm) for automatic segmentations of the (a) femoral and (b) acetabular cartilage plates obtained from manual or automatic segmentations of MR examinations in 18 volunteers: (from *left* to *right*) manual segmentations (ground truth), TrueFISP, DESS, 3D SPACE. 117

LIST OF TABLES

2.1 Acquisition parameters for each MR sequence. 32

3.1 Comparison of validation measures (mean ± SD) between the multi-atlas and ASM based method. 44

5.1 Inter- and intra-rater reliability of manual segmentations for the combined, femoral and acetabular cartilage volumes. 89

5.2 Comparative volumetric and distance-based validation metrics for comparisons between manual and automatic segmentations of the combined, femoral and acetabular cartilage plates. The obtained automatic cartilage segmentations were obtained using the multi-atlas-based (state-of-the-art) and our proposed segmentation method, respectively. 92

6.1 Cartilage thickness (mm) statistics within the majority of the articulating surfaces for the femoral and acetabular cartilage plates obtained from manual and automatic segmentations of all 46 TrueFISP images. 108

6.2 Quantitative volume and thickness measurements of the partitioned subregions for the individual femoral and acetabular cartilage plates. 112

LIST OF ABBREVIATIONS

***d*GEMRIC**	delayed gadolinium-enhanced magnetic resonance imaging of cartilage 24, 25, 74, 110, 122, 124
2D	two-dimensional 19, 21, 22, 52, 56, 60, 61, 64, 66, 67, 75, 91, 98, 109, 110, 122
3D	three-dimensional i, ii, 1, 3--8, 19, 21, 22, 30, 31, 35, 37, 49, 51--53, 55--62, 64--68, 73--76, 79--81, 88, 90, 91, 97--101, 103, 104, 106, 108--110, 119--122, 124
ANOVA	analysis of variance 62, 66, 99, 104, 106
AP	anterior-posterior 17, 19
ASM	active shape model i, ii, 29, 32, 35, 37, 40, 42, 45, 47--49, 51--53, 55, 59, 60, 66, 73, 74, 80, 81, 90, 103, 120, 122
BCI	bone-cartilage interface 3, 4, 32, 47, 48, 51--53, 73, 74, 76, 78, 79, 81, 82, 85, 86, 89--91, 98, 101, 102, 120, 121, 123
BMI	body mass index 57, 77
CEST	chemical exchange saturation transfer 25
CI	confidence interval 44, 45, 62, 65
CoV	coefficient of variation 98
CPU	central processing unit 49
CT	computed tomography 15, 19, 20, 27, 32, 38, 39, 42, 52, 56, 75, 77
DESS	dual echo steady state ii, xxi, 22, 31, 35, 37, 38, 40, 45, 47, 49, 52, 53, 55--58, 61--68, 91, 97, 99--101, 107, 108, 110, 120--122
DSC	Dice's similarity coefficient 37, 43--47, 49, 51--53, 58, 61, 62, 75, 87--90, 120, 121
ECM	extracellular matrix 12, 13, 24
FAI	femoroacetabular impingement i, ii, 2, 7, 14, 16--20, 25, 36, 37, 49, 51, 52, 56, 66, 67, 119, 121, 122, 124
FFE	fast-field echo 22
FHC	femoral head center 60--62, 64, 67

FHN femoral head-neck 2, 4, 5, 7, 8, 16--20, 37, 49, 51, 53, 55--58, 60--62, 64--68, 120, 121, 123, 124

FIESTA fast imaging employing steady-state acquisition 22

FLASH Fast Low-Angle Shot 21, 22, 98, 109

FN femoral neck 60--62, 64, 67

FOV field of view ii, 6, 23, 31, 35--37, 42, 47, 49, 52, 57, 77, 78, 81, 100, 101, 120

FS femoral shaft 60, 62, 64, 67, 91

FSE fast spin-echo 21, 22, 122

GAGs glycosaminoglycans 24, 25

GRAPPA Generalized Autocalibrating Partially Parallel Acquisition 31

HOAMS Hip Osteoarthritis MRI Scoring System 100

HSD honestly significant difference 104, 106, 107

ICC intra-class correlation coefficient 44, 45, 62, 66

JSW joint space width 19

LOGISMOS layered optimal graph image segmentation of multiple objects and surfaces 90

MASD mean absolute surface distance 43, 44, 47, 49, 61, 62, 87, 120

MEDIC multi echo data image combination ii, 22, 31, 35, 37, 38, 45, 47, 49, 52, 53, 75, 91, 98, 109, 120, 122

MPR multiplanar reformation 21

MR magnetic resonance i, ii, 1--8, 15, 17, 19--27, 31, 32, 35--38, 40, 42, 45, 47, 49, 51--53, 55--57, 59--61, 65--68, 73--77, 88, 90, 91, 97--101, 107--111, 119--124

MRF Markov random field 123

MSK musculoskeletal 1, 38, 77

NMI normalized mutual information 40, 41, 78

NMR nuclear magnetic resonance 26

NRR non-rigid registration 28, 37, 39, 40, 52, 78

OA osteoarthritis i, ii, 1--3, 5, 8, 14--16, 19, 20, 22, 25, 31, 36, 37, 53, 55, 56, 73--75, 77, 91, 98, 99, 110, 111, 119, 121--124

PCA principal component analysis 29, 36, 37, 39, 49, 56

PDM point distribution model 29

PDw proton density weighted 99, 100

PVE partial volume effects 6, 24, 26, 27, 32, 74, 76, 90, 101, 110, 123

RAVD relative absolute volume difference 43, 44, 87--89

RMS root mean square 62, 64

ROI region of interest 26, 60, 61, 74, 78, 106, 109, 122

RVD relative volume difference 47

SD standard deviation xix, 30, 37, 44, 45, 47, 48, 51, 62, 64, 79, 86--89, 104, 106, 108, 109

SMILI Simple Medical Imaging Library Interface 58

SNR signal-to-noise ratio 6, 22--24, 101

SPACE 3D turbo spin echo with variable flip angle ii, xxi, 22, 31, 75, 91, 97, 99--101, 103, 107, 108, 110, 120--122

SPGR spoiled gradient echo 21, 22, 98, 122

SPRI Steadman Philippon Research Institute 99, 101, 103, 110

SSFP steady-state free precession 22

SSM statistical shape model 28--30, 32, 35, 36, 39, 42, 49, 52, 60, 79, 81, 123

THA total hip arthroplasty 2, 16

TrueFISP True Fast Imaging with Steady-state Precession ii, xxi--xxiii, 22, 31, 55, 57, 61, 62, 64--68, 73, 75, 77, 78, 81, 88--91, 97, 99--101, 103, 104, 106--108, 110, 120, 121, 123

VIBE Volumetric Interpolated Breath-hold Examination 22

WOMAC the Western Ontario and McMaster Universities Osteoarthritis Index 15

1 INTRODUCTION

1.1 Scope of the Research

This research focuses on the development of a novel computer-aided system for three-dimensional (3D) magnetic resonance (MR) images of the hip joint that incorporates advanced image segmentation and quantification techniques. The scope of this system will be, given an input 3D MR image, to:

1. Automatically segment articular elements including the bones (i.e., the proximal femur, the innominate bone) and articular cartilages (i.e., the femoral and acetabular cartilage plate) within the hip joint and;
2. Perform quantitative measurements of the segmented structures for provision of reliable and reproducible morphometric data.

The hypothesis behind this research is that accurate and reproducible quantitative data can be automatically obtained from high-resolution noncontrast-enhanced 3D MR images of the hip joint, through the use of advanced image processing techniques.

This thesis constitutes part of a larger research project known as Musculoskeletal (MSK) Segmentation project, which is a collaboration between the School of Information Technology and Electrical Engineering, University of Queensland, Australia, CSIRO Digital Productivity and Services Flagship, Australian e-Health Research Centre, Australia, and Siemens Healthcare, Erlangen, Germany. The aim of this MSK project is to develop automated quantitative joint analysis systems based on advanced and innovative MR image processing algorithms for clinically-based morphometric and biochemical analyses of the bone, articular cartilage and intra-articular tissues of joints within upper and lower limb, as well as the spine.

1.2 Motivation

1.2.1 Clinical context

Osteoarthritis (OA) is a progressive degenerative disease of joints affecting over 1.8 million Australians (AIHW 2014). It is predominantly present in the large weight-bearing joints such as the hip

and knee, which causes joint pain, swelling, stiffness and reduced joint mobility leading to a significant functional impairment and disability (Dagenais et al. 2009; Felson 2006). In the hip joint, advancing stages of OA are associated with irreversible cartilage loss with concomitant changes in the subchondral bone (e.g., marginal outgrowths, osteophytes and bony sclerosis) and pathophysiological changes to soft-tissue structures in and around the joint (e.g., synovium, ligaments and surrounding muscles) (Felson et al. 2000; Roemer et al. 2011). Symptoms from this cartilage degradation may include groin pain, stiffness and subsequent deformity of the hip joint, which eventually progress to severe conditions requiring surgical intervention in the form of total hip arthroplasty (THA). While early joint structural abnormalities often present prior to the onset of clinically apparent hip OA, defining and characterizing early and pre-osteoarthritic conditions is important in assessing the trajectory of disease development and progression as well as developing and evaluating strategies for prevention and treatment of hip OA (Chu et al. 2012; Ding et al. 2010).

Femoroacetabular impingement (FAI) has been widely suggested to be a pre-osteoarthritic mechanism (Ganz et al. 2003; Tanzer and Noiseux 2004). Cam-type FAI characterized by an abnormal shape of the femoral head-neck (FHN) junction can result in abnormal shear and compressive forces during flexion and internal rotation of the hip joint, which instigates the initial chondrolabral damage at the acetabular rim and further acetabular cartilage lesions (Tannast et al. 2008; Wagner et al. 2003). Accurate detection and quantification of cam lesions may therefore assist initiating appropriate therapy for cam-type FAI and reducing the subsequent damage to the articular cartilage and associated surrounding soft tissues before the onset of hip OA.

Clinically, plain radiography (X-ray) is the standard imaging modality to assess the structural anatomy of the hip joint and to examine related disease conditions such as joint spacing narrowing in OA and abnormal FHN junction in cam-type FAI. However, plain radiographs do not directly demonstrate the articular cartilage and have been considered to be insensitive to diagnose early stages of OA (Karachalios et al. 2007). In contrast, MR imaging is an optimal tool for *vivo* assessment of the full joint structure including the bones and articular cartilages. It provides multiplanar capabilities, no ionizing radiation, a direct, thorough visualization of the cartilage and superb contrast between the cartilage and other surrounding tissues (Burstein et al. 2000; Karachalios et al. 2007). Therefore, these bring about extensive clinical interest in the development of MR technologies to quantitatively analyze the cartilage morphology (e.g., volume, thickness and surface area) (Li et al. 2008) and to assess biochemical compositions of the hyaline cartilage (Bittersohl et al. 2009; Carballido-Gamio et al. 2008b) as well as to evaluate other articulating structures (e.g., the osseous tissue, labrum) (Roemer et al. 2011) that facilitates early diagnostic and management options for hip OA and pre-osteoarthritic conditions such as FAI.

1.2.2 Technical motivation

Quantitative measurements of the bones and articular cartilages can provide reliable morphometric data from the complex MR image information for potential use in research and clinical studies about pathoanatomical conditions of the hip joint such as early OA and FAI.

The segmentation of the anatomy of interest, i.e., the articulating bones and cartilages within the hip joint in this research, is an essential prerequisite for subsequent quantitative analyses. In order to precisely capture small morphological changes, particularly for the individual cartilage layer normally with 1∼3 mm thickness, this segmentation process must be performed with a high level of accuracy, robustness and reliability, which, in most clinical studies, was performed using fully manual or semi-automatic methods (Li et al. 2008; Naish et al. 2006). The disadvantages of these manual/semi-automated approaches are that they are very time-consuming and require skilled operators with considerable experience but still have considerable inter- and intra-rater variability, particularly under the influence of poor image quality, insufficient tissue contrast and various MR artefacts.

The development of a fully automatic segmentation method for MR images of the hip joint is highly desirable not only to circumvent the need for the time- and expertise-intensive manual/semi-automated methods but also to facilitate the provision of reliable and reproducible morphometric data for dedicated use in large-scale research and clinical investigations about early and pre-OA of the hip joint. However, this task is very challenging due to anatomical (e.g., the deeply located hip joint structure and very thin, highly spherical articular cartilage) and imaging (e.g., the limited image resolution, complex tissue contrast and inhomogeneity in signal) difficulties.

1.3 Research Aims and Challenges

There are two main aims in this research in order to realize the proposed computer-aided system (see Figure 1.1):

Aim 1: To develop and evaluate a fully automated segmentation approach with advanced image segmentation techniques in order to deliver accurate and reproducible bone and cartilage segmentations from high-resolution 3D MR images of the hip joint;

- **Aim 1.1:** *To develop and evaluate the 3D automatic MR-based approach for segmenting the articulating bones within the hip joint;*

  At the initial stage of this thesis, an automatic MR-based approach needs to be implemented to deliver accurate segmentations of the bone elements (i.e., the proximal femur and innominate bone) of the hip joint. The fulfilment of this aim will not only provide a basis for quantitative measures of the bone morphology (**Aim 2.1**), but also allow the extraction of reliable bone-cartilage interfaces (BCIs), which can be served as an initial reference framework for subsequent cartilage segmentation (**Aim 1.2**). This proposed segmentation method needs to be carefully validated against manually segmented volumetric data of the bones using various volume and distance based validation metrics in a dataset of high-resolution 3D MR images of the hip joint with different acquisition sequences.

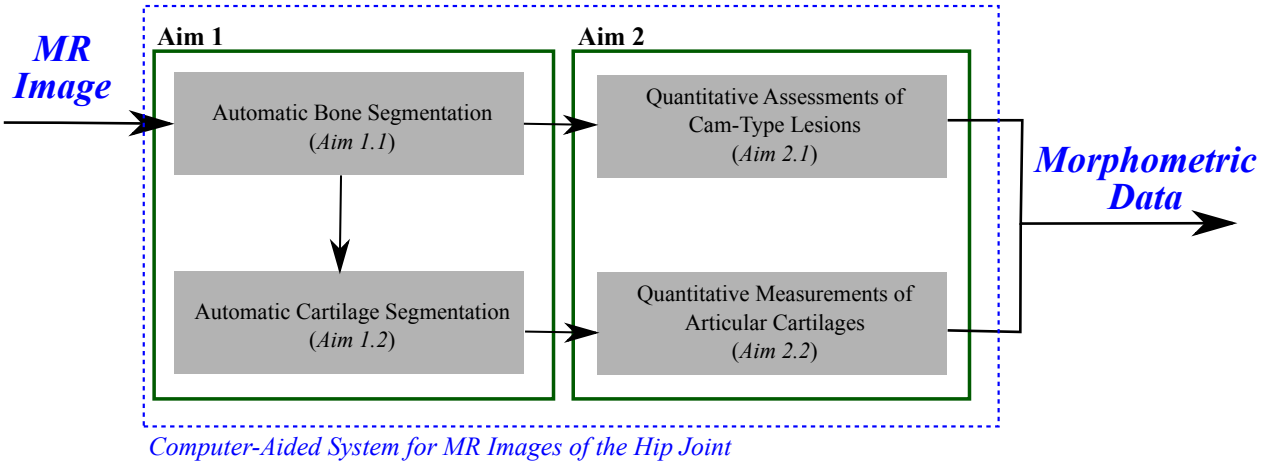

Figure 1.1: Computer-aided system for MR images of the hip joint.

- **Aim 1.2:** *To develop and evaluate the 3D automatic MR-based approach for segmenting the hip joint cartilages.*

  Accurate segmentation of the articular cartilage is important for subsequent quantitative measurements of the cartilage morphology (**Aim 2.2**). It is extremely problematic to develop an automatic segmentation method for the hip joint with the highly spherical and very thin cartilage with a large anatomical variability. In most previous studies, this segmentation task is manually performed by well-trained clinical analysts.

  The proposed cartilage segmentation approach will be developed based on the reliable BCIs, an initial reference framework established from the bone segmentations (**Aim 1.1**). The individual femoral and acetabular cartilage plates need to be well delineated with a good accuracy from MR images of the hip joint without auxiliary techniques such as continuous leg traction (Nishii et al. 1998). It will thereby allow small changes of the cartilages to be captured in the following quantitative analyses. The evaluation needs to be performed using manually segmented cartilage volumetric data from a dataset of high-resolution 3D MR images.

Aim 2: To automatically extract reliable and reproducible morphometric data based on the segmented subchondral bones and articular cartilages.

- **Aim 2.1:** *To automatically extract reliable and reproducible 3D morphological information of the head-neck junction from the segmented surface of the proximal femur;*

  Morphological measurements of the FHN junction based on 3D volumetric data of the proximal femur from MR images provide great potential to accurately detect and quantify possible cam-type lesions that always present on a patient-specific basis. The traditional quantitative assessment of cam lesions is performed on plain radiographs, which has inherent limitations in two-dimensionally depicting the variable osseous deformities and visualizing potential dam-

ages to the radiolucent articular cartilage. The development of a 3D quantification method is necessary to extract reliable quantitative data of the bone morphology at the FHN junction for assessing possible cam-type lesions from MR images.

The proposed quantification method will be performed based on the segmented 3D surface of the proximal femur. The alpha angle, the most common radiographic measure (Nötzli et al. 2002), will be automatically measured around the circumference of the FHN junction. The validity and reliability of the proposed automatic quantitative measurement method will be evaluated using manual alpha angle measures from auto-extracted reformatted radial MR images in the hip joints with varying FHN junction presentations.

- **Aim 2.2:** *To perform quantitative measurements of the segmented femoral and acetabular cartilages within the hip joint.*

  Quantitative measurements of hip joint cartilages provide great potential to deliver useful morphometric information for assessment of the hip joint in pathoanatomical conditions such as early and pre-OA. Morphometric data of articular cartilages from healthy hip joints can also provide reference values to underpin quantitative biomarker imaging for characterization of pre-osteoarthritic conditions in research and clinical studies, which target modifiable disease stages in OA to monitor pathophysiological processes and evaluate therapeutic interventions during the earliest stages of degeneration (Chu et al. 2012).

  The proposed measurements will be mainly centred on the volume and thickness of the individual femoral and acetabular cartilage plates, which are considered to be sensitive to subtle changes at very early stages of cartilage degeneration (Li et al. 2008; Nishii et al. 2004). The volume measurement is a direct numerical integration of the cartilage voxels indicating the global cartilage loss to a certain degree. The cartilage thickness is an efficient measurement of localized morphological changes that can be qualitatively visualized as a thickness map across the articulating surface of each cartilage plate. Moreover, subregional analyses of the femoral and acetabular plates offer a more sensitive tool to accurately locate abnormal changes of the cartilage in independent subregions and better understand the trajectory of the degeneration which often starts with small focal lesions.

  A preliminary evaluation will be performed to compare the morphometric data obtained from manual and automatic cartilage segmentations from high-resolution 3D MR images. The reproducibility will be also investigated using several MR acquisition protocols with different spatial image resolutions and tissue contrast characteristics.

To achieve the above aims, there are some challenges that can be summarized in three major aspects, which will be further explained in the following chapter in the aspects of the anatomical,

imaging and technical background in the following chapter:

- **Anatomical structure**: The articular cartilages are relatively thin and highly curved within the ball-and-socket hip joint deeply located in the human body. Wyler et al. (2009) has recently reported a mean cartilage thickness range of 0.32 - 2.83 mm on the femoral head and 0.95 - 3.13 mm on the acetabulum according to a MR-arthrographic evaluation on 12 normal cadaver hips. Furthermore, the individual femoral and acetabular cartilage plates are closely apposed, which, with limited image resolution, makes it difficult to discern between two cartilage plates, particularly in the weight-bearing areas (Nishii et al. 1998). Although this issue has been addressed in previous studies using leg traction devices during the acquisition process (Cheng et al. 2013; Nishii et al. 2004; Sato et al. 2001), it might not be suitable in our study targeting routine MR imaging examinations.

- **MR acquisition**: MR imaging of the hip joint is more challenging than the knee given that it is deeply located in the body and surrounded by a large group of muscles with complex attachments to tendons. The use of a general body coil or a phased array coil rather than a dedicated hip surface array coil also makes it difficult to obtain a high spatial resolution with adequate signal-to-noise ratio (SNR) and contrast-to-noise ratio between bone, cartilage, synovium and other soft tissues. Moreover, various imaging artefacts including noise, partial volume effects (PVE) and intensity inhomogeneity commonly seen in MR images of the hip joint can affect accurate depiction of the articular cartilages as well as reliable detection of the cartilage lesions.

- **Segmentation algorithm**: The development of a fully automatic segmentation method for the hip joint cartilages is quite difficult due to a combination of factors including the morphological variety of the cartilages, unsatisfying image quality and limited resolution in MR images, particularly for routine clinical examinations. To be of clinical significance, automatic segmentation algorithms need to be accurate, precise and reliable to allow small changes to be captured in cases across a wide range of the cartilage morphology as well as from a variety of MR images using different acquisition protocols (e.g., sequence, field of view (FOV), tissue contrast, in-plane image resolution).

1.4 Expected Contributions of the Thesis

The major expected contributions of the research lie in the development and validation of automatic segmentation and quantification approaches being proposed:

- **Automatic segmentation of the bone elements within the hip joint**
  Methods will be developed for automatic segmentation of the bones in the hip region, i.e., innominate bones and proximal femurs, using different advanced image segmentation techniques. A validational study will be performed to evaluate automatic bone segmentations against manual segmentations from high-resolution 3D MR images of the hip joint region, which demonstrates the capacity for generating morphometric data on the subchondral bone of the hip joint and pro-

viding a basis for subsequent cartilage segmentation.

- **3D assessment of the femoral head-neck (FHN) junction for cam-type FAI**
  The 3D segmentation of the proximal femur offer opportunities for accurately visualizing and quantifying possible cam-type lesions. Based on 3D reconstructions of the proximal femur from MR images, a method will be presented to automatically evaluate 3D bone morphology and provides alpha angle measurements around the circumference of the FHN junction. The proposed method will deliver reliable and reproducible measurements, particularly at the anterosuperior and anterior FHN junction where cam-type lesions likely occur. This will be the first MR-based study that allows fully automatic 3D quantitative assessment of cam-type lesions based on the alpha angle measures.

- **Automatic segmentation of the individual femoral and acetabular cartilages**
  A method will be proposed based on the bone pre-segmentation for automatic cartilage segmentation from high-resolution 3D MR images of the hip joint. It will be the first method to allow automatic and reliable delineation of the individual femoral and acetabular cartilage plates from MR images acquired without continuous leg traction or contrast agents for a clear separation between two cartilage plates. A high level of validity and reliability of automated cartilage segmentations, in comparisons with benchmark manual segmentations, is expected to be achieved for subsequent quantitative analyses.

- **Quantitative measurements of the cartilages and partitioned subregions**
  Quantitative measurements (i.e., volume, thickness) of the segmented cartilage volumes will be performed and compared with the results obtained from manual cartilage segmentations. Subregional analyses of the femoral and acetabular cartilage plates will be investigated, particularly at the weight-bearing areas of the articular surfaces, where focal cartilage lesions most likely appear and subsequently lead to progressive degenerative conditions. Preliminary evaluation of the reproducibility will be confirmed between several MR acquisition protocols with different tissue contrast and image resolutions.

1.5 Organization of the Thesis

The thesis outline is as follows:

Chapter 2 provides the relevant clinical, imaging and technical background involving the hip joint anatomy and pathology, MR imaging of the hip joint and current medical image segmentation techniques. A methodological overview is then followed to systematically clarify the data acquisition process and methods to be implemented in this thesis.

The subsequent four chapters then present a more detailed literature review, the proposed methodology and associated evaluation results respectively targeted for each of the four specific aims described in Section 1.3.

Chapter 3 presents the work to achieve **Aim 1.1**, which will develop and evaluate two state-of-art methods for automatic segmentation of the bone elements from 3D MR images of the hip. This is motivated by the need for quantitative analyses of the bone morphology, particularly at the FHN junction and subsequent automatic cartilage segmentation.

In order to accomplish **Aim 2.1**, **Chapter 4** proposes an automatic 3D quantification method for quantitative assessing the bone morphology at the FHN junction for potential use in accurate detection and quantitative measurement of possible cam lesions. The reliability and reproducibility is assessed using 3D MR images of the hip joints with varying FHN junction presentations.

Chapter 5 centers on **Aim 1.2** and introduces a novel hybrid cartilage segmentation scheme for MR images of the hip joint with a prerequisite of the bone pre-segmentation. The proposed method is validated against manual segmentation of the cartilages in a dataset of high-resolution 3D MR images.

For **Aim 2.2**, **Chapter 6** performs quantitative measurements (i.e., volume and thickness) and subregional analyses of the cartilage morphology based on the individual femoral and acetabular cartilage volumes automatically segmented from 3D MR images of the hip joint. The reliability and reproducibility of these morphological measures is evaluated in order to examine the feasibility for potential provision of the morphometric data in large-scale clinical and research studies about early hip OA.

Finally, **Chapter 7** concludes this thesis with a discussion of the methodologies used and the primary contributions. Furthermore, it describes general limitations of the proposed techniques with a summary of possible future work.

2 BACKGROUND AND METHODOLOGICAL OVERVIEW

2.1 Basic Anatomy of the Hip Joint

The hip joint is a synovial joint of the ball-and-socket type formed between the head of the proximal femur, i.e., "ball", and the acetabulum of the pelvis, i.e., "socket" (Figure 2.1). The hip, as the largest weight-bearing joint in the human body, connects the upper and lower body halves and regularly experiences loads over 2.5 times the bodyweight (Bergmann et al. 2001). As a wide range of movement patterns (e.g., flexion and extension, abduction and adduction, medial and lateral rotation, and circumduction) largely rely on the articulation of this joint, a complicated anatomic structure involving bony, cartilaginous, ligamentous and muscular supports has been developed within and around the hip joint in order to achieve these mechanical functions (Anderson and Blake 1994; Johnston 1973).

2.1.1 Bone structure

The bone structure within the hip joint consists of two components: the proximal femur and the pelvic bone (or innominate bone).

The femur is one of the longest bones in the human body and extends from the hip joint proximally to the knee joint distally (Drake et al. 2009). It can be divided into three sections, where the proximal one, as a part of the hip joint, contains the femoral head and neck, greater trochanter, lesser trochanter, intertrochanteric line and crest (see Figure 2.1). The head of the proximal femur, a two-thirds of a sphere (i.e., 45 - 56 mm diameter), locates into the acetabulum in a medial, cranial and slightly ventral position. *Fovea capitis femoris* is a non-articular pit on the medial surface of the femoral head, which is used for the attachment of *ligamentum teres* into the acetabular notch at the other side. The femoral neck connects the femoral head to the shaft of the femur and usually projects superiorly, anteriorly and medially from the upper femoral shaft. As the orientation of the femoral neck is closely related to the range of movement and the loading of the hip joint, it is commonly examined by the *angle of anteversion* and *angle of inclination* (Toogood et al. 2009). The angle of inclination, also referred as the neck-shaft angle, is formed between the femoral neck and shaft at a frontal view, which is approximately 125° (± 5°) in the adult and varies in the life cycle (Fagerson 1998).

The pelvis is comprised of two halves (i.e., the innominate bones), each of which is formed through

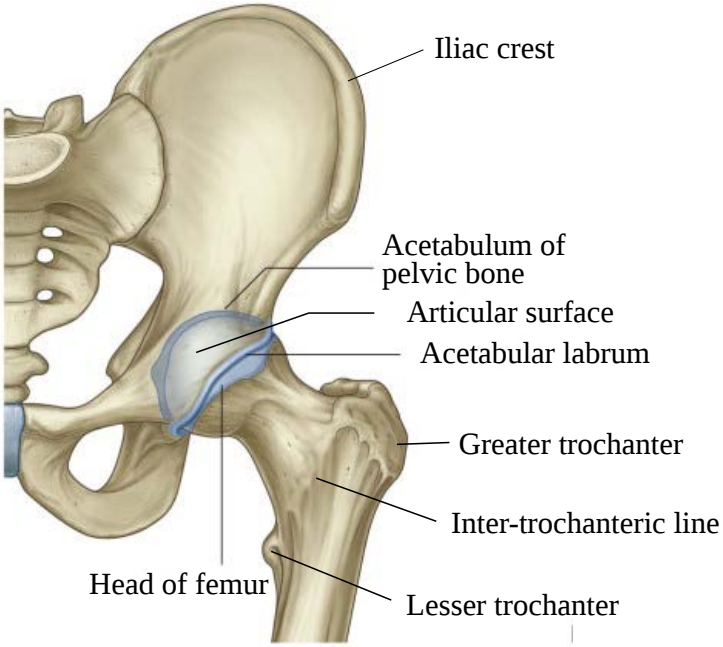

Figure 2.1: Articular surfaces of the hip joint (anterior view) (Used without permission from (Drake et al. 2009)).

the fusion of three bone components, the ischium, pubis and ilium. The acetabulum, as the confluence of these three bones, is a shallow, semi-spherical-cup-shaped cavity and locates anteriorly, laterally and inferiorly on the outside of the pelvic bone. The *center edge angle* defined between the vertical line and a line connecting the lateral rim of the acetabulum and the femoral head center Wiberg (1939), is used to indicate the amount of inferior tilt of the acetabulum (Levangie and Norkin 1992). The inferior margin of the acetabulum is known as the acetabular notch that incorporates the attachment of *ligamentum teres* and vascular structures (Anderson and Blake 1994), which makes the acetabular articular surface as an inverted horseshoe-shaped area covering other anterior, superior and posterior margins (Drake et al. 2009).

2.1.2 Articular cartilage

In the hip joint, the articular surfaces include the spherical head of the femur and the lunate surface of the acetabulum (Figure 2.1). Both articular surfaces are highly curved but *neither coextensive nor completely congruent* (Standring et al. 2005). The articular surface on the femoral head is a spheroidal and slightly ovoid surface in young subjects and becomes more spherical during the ageing process. The acetabular articular surface is lunate-shaped and appears like an incomplete ring, which is the broadest at the anterosuperior region and deficient in the inferior region opposite the acetabular notch (Drake et al. 2009). Both the articular surfaces are completely covered by the articular cartilage with the exceptions of the non-articular acetabular fossa and the femoral fovea. This cartilaginous tissue helps to absorb the shock, distribute joint loads over a wider area of the bones and, with assistance of intra-articular synovial fluid, provides a slick surface that allows almost frictionless movement between the opposite bones within the joint (Standring 2008).

In healthy adult hip joints, the thickness of the articular cartilage ranges from 1.0 to 2.5 mm on the

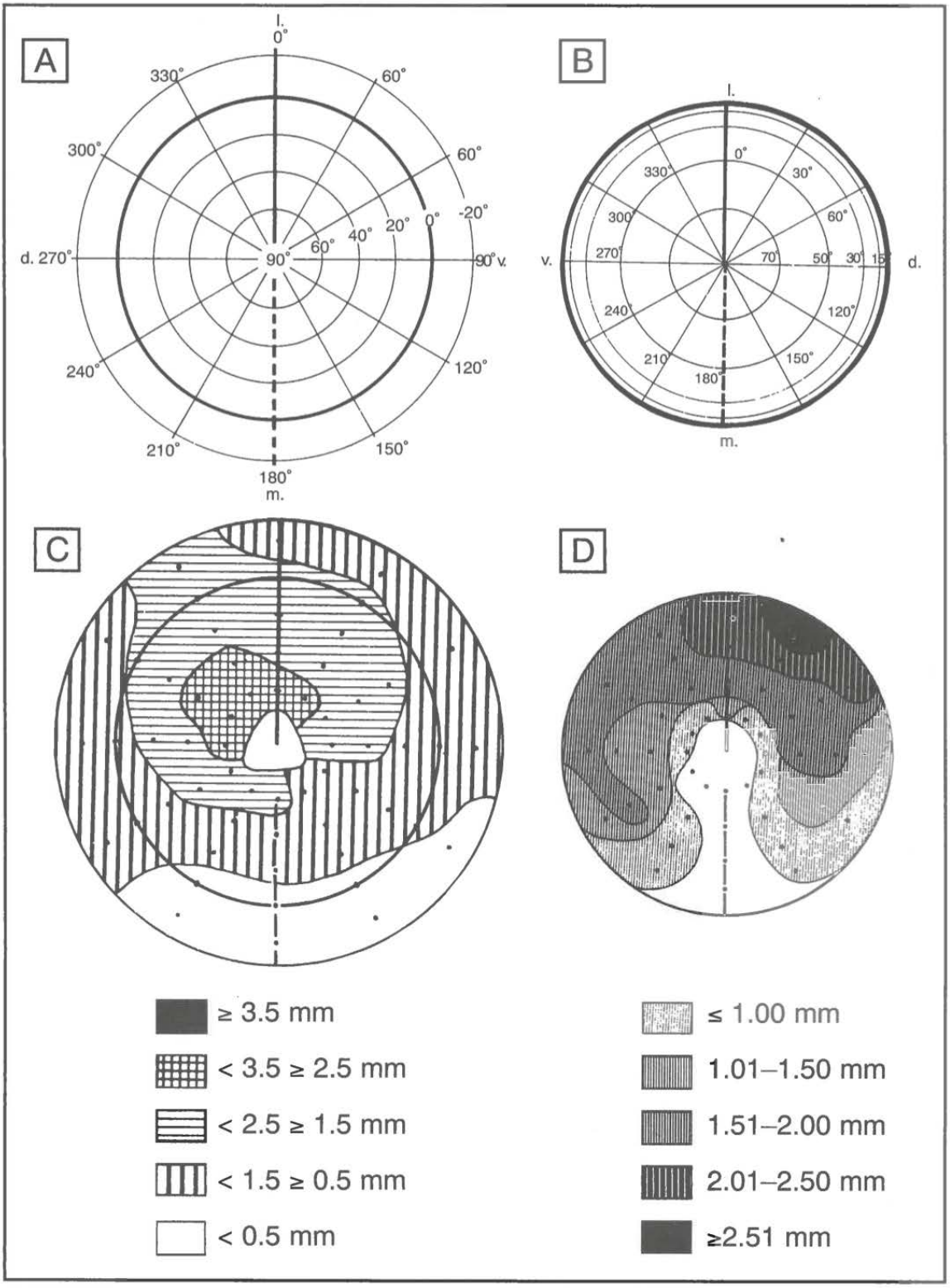

Figure 2.2: Thickness variation of articular cartilage of the femoral head (left) and the acetabular lunate surface (right). A and B are designated reference grids, where the distance and angular direction of sampling points (black dots in C and D) are measured from the center of the femoral head and the acetabulum center. C and D show average contours of the thickness ranges indicated by the shaded codes below the diagrams (Used without permission from (Fagerson 1998)).

femoral head and 1.2 to 2.3 mm in the acetabulum (Fagerson 1998). Figure 2.2 presents a general distribution pattern for the individual femoral and acetabular cartilage plates within the hip joint (Fager-

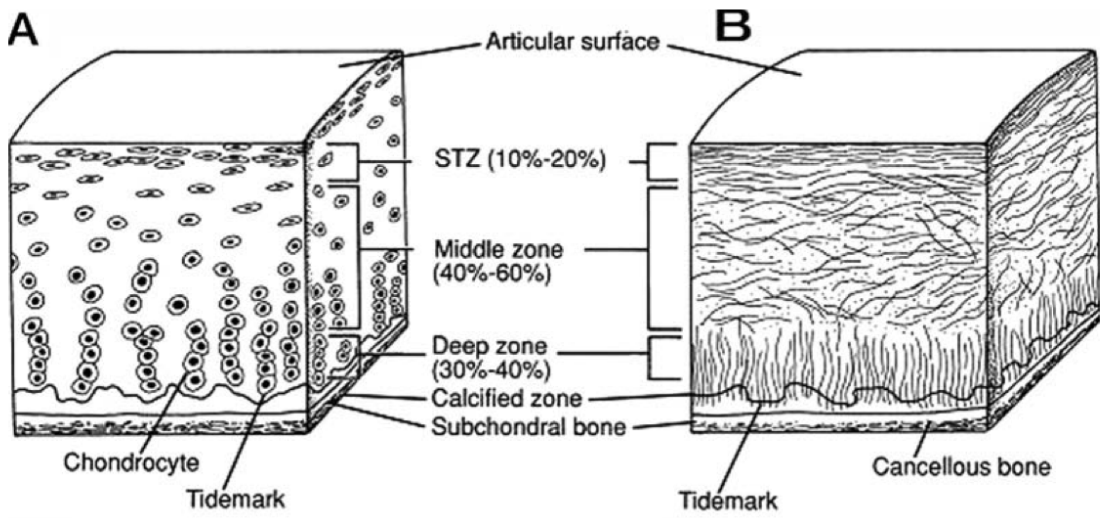

Figure 2.3: Cross-sectional diagram of healthy articular cartilage: A, cellular organization in the zones of articular cartilage; B, collagen fiber architecture. (Used without permission from (Sophia Fox et al. 2009)).

son 1998; Kurrat and Oberländer 1978). For the femoral cartilage plate, the medial central surface, which is part of the contact area with the acetabulum, has the thickest cartilage coverage (2.5 - 3.5 mm), while the periphery of the articular surface has the thinnest one. The acetabular cartilage is found thickest on the upper area of the horseshoe shape ($>$ 2.5 mm), the major weight-bearing area, and also the outer periphery (1.5 - 2.0 mm), while the thinnest cartilage coverage ($<$ 1.0 mm) is in the lower region at the caudal edge of the horseshoe shape close to the acetabular fossa.

The mechanical properties of the relatively thin articular cartilage within the hip joint result from its unique structure and composition. The normal articular cartilage is comprised of an extracellular matrix (ECM) and chondrocytes, the only type of cells. In the ECM, three classes of proteins are involved: collagens, proteoglycans and other noncollagenous proteins. The collagen including 90-95% type II collagen accounts for 10-15% of the wet weight and provides a tensile strength to the articular cartilage, while the presence of proteoglycan aggregates gives the cartilage the ability to resist the compression (Sophia Fox et al. 2009). Chondrocytes, which make up about 1-5% of the total cartilage volume in adults, serve as observers rather than participants in the function of mature articular cartilage, which are responsible for synthesizing and maintaining the ECM (Buckwalter et al. 2005). Therefore, the remarkable biomechanical properties of the articular cartilage is the result of both the integrity of the collagen network and the maintenance of the high proteoglycan content within the matrix (Sophia Fox et al. 2009; Tuan and Chen 2006).

In the structure of mature articular cartilage, four zones or layers can be identified as shown in Figure 2.3, which are the superficial zone, transitional (or middle) zone, deep zone and calcified cartilage zone accordingly from the articular surface to the subchondral bone (Potter et al. 2009; Standring 2008). The thin superficial zone (10-20% of the total cartilage volume) contains an acellular sheet of tightly-packed collagen fibres with their long axes parallel to the articular surface and a relatively high number of flattened chondrocytes, which provides the greatest tensile and shear strength to protect deeper layers (Sophia Fox et al. 2009). The transitional zone as a bridge between the superficial

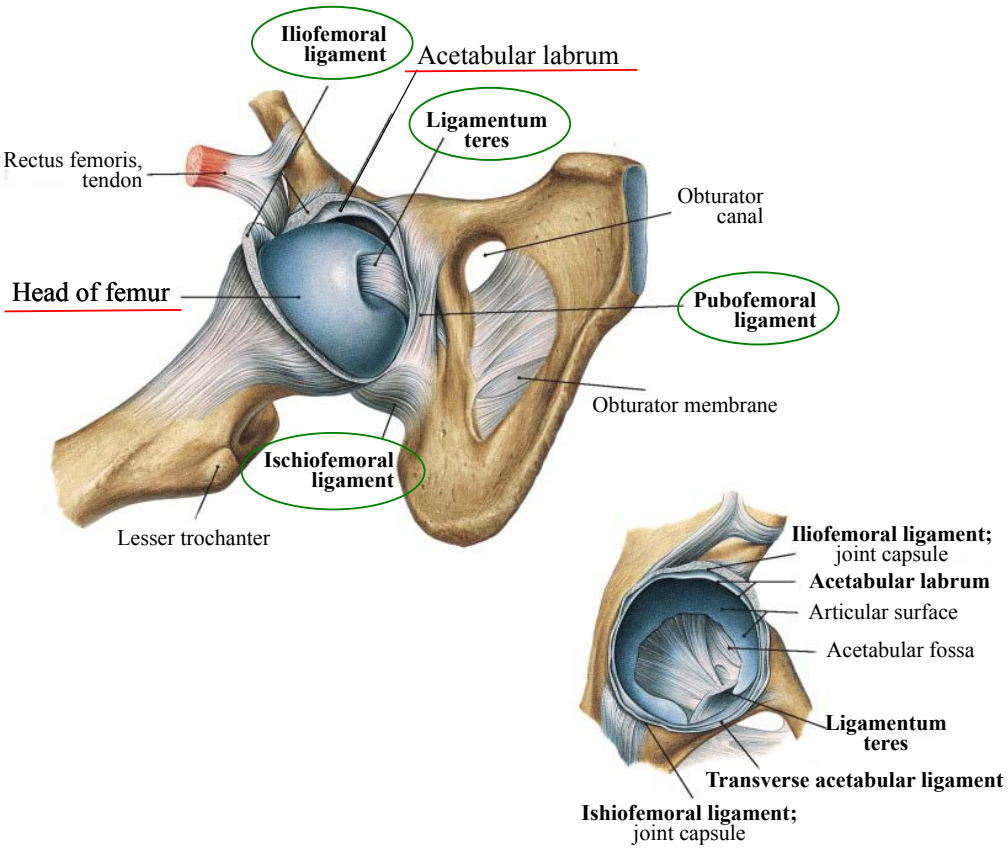

Figure 2.4: Ventral view of the intra-articular structure of the (right-side) hip joint after opening of the capsule and partial (top left) or complete (bottom right) exarticulation of the femoral head (Used without permission from (Paulsen and Waschke 2013)).

zone and deeper zones, occupies 40-60% of the total cartilage volume with spheroid-shaped chondrocytes and abundant ECM. The deep zone has the largest diameter of collagen fibrils, highest concentration of proteoglycans and least water, which can provide the greatest resistance to compressive forces (Sophia Fox et al. 2009). The thin calcified cartilage zone with a small volume of chondrocytes embedded in a calcified matrix always shows a low metabolic activity and provides an important transition to the less resilient subchondral bone (Bhosale and Richardson 2008).

2.1.3 Labrum, capsular and ligamentous structures

As illustrated in Figure 2.4, the acetabular labrum in the hip joint is a ring of fibrocartilaginous tissue with the shape of an inverted "U" that is attached to the osseous margin of the acetabulum with the continuity until the acetabular notch. This tissue structure is triangular in cross section with its base attached to the acetabulum and apex forming the free edge of the labrum, which is turned in against the femoral head (Fagerson 1998). The labrum deepens the acetabular socket and increases the containment of the femoral head, which, therefore, helps with load distribution and stabilization of the hip joint (Henak et al. 2011). In some previous studies, the labrum was also demonstrated to act as a seal to prevent the direct contact between joint surfaces with pressurised fluid layer and uniformly distribute compressive loads across the cartilage surfaces, thereby lowering maximal cartilage compressive forces during weight-bearing (Crawford et al. 2007; Ferguson et al. 2003).

The hip capsule encompassing the entire hip joint and mostly the neck of the femur, proximally attaches to the entire periphery of the acetabulum beyond the acetabular labrum and transverse ligaments (Fagerson 1998). Meanwhile, the capsule also runs distally and attaches anteriorly to the intertrochanteric line and the root of the greater trochanter. While most of the fibres run longitudinally parallel to the femoral neck with blood vessels, a small portion of the fibres, *zona orbicularis*, wrap circularly around the neck of the femur to ensure the stability of the hip joint in distraction (Paulsen and Waschke 2013).

Three strong extracapsular longitudinal ligaments are used to further reinforce the hip joint, which include iliofemoral, pubofemoral and ischiofemoral ligaments (Fagerson 1998). As these ligaments all start from the pelvic bone, they are named for their bony attachments on the femur at the other side, respectively. These ligamentous structures are important to limit the range of hip extension and prevent the backward tilting of the pelvis (Paulsen and Waschke 2013). The intracapsular *ligamentum teres* is the fourth ligament within the hip joint covered by synovial membrane (see Figure 2.4), which can protect blood vessels to and from the femoral head (Fagerson 1998).

2.2 Hip Osteoarthritis and Femoroacetabular Impingement

The hip joint as one of the largest weight-bearing joints usually suffers from a high prevalence of degenerative conditions. Osteoarthritis (OA) and femoroacetabular impingement (FAI) are the primary thrust of this thesis, and thus will be the focus in the further discussion.

2.2.1 Osteoarthritis (OA) of the hip joint

Osteoarthritis (OA) is a degenerative joint disease shown in Figure 2.5 defined by the American College of Rheumatology as "*a heterogeneous group of conditions that lead to joint symptoms and signs which are associated with the defective integrity of articular cartilage in addition to related changes in the underlying bone at the joint margins*" (Roach and Tilley 2007). It is always associated with signs and symptoms of inflammation including joint pain, swelling, stiffness and reduced joint mobility leading to significant functional impairment and disability (Felson 2006). The hip degeneration process involves not only the focal and progressive cartilage loss, but also degenerative conditions of the entire joint, which include concomitant changes in the subchondral bone (such as the development of marginal bony outgrowths, osteophytes and bony sclerosis) and damages to the soft tissue in and around the hip joint (synovial membrane, ligaments, capsule and periarticular muscles) (Lane 2007; Lories and Luyten 2011).

The articular cartilage has been generally recognized as the earliest evidence of joint degeneration (Lloyd-Roberts 1955). Initial cartilage alterations usually occur in the molecular composition and organization of the cartilage matrix, which further lead to deterioration in material properties and structural integrities of the articular surfaces and underlying hyaline cartilages. The progression of hip OA commonly results in the roughened and irregular articular surfaces, deeper fibrillation into the cartilage until the fissures reach the subchondral bone (Buckwalter et al. 2005). Moreover, the

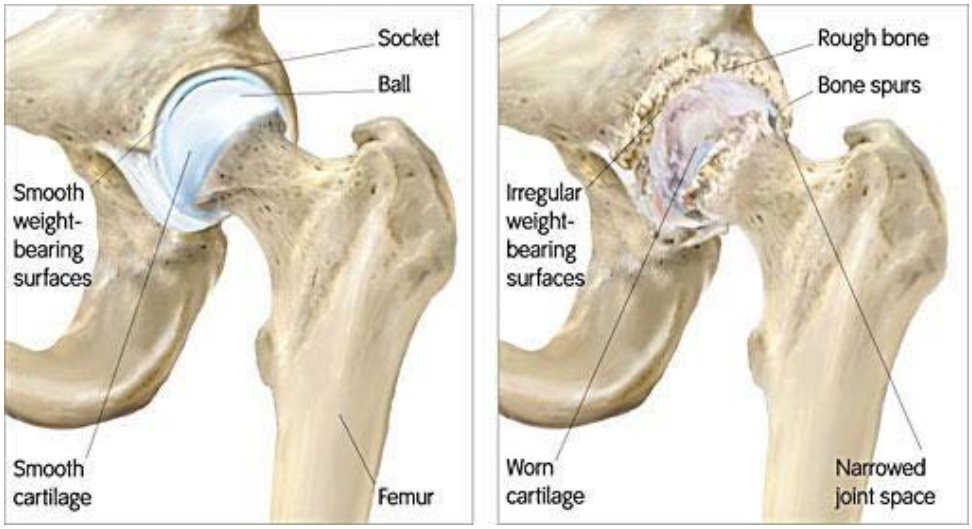

Figure 2.5: Illustration of (left) normal and (right) osteoarthritis hip joint (Used without permission from http://www.everettboneandjoint.com/birmingham-hip-resurfacing/diseases.htm)

degradation of the cartilage layers can usually be observed in the weight-bearing area of the femoral head on the upper quadrant in contact with the acetabulum.

The subchondral bone is currently considered to be another important aspect in the pathogenesis of the disease, which can have progressive bone alternations involving stiffening and thickening of the subchondral bone, osteophyte formation, subchondral sclerosis and development of subchondral bone cysts (Lories and Luyten 2011; Perepezko et al. 2002). These abnormal bony changes are suggested to precede alterations in the articular cartilages and adversely affect the biomechanical environment of the overlying cartilage leading to secondary changes in the cartilage structure and integrity (Goldring and Goldring 2010; Radin and Rose 1986).

Diagnosis and treatment of hip OA

The diagnosis of hip OA is performed on a basis of the patient history, clinical examinations, radiographic evidences and laboratory data. According to the American College of Rheumatology, current clinical diagnosis guideline contains physical examinations together with radiographic findings evident on plain radiographs (Wolfe et al. 1990). As the strongest clinical indicator of hip OA is pain, particularly exacerbated by internal or external rotation of the hip (Lane 2007), a physical examination is usually performed to rule out other causes of the hip pain. The Western Ontario and McMaster Universities Osteoarthritis Index (WOMAC) is a widely-used measure with the long established reliability and validity, for assessing pain, stiffness and physical function in patients with OA of the hip and/or knee (McConnell et al. 2001). The radiographic findings chronologically include joint space narrowing, osteophyte formation and development of subchondral sclerosis, which usually occur in patients with severe OA (Conrozier et al. 1998; Dougados et al. 1996). For patients with early OA that do not have these radiographic changes, more sophisticated imaging technologies such as multi-detector computed tomography (CT) and MR imaging are necessary for further diagnosis confirmation. Currently, these modalities are not routinely used in clinics.

To our best knowledge, there is no cure for hip OA or effective treatment proven to slow OA progression. Current treatments to hip OA include lifestyle interventions, pharmacological therapy and surgical approaches, which still aim to relieve pain and preserve physical functions (Lane 2007). Although both non-pharmacological, e.g., weight loss and exercise, and pharmacological treatments are important in the therapeutic program for hip OA, little literature has shown their cost-effectiveness. Surgical intervention is normally considered when the joint pain cannot be controlled by conservative treatments and significantly limits normal functional activities of daily living. Total hip arthroplasty (THA), as one of the most beneficial surgical procedures, has demonstrated marked improvements in physical function, social interaction and overall health; however, the optimal time for this type of joint replacement surgeries is still not known (Laupacis et al. 1993; Murray et al. 1995).

2.2.2 Femoroacetabular impingement (FAI)

Femoroacetabular impingement (FAI) is a pre-osteoarthritic pathomechanical process of the hip joint frequently seen in young active subjects, especially in conjunction with top-level sport activities. It is characterized with varying bony abnormalities of the acetabulum and/or proximal femur causing abnormal contact stresses and repetitive collisions during hip joint motion (Leunig et al. 2009). It has been suggested that these deformities can initiate a cascade of degenerative, intra-articular events including tears in the labrum, disruption of the labrochondral junction and cartilage damages at the superior aspect of the acetabulum, and may eventually lead to hip OA (Ganz et al. 2003). Hence, early recognition and intervention for the FAI syndrome is likely to have considerable impact on delaying and preventing the development of progressive hip OA.

There are two distinct types of hip impingement based on the origin and the mechanism of the impingement: cam and pincer (Lavigne et al. 2004), as illustrated in Figure 2.6.

- **Cam FAI**, mostly seen in young, active male patients, results from the excessive bone at the head-neck junction of the femur that leads to jamming of an abnormal femoral head into the acetabulum in vigorous flexion and internal rotation of the hip joint (Ito et al. 2001). It is postulated that abnormal shear and compressive forces arising from a cam effect instigates the initial chondrolabral damage at the anterosuperior acetabular rim, which would be followed by the acetabular cartilage lesions and further reciprocal damage to the femoral head cartilage (Tannast et al. 2008; Wagner et al. 2003). A larger extent of these anomalies at the FHN junction is associated with increasing chondral damage, labral injury, and decreased range of motion (Johnston et al. 2008).
- **Pincer FAI**, more frequently in middle-aged females with participation of athletic activities involving hip motion, is secondary to the acetabular over-coverage resulting in impingement of the acetabular rim against the femoral neck during range of motion (Larson 2012). The over-coverage of the acetabular rim can be caused by retroversion of the acetabulum, coxa profunda or protrusio, which, with repeated abutment with a normal FHN junction, leads to the labral degeneration, ossification of the rim, and circumferential chondral damages (Yen and Kocher 2013).

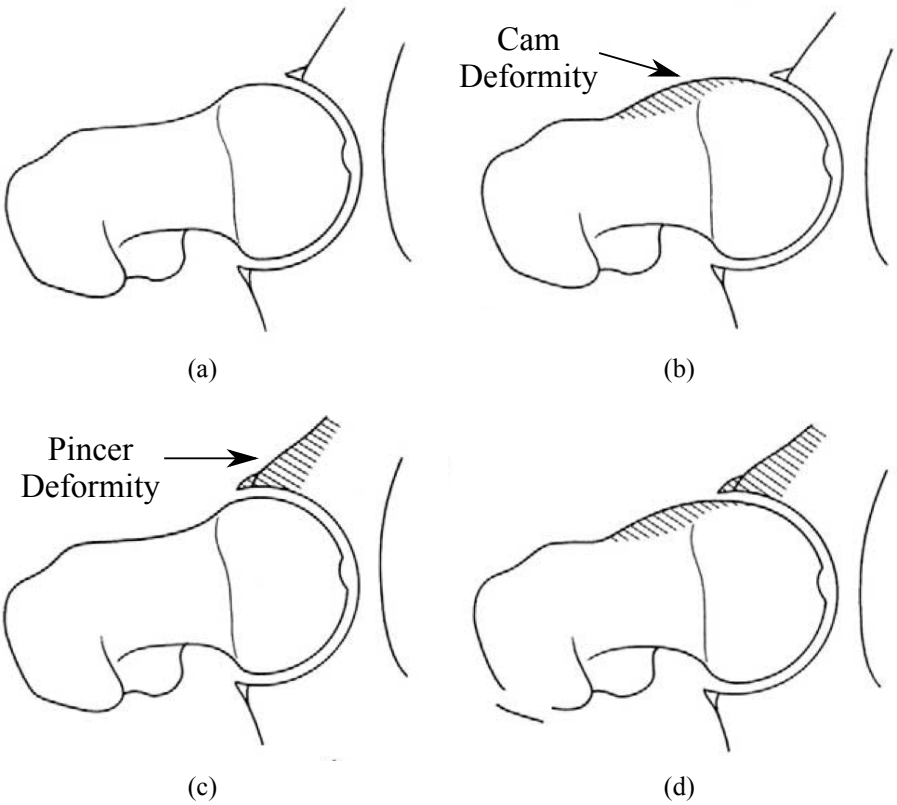

Figure 2.6: Cross-section of a hip joint displaying (a) the normal femoral and acetabular anatomy, (b) cam FAI (bony excrescence causing reduced head-neck offset), (c) pincer FAI (acetabular over-coverage of the femoral head) and (d) mixed FAI. (Used without permission from (Lavigne et al. 2004))

A combination of these two impingement conditions is classified as a mixed-type FAI (Tannast et al. 2007), which is most commonly observed in symptomatic patients (Philippon et al. 2007).

Diagnosis of FAI

Diagnosis of FAI is based on clinical findings and radiographic analyses, including MR arthography. Clinical evidences of FAI are characterized by anterior inguinal pain and decreased range of motion with flexion, adduction and internal rotation, which are commonly assessed by a series of physical examinations including the anterior conflict test (flexion, abduction, intra-rotation = FADIR), Drehmann test (flexion, abduction, extra-rotation = FABER) and posterior impingement test (Aliprandi et al. 2014).

Radiographic (X-ray) evaluation is firstly used to evaluate patients with a clinical suspicion of FAI that allows for detecting the anatomical and skeletal abnormalities in both cam-type and pincer-type FAI. The standard radiographic imaging comprises at least two projections: an anterior-posterior (AP) pelvic view and an axial cross-table view (or Dunn view at 45° of hip flexion) shown in Figure 2.7. Additionally, more projections can be performed such as Lequesne's false profile and lateral pelvic projections to better evaluate morphological features associated with FAI. For cam-type FAI, the abnormal femoral sphericity with the convex appearance of the FHN junction can be detected as the presence of a typical anterior or posterior bump on the radiographs. These osseous deformities can be

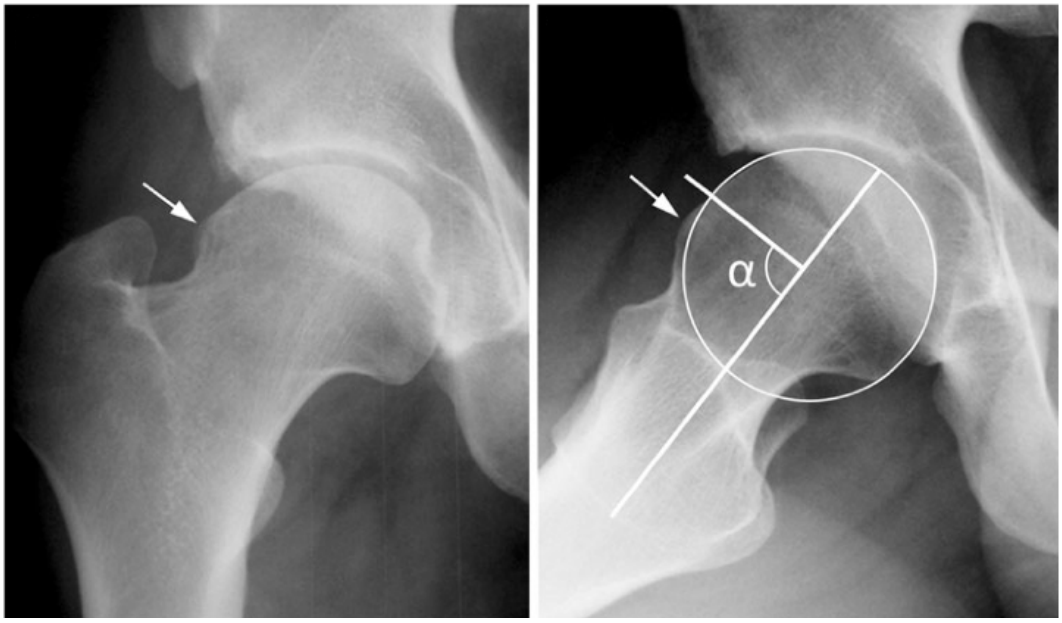

Figure 2.7: Bony bump (arrow) in cam-type FAI observed on (left) the AP pelvic view and (right) Dunn view at 45° of hip flexion. The alpha angle measurement (α) is illustrated in the latter view. (Used without permission from (Aliprandi et al. 2014)).

quantified using several methods:

- **Alpha Angle** introduced by Nötzli et al. (2002) is used to quantify the amount of asphericity, which is defined as the angle between the femoral neck axis and a line connecting the head center with the point where the asphericity of the head-neck contour begins (see Figure 2.7). On axial radiographs, an alpha angle exceeding 50° is an indicator of an abnormally shaped FHN contour (Tannast et al. 2007). However, to our knowledge, no consensus has been reached yet for its threshold value that allows to precisely distinguish between asymptomatic controls and symptomatic FAI patients (Pollard 2011).
- **Femoral head-neck (FHN) Offset** is defined as the difference in radius between the anterior femoral head and anterior femoral neck on a cross-table axial view of the proximal femur (Ito et al. 2001; Siebenrock et al. 2004). As a general rule for clinical practice, an anterior offset less than 10 mm is a strong indicator for cam-type impingement (Marín-Peña 2012).
- **Triangular Index** is constructed by measuring half of the head radius (r) on the neck axis and drawing a line perpendicular to the neck axis in the measured point. The new radius (R) is defined as the distance between the head center and the point intersection between the perpendicular line and FHN contour (Gosvig et al. 2007). The significant difference between r and R reveals a cam-type impingement.

The excessive acetabular coverage in pincer-type FAI is quantified with the lateral center edge angle or the acetabular index. The **lateral center edge angle** is the angle formed by a vertical line and a line connecting the femoral head center with the lateral edge of the acetabulum. A "normal" lateral center edge angle has been described to range between 25° and 39° (Murphy et al. 1995). The **acetabular index** is the angle formed by a horizontal line and a line connecting the medial point of the sclerotic zone with the lateral center of the acetabulum. In hip with coxa profunda or protrusio

acetabuli, the acetabular index is typically 0° or even negative. The **femoral head extrusion index** is another parameter for quantification of femoral coverage, which defines the percentage of femoral head that is uncovered when a horizontal line is drawn parallel to the inter-teardrop line. An extrusion index higher than 25% is associated with hip dysplasia (Li and Ganz 2003).

2.3 Imaging of the Hip Joint

2.3.1 Plain radiography

Plain radiography (X-ray) is the primary diagnostic modality for the hip pathology, which has standard projections including AP, lateral ("frog-leg"), axiolateral views (see Figure 2.8). To evaluate the progression of hip OA, radiographic changes can be observed shown in Figure 2.8c including signs related to bone changes (cysts, sclerosis, osteophytes) and the cartilage loss (joint space narrowing) (Ravaud and Dougados 1997). The first radiological sign often shows the development of osteophytes but measurement of joint space width (JSW) is the most reliable and sensitive method of grading severity of the disease (Gossec et al. 2009). While several parameters can be examined, e.g., minimum JSW, mean JSW and a region of interest of the joint space, Conrozier et al. (2001) has suggested measurement of the minimum interbone distance of the joint space width as the most suitable method for evaluation of hip OA progression.

Standard radiographic imaging for FAI usually includes an AP pelvic view and an axial cross-table view of the proximal femur while an alternative to the axial view, a Dunn view at 45° of hip flexion can be acquired to reveal pathomorphologies of the anterior FHN junction (see Figure 2.7) (Tannast et al. 2007). From different views of the radiographs, several radiographic parameters can be measured allowing accurate quantify the amount of asphericity of the femoral head (i.e., the alpha angle and anterior offset) and excessive acetabular coverage (i.e., the lateral center edge angle and acetabular index) (Siebenrock and Henle 2012).

Although radiographs can be used to identify morphological risk factors for OA and FAI and to define disease conditions in advancing stages, they lack a direct visualization of the radiolucent articular cartilage and associated surrounding soft tissues, particularly for the tissue damages at the early stage of hip OA. As the cartilage degeneration is initially focal and non-uniform and needs to be severe enough to manifest on X-rays, the assessment of JSW alone has been reported insufficiently accurate to indicate the structural integrity of the articular cartilage (Fife et al. 1991). Furthermore, this two-dimensional (2D) radiographic visualization is dependent on patient positioning on the gantry and the experience of the technologist, which would further affect the reliability of radiographic measurements. Therefore, these limitations demonstrate a clear need for incorporation of advanced imaging modalities, such as CT and MR imaging.

2.3.2 Computed tomography (CT)

Computed tomography (CT) imaging provide a clear cross-sectional visualization of the osseous anatomy using computer-processed x-rays and allows for multiplanar 3D imaging options. Although

(a) (b) (c)

Figure 2.8: (a) Anteroposterior (AP) and (b) lateral radiographs of the hip joint (Used without permission from (Skripkus and Gentili 2006)); (c) demonstrates medial OA features observed on plain radiographs including joint space narrowing (balck arrow), osteophyte formation (white arrow) and abnormal head-neck offset (open arrow) (Used without permission from (Karachalios et al. 2007).

CT does not have a significant role in the evaluation of early OA, it is commonly used in three-dimensionally quantifying bony abnormalities of the hip joint, which permits a better appreciation of bony contours in multiple planes and particularly facilitates the assessment of the FHN junction (Beaulé et al. 2005a; Harris et al. 2013a; Kang et al. 2010). It has also proven to be a suitable technique for non-invasive investigation of subchondral bone changes within OA patients (Müller-Gerbl et al. 1992). However, in CT imaging, the ionizing radiation makes this image modality unsuitable for non-patients participating in large-scale research studies about FAI and early hip OA. Like X-rays, CT scans can not provide a through visualization of the surrounding soft tissues including the cartilages and lack the sensitivity for diagnosis and assessment of early and pre-OA conditions within the hip joint such as concomitant lesions of the labrum and articular cartilage.

2.3.3 Magnetic resonance (MR) imaging

Magnetic resonance (MR) imaging is the most promising *in vivo* imaging modality for the full joint assessment in both research and clinical studies, which, in comparison with the conventional radiography, has advantages of high spatial resolution, multiplanar capabilities, no ionizing radiation and excellent tissue contrast allowing a direct visualization of the labrum and articular cartilage. As MR imaging affords exquisite soft tissue contrast, this imaging modality enables improved evaluation and monitoring of anatomical features of the injury and disease that may not be assessed adequately with other imaging methods such as X-ray or CT.

Therefore, MR imaging offer the superiority in three ways for detection and monitoring of early OA changes (Palmer et al. 2013):

1. very high image spatial resolution to visualize the articular cartilage;
2. biochemical MR imaging techniques for evaluation of cartilage composition;
3. whole hip joint assessment (i.e., all the structures within the joint), permitting the identification of early changes distant to the cartilage.

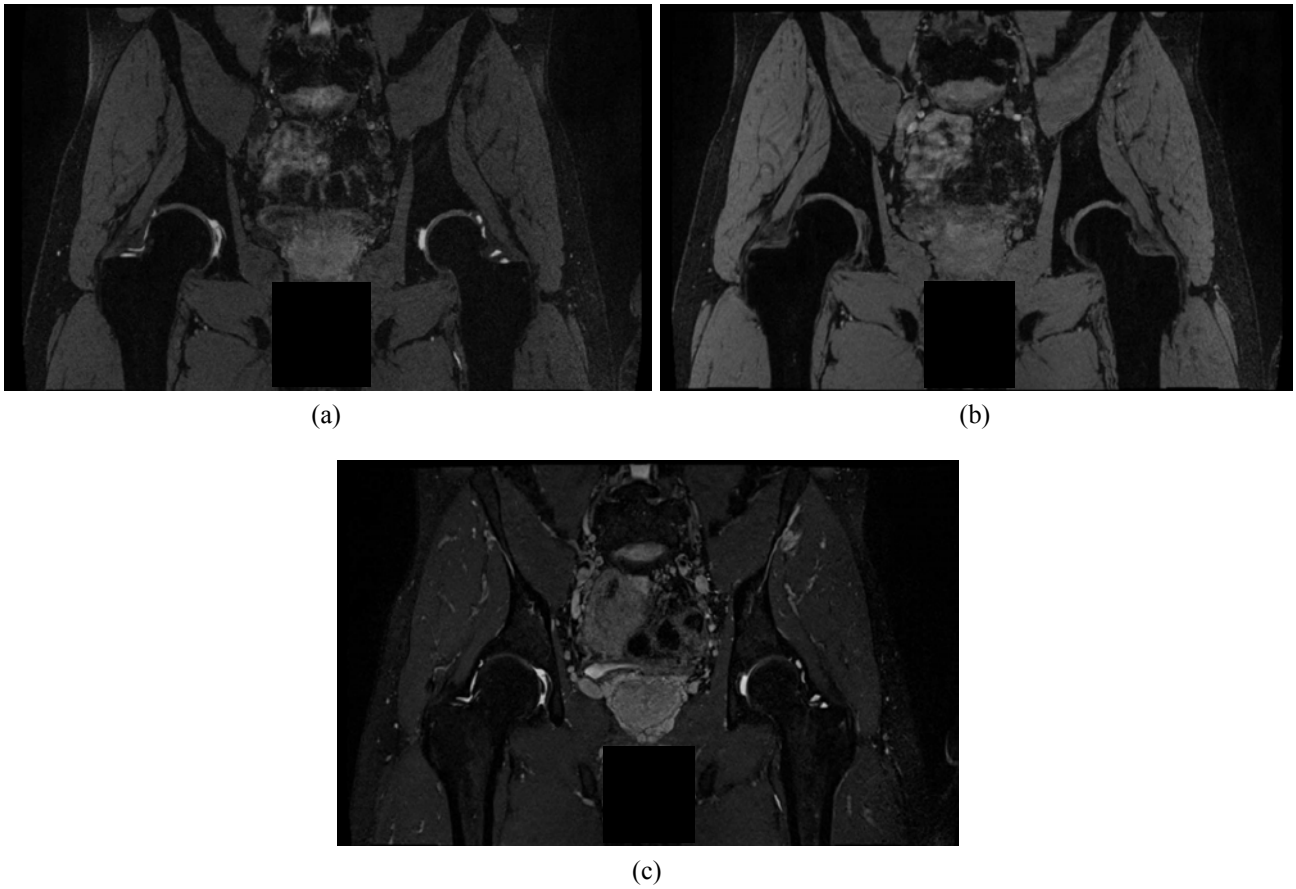

(a) (b)

(c)

Figure 2.9: High-resolution large field-of-view MR images within the hip region acquired at 3.0 T from the same subject: (a) water-excitation DESS (0.67 $\times$ 0.67 $\times$ 0.61 mm^3), (b) MEDIC (0.65 $\times$ 0.65 $\times$ 0.70 mm^3) and (c) 3D proton density-weighted fat suppression SPACE (0.77 $\times$ 0.77 $\times$ 0.70 mm^3).

2D and 3D MR sequences for cartilage imaging

In clinical practice, 2D fast spin-echo (FSE) sequences repeated in multiple planes have been commonly used to evaluate the articular cartilages because of the excellent tissue contrast and high in-plane spatial resolution (Mintz et al. 2005). However, they have relatively thick slices and small gaps between slices, which can obscure pathologies secondary to partial volume averaging (Kijowski and Gold 2011). Moreover, several measurement steps have to be performed to display the joint in multiple planes because voxels are not isotropic and thus multiplanar reformation (MPR) process cannot be performed without loss of image quality.

Three-dimensional (3D) sequences acquire MR data from an imaging volume through the joint in terms of thin, continuous slices, thereby reducing the partial volume averaging. They also provide MPR images that allow the hip joint to be evaluated in any orientation following a single acquisition. Gradient-echo sequences are the first 3D sequences used for cartilage imaging including T1-weighted spoiled gradient echo (SPGR) (Nakanishi et al. 2001; Nishii et al. 2004) and Fast Low-Angle Shot (FLASH) sequences (Mechlenburg et al. 2007), with incorporation of fat suppression to reduce chemical shift artefacts and optimize the overall dynamic contrast range of the image. With these sequences, the hyaline cartilage is high in signal intensity, and high contrast-to-noise ratios are achieved compar-

ing with adjacent structures such as joint fluid, fat, cortical bone and muscle (Disler 1997). Also, the Volumetric Interpolated Breath-hold Examination (VIBE) sequence recently proposed by Zheng et al. (2010) is a faster and motion-impervious alternative to 3D FLASH for cartilage imaging. A disadvantage of SPGR and FLASH sequences is that the images show uniform high signal intensity throughout the hyaline cartilage and therefore may not show intrasubstance cartilage lesions without articular surface morphological changes and associated articular surface contour defects (Naraghi and White 2012).

Three-dimensional (3D) dual echo steady state (DESS) imaging is another commonly used technique for morphologic assessment of the articular cartilage with reduced scan time, higher SNR and cartilage-to-fluid contrast when compared with 3D SPGR (Mosher and Pruett 1999). In knee OA trials, 3D DESS has been validated for clinical applications allowing quantitative 3D assessment of cartilage with good accuracy and precision (Eckstein et al. 2006), and is the sequence of choice for the Osteoarthritis Initiative (Peterfy et al. 2008).

Another group of MR imaging techniques is steady-state free precession (SSFP). Balanced SSFP is also known as fast imaging employing steady-state acquisition (FIESTA) (GE Healthcare), True Fast Imaging with Steady-state Precession (TrueFISP) (Siemens Healthcare) and balanced-fast-field echo (FFE) (Philips Healthcare). These techniques depict fluid with higher signal while the cartilage signal intensity is preserved, which thereby offer excellent synovial fluid-to-cartilage contrast (Vasanawala et al. 2005) and have a good diagnostic performance in the assessment of cartilage morphology in the knee joint (Duc et al. 2007a;b; Kornaat et al. 2005).

Recently, 3D FSE with variable flip angle sequences (3D turbo spin echo with variable flip angle (SPACE), Siemens Healthcare) have recently been developed to overcome the drawbacks of 2D imaging and to acquire isotropic images with high quality, high spatial resolution and relatively short scan time, for evaluating the articular cartilage (Notohamiprodjo et al. 2009). In this technique, large eligible turbo factors generated by a restore pulse and variable flip angle distribution are used to produce a pseudo steady state. It may provide high, T2 weighted tissue contrast and has better SNR and SNR efficiency (Friedrich et al. 2011). However, these techniques have lower in-plane spatial resolution when compared to other 3D cartilage imaging sequences with similar acquisition time and have reduced magnetization transfer effect when compared to 2D FSE sequences (Van Dyck et al. 2012), which may potentially reduce the conspicuity of superficial cartilage lesions (Kijowski and Gold 2011).

To our best knowledge, no comparison between different MR sequences has been investigated for the hip joint. Figure 2.9 displays different MR characteristics observed in three different sequences, i.e., DESS, multi echo data image combination (MEDIC) and SPACE, acquired from the same subject. There are several studies evaluating a variety of sequences for the knee joint (Duc et al. 2007a; Friedrich et al. 2011; Kijowski et al. 2009). Similar sensitivity and specificity values for water-excitation FLASH, water-excitation DESS and water-excitation TrueFISP sequences were reported by Duc et al. (2007a) for detecting surgically confirmed cartilage lesions in 30 patients at 1.5 T.

1.5 T, 3.0 T and 7 T

MR imaging of the hip joint is commonly performed on 1.5 T or 3.0 T scanners while imaging with a 1.5 T large-bore magnet is still regarded as the clinical standard. Most MR-based studies for morphological and compositional assessment of the articular cartilage within the hip joint were performed at this field strength of 1.5 T (Li et al. 2008; Nakanishi et al. 2001; Siversson et al. 2014; Zhai et al. 2005). On the other hand, 3.0 T systems have demonstrated promising improvements in the image quality (e.g., higher SNR) and spatial resolution while using similar acquisition time, and may therefore be better suited for the overall assessment of focal cartilage abnormalities (Link 2011). Moreover, Link et al. (2006) have reported improved lesion detectability for cartilage MR imaging at 3.0 T.

More recently, ultra high field 7 T MR imaging has been applied in the musculoskeletal system, which mainly benefits in increased SNR that scales approximately linearly with the magnitude of the main magnetic field (see Figure 2.10). Deniz et al. (2013) found that 7 T provided a 2.3-fold SNR gain over 3.0 T in the hip articular cartilage. With the extra SNR at 7 T, it can be used not only to image with higher spatial resolution, which is critical for morphological assessment of the hip joint cartilage, but also to shorten the scan time avoiding the motion artefact (Chang et al. 2014). However, at the current stage, this ultra high field system is still in the research settings and numerous technical challenges (e.g., the lack of the radiofrequency coils, B_1^+ field inhomogeneity) must be addressed in order to take full advantages of the potential benefits at 7 T.

Challenges in hip MR imaging

MR imaging evaluation of the articular cartilage within the acetabulum and femoral head can be very challenging as the hip joint is usually located off the isocenter in the MR scanner during acquisition, thereby decreasing the image quality. From the anatomical aspect of the hip joint, the femoral head and acetabular cartilage layers are closely apposed making the separate articular surfaces difficult to be discriminated from each other. Additionally, the articular cartilage is very thin, which also poses difficulties in the detection of cartilage lesions. Although the continuous leg traction technique during MR imaging and MR arthrography can be used for a good separation of the two articular surfaces (Nishii et al. 1998), in most cases, the joint space between the femoral and acetabular articular cartilage is extremely narrow despite the traction.

Another imaging challenge for the hip joint arises from the need for a large FOV, particularly to encompass hip joints of both sides, and the absence of specialized radiofrequency coils. This results in acquired images with low spatial resolution. Contrary to many investigations reporting excellent results when imaging the articular cartilage of the knee joint, evaluation of the articular cartilage of the hip joint is much more difficult. Alternatively, hip MR imaging is performed with either a surface-phased array coil or a multichannel cardiac coil.

Several artefacts seen in MR images of the hip joint also bring about more challenges in the hip imaging, which involve:

1. Noise: Due to the depth of the hip joint within the body, inadequate MR signal is usually obtained in the MR image. As the image with a higher spatial resolution is acquired in order to

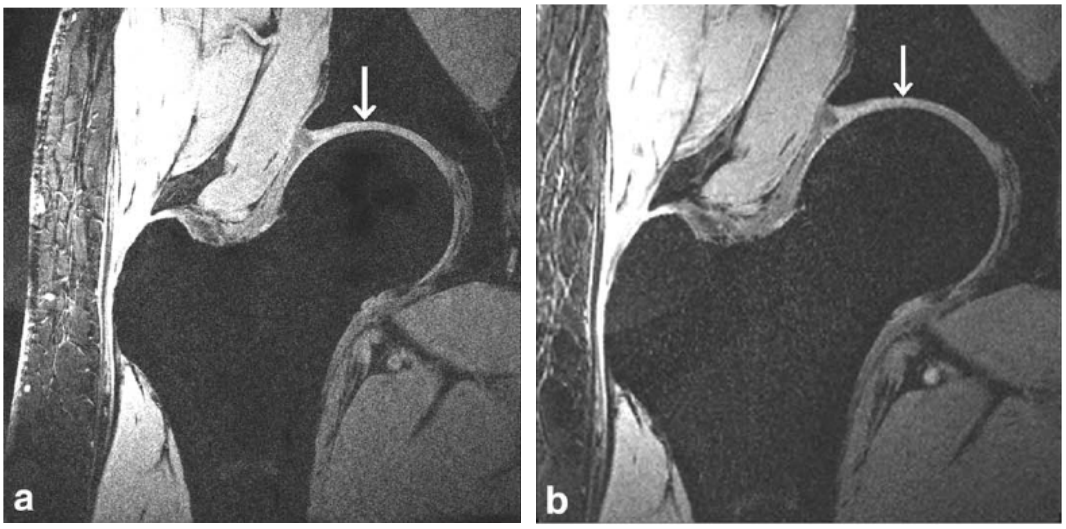

(a) (b)

Figure 2.10: High-resolution MR imaging of hip joint cartilage at 7 T: (a) 3D water-excitation FLASH and (b) 3D frequency-selective fat suppressed VIBE sequences at a resolution of 0.23 × 0.23 × 1.5 mm^3 (Used without permission from (Chang et al. 2014)).

assess the articular cartilage, lower SNR is inevitable, even scanning at 3.0 T.

2. Bias field: The bias field is a phenomenon resulting in non-uniform signal obtained from the same tissue at different locations of the MR image. Consequently, the image intensity of the same tissue type can appear significantly different (see Figure 2.11a). The bias field originates in the non-uniform B_1 excitation field owing to non-uniformity in the interaction between the radiofrequency field and the tissue being imaged.
3. Partial volume effects (PVE): Partial volume averaging is considered to be an inevitable effect because of finite and discrete characteristics of MR images. It commonly refers to loss of contrast at the edge of two adjacent tissues, which is caused by the lack of sufficient spatial resolution or tissue fraction effect referring to the assignment of average intensity values to voxels containing more than one tissue. This effect is more pronounced in larger voxels or anisotropic voxels. Especially for MR assessment of the hip joint cartilage, most cartilage voxels are subject to significant PVE due to the strong curvature of the relatively thin cartilage layers (see Figure 2.11b).

Biochemical MR techniques for cartilage assessment

As minor structural changes in cartilage degeneration or regeneration can hardly be observed using conventional MR imaging techniques, even with the high field strength, biochemical MR imaging offers a useful tool to visualize the cartilage quality in evaluating water, collagen and proteoglycan content of articular cartilages.

The use of delayed gadolinium-enhanced magnetic resonance imaging of cartilage (*d*GEMRIC) was first described by Bashir et al. (1999) to allow the measurement of glycosaminoglycans (GAGs) loss from cartilage ECM in a quantitative manner, and therefore is quite commonly used for quantita-

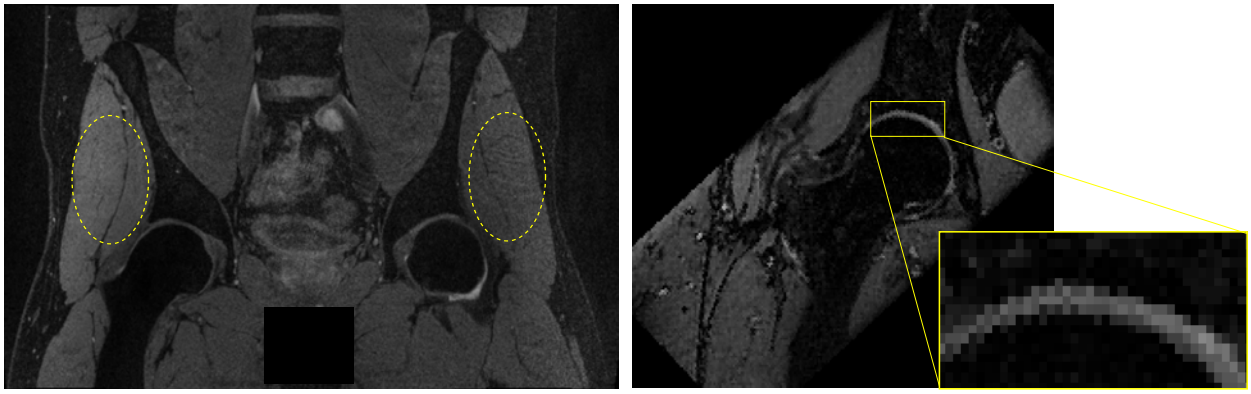

(a) (b)

Figure 2.11: MR artifacts observed in the image of the hip joint: (a) bias field in water-excitation DESS image with a large field-of-view of bilateral hip joints and (b) partial volume averaging in water-excitation DESS image with a small field-of-view of the right-side hip joint.

tive cartilage analyses (Bittersohl et al. 2009; Lattanzi et al. 2014; Mamisch et al. 2011). In *d*GEMRIC, T1 relaxation time in cartilage is calculated after administration of a negatively charged contrast agent (Gd-DTPA^{2-}) as an indirect measure of the loss of GAGs, which is considered as an early degenerative biochemical change that precedes any structural damage in the cartilage (Pritzker et al. 2006). T1 relaxation times are inversely proportional to the concentration of Gd-DTPA^{2-} that is low in the healthy cartilage (i.e., containing abundance of GAGs) and high in the areas of the degraded cartilage where GAGs have been lost (Sur et al. 2009). Bittersohl et al. (2009) also reported a marked reduction of GAGs in the hip cartilage of FAI patients compared to asymptomatic volunteers when using *d*GEMRIC, which might be an index for OA in an early phase. More recently, *d*GEMRIC has proven to be accurate to detect cartilage damages in FAI patients with the promising intra- and inter-observer repeatability (the kappa coefficient 0.76 and 0.68) (Lattanzi et al. 2014). Although *d*GEMRIC has been extensively validated (Bashir et al. 1999; Bittersohl et al. 2009; Lattanzi et al. 2014; Mamisch et al. 2011), it is still under discussion about how to best interpret *d*GEMRIC T1 maps to impact clinical decisions.

T2 mapping has also made a contribution to the research on cartilage damages within the hip joint (Nishii et al. 2010; 2008; Watanabe et al. 2007). It has been suggested that increasing T2 relaxation time was proportional to the distribution of the cartilage water and is sensitive to small water content changes (Liess et al. 2002). This technique involves the acquisition of several images per slice with different echo times. Calculating the slope of the T2 decay curve allows for determination of T2 on a pixel-by-pixel basis. Most studies in the literature have investigated the difference of T2 relaxation time between healthy and diseased hip joints. Carballido-Gamio et al. (2008b) demonstrated the feasibility of *in vivo* quantification of T2 map for the hip cartilage achieving a short-term precision of 5.89%. Nishii et al. (2008) found a positive correlation between the radiographic findings and T2 changes among patients with hip dysplasia. However, T2 mapping may not detect changes as early as techniques that are sensitive to GAGs content, such as *d*GEMRIC or T1ρ.

Besides *d*GEMRIC and T2 mapping, other imaging techniques such as T1ρ (Carballido-Gamio et al. 2008b), sodium MR imaging (Zbýň et al. 2014), chemical exchange saturation transfer (CEST) (Ling

et al. 2008) and fast field cycling nuclear magnetic resonance (NMR) (Broche et al. 2012) have been developed for quantitative measurements of articular cartilage quality. However, these are still in need of extensive validation in the general population before a general clinical application can be considered. The segmentation of the articular cartilage with high accuracy and reproducibility is an essential prerequisite for provision of reliable region of interests (ROIs) in subsequent quantitative measurements on biochemical MR scans.

2.4 Medical Image Segmentation

Medical image segmentation is an essential prerequisite in providing non-invasive information about anatomical structures of interest from original images in all medical imaging applications, which helps clinicians or radiologists to better visualize the anatomy of structures, simulate biological processes, localize pathologies, track the progress of diseases and evaluate the need for the radiotherapy or surgeries. The goal of the image segmentation is to segregate an original image into separate regions or classes, where each has one or more homogeneous characteristics or features under certain criteria (Farag et al. 2005). In a typical computer-aided diagnosis system, segmentation is an essential stage, which is required to be accurate and reproducible to ensure the functionality of the system for clinical applications. However, owing to issues such as low spatial resolution, poor-defined structure boundaries, noise, variability of the anatomy and other image artefacts, the image segmentation still remains a difficult task.

Manual segmentation is the most straightforward approach and is commonly used clinically that involves a well-trained expert (clinician or radiographer) examining every image and outlining the ROIs manually. In practice, manual segmentation is tedious and very time-consuming for slice-by-slice ROI delineation. Although the advantages of manual methods stem from the knowledge of an experienced expert, manual delineation of the ROIs can be subject to the large intra- and inter-rater variability as it completely depends on the knowledge and beliefs of the clinicians performing the operation, especially with no standardized rules to follow. Moreover, this is especially a problem in MR images of the hip joint with various artefacts (i.e., noise, bias field, PVE) and poorly delineated articular cartilage plates, which increases the variability between the resulting manual segmentations obtained from different raters.

Semi-automatic segmentation methods are also preferred in common radiographic protocols because they allow expert clinicians to control the segmentation quality and play a critical role in the final diagnostic decision. Although such semi-automatic methods are usually faster than manual approaches, they are also inconsistent by design when administered by different clinicians and/or used with different internal parameter values.

Fully automatic segmentation algorithms are highly desired to circumvent the need for those time- and expertise-intensive manual/semi-automated segmentation methods and facilitate the provision of reproducible morphometric data in large-scale research and clinical studies. However, it is very challenging for automatic methods to achieve equivalent precision and robustness with manual or semi-automatic approaches. This is mainly because of segmentation difficulties for MR images including

intrinsic limitations of MR imaging (e.g., limited spatial resolution, insufficient tissue contrast, blurring boundaries), the variety of the structure of interest (e.g., shape, size, tissue texture and pathology) and artefacts (e.g., noise, bias field and PVE) seen in the medical image.

The development of automatic algorithms has been the focus of much research in the literature. The common approaches for medical image segmentation include but not limited to classical image analysis, atlas-based, model-based and graph-based segmentation techniques. In the following sections these paradigms will be briefly introduced.

2.4.1 Classical image analysis techniques

Standard image processing algorithms such as thresholding, region growing, edge detection, morphological operators and filters are the fundamental approaches to segment an image into several separate regions (Rogowska 2000).

- *Thresholding* is a simple and straightforward technique to convert a multilevel image into a binary image with groups of pixels/voxels having intensity values less than, greater than or equal to the selected threshold. There are two main categories of thresholding algorithms including global (based on grey-level histograms or local properties) and local thresholding methods (e.g., local adaptive thresholding). These techniques are commonly used in segmentation of the CT image with its superior contrast resolution of the bony tissue (Zhang et al. 2010; Zoroofi et al. 2003).
- *Region growing* is a procedure that starts from a group of seed pixels/voxels in the query image and assigns adjacent pixels/voxels or regions to the same segment if their image values are close enough, according to certain predefined stop criterion. The advantage of region growing is that it is capable of correctly segment spatially separated regions having the same properties while preserving the connectivity within the same region. These techniques are dependent on the selection of representative seed pixels/voxels and are usually semi-automatically applied for segmentation of small volumetric structures such as the articular cartilage (Bae et al. 2009; Waterton et al. 2000).
- *Edge detection* algorithms aim to detect object boundaries (i.e., sharp discontinuities in the image) and segment regions enclosed by the boundaries, which are usually based on edge operators such as Laplacian or gradient operators with consideration of local neighbouring pixels/voxels. Edge detection, particularly based on gradient information is very sensitive to noise since both the noise and the edges contain high frequency signals.

Since such fundamental image segmentation methods are sensitive to noise and are usually insufficient for obtaining a fine segmentation, they are commonly used in the preprocessing or initial segmentation.

2.4.2 Atlas-based segmentation

Atlas-based segmentation approaches form a middle-ground between fully-manual and fully-automatic segmentation approaches providing accurate segmentation of the structures of interest in many areas.

It commonly requires the selection or construction of one or multiple atlases with corresponding delineations of the target objects that are usually acquired manually. Image registration is used to compute the transformations in order to propagate the atlas segmentation and match the query image. During the registration, the similarity between the atlas and the query image is maximized, while, at the same time, the deformation is constrained to ensure that the spatial information of the atlas is maintained.

Single-atlas based segmentation is based on an atlas constructed from one or multiple labelled segmented images. In the latter method, an average atlas can be generated by iteratively registering multiple manual labeled training images and averaging the deformations. The resulting deformations are then applied to both the training images and the related manual labels, which are further combined into a smoothed intensity image and a probability map. This single atlas presents the average anatomical variation of the training population. To segment a new image, the constructed atlas is registered to the input image and the corresponding atlas label image is propagated to the target image using the computed geometric mapping obtained from the registration. Obviously, the segmentation accuracy significantly depends on the registration (if the registration fails, so does the segmentation). The accuracy of single atlas-based methods is limited due to the dissimilarity in the structure (e.g., anatomy) and image appearance between the atlas and the target image (Wang et al. 2013).

Multi-atlas based segmentation have been shown to be more accurate than other atlas-based methods using a single or average shape atlas (Rohlfing et al. 2004). In multi-atlas methods, multiple atlases are obtained either from constructing one representative atlas for each mode based on clustering training images (Blezek and Miller 2007) or from simply selecting the most relevant atlases for the unknown image to segment (Aljabar et al. 2009; Rohlfing et al. 2004). The constructed multiple atlases are separately registered to the target image and the voxelwise label conflicts between the registered atlases are then resolved using label fusion. In this case, by incorporating more than one atlas, it offers advantages in reducing large anatomical discrepancy against a single atlas and improving robustness against occasional registration failure. These multi-atlas approaches have been successfully applied to the segmentation of the brain (Artaechevarria et al. 2009; Heckemann et al. 2006) and the prostate (Dowling et al. 2012). Different similarity measures for optimal atlas selection have been investigated in (Aljabar et al. 2009). However, this algorithm can cause substantial computational burdens when performing pairwise non-rigid registration (NRR) between the new image to be segmented and each atlas in the training set.

2.4.3 Model-based segmentation

Methods based on the model paradigm is to delineate the structure of interest using closed parametric curves or surfaces and deform under the influence of internal and external forces during the segmentation process. In these techniques, global shape or texture prior knowledge can be incorporated to constrain the freeform deformation.

Statistical shape model (SSM) has becoming a promising model to deliver reliable segmentation results across a wide range of anatomical shapes (Cootes et al. 1994; 1995; Fripp et al. 2007; Heimann and Meinzer 2009; Kainmueller et al. 2009; Seim et al. 2010). As strong shape constraints are enforced

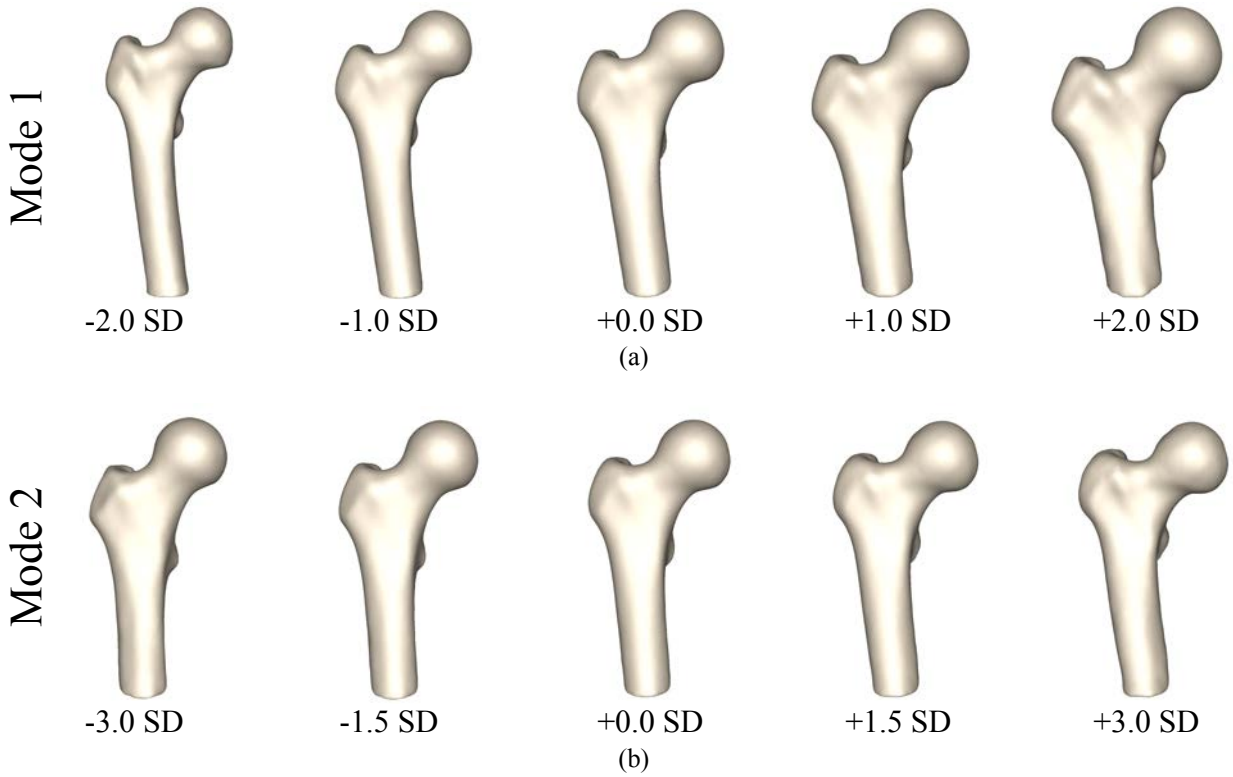

Figure 2.12: Different shapes of the proximal femur with varying shape parameters b_1 and b_2 for (a) first and (b) second mode of variation of the SSM, respectively.

in the shape model, this algorithm is better equipped to deal with low-contrast boundaries. Generally, the shape model is constructed by characterizing shape and shape variations based on the point distribution model (PDM) (Cootes et al. 1992), which represents the geometry of the biological shape with enough corresponding landmarks. During the training process, the shapes of manually labeled examples are represented using the PDMs, from which their mean shape and typical variations are obtained using principal component analysis (PCA) (Jolliffe 2005).

Active shape model (ASM) proposed by Cootes et al. (1994; 1995) is one of the approaches that utilize the SSM to describe a shape in terms of a trained mean shape and variants for each mode on the shape. Given N training surfaces with the point-wise correspondences x_i, $i = 1, 2, \ldots, N$, all the surfaces were Procrustes aligned (Gower 1975) to compute the mean shape $\bar{x}$ and covariance matrix C defined in 2.1.

$$\bar{x} = \frac{1}{N}\sum_{i=1}^{N} x_i, \; C = \frac{1}{N-1}\sum_{i=1}^{N}(x_i - \bar{x})(x_i - \bar{x})^T \tag{2.1}$$

PCA is used to model the variations seen in a population, which produces an eigenvalue decomposition on C that delivers the modes of variation ϕ_i, i.e., eigenvectors, and their respective variances λ_i, i.e., eigenvalues, $i = 1, 2, \ldots, N$. This allows approximating every valid shape x within the shape constraints of the training dataset by a linear combination of the first n modes,:

$$x = \bar{x} + \sum_{i=1}^{n} b_i \phi_i \tag{2.2}$$

where b_i is the shape parameter for the ith orthogonal mode of variation that weights the influence of that mode (Cootes et al. 1995). Figure 2.12 illustrates varying shape parameter b_1 (-2.0 $\sim$ +2.0 standard deviations (SDs)) and b_2 (-3.0 $\sim$ +3.0 SDs) for the first and second mode of variation in an example SSM of the proximal femur.

The model can then be used to estimate the pose and shape parameters of a given surface and generate new surface with the given pose and shape parameters. When used in a segmentation algorithm, the shape model constrains the deformation within an allowable shape space, which improves the robustness of the segmentation algorithm to weak and variable boundaries of the structure.

2.4.4 Graph-based segmentation

Graph-based segmentation approaches are another type of image segmentation techniques that are becoming increasingly popular for automatic segmentation of medical structures/objects of interest within 3D images. In previous studies (Boykov and Kolmogorov 2004; Wu and Chen 2002), the graph-based approaches showed the ability to efficiently produce global optimal 3D segmentations in a single pass (and correspondingly not get stuck in local optima) (Garvin and Wu 2014).

The optimal graph search approach originally presented in (Li et al. 2006; Wu and Chen 2002) has been used extensively in medical image analysis applications (Li et al. 2005; Song et al. 2013; 2010; Yin et al. 2010) for successful simultaneous segmentation of multiple object surfaces with mutually interacting surface constraints (e.g., no intersection) encoded.

Generally, the graph search approach starts from the construction of a graph $G = (N, A)$, where N is a node set and A is an arc set. An arc connecting a node $n_i \in N$ and $n_j \in N$ can be written as $\langle n_i, n_j \rangle \in A$. In a directed graph, $\langle n_i, n_j \rangle$ and $\langle n_j, n_i \rangle$ ($i \neq j$) are considered distinct. Each node can be assigned a real-valued weight and every arc can have a non-negative cost.

In an optimal graph search framework proposed by Li et al. (2006), a properly ordered multi-column graph $G = (N, A)$ in d-D can be constructed from a base graph $M = (V, E)$ in $(d-1)$-D with a positive integer K. Each node $v_i \in V$ has a set of K nodes in N, which is called the ith column of G denoted by $N(v_i)$ here. The column $N(v_i)$ and $N(v_j)$ are adjacent if there is an arc $\langle v_i, v_j \rangle \in E$ connecting v_i and v_j in the base graph M.

In order to simultaneously detect λ surfaces ($\lambda > 1$), the constructed graph $G = (N, A)$ consists of λ node-disjoint subgraphs $\{G_i = (N_i, A_i) : i = 1, 2, \ldots, \lambda\}$. Each node can be assigned a cost value, which is inversely related to the likelihood that the desired surface contains this node. Arcs (e.g., intra-column, inter-column and inter-surface arcs) are added in order to enforce multiple surface feasibility constraints such as the monotonicity, the smoothness and surface distance constraints. Therefore, the goal of the graph search algorithm is to find an optimal surface set $\mathcal{S}$ with the minimum cost that also satisfies:

1. Each surface intersects each column of G at exactly one node and preserves all topologies of the base graph M;
2. Each surface satisfies the pre-defined surface feasibility constraints, e.g., smoothness, inter-surface distance.

Consequently, the optimal surface segmentation problem can be transformed into seeking a minimum-cost nonempty closed set in a directed node-weighted graph $\tilde{G} = (\tilde{N}, \tilde{A})$ as reported in (Wu and Chen 2002), which can be further solved by a minimum $s - t$ algorithm.

2.5 Methodological Overview

2.5.1 MR data acquisition

In this research, MR images were obtained using a 3 T MR scanner (Magnetom Trio; Siemens, Erlangen, Germany) at the University of Queensland. Volunteers with activity history levels ranging from normal everyday activities to high level participation in sports such as water polo, rugby league and rugby union were recruited. The participants are mostly relative young, healthy adults with no history of developmental hip disorders or diagnosed symptoms of hip OA. The medical research ethics committee of the University of Queensland approved the current study and informed written consent was obtained from all participants involved in the research.

A large 4-channel body matrix coil was used during MR image acquisition with Generalized Auto-calibrating Partially Parallel Acquisition (GRAPPA) ($\times 2$) enabled. MR examinations from a total of 63 volunteer subjects were used in this thesis. All the participants were imaged using several different MR sequences after an initial scout image was obtained to assess the position of the subject within the MR scanner. In some participants of the dataset, examinations using multiple MR sequences were acquired from the same subject that can be used for reproducibility experiments.

This MR data acquisition process in this research can be summarized into two stages according to the use in the later segmentation experiments:

- **Stage I - Bilateral MR scans**
  MR images with a large FOV that encompass hip joints of both sides were acquired at the first stage. Different MR sequences were investigated in the first 8 participants, which included T2w 3D DESS, T2w 3D MEDIC and 3D fat-suppressed SPACE (see Figure 2.9). It was found that DESS and MEDIC had a similar bone-cartilage contrast that was much better than 3D SPACE, but DESS had an improved cartilage-synovial fluid contrast. As such, MR images of bilateral hip joints were obtained from another 27 participants only using DESS;

- **Stage II - Unilateral MR scans**
  In order to allow accurate segmentation of the cartilage segmentation, high-resolution 3D True-FISP images (in-plane spacing: 0.47 mm, slice thickness: 0.49 mm) with a relatively small FOV of the unilateral hip joint were involved into the acquisition routine for the latter 46 participants, where there were 18 participants had MR examinations using both bilateral DESS and unilateral TrueFISP. Slice interpolation (K-space) was enabled for a subset of 41 TrueFISP scans to obtain an in-plane image resolution of 0.234 mm. In addition, another two unilateral MR sequences (DESS and SPACE) were also used in the last 18 participants for reproducibility experiments.

Table 2.1 lists the parameters and number of acquired scans for each MR sequence that was in-

Table 2.1: Acquisition parameters for each MR sequence.

	BILATERAL		UNILATERAL		
Parameter	MEDIC	DESS	TrueFISP	DESS	SPACE
No. of subjects	8	35	46	18	18
Plane Spacing (mm)	0.65	0.67	0.47	0.63	0.75
Slice Thickness (mm)	0.70	0.61	0.49	0.70	0.90
Acquisition Matrix	576×360	576×360	320×320	256×192	256×256
FOV (cm)	37.6×23.5	38.6×24.1	15×15	16.0×12.0	18.9×19.2
Repetition Time (ms)	22	15.46	10.65	12.71	1500
Echo Time (ms)	12	5.16	4.46	4.92	42
Bandwidth (Hz)	155	202	230	326	543
Flip Angle (degrees)	12	25	30	25	120

volved in this research. These MR scans served different aims in the thesis, which will be detailed in the following chapters.

2.5.2 Segmentation methods

A *priori* is of great importance to provide crucial information such as the image environment or structures' shape/appearance for designing an effective algorithm, especially when the images are influenced by noise or PVE. As stated before, the segmentation of the hip joint, particularly the cartilages, is very challenging due to various anatomical, imaging and segmentation difficulties. It is only by incorporating effective prior knowledge of the bones (e.g., shape) and cartilages (e.g., spatial relationship and morphological features) from the training process using expert manual segmentations, that one can expect to have any hope to automatically, accurately and robustly segment the hip joint.

In this research, the ASM based method using SSMs with shape prior knowledge is first considered for the first segmentation task, automatic bone segmentation of the hip joint, because it is a well-developed algorithm that has been successfully applied for segmentation of various anatomical shapes including bone segmentation for the hip (using CT data) (Kainmueller et al. 2009) and knee joint (Fripp et al. 2007; Seim et al. 2010). With the inclusion of shape constraints into the segmentation algorithm, the ASM segmentation constrains the freeform gradient-driven deformation of the bone shapes within a certain level of anatomical variations obtained from the training dataset. The SSMs of the bones within the hip joint can be also served as a framework to incorporate prior knowledge of the cartilage morphology, which is achieved by utilizing the corresponding landmarks of the bone shape to extract morphological information from the training data of manual cartilage segmentations. This information is analysed and utilized in the subsequent cartilage segmentation algorithm, e.g., identifying the BCI from the segmented bone surfaces.

The graph search approach is a preferable option for delineation of the individual femoral and acetabular cartilage plates, which are closely apposed within the hip joint. The original multi-layered graph search framework (Yin et al. 2010) has successfully applied to the knee joint for simultaneous segmentation of the cartilages. However, this approach is not readily applicable to the delineation of multiple surfaces with poor separation of boundaries, e.g., the femoral and acetabular plates. There-

fore, improvements need to be done to the original multi-layered graph search framework by incorporating prior knowledge of the cartilage morphology to obtained reliable segmentation of the two cartilage plates under the insufficient image environment.

Moreover, the multi-atlas segmentation method acts as the state-of-the-art method in comparisons with our proposed methods for both bone and cartilage segmentation. This is because it is easy to implement and can provide accurate segmentation of the structures of interest when a large number of training images with a wide range of anatomical variations are involved.

3

BONE SEGMENTATION FROM LARGE FIELD OF VIEW 3D MR IMAGES OF THE HIP JOINT

This chapter presents the work to attain **Aim 1.1**, which is to develop and evaluate automatic segmentation methods for accurate and reliable segmentation of the bone elements (i.e., the proximal femurs and innominate bones) from 3D MR images of the hip. Two state-of-the-art methods (multi-atlas and ASM based approaches) are developed to automatically segment the bones from MR images with a large FOV encompassing hip joints of both sides. A validational study is performed using DESS and MEDIC images of bilateral hip joints acquired from 35 volunteers, which aims at examining the potential suitability of these methods for generating morphometric data on the bone elements of the hip joint and providing a basis for subsequent cartilage segmentation.

The core material of this chapter has been published in (Xia et al. 2012; 2011; 2013). The training process of SSMs of the bones in the hip joint region and the ASM based bone segmentation algorithm was initially proposed in (Xia et al. 2012; 2011). More advanced work in (Xia et al. 2013) was presented to extend the evaluation to two state-of-the-art (multi-atlas and ASM based) methods for automatic bone segmentation of high-resolution 3D MR images of the hip region and the preliminary validation was applied to DESS and MEDIC images from 30 volunteers. In this chapter, results are updated by incorporating manual segmentations from MR images in the full dataset of 35 volunteers for the implementation of the multi-atlas method and the validation of automatic bone segmentations.

Related publication details

Xia, Y., Fripp, J., Chandra, S. S., Schwarz, R., Engstrom, C., and Crozier, S. (2013). Automated bone segmentation from large field of view 3D MR images of the hip joint. *Physics in Medicine and Biology*, 58(20):7375. http://iopscience.iop.org/0031-9155/58/20/7375/ (Xia et al. 2013)

Manuscript revision history

Submitted to *Physics in Medicine and Biology*	6 July 2013
Interim decision (minor revision)	1 August 2013
Revision submitted	28 August 2013
Accepted	30 August 2013

Xia, Y., Chandra, S., Salvado, O., Fripp, J., Schwartz, R., Lauer, L., Engstrom, C., and Crozier, S. (2012). Automated bone segmentation and bone-cartilage interface extraction from MR images of the hip. In *International Society for Magnetic Resonance in Medicine (ISMRM) 20th Annual Meeting & Exhibition: Adapting MRI in a Changing World* (Xia et al. 2012)

Manuscript revision history	
Submitted to the *ISMRM* conference	10 November 2011
Accepted	28 January 2012
Presented (traditional poster) in the ISMRM conference	10 May 2012

Xia, Y., Chandra, S. S., Salvado, O., Fripp, J., Schwarz, R., Lauer, L., Engstrom, C., and Crozier, S. (2011). Automated MR hip bone segmentation. In *Digital Image Computing Techniques and Applications (DICTA), 2011 International Conference on*, pages 25--30. http://dx.doi.org/10.1109/DICTA.2011.13 (Xia et al. 2011)

Manuscript revision history	
Submitted to the *DICTA* conference	13 July 2011
Accepted	8 August 2011
Presented (oral presentation) in the DICTA conference	6 December 2011

3.1 Introduction

Morphometric analyses of the osteochondral elements in the hip joint region using MR imaging have the capacity to provide quantitative data for research and clinical investigations into pathoanatomical conditions such as FAI through to early or more advanced stages of OA to assess bone and cartilage changes. To facilitate this, automated MR-based segmentation approaches are being developed to circumvent the need for extensive time- and expertise-intensive manual/semi-automated segmentation of osteochondral elements in the hip region (Kavanagh et al. 2011; Naish et al. 2006). In previous MR studies, advanced image analysis approaches such as SSM (Cootes et al. 1995), atlas-based and graph search approaches have been successfully applied to automatic bone segmentation of the knee (Ababneh et al. 2011; Fripp et al. 2007; Shan et al. 2012; Yin et al. 2010), ankle (Li et al. 2005) and spine (Neubert et al. 2012) and for use in subsequent segmentation of the cartilage (Fripp et al. 2010; Seim et al. 2010).

In a recent MR study of the bone elements of the hip region, Schmid et al. (2011) reported a robust bone segmentation algorithm especially for unilateral MR images of the hip joint with a limited FOV where the bones were partially visible. In their approach, a SSM with robust PCA was proposed to

address the segmentation difficulties arising from images with a small FOV and achieved an average distance error of 1.21 ± 0.53 mm for the femur and 1.03 ± 0.38 mm for the innominate bone. In order to segment large FOV MR images of the hip joint region (encompassing both hip joints) used in our study, the widely utilized PCA (Section 2.4.3), we believe, is well suited for this application.

Alternatively, Dowling et al. (2012) used NRR to an average atlas for automated segmentation of the pelvic organs including the bone elements of the hip region in MR images. There was moderate agreement between manual and atlas segmentation results for the bone volume with a mean (± SD) Dice's similarity coefficient (DSC) score of 0.79 (± 0.12). As the general atlas-based approaches have been discussed in Section 2.4.2, multi-atlas-based algorithms are more accurate and robust against occasional registration failures than other single-atlas-based methods (Rohlfing et al. 2004). To the best of our knowledge, no other published work has been used the multi-atlas-based algorithm to automatically segment the bone elements from MR images of the hip.

In this chapter, we evaluate automated bone segmentations, against manual segmentations, from large FOV MR images of the hip region (proximal femurs, innominate bones) using two state-of-the-art methods: (i) multi-atlas-based method using pairwise NRR and (ii) 3D ASM-based method to assess their accuracy and computational efficiency. This aims examining the potential suitability of the two approaches for large prospective clinical and research investigations into morphological bony changes in conditions such as FAI and subsequent cartilage segmentation in OA.

3.2 Materials and Methods

3.2.1 Image dataset and MR acquisition protocol

Anonymized MR images of the hip joints (bilateral) from 35 volunteers (aged 18-49 years, 31 males and 4 females, mass 85.0 ± 13.0 kg) were included in this study. This acquired dataset involved a variety of the FHN junction presentations, which were examined based on MR images by a radiologist (Dr. Duncan Walker) and measured alpha angles (40° - 88°) at two radial positions of 1:30 and 3:00 (Mr. Phillip Melville) for assessment of the cam-type bony architecture in a number of the high-performance athletes.

The first eight subjects were imaged using T2w DESS and MEDIC sequences. These had similar bone-cartilage contrast, but DESS had improved cartilage-synovial contrast. As such, all subsequent subjects were only imaged using DESS. A total of 35 DESS and 8 MEDIC images were used in this study. The parameters used in each imaging sequence are listed in Table 2.1. Example coronal slices of the hip region from the different acquisition protocols are illustrated in Figure 3.1a and 3.1b.

Manual segmentation

For this study, the bone elements of the hip (left/right femur, left/right innominate bone) were manually labelled by the author (Rater 1) and Dr. Mark W Strudwick (an experienced radiographer, Rater 2) using ITK-SNAP (Yushkevich et al. 2006) with expert guidance from Dr. Craig Engstrom (an

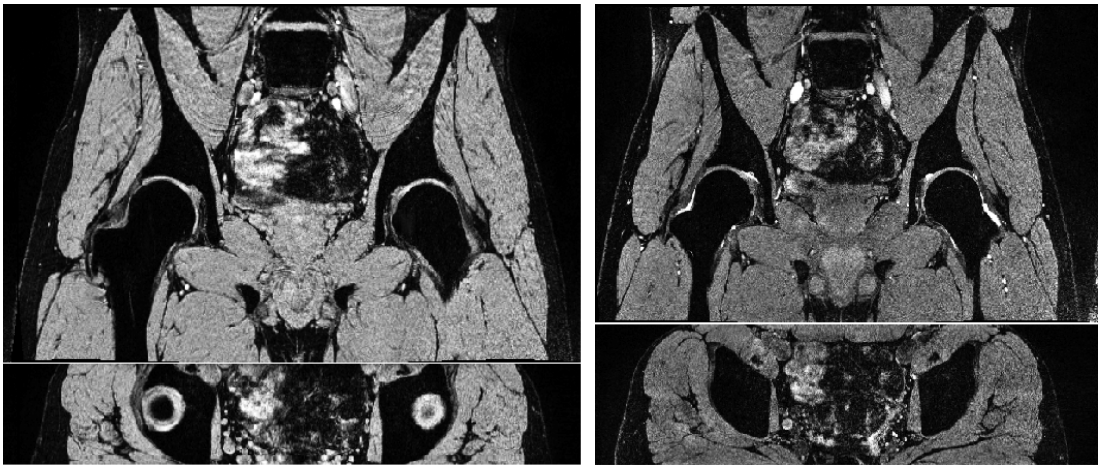

(a) (b)

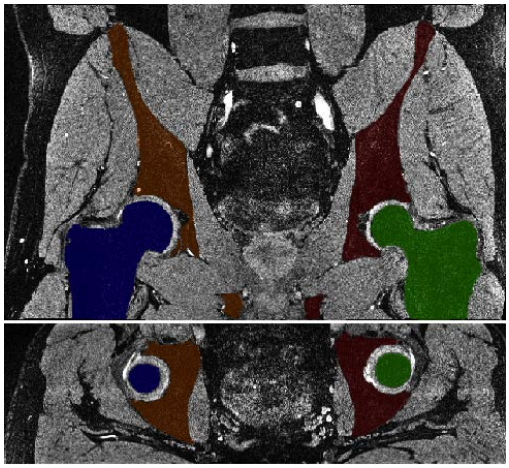

(c)

Figure 3.1: Example (top) coronal and (bottom) axial slices of MR images with multiple sequences as well as an example of manual segmentations of the proximal femur (blue, green) and innominate (brown, red) bone elements: (a) MEDIC; (b) DESS; (c) manual labels overlaying on a DESS image.

experienced MSK analyst). Figure 3.1c shows a typical example of manual segmentations of the bone elements in the hip region as an overlay on the MR images.

The bones in the entire dataset of MR images (DESS for 35 subjects, MEDIC for 8 subjects) were manually labelled on every slice by Rater 1. To investigate the inter-rater reliability, DESS images from eight subjects were manually segmented in the coronal view on every fourth slice by Rater 2. The images from four of these subjects (randomly selected) were re-segmented in a blinded fashion two weeks later by Rater 2 for evaluation of the intra-rater reliability test.

3.2.2 Training process: shape modelling and atlas creation

Surface model creation from Newcastle CT

An independent set of CT images of the pelvis from 28 male patients involved in a prostate cancer study at Calvary Mater Newcastle Hospital (Dowling et al. 2010) was utilized as a training dataset in order to create shape models with a relatively large coverage of the bone elements within the hip

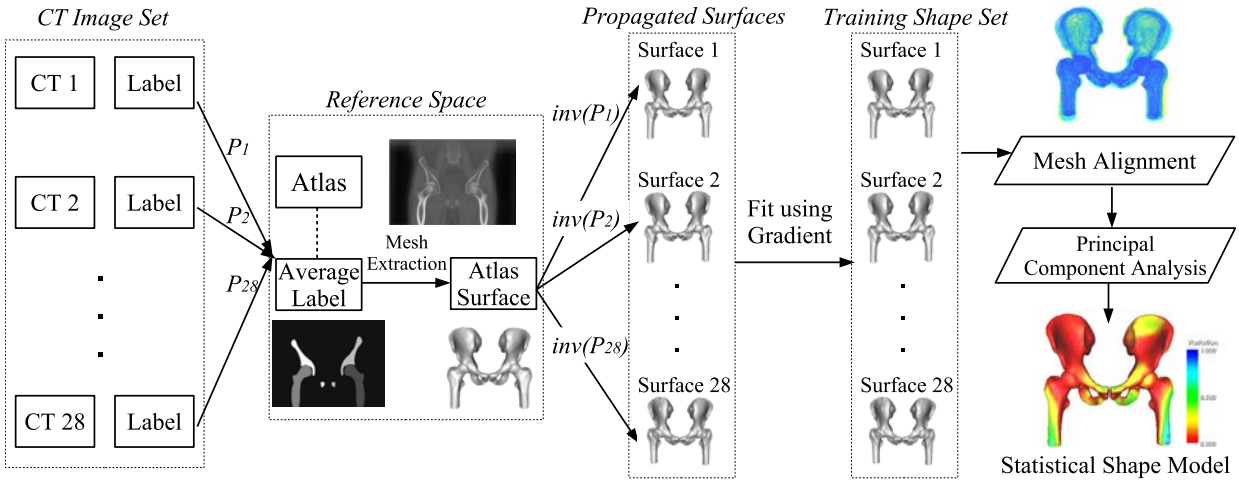

Figure 3.2: Illustrative shape model creation process.

region. This involved:

1. *Individual CT labelling*: CT images were semi-automatically segmented using a multi-atlas-based registration approach as detailed in (Xia et al. 2011). Briefly, six cases were randomly chosen from the CT dataset for manual bone segmentation and then registered to all the other 22 cases using diffeomorphic demons NRR (Vercauteren et al. 2009). For each case, the propagated atlas labels of the bones were averaged and thresholded at 50% to obtain an average bone segmentation, which was then followed by necessary morphological post-processing steps such as dilation and iterative voting hole filling.
2. *Average CT atlas*: all the CT images and bone labels were propagated to a common reference space using the computed deformation fields, and further averaged into a CT atlas and a probabilistic label atlas, as illustrated in Figure 3.2. A CT atlas surface was then extracted from the thresholded (50%) label atlas followed by triangular decimation and mesh smoothing.
3. *Individual CT surface with correspondence*: the resulting surface was then transformed back onto all 28 original CT images to obtain a batch of bone surfaces with the point-wise correspondences. The propagated surfaces were iteratively deformed (< 3 iterations) towards the negative gradient of the manual label images to 'snap' to the bone elements in CT images.

Statistical shape modelling

Using the standard PCA algorithm presented in Chapter 2, the SSM was created from all the bone surfaces with the point-wise correspondences. In this chapter, we created 7 SSMs, including a bilateral hip SSM involving all four bony elements of the hip trained from a set of 28 meshes, and two unilateral hip SSMs (femur + innominate bone) as well as four SSMs of individual bones (left/right femur, left/right innominate bone). The unilateral and individual bone SSMs employed 56 training surfaces each (28 surfaces from one side and 28 flipped surfaces from the other side) in order to incorporate additional anatomical variations in the shape models. Four types of the SSMs are shown in Figure 3.3 illustrating their first mode of variation (the left-side SSMs modelled the same shape variability as the right-side shape models). The compactness for each type of the constructed SSMs is analysed in

Figure 3.4.

3.2.3 Segmentation algorithms

Each MR image was preprocessed before two parallel segmentation pipelines (multi-atlas-based and ASM-based algorithm) were applied to extract the bones. The overall segmentation diagram is provided in Figure 3.5.

Image preprocessing

All the acquired MR images were firstly pre-processed with:

1. N4 bias field correction (Tustison et al. 2010) (B-spline fitting: [spline distance = 200, spline order = 3, sigmoid alpha = 0, sigmoid beta = 0.5], convergence: [maximum number of iterations at each resolution = $100 \times 80 \times 80$, convergence threshold = 0.001], shrink factor: 3).
2. Smoothing using gradient anisotropic diffusion (5 iterations, time step: 0.02, conductance: 1.0).

Multi-atlas-based segmentation pipeline

In this chapter, we implemented a multi-atlas-based method, which has been previously described in (Chandra et al. 2012a) for use in the prostate segmentation.

To allow a more direct comparison of the performance of the two methods, only male subjects were selected for use as atlases. The multi-atlas set was composed of preprocessed images from DESS examinations acquired from 31 male subjects, whose bone areas were manually labelled on every slice. Images acquired from four female subjects with corresponding manual segmentations were not included in the multi-atlas training dataset for a more even comparison between the two proposed methods. All the bilateral MR images in the multi-atlas set were split left-right. The atlases of the right-side hip joint were flipped to the left-side doubling the number of atlases (N = 62 or N = 60 if a leave-one-subject-out validation was used).

To automatically segment an image, the image was firstly divided into two parts in the same way as the atlas. For each side of the hip joint, the following steps were followed:

1. *Pairwise NRR*: the Nifty-Reg package (Modat et al. 2010) was employed to perform NRR between each atlas and this new preprocessed MR image.
2. *Atlas selection*: the most similar atlases were selected based on normalized mutual information (NMI) that was computed between the MR image C and the deformed atlases $A_i \cdot P_i$, where P_i was the computed NRR transformation for the ith atlas.
3. *Label fusion*: the automatic bone segmentation was hence obtained by fusing the bone contours of the chosen atlases via majority voting (Artaechevarria et al. 2009), whose number can be variable in different cases according to the predefined selection criteria.

At Step 2, an atlas was selected for automatic labelling if it satisfied $r_i \geq \phi$ ($0 \leq \phi \leq 1$, $\phi = 0.8$ was used here), where the ratio r_i for atlas A_i was calculated using its NMI value as well as the minimal

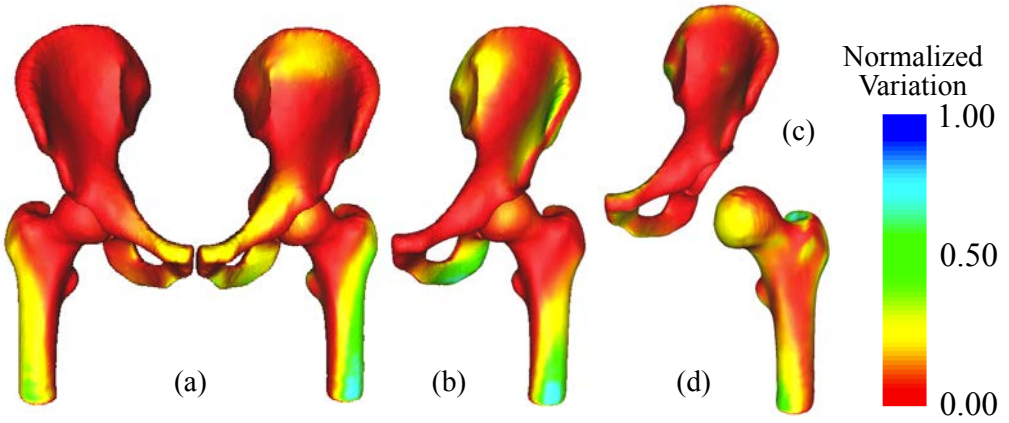

Figure 3.3: Hip bone shape models with the colour map illustrating normalized variation of the primary mode: (a) the bilateral hip SSM; (b) the unilateral hip SSM; (c) innominate bone SSM; (d) femur SSM.

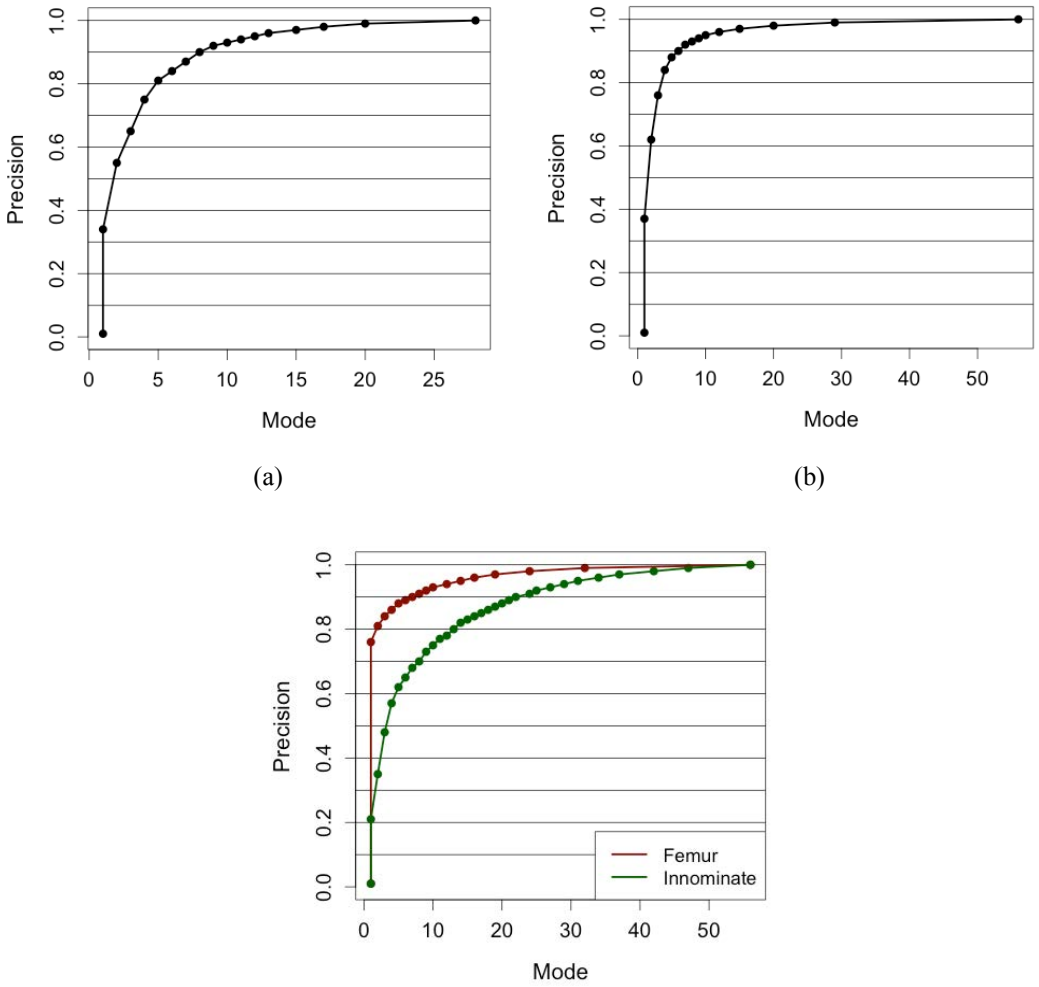

Figure 3.4: The compactness of (a) the bilateral hip SSM, (b) the unilateral hip SSM and (c) SSMs of the proximal femur and innominate bone.

and maximal NMI values among all the atlases shown as (3.1).

$$r_i = \frac{\text{NMI}(C, A_i \cdot P_i) - \min_k\{\text{NMI}(C, A_k \cdot P_k)\}}{\max_k\{\text{NMI}(C, A_k \cdot P_k)\} - \min_k\{\text{NMI}(C, A_k \cdot P_k)\}} \tag{3.1}$$

ASM-based segmentation pipeline

At the initialization stage, the acquired MR image and the CT atlas were firstly joint-center-based aligned using an automated joint locator algorithm (Nishii et al. 2004). The CT atlas was then resampled to have the same FOV with the MR image. An affine transform was computed from an affine registration performed using the ITK registration toolkit (Ibanez et al. 2003) between the resampled atlas and the image to be segmented. An initialized surface can be then obtained by propagating the associated atlas surface. To enhance the robustness of the initialization, checks for abnormal scaling factors in the affine transform (20% different from the unity) were made, a failure of which resulted in using the simply centered surface for initialization.

The automated bone segmentation was performed in a three-level multi-resolution Gaussian pyramid the details of which are given in (Fripp et al. 2007) for the knee joint. The ASM segmentation was iteratively performed as follows until it reached the convergence or the maximum number of iterations, as shown in Figure 3.6:

- *Deformation:* Each vertex of the surface was independently adjusted towards the mean gradient of the one-dimensional profile extracted along its normal direction.
- *Shape constraints:* The SSM was used to estimate the pose and shape parameters in order to bring the deformation of the surface back to an anatomical reference built during the training of the shape model.

Due to the CT dataset used for training, the atlas surface used for initialization always had larger bone coverage than the MR image. In order to prevent overly compressing the deforming shape into the MR image, the ASM segmentation was modified to force zero displacement to vertices lying outside the MR image during the deformation process while still applying the shape constraints to the whole shape.

To achieve the full bone segmentation of the hip joints on both sides, three main steps were involved.

1. Coarse bone segmentation using the bilateral hip SSM, which maintained the constraints from the whole bone structure of the hip region and improved the initialized alignment of the bone surfaces from the affine transform.
2. Bone segmentation refinement for both sides using the unilateral hip SSMs followed by the femur and innominate bone SSMs.
3. Bone surface relaxation (Fripp et al. 2007) to better fit the bone edges by applying the ASM for a small number (<5) of iterations without shape constraints but smoothing.

3.2.4 Validation method

To verify their accuracy and robustness, automated bone segmentation results from the multi-atlas-based and ASM-based methods were validated against manual segmentations. A leave-one-subject-out approach, which removed atlas images of both hip joints from the same subject, was used for the multi-atlas-based method.

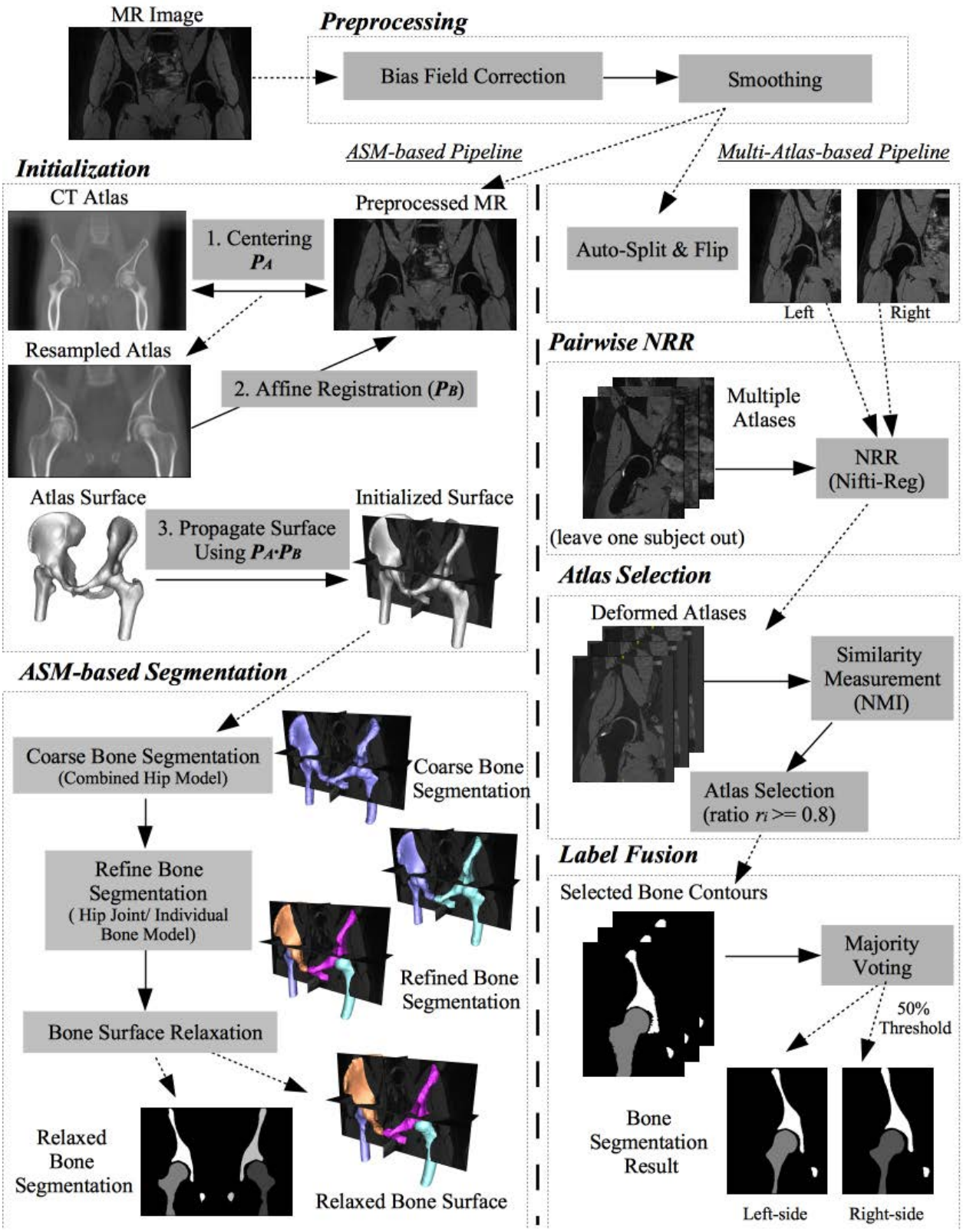

Figure 3.5: Flow diagram of the multi-atlas-based and ASM-based segmentation pipelines.

The validation of the bone segmentation is reported using five volume/distance-based measures: Sensitivity, Specificity, DSC (Dice 1945), mean absolute surface distance (MASD) (Gerig et al. 2001) and relative absolute volume difference (RAVD) (Van Ginneken et al. 2007). Let N_{TP}, N_{TN}, N_{FP} and N_{FN} respectively denote true positive, true negative, false positive and false negative voxel counts, the Sensitivity = $N_{TP}/(N_{TP} + N_{FN})$ is the true positive fraction and Specificity = $N_{TN}/(N_{TN} + N_{FP})$

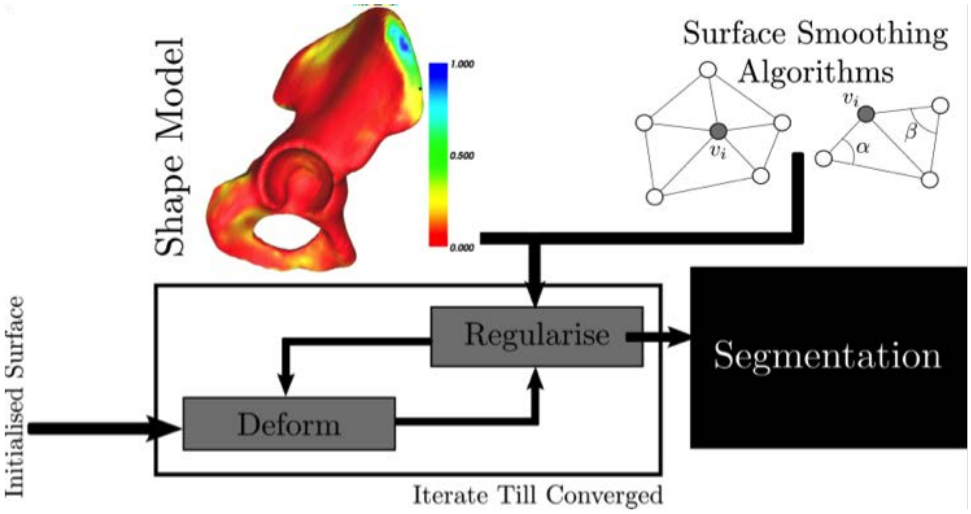

Figure 3.6: Illustrative ASM segmentation process using an example SSM of the innominate bone.

Table 3.1: Comparison of validation measures (mean ± SD) between the multi-atlas and ASM based method.

	Multi-atlas-based		ASM-based	
	Femur	Innominate bone	Femur	Innominate bone
Sensivity	0.952 ± 0.037	0.927 ± 0.040	0.966 ± 0.017	0.965 ± 0.012
Specificity	0.998 ± 0.001	0.996 ± 0.004	0.998 ± 0.001	0.995 ± 0.001
DSC	0.954 ± 0.021	0.934 ± 0.032	0.949 ± 0.012	0.920 ± 0.018
MASD (mm)	0.715 ± 0.374	0.730 ± 0.476	0.904 ± 0.250	0.882 ± 0.145
RAVD (%)	2.99 ± 3.34	3.27 ± 4.17	4.15 ± 2.60	9.77 ± 3.73

is the true negative fraction. The DSC value is a spatial overlap ratio between automatic and manual segmentations calculated as DSC = 2 N_{TP}/(2 N_{TP} + N_{FP} + N_{FN}). The MASD (mm) is defined as: $d_{\text{MASD}} = [d_{\text{avg}}(S_A, S_M) + d_{\text{avg}}(S_M, S_A)]/2$, where $d_{\text{avg}}(S_A, S_M)$ is the average directed surface distance from all the points on the automated surface S_A to the manual surface S_M. The RAVD is given in percentage terms, RAVD(%) $= 100 \times |A - M|/M$, where A and M are the automatic and manual segmentation volumes.

Moreover, the mean and SD Hausdorff distance $d_{\text{Hausdorff}}(S_A, S_M)$ maps (Aspert et al. 2002; Commandeur et al. 2011) are used to demonstrate the distribution of segmentation errors across the anatomical regions of the bone components (i.e., the proximal femurs, innominate bones), where $d_{\text{Hausdorff}}(S_A, S_M)$ = max(max($d(v_A, S_M)$, $v_A \in S_A$), max($d(v_M, S_A)$, $v_M \in S_M$)), S_M and S_A are manual and automatic segmentations of the bone component.

3.3 Results

3.3.1 Inter- and intra-rater reliability

Exploratory analyses showed good inter-rater reliability between the two raters with a mean DSC of 0.970 and 0.963 for manual segmentation of the femur and innominate bone volumes, respectively. The intra-class correlation coefficients (ICCs) were found to be 0.997 (95% confidence interval (CI):

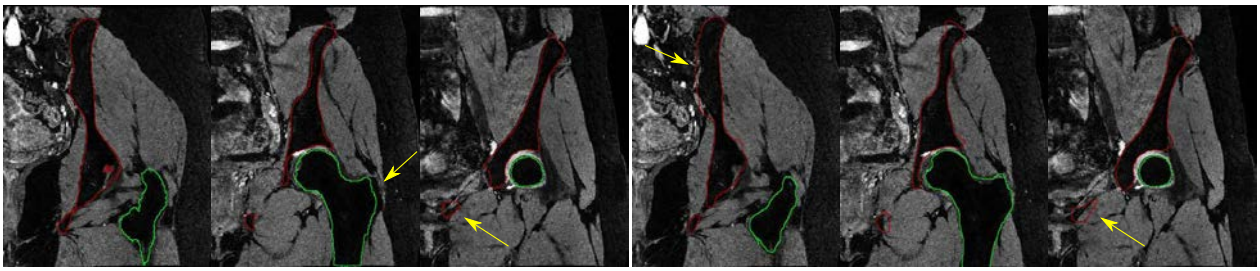

DSC (femur, innominate bone) = (0.924, 0.900) DSC (femur, innominate bone) = (0.945, 0.886)

(a) Subject 17 DESS

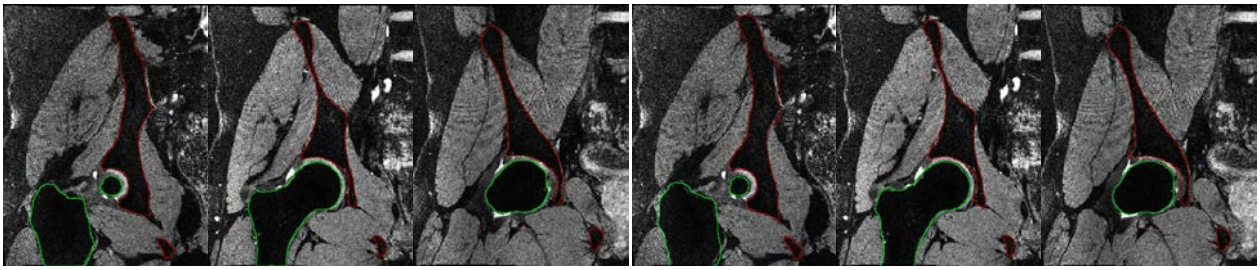

DSC (femur, innominate bone) = (0.955, 0.941) DSC (femur, innominate bone) = (0.948, 0.925)

(b) Subject 26 DESS

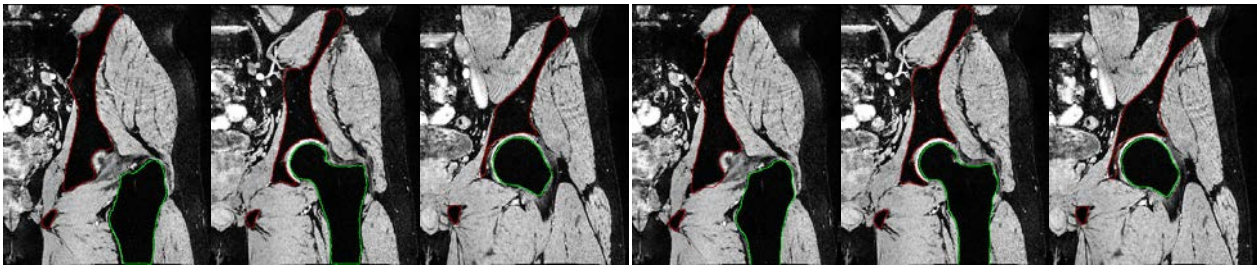

DSC (femur, innominate bone) = (0.972, 0.962) DSC (femur, innominate bone) = (0.966, 0.943)

(c) Subject 11 MEDIC

Figure 3.7: Example coronal slices of bone segmentation results with DSC values for the multi-atlas method (left) and ASM-based method (right): (a) below the mean DSC showing over/under-segmentation occurred (arrows); (b) around the mean DSC; (c) above the mean DSC.

0.984 - 0.999) and 0.992 (95% CI: 0.880 - 0.998) for the inter-rater reliability of the femur and innominate bone volumes.

Similarly, there was a good intra-rater reliability of Rater 2 for determination of the (femur, innominate) bone volumes with mean DSC scores of (0.971, 0.965). The intra-rater ICCs were 0.997 (95% CI: 0.982 - 0.999) and 0.997 (95% CI: 0.986 - 0.999) for manual volumes of the femur and innominate bone.

3.3.2 Segmentation accuracy

Both segmentation pipelines were successfully applied to all 43 MR image sets (35 DESS and 8 MEDIC studies). A summary of the volumetric and distance-based validation metrics for automatic bone segmentations can be seen in Table 3.1 for both multi-atlas-based and ASM-based approaches in comparison with the manual segmentation data. The two methods achieved mean ($\pm$ SD) DSC values for the femur and innominate bone volumes of 0.954 ($\pm$ 0.021), 0.934 ($\pm$ 0.032) and 0.949 ($\pm$ 0.012),

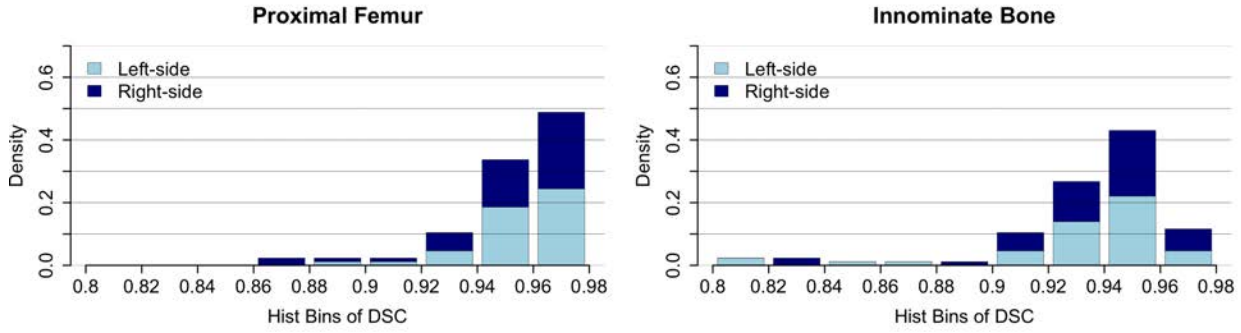

(a)

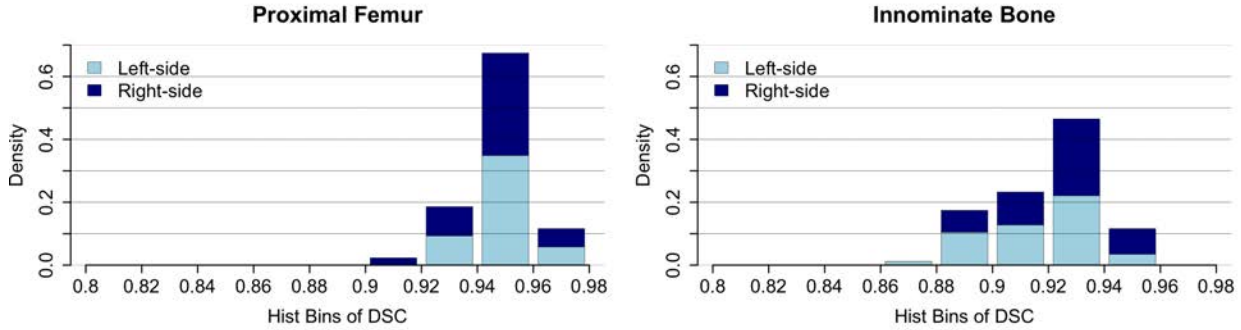

(b)

Figure 3.8: Histograms of DSC values for the (left) proximal femur and (right) innominate bone segmentations using (a) multi-atlas-based method and (b) ASM-based method (light blue: left-side cases and blue: right-side cases).

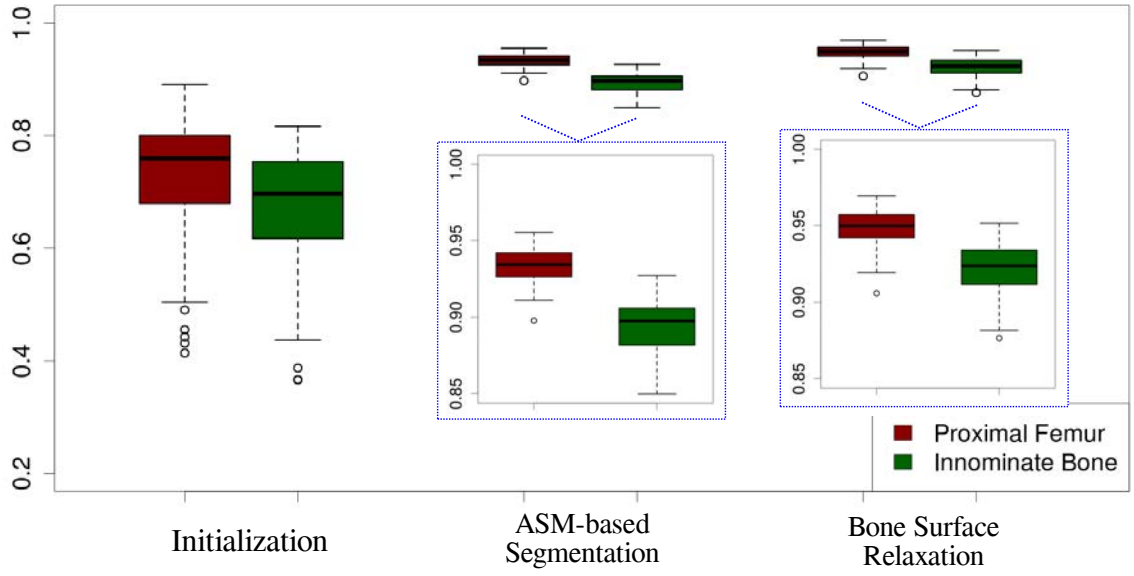

Figure 3.9: DSC scores for automatic segmentations of the proximal femur (green) and innominate bone (yellow) obtained at (left) initialization, (middle) ASM-based segmentation and (right) bone surface relaxation stage in the ASM-based segmentation pipeline.

0.920 ($\pm$ 0.018) comparable to the manual inter- and intra-rater reliability data. Using paired *t*-test analyses (Null hypothesis: no difference made between these two segmentation methods), the multi-atlas-based method showed significant advantages in both DSC values ($t(86) = 2.040$, $p < 0.05$ and

$t(86) = 4.398$, $p < 0.05$) and MASD ($t(86) = -3.849$, $p < 0.05$ and $t(86) = -3.199$, $p < 0.05$) for the proximal femurs and innominate bones.

For the subset of 8 volunteers with both MR examinations, the multi-atlas-based and ASM-based methods achieved mean $\pm$ SD DSC values (femur, innominate bone) of (0.949 $\pm$ 0.022, 0.911 $\pm$ 0.043) and (0.948 $\pm$ 0.010, 0.909 $\pm$ 0.043) for DESS images, (0.963 $\pm$ 0.016, 0.947 $\pm$ 0.019) and (0.957 $\pm$ 0.007, 0.923 $\pm$ 0.019) for MEDIC images. The slight improvement in DSC for the MEDIC is likely due to its higher contrast between the bone and other tissues.

Figure 3.7 provides qualitative comparisons of both bone segmentation results, showing a series of illustrative coronal images from the DESS and MEDIC examinations of individual subjects with DSC values below, about and above the overall mean study results. The histograms of both validation results are shown in Figure 3.8 demonstrating that most DSC values for the femur segmentations from the two methods were distributed between 0.92 and 0.98. The DSC values of the innominate bone segmentations using the ASM-based method ranged from 0.86 to 0.96, while the multi-atlas-based method had a slightly wider range between 0.8 and 0.98. In Figure 3.9, it presents the boxplots of DSC values for validation results at three different stages of the ASM-based segmentation pipeline, including the initialization, ASM-based segmentation and bone surface relaxation. Based on the initialized bone surfaces with varied levels of accuracy due to varying posture of subjects and FOV of MR scans, the ASM fit largely improved the accuracy of automatic bone segmentations with DSC values of 0.93 $\pm$ 0.01 for the proximal femur and 0.89 $\pm$ 0.02 for the innominate bone, which was further slightly refined by the bone surface relaxation.

Both the multi-atlas and ASM automated segmentation results showed high correlation (coefficient of determination $R^2 > 0.9$) with the manual data (Figure 3.10a). From the Bland-Altman analyses (Figure 3.10b) (Bland and Altman 1986), the segmented volumes for the proximal femur had a mean bias (i.e., relative volume difference (RVD)) of -0.47 $\pm$ 4.47% for the multi-atlas-based method and 3.61 $\pm$ 3.31% for the ASM-based method; for the innominate bone, the ASM-based method overestimated the bone volume with a bias of 9.77 $\pm$ 3.73% while the multi-atlas-based method showed a bias of -1.41 $\pm$ 5.12%.

3.3.3 Hausdorff distance maps

To evaluate the accuracy of the bone 'edge' segmentations, particularly neighbouring the likely articular cartilage surfaces of the femoral head and acetabulum (approximating the BCI of the hip joint), the distribution of segmentation errors near these anatomical regions of interest was calculated using mean and SD Hausdorff distance maps (Aspert et al. 2002; Commandeur et al. 2011) generated for both the bone components, i.e., the femoral head and acetabulum (Figure 3.11).

It can be seen that the femoral head was accurately segmented using both methods at the likely-BCI region (Figure 3.11a, dashed circle 1), where the mean Hausdorff distance was mostly < 0.5 mm (corresponding to the in-plane image resolution of 0.65 and 0.67 mm for MEDIC and DESS, respectively) with a small variance (< 1.0 mm). At the femoral fovea (Figure 3.11a, dashed circle 2), which was typically devoid of a layer of articular cartilage, both automated approaches had a slightly

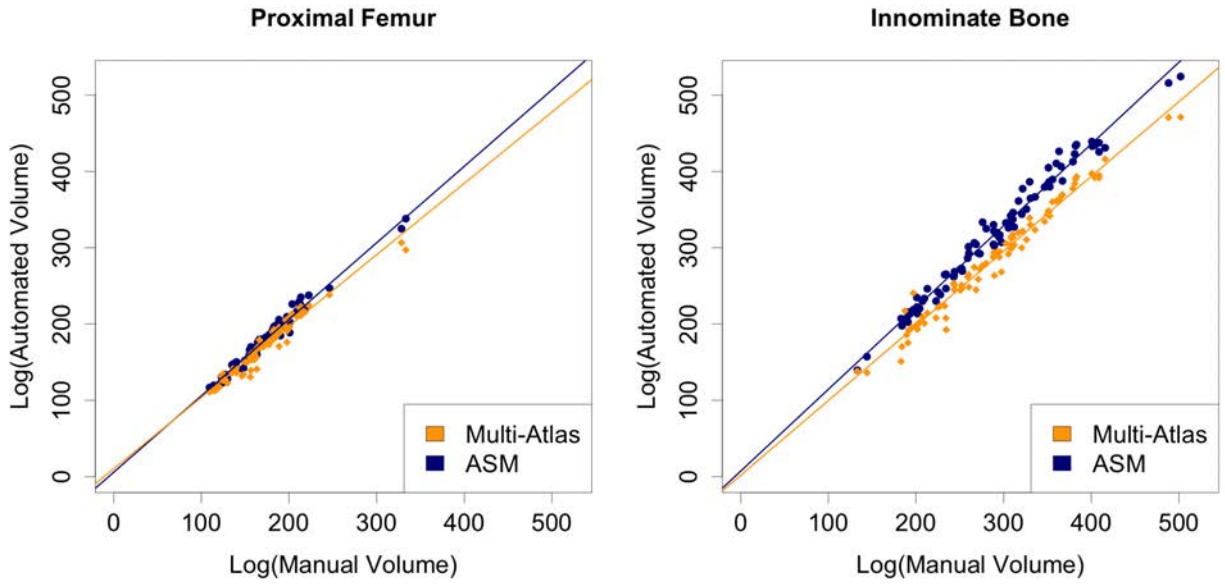

(a)

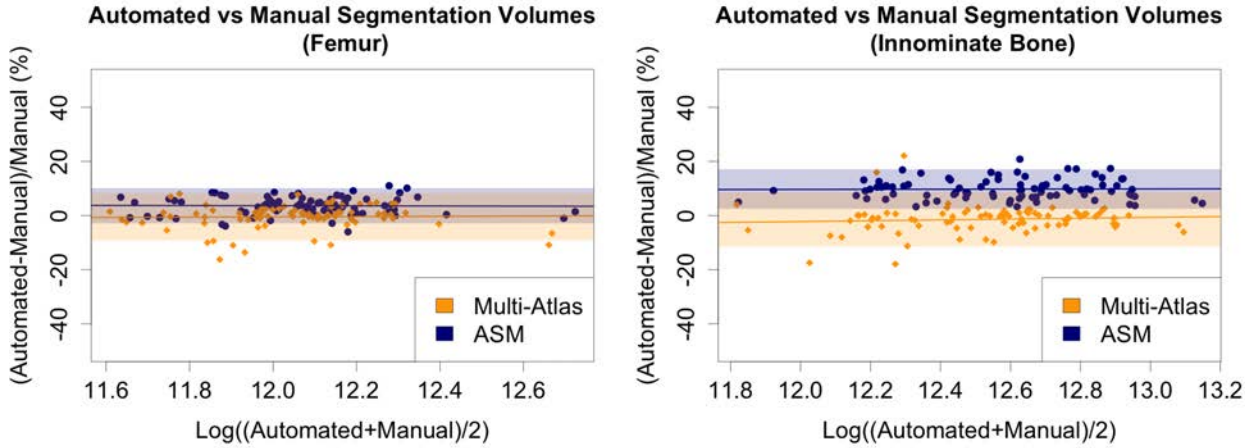

(b)

Figure 3.10: Statistical analyses of automated segmentation results: (a) scatter plots plus the regression lines for automated and manual segmentation: $R^2_{\text{Multi-atlas}} \simeq 0.948$, $R^2_{\text{ASM}} \simeq 0.975$ for the proximal femur and $R^2_{\text{Multi-atlas}} \simeq 0.974$, $R^2_{\text{ASM}} \simeq 0.981$ for the innominate bone; (b) Bland-Altman plots showing the relative volume differences against the logarithm of the average of automated and manual volumes. (The colored regions indicate the confidence intervals of ± 1.96 SD limits for each automated segmentation method.)

larger average distance error approaching 1-1.25 mm with a maximum error found to be 1.286 mm for the multi-atlas-based method and 1.014 mm for the ASM-based method.

For the segmentation of the more complex-shaped acetabulum, larger Hausdorff distances were found compared with the spherical-like femoral head. For both the multi-atlas-based and ASM-based approaches, the average Hausdorff error at each vertex of the likely-BCI (Figure 3.11c, 'C'-shaped region inside dashed circle 3) was in general below 1.0 mm although in the inferior-lateral lunate region of the acetabulum the ASM approach had a slightly larger Hausdorff distance error (Figure 3.11c, dashed circle 4).

Both approaches provided good segmentation of the femoral neck region (Figure 3.11a), which was frequently used for measurement of alpha angles to assess cam-type FAI lesions, with the mean Hausdorff distance < 0.5 mm in the DESS and MEDIC images. Figure 3.12 demonstrates the robust performance of both methods for bone segmentation of the head-neck region of the femur in subjects with a normal geometry (i.e., no cam-type lesion) and with moderate or large cam-type abnormalities. Qualitatively, when a large cam lesion is present (Figure 3.12c, dashed circle), the FHN junction of the example ASM segmentations appears to be less accurate than the multi-atlas segmentations. This might be caused by the training dataset of asymptomatic subjects used for the shape model creation.

3.3.4 Computational time

Computational time was investigated to quantify the relative efficiency of these two segmentation pipelines for potential clinical use. Each of the segmentation methods was performed under specialized research laboratory conditions using 12 processors with 24 GB RAM on a local cluster system.

For the multi-atlas algorithm (central processing unit (CPU)-based implementation) running on the cluster, the average time required for segmentation of both the left and right hip joint was 382.08 $\pm$ 66.09 minutes (i.e., approximately 6 hours) including 4.84 $\pm$ 0.75 minutes for preprocessing, 373.01 $\pm$ 65.42 minutes for all pairwise registration ($N = 124$ for a bilateral image), 3.48 $\pm$ 0.86 minutes for atlas selection and 0.75 $\pm$ 0.17 minutes for label fusion.

An average time of 12.96 ($\pm$ 1.60) minutes was required to segment an MR study using the ASM-based scheme running on the cluster, which included 4.84 $\pm$ 0.75 minutes for preprocessing, 1.32 $\pm$ 0.31 minutes for initialization and 6.77 $\pm$ 0.95 minutes for ASM-based segmentation. For comparison, using a normal personal computer (quad-core 2.53 GHz, 12 GM RAM), the average computational time for the ASM-based scheme was still only 16.32 $\pm$ 2.19 minutes.

3.4 Discussion

The multi-atlas and ASM based approaches described in this chapter proved to be effective and robust, achieving good segmentation of the bone elements within the hip joint region from high-resolution 3D quasi isotropic MR images (DESS and MEDIC) acquired from a sample of volunteer subjects with various histories of physical activity levels. Although slightly higher accuracy (in terms of DSC and MASD), especially for segmentation of the innominate bone, was achieved using the multi-atlas-based method, the ASM-based method required substantially less computational time than the multi-atlas method (13 min versus 6 hours).

Compared to the recent work of Schmid et al. (2011), we demonstrated a fully automated ASM-based method to segment MR images of the hip region with large FOV (encompassing both joints simultaneously), which employed the widely utilized PCA that was easy for implementation and well-suited for this application. Our MASD of 0.904 $\pm$ 0.250 mm for the femur and 0.882 $\pm$ 0.145 mm for the innominate bone compared favourably with the robust SSM approach of Schmid et al. (2011). In contrast with the average-atlas-based method (Dowling et al. 2012), we presented a more sophisticated

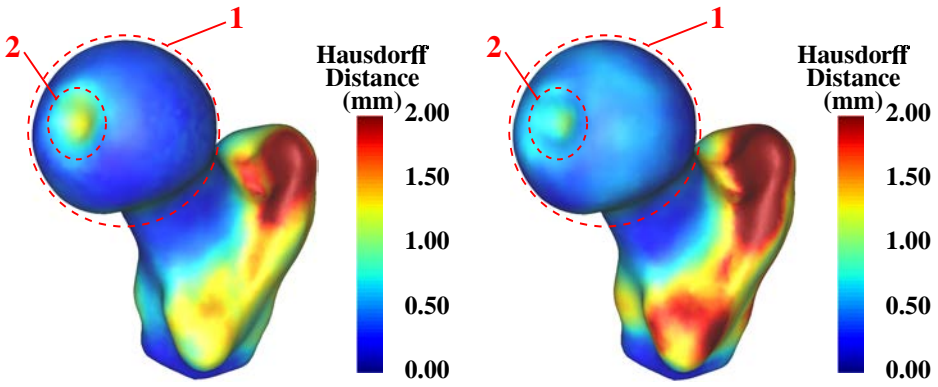

(a) Mean Hausdorff distance maps

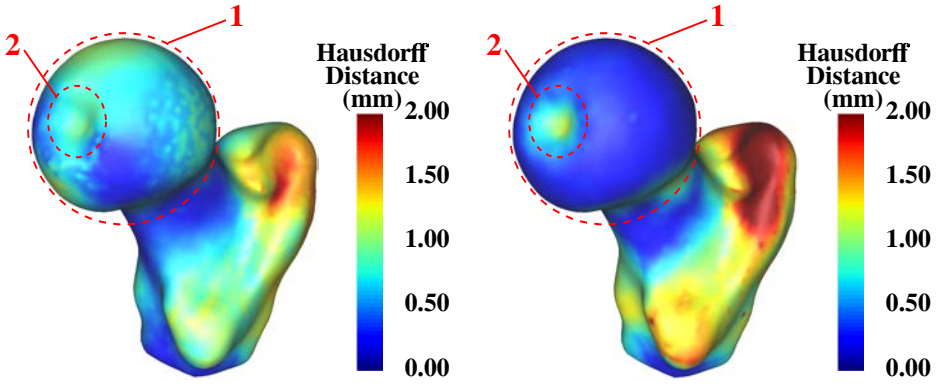

(b) SD Hausdorff distance maps

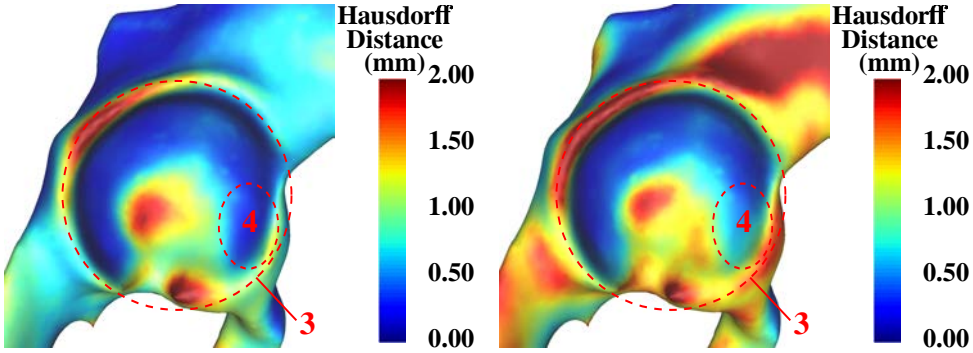

(c) Mean Hausdorff distance maps

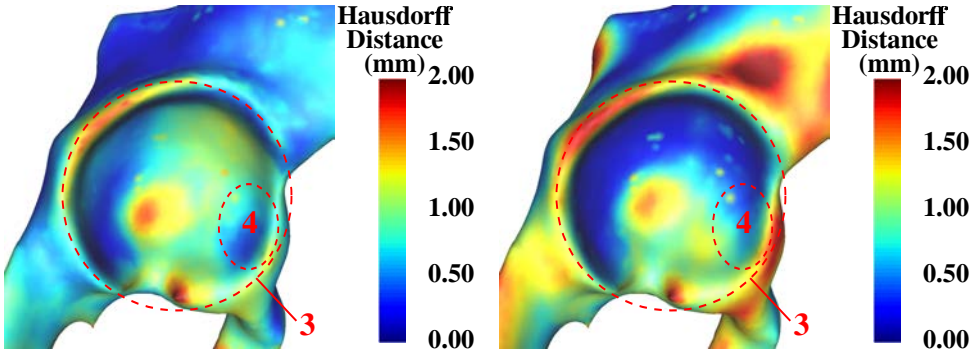

(d) SD Hausdorff distance maps

Figure 3.11: Comparison of mean and SD Hausdorff distance maps computed from the validation results of both sides using the multi-atlas-based method (left) and ASM-based approach (right) focusing on the femoral head (dashed circle 1) with fovea (dashed circle 2) and acetabulum (dashed circle 3) and inferiolateral lunate (dashed circle 4) regions.

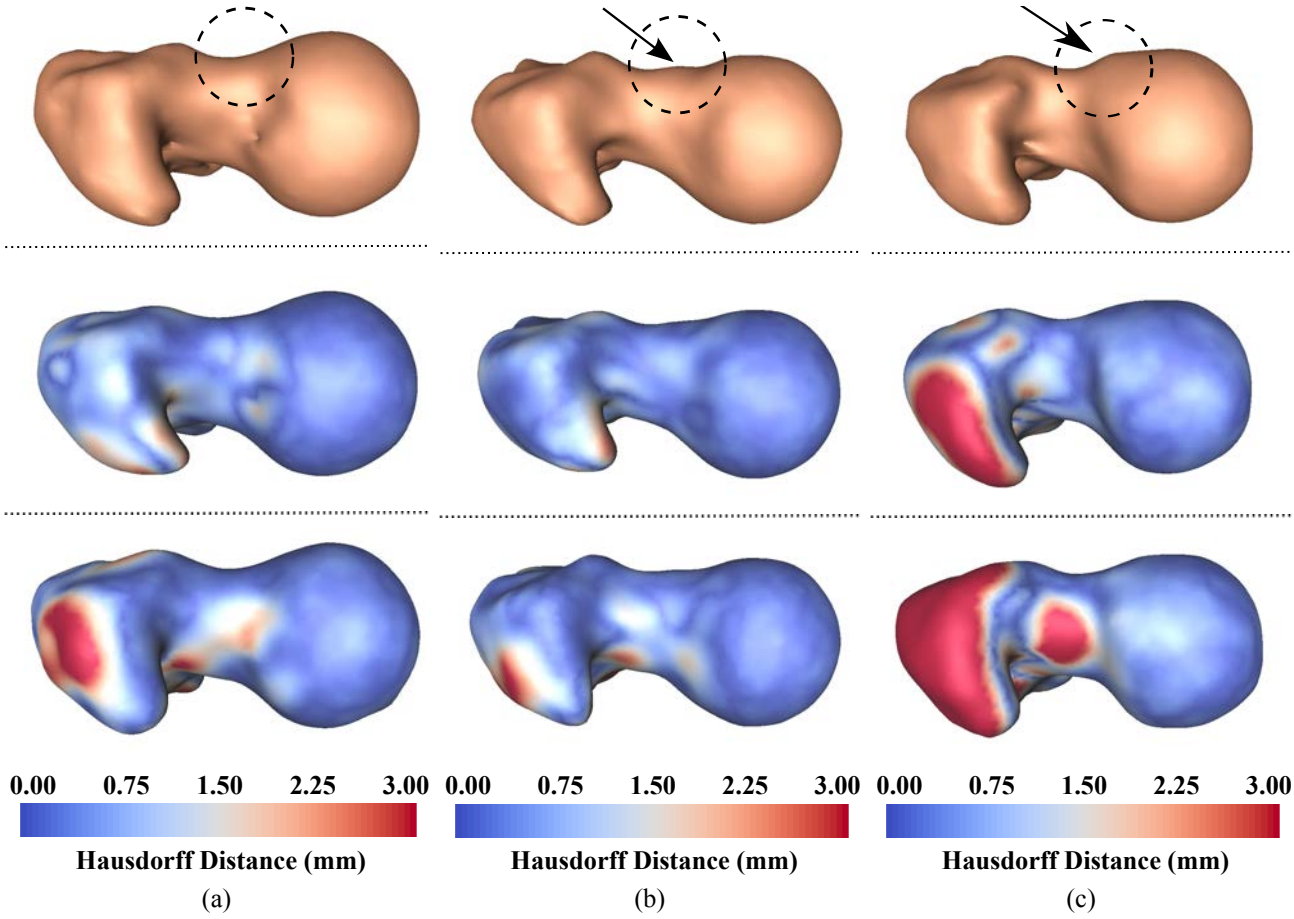

Figure 3.12: Example manual (top), automated multi-atlas (middle) and automated ASM (bottom)) segmentations of the head-neck region (dashed circle) of the femur including the directed Hausdorff distance maps with: (a) normal geometry of the head-neck junction (no cam-type abnormality), (b) moderate cam-type abnormality (arrows) and (c) large cam-type abnormality (arrows).

method using a multi-atlas scheme and obtained much better segmentation results for the femur and innominate bone with mean DSC values of 0.954, 0.934, respectively.

Both multi-atlas-based and ASM-based approaches were validated against manual segmentation of hip bone elements from high resolution MR images, which were acquired from volunteers with varying FHN junction geometries. Overall, the validation results (Table 3.1) indicate accurate and robust segmentation performance for both methods, including when cam lesions (alpha angle > 60°) were present (see examples in Figure 3.12). These approaches therefore offer the capacity for automated 3D morphometric analyses of bone changes in conditions such as FAI to facilitate future quantitative clinical applications.

The mean and SD Hausdorff distance maps (Figure 3.11) were computed to demonstrate the distribution of the surface errors and to further evaluate the accuracy of the bone segmentation, particularly neighbouring the likely BCIs of the femoral head and acetabulum. Using the multi-atlas-based and ASM-based approaches, both the likely femoral and acetabular BCIs were well delineated. These likely BCI surfaces could be readily used providing a reference frame for the assessment of the articular cartilage and allow the extension of the current segmentation pipeline to incorporate subsequent automated segmentation and quantitative analyses (thickness, volume) of the cartilage in the hip as

has been performed with the knee joint (Carballido-Gamio et al. 2008b; Fripp et al. 2010).

In our proposed multi-atlas-based method, segmentation performance relies heavily on the dataset of atlases and the chosen ϕ value. It has been well recognized that dissimilarity between the atlas set and the target image in terms of structure (e.g., anatomy) and appearance (e.g., image sequence, different FOV) could cause a registration failure (Rohlfing et al. 2004). The threshold ϕ used in atlas selection is important to exclude atlases with failed NRR results, which would introduce errors in the subsequent stage of label fusion. Figure 3.13a demonstrates the fluctuation of average DSC scores according to the ϕ value chosen from 0.0 (i.e., using all the atlases) to 0.99 (i.e., using the most similar atlas). In our study, ϕ between 0.7 and 0.8 were reasonable thresholds to obtain successful bone segmentations (DSC $\geq$ 0.8) as shown in Figure 3.13b. Even so, the multi-atlas-based method still delivered insufficient accuracy (i.e., low DSC scores) in cases with different FOV of MR examinations (Figure 3.14a) or different anatomical structures of the hip in female subjects (Figure 3.14b).

Compared with the validation results published in (Xia et al. 2013), there are two obvious improvements reported in this chapter. Firstly, slightly high DSC scores were achieved, particular for segmentation of the innominate bone using the multi-atlas-based approach (DSC = 0.922 $\pm$ 0.031 as reported in the published work). This is because of the increased number of training cases that brought more anatomical variability in the training dataset. As the SSMs used in the ASM-based approach were generated from an independent dataset of CT images, little influence to its accuracy was observed. Secondly, the computation time of the multi-atlas algorithm ($\sim$ 6 hours) was half of the time reported in (Xia et al. 2013) due to doubled parallel threads used for pairwise registrations. Nevertheless, the proposed ASM-based approach is significantly more computational efficient than the multi-atlas-based method.

One limitation of the current study is that the training set for model creation was restricted to male cases, which may affect the performance of the SSM to robustly describe the anatomical variability among female subjects, especially for the (irregular) innominate bone structure. Both methods achieved less accurate segmentation results of the innominate bone in female cases with mean DSCs of 0.890 and 0.899 respectively, while the mean DSCs for male cases were 0.941 and 0.924 for comparison. Future work will involve using a larger training dataset, possibly with specific male and female models, to better encode the shape variation and better handle different anatomical bone structures. Notwithstanding this, the results from the current training data appear highly promising for subsequent analyses or approaches for cartilage segmentation within the hip joint.

Two different MR sequences (DESS, MEDIC) were investigated in this work with the multi-atlas-based and ASM-based approaches achieving high segmentation accuracy with either sequence. Although indicative, further investigation on a larger cohort of data, especially pathological scans, is required to evaluate these methods for subsequent clinical use.

In this research, we have limited our validational study to high-resolution DESS and MEDIC images. Fuller evaluations on routine lower-resolution clinical sequences (e.g., 2D or 3D fast spin-echo), different scanner strength and subject cohorts are required to assess potential clinical applications for automated calculation MR bone-based metrics (e.g., alpha angle for FAI) and associated segmentation of the BCI in the hip joint for use in cartilage morphological studies for research and clinical

examinations of OA.

3.5 Conclusion

In this chapter, we presented two state-of-the-art methods developed for automated bone segmentation from bilateral MR images of the hip using two 3D nearly isotropic MR sequences (MEDIC and DESS) previously used for cartilage assessment. The multi-atlas-based and ASM-based segmentation pipelines obtained bone volume (proximal femur, innominate bone) segmentation results with mean DSC values of (0.954, 0.934) and (0.949, 0.920), respectively. Both methods delivered results with high accuracy for the femur with varying FHN junction presentations, and the likely femoral and acetabular BCIs were also well delineated (Figure 3.11); notably, the ASM-based approach is significantly more time-efficient which is an important consideration for potential clinical utility (e.g., timeliness, patient throughput).

These obtained accurate bone segmentations can provide a basis for morphological measures to be calculated (e.g., the alpha angle) of the femur (e.g., FHN junction), which will be investigated in Chapter 4. Meanwhile, the ASM-based segmentation method can be further extended based on the provision of reliable BCI surfaces for subsequent cartilage segmentation in Chapter 5.

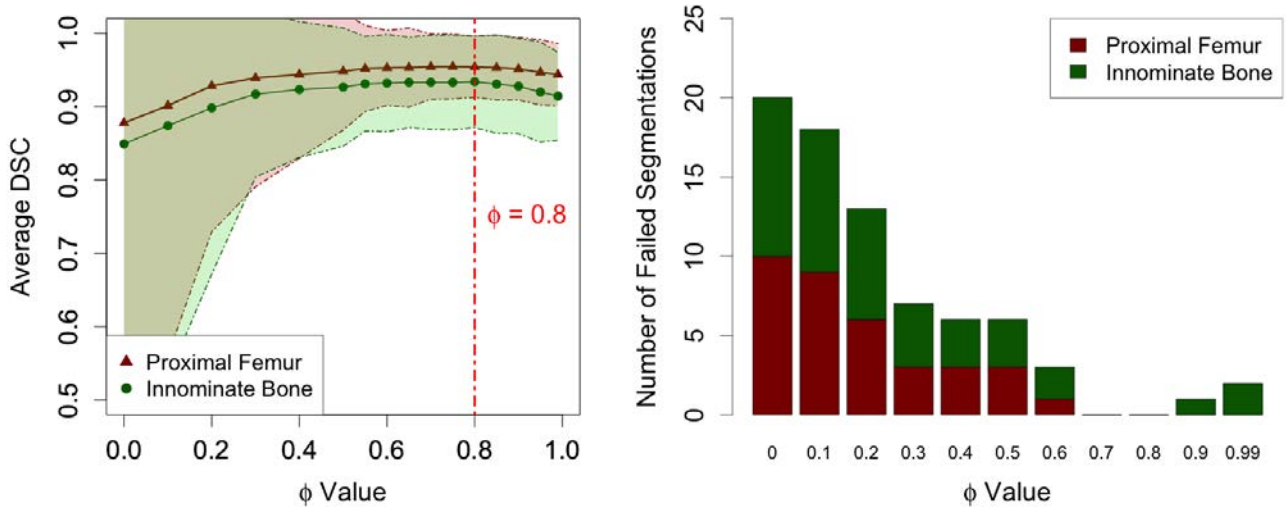

(a) (b)

Figure 3.13: Segmentation accuracy for various ϕ used in the multi-atlas-based segmentation pipeline from 0, i.e., using all the atlases, to 0.99, i.e., using the most similar atlas: (a) average DSC values with regions of 95% confidence interval for segmentations of the proximal femur and innominate bone against ϕ; (b) the histogram of failed segmentations (DSC < 0.8) for both the proximal femur and innominate bone with various ϕ values.

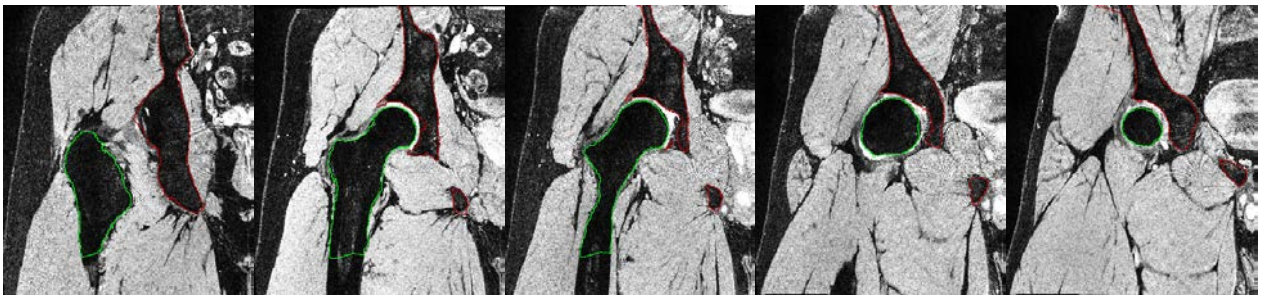

(a) DSC(femur, innominate bone) = (0.898, 0.923)

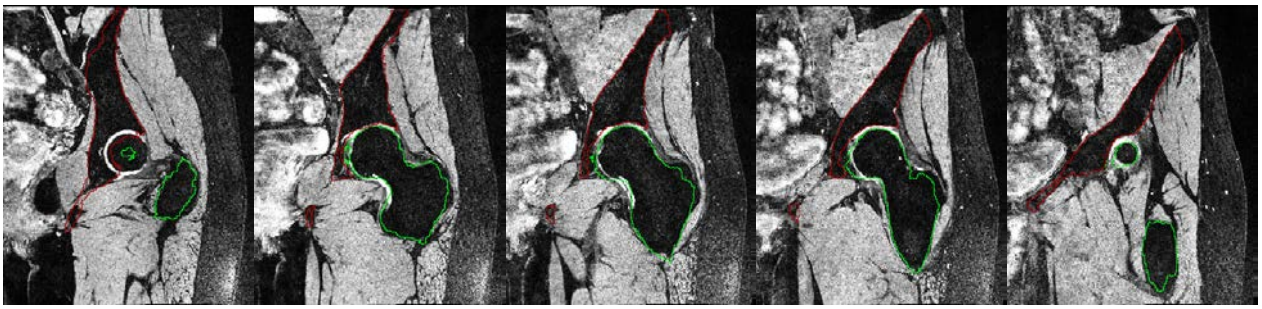

(b) DSC(femur, innominate bone) = (0.876, 0.835)

Figure 3.14: Example multi-atlas-based bone segmentations for MR images with: (a) different FOV and (b) varied anatomical structure (i.e., the female subject).

4

AUTOMATED MR-BASED 3D QUANTITATIVE ASSESSMENT OF THE FEMORAL HEAD-NECK JUNCTION

This chapter presents the work to attain **Aim 2.1**, which is, based on automatic segmentation of the bones for the hip joint, to automatically deliver reliable 3D morphological measurements of alpha angles around the FHN junction of the proximal femur.

Accurate detection and quantification of cam-type deformities at the FHN junction may provide great potential to reduce or delay the onset of hip OA. An automatic quantitative assessment method is developed to evaluate the circumferential morphology of the FHN junction and calculate 360° alpha angle measurements from 3D MR images. This method is performed based on 3D bone reconstructions of the proximal femur using an ASM based algorithm (Chapter 3). A dataset of 30 male subjects (including 18 water polo players) with varying FHN junction presentations is used in preliminary evaluation of the proposed assessment method, where its reproducibility is also evaluated using paired bilateral DESS and unilateral TrueFISP examinations from a subset of 18 water polo players therein.

This work has been included in a manuscript that has been submitted to *Physics in Medicine and Biology*, which specifically centres on **Aim 2.1** and is thereby incorporated as this chapter.

Related publication details

Xia, Y., Fripp, J., Chandra, S. S., Walker, D., Crozier, S., and Engstrom, C. (2015). Automated 3D quantitative assessment and measurement of alpha angles from the femoral head-neck junction using MR imaging. *Physics in Medicine and Biology*. (Submitted) (Xia et al. 2015)

Manuscript revision history	
Submitted to *Physics in Medicine and Biology*	2 April 2015

4.1 Introduction

Accurate detection and quantification of cam lesions is important for research studies and evaluation of treatments focusing on modifying the course of hip OA (Ganz et al. 2003; Tannast et al. 2008). A 2D alpha angle is frequently used to assess the severity of cam lesion (Nötzli et al. 2002). An alpha angle exceeding 50° is commonly used as an indicator of femoral head asphericity and irregularity of the FHN junction (Tannast et al. 2007). However, this 2D alpha angle clinically measured from standard radiograhs (X-rays) has limitations in depicting the severity of cam lesions given the variable 3D morphology and location (Barton et al. 2011; Clohisy et al. 2009; Dudda et al. 2009; Meyer et al. 2006). Meyer et al. (2006) reported that femoral head asphericity (i.e., alpha angle) was likely to be underestimated from routine anteroposterior radiographs. Radiographic diagnosis of cam-type FAI also had low intra- and inter-observer agreement (Cohen's kappa coefficients < 0.6) with radiographic structural features (e.g., head sphericity, head-neck offset/junction) (Clohisy et al. 2009).

Volumetric techniques such as CT and MR imaging, the latter providing images without the use of ionizing radiation, afford direct 3D assessments of bone morphology at the FHN junction for enhanced measurement of cam lesions (Audenaert et al. 2011; Beaulé et al. 2005b; Bedi et al. 2012). In a study on dray femur specimens with nondysplastic hips, Audenaert et al. (2011) reported that 3D CT reconstructions of the proximal femur for calculation of alpha angles using radial plane slices showed very strong correlations (r = 0.88) with manual measures obtained from images acquired across multiple planes. Manual CT reconstructions of the proximal femur have also been used for calculating the sum of head-neck ratios at five cross-sectional areas along the femoral neck for investigation of patients with symptomatic cam lesions (Masjedi et al. 2013b). In a recent CT-based study involving fitting of a sphere or conchoid model to the femoral head, Harris et al. (2013a) observed significantly greater maximum deviations in patients with cam lesions compared with asymptomatic control subjects. These shape variations in bone protrusion around the FHN junction were further confirmed using PCA modelling (Harris et al. 2013b). In a patented method, Chabanas et al. (2011) used an automatic approach based around 3D surface models to determine the contour of the FHN junction and identify the location of cam lesions from CT images.

In MR imaging, manual or semi-automated selection and analysis of slices through the FHN junction obtained in one or several reformatted 2D planes is commonly used for the assessment of cam lesions (Nötzli et al. 2002; Rakhra et al. 2009; Sutter et al. 2012). Sutter et al. (2012) used radially reformatted MR images of the proximal femur for assessing the presence of cam lesions at the anterosuperior FHN junction and found a 60° alpha angle diagnostic cut-off value (sensitivity and specificity > 70%) between asymptomatic FAI patients and asymptomatic volunteers. Zilkens et al. (2013) reported high reproducibility of alpha angle measures across 7 positions of the FHN circumference obtained from reformatted 3D water-excitation DESS images. Recently, Kang et al. (2013) described a method using 2D diagnostic graphs for assessment of cam lesions around the full circumference of the FHN junction employing a combination of manual bone segmentation and modelling algorithm applied to high-resolution T1w dual sense spin echo images acquired from a small dataset of FAI patients and asymptomatic volunteers.

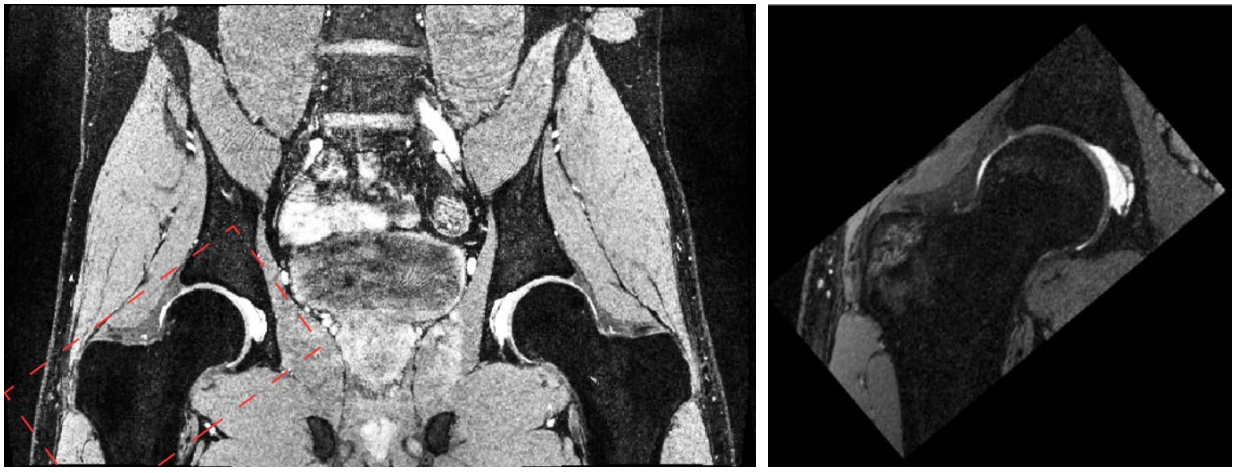

(a) (b)

Figure 4.1: Example coronal slices of MR images acquired from the same subject using (a) bilateral DESS and (b) unilateral TrueFISP sequences. (Red dash line in (a) the DESS image slice (a) indicates a small FOV used in (b) the paired TrueFISP examination.)

To our knowledge, there is no fully automated method for 3D MR-based quantitative assessment and measurement of the FHN junction for the diagnosis of cam lesions. In this chapter, we present a novel automated method based on our bone segmentation algorithm (Chapter 3) that allows 3D reconstruction of the proximal femur, which is then used to reliably determine the FHN morphometric and alpha angle data. The automated measurement of alpha angles is validated against manual measures obtained from bilateral DESS images of the hip joints. Further, analyses of automated 3D reconstructions of the proximal femur and alpha angle measurements are also compared for paired DESS and TrueFISP examinations to assess its performance for MR images of different contrast characteristics.

4.2 Materials and Methods

4.2.1 Image datasets and MR acquisition protocols

Bilateral MR images of the hip joints were acquired from 30 male volunteers (including healthy active individuals and high-performance athletes, aged 18-49 years, body mass index (BMI) 25.9 $\pm$ 2.6 kg/m^2, all subjects were screened for a history of developmental hip disorders for exclusion purposes) using a 3D water-excited DESS sequence. In a subset of these volunteers (18 water-polo players), additional unilateral 3D TrueFISP images were acquired from the right hip joint. The parameters used in each imaging sequence are described in Section 2.5.1 and listed in Table 2.1. Example coronal slices are presented in Figure 4.1 to illustrate the different FOV coverage of the hip region between these two acquisition protocols.

4.2.2 Manual bone segmentation and alpha angle measurements

The proximal femur was manually labelled from the acquired DESS and TrueFISP) images by the author using ITK-SNAP (Yushkevich et al. 2006). As reported in Section 3.3.1, the intra- and inter-

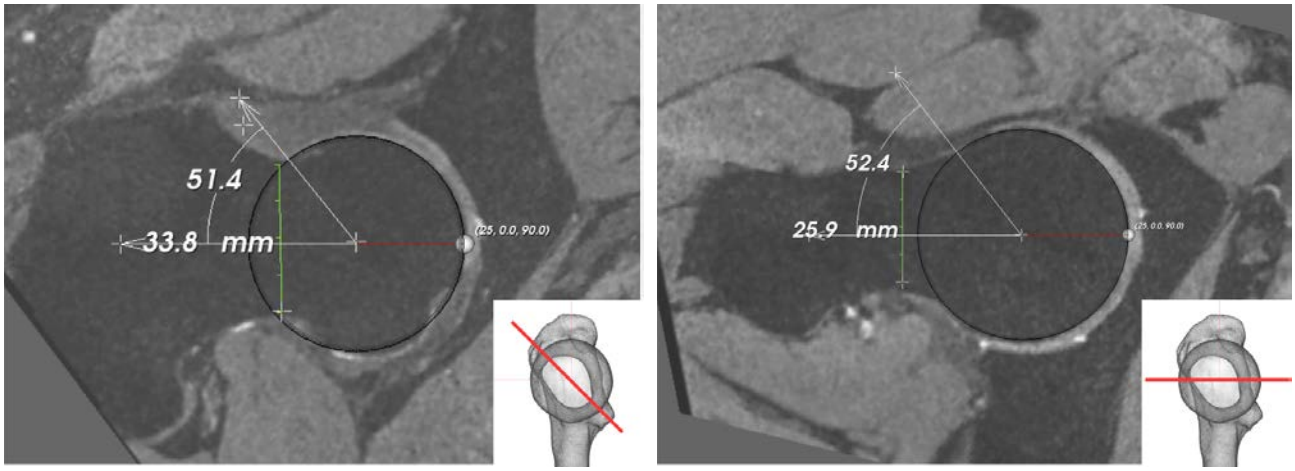

(a) (b)

Figure 4.2: Examples of manual alpha angle measurements for the (a) anterosuperior and (b) anterior positions of the FHN junction from auto-extracted 2D radial planes reformatted from bilateral DESS images.

rater reliability for manual bone segmentations of the proximal femur have mean DSC scores of 0.96 and 0.97, respectively.

Manual measurements (ground truth) of alpha angles were performed by two raters (Rater 1, Dr. Duncan Walker, an experienced radiologist and Rater 2, Dr. Craig Engstrom, an experienced anatomist) on all 30 DESS (bilateral) examinations. From the 3D images of each hip joint, image reformation was autoamtically performed using our proposed method (as described below) to generate images from a series of radial plane slices to provide standardized (Rater independent) visualization of bone morphology specifically around the upper anterior quadrant of the FHN junction. Following the method of Nötzli et al. (2002), alpha angles were manually measured from two reformatted, auto-extracted radial slices, i.e., anterosuperior - 45° and anterior - 90° images (Figure 4.2) using a plugin developed from our inhouse Simple Medical Imaging Library Interface (SMILI)[1] package (Chandra et al. 2015a). These auto-extracted radial slices were all considered highly consistent with traditionally acquired (i.e., manually processed) radial images by both Raters.

In the dataset of bilateral DESS images, the intra-rater (Rater 2) and inter-rater reliability for alpha angle measurements was determined for both the anterosuperior and anterior radial planes. All manual measurements were performed in a blinded fashion and in the present study, the larger alpha angle from the two repeated measures of Rater 2 for each hip and both radial planes was used here for comparison with the corresponding automatic measures.

4.2.3 Automated MR-based 3D bone reconstruction and alpha angle measurements

As shown in Figure 4.3, the full workflow diagram for automated extraction of the 3D bone morphology of the proximal femur and measurement of alpha angles for assessment of cam-type lesions

[1] http://smili-project.sourceforge.net/

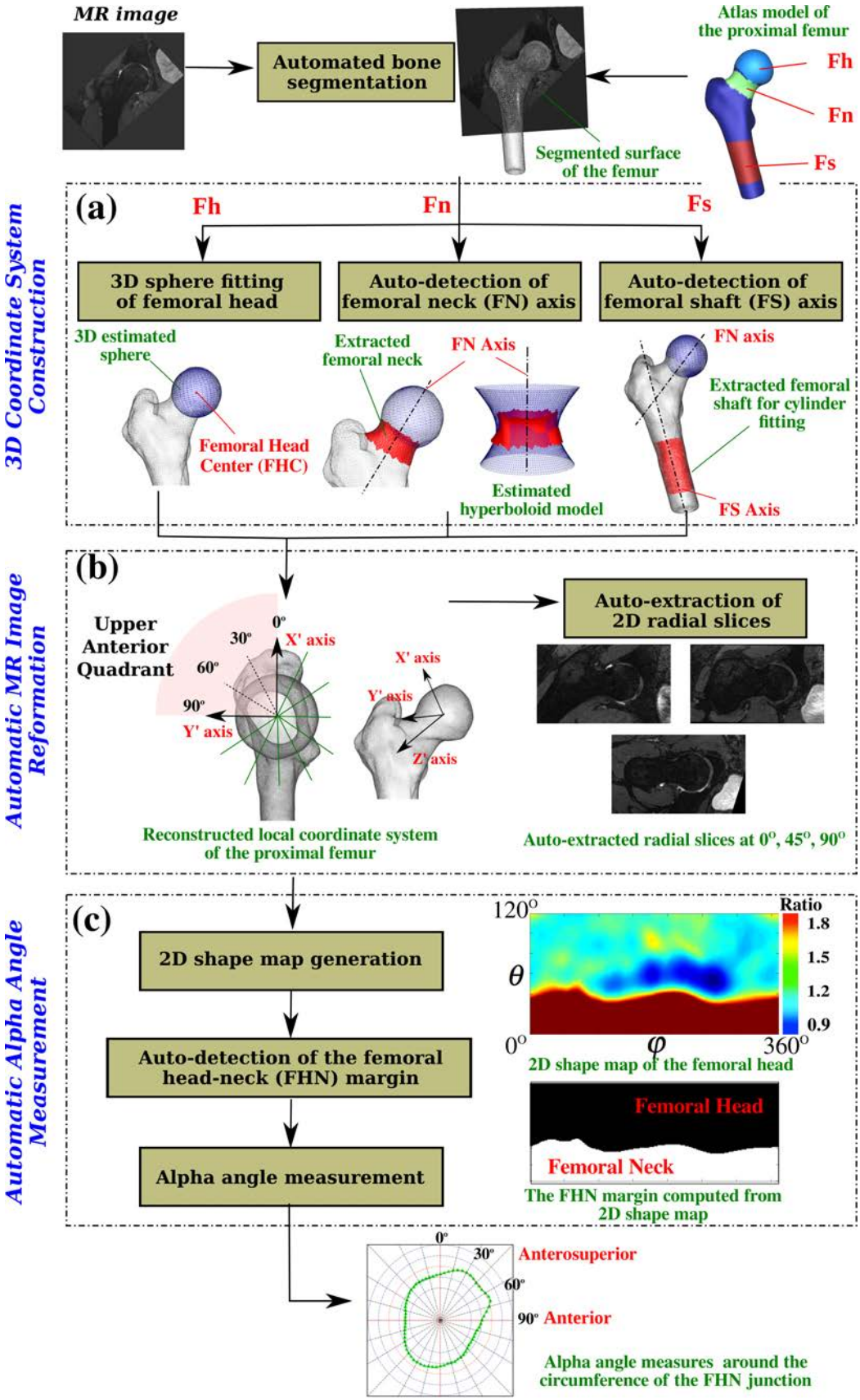

Figure 4.3: Workflow diagram of automated alpha angle measurement scheme for assessment of cam lesions from MR images of the hip joint.

involves the ASM based bone segmentation pipeline (Chapter 3), construction of a 3D local coordinate system (Figure 4.3a), automatic MR image reformation (Figure 4.3b) and alpha angle measurement

(Figure 4.3c).

Automatic bone segmentation

As a preprocessing step, the bone surface of the proximal femur was automatically segmented from MR images using a 3D ASM based method presented in Chapter 3. Briefly, the automatic bone segmentation approach was applied to MR images of the hip region and consisted of i) model initialization using a joint locator (Nishii et al. 2004), ii) coarse bone segmentation using a composite SSM of the bone elements of the hip joint, e.g., a bilateral hip SSM (only for MR images encompassing bilateral hip joints) and SSMs of an individual hip joint, iii) bone segmentation refinement using SSMs of an individual bone element (proximal femur, os coxa) and iv) bone surface relaxation without shape constraints. An additional improvement to the above segmentation method involved, before bone surface relaxation, further refinement of the of the segmentation of the proximal femur using a focused SSM of the femur (Chandra et al. 2014), which was built from the same training data but with predetermined weights representing a specified ROI, i.e., the FHN junction. This focused shape model provided lower reconstruction errors and higher accuracy achieved at the selected ROI of the femur.

Automatic 3D reference coordinate system construction

Based on the segmented 3D bone surfaces of the femur, a point landmark (femoral head center (FHC)) and two reference axes (femoral neck (FN) and femoral shaft (FS) axes) were automatically determined based on sample points within the ROIs of the femoral head, neck and proximal shaft of the femur, respectively (i.e., pre-defined in the atlas surface of the proximal femur shown in Figure 4.3), for construction of a new local reference coordinate system.

- The FHC was initialized using the Hough transform (Nishii et al. 2004) applied to MR images followed by an iterative least squares algorithm for 3D sphere fitting to the femoral head of the segmented bone model (the predefined ROI of "Fh" in Figure 4.3a).
- The FN axis was determined as the central axis of an optimal one-sheeted hyperboloidal surface model (Masjedi et al. 2013a; Sholukha et al. 2011), which was best fitted to the 3D point cloud of the femoral neck that was the pre-defined ROI "Fn" in Figure 4.3a in the atlas model of the proximal femur. A random sample consensus paradigm (Fischler and Bolles 1981) integrated with the least-square-based quadric surface fitting algorithm (Dai et al. 2007) was applied to estimate geometric parameters of this hyperboloid model and, simultaneously, to handle a large portion of outliers in the relatively large number of sample points at the femoral neck.
- The FS axis was estimated by fitting an optimal elliptic cylinder model to the partial surface of the femoral shaft (ROI of "Fs" in Figure 4.3a).

Based on the detected FHC, FN and FS axes, the segmented bone surface of the proximal femur was rigidly transformed to a local 3D reference coordinate system (x', y', z') with the FHC as its origin. As illustrated in Figure 4.3b, the Z' axis was defined by the FN axis with its positive direction pointing towards the greater trochanter of the femur. The Y' axis was along the normal direction of the 2D plane determined by the axes of FN and FS and pointing anteriorly and the X' axis was thereby orthogonal

to the resulting Y' and Z' axes and pointing superiorly. Each point (x', y', z') was expressed using spherical coordinates (r, θ, φ), where r, θ and φ denoted the radius, inclination angle and azimuth angle of this point, respectively.

With the constructed reference coordinate system, the MR images were automatically reformatted into a series of standardized radial 2D slices centred at the FHC and rotated around the FN axis. This emulated the manual reformation process commonly performed in previous studies (Sutter et al. 2012; Zilkens et al. 2013).

Automatic alpha angle measurement

Based on the local spherical coordinates (r, θ, φ), a 2D shape map, following the work of Kang et al. (2013), was generated to assess the asphericity of the femoral head, where radial distances d_R from the FHC to the points of intersection with the bone surface of the femoral head were calculated and represented as a function of θ and ϕ. The generated 2D shape map (Figure 4.3c) was a 120-by-360 matrix used to describe the 3D surface of the femoral head and neck, in which each element denoted a direction from the FHC as a coordinate pair (θ, ϕ), where $\theta = 1°, 2°, ..., 120°$ and $\phi = 1°, 2°, ..., 360°$, and the intensity of each pixel was calculated as $I(\theta, \phi) = d_R/R$, where R was the radius of the fitted sphere model.

With the computed 2D shape map of the femoral head, the FHN margin (Figure 4.3c) was automatically located by finding a horizontal cut of the shape map with smoothness constraints allowing a maximum change of 1° between neighbouring columns. Thereafter, alpha angles for all the radial positions $1° \sim 360°$ (i.e., the entire circumference) of the FHN junction, were calculated for identification of cam lesions with reference to alpha angle measures as well as provision of data on the location (i.e., the epicentre) and size (e.g., extent of exostosis) of abnormal bone protrusion around the FHN junction.

Automated workflow time

For the bilateral DESS images, the entire automatic processing and measurement steps took around 13 - 14 minutes for an MR examination from one individual case using a normal PC (quad-core 2.53 GHz, 12 GB RAM). The majority of this time (i.e., ~12 minutes) was spent on bone segmentation (detailed in Section 3.3.4), from which the 3D femoral coordinate system and alpha angles around the entire circumference of the FHN junction were obtained. A similar computation time (< 15 minutes) was required for automated analyses of the higher resolution unilateral TrueFISP images.

4.2.4 Validation method and statistical analyses

The validation of the bone segmentation was assessed using DSC (Dice 1945) and MASD values (Gerig et al. 2001) as defined in Section 3.2.4. The directed Hausdorff distances (Aspert et al. 2002; Commandeur et al. 2011) were presented in the current study to visualize the distribution of segmentaiton errors locally at specific ROIs (i.e., the femoral head and neck). Further, biases of the 3D coordinate systems constructed from MR images using the different DESS and TrueFISP acquisition sequences

were compared using root mean square (RMS) errors (mm) for the FHC and angular differences (degrees) for the FN and FS axes.

All statistical analyses were performed using the R statistical package and $p < 0.01$ was set as an a *priori* significance level in the current study. The ICC, with 95% CIs, was used to evaluate the intra- and inter-rater reliability of manual alpha angle measures. The agreement between manual and automatic alpha angle measurements was assessed using linear regression and Pearson's correlation coefficients, with categorization of significant values of $r = 0.60$ - 0.79 as strong and 0.80 - 1 as very strong correlations (Harris et al. 2014). Bland-Altman plots (Bland and Altman 1986) were used to visualize the agreement in alpha angle measures between the manual and automatic approaches. In terms of comparing the automated measures between the paired DESS and TrueFISP datasets, a two-way repeated measures analysis of variance (ANOVA) was performed using alpha angle data obtained at four pre-selected positions within the upper anterior quadrant of the FHN junction.

4.3 Results

For all 3D bilateral DESS and unilateral TrueFISP examinations, the automatic scheme provided successful segmentations of the proximal femur for 360° measurement of alpha angles around the FHN junction. No user-interaction was required for any of the automatic segmentation and quantification steps or for any *post-hoc* manual editing of the resulting bone surfaces and alpha angle measures.

4.3.1 Intra- and inter-rater reliability of manual alpha angle measures from auto-extracted slices

The intra-rater reliability (Rater 2) for manual measurement of alpha angles from the auto-extracted reformatted radial slices from the DESS images was very high for both the anterosuperior (ICC(1,1) = 0.98; 95% CI: 0.96 - 0.99, $p < 0.01$) and anterior positions (ICC(1,1) = 0.97; 95% CI: 0.95 - 0.98, $p < 0.01$). Likewise, the inter-rater reliability for manual measurement of alpha angles from these auto-extracted radial DESS slices was very high for both the anterosuperior (ICC(2,1) = 0.95; 95% CI: 0.91 - 0.97, $p < 0.01$) and anterior positions (ICC(2,1) = 0.96; 95% CI: 0.94 - 0.98, $p < 0.01$). As shown in Figure 4.4, linear regressions ($r > 0.95$) for the manual alpha angle data obtained by the Raters revealed very small biases of -0.94° ± 3.50° and 0.12° ± 3.50° for the measures from the anterosuperior and anterior radial plane slices with very strong correlations of $r = 0.96$ and 0.95 ($p < 0.01$), respectively.

4.3.2 Comparisons between manual (ground truth) and automatic measures

Bone reconstruction: The validation of automatic bone reconstructions for the proximal femur, in comparison with the corresponding manual segmentations, for the DESS images, achieved DSC and MASD values of 0.95 ± 0.01 and 0.80 ± 0.21 mm, respectively. For the TrueFISP images, the corresponding DSC and MASD values between the manual and automatic segmentations were 0.95 ± 0.01 and 0.99 ± 0.19 mm, respectively. The mean and SD of the directed Hausdorff distances are shown in

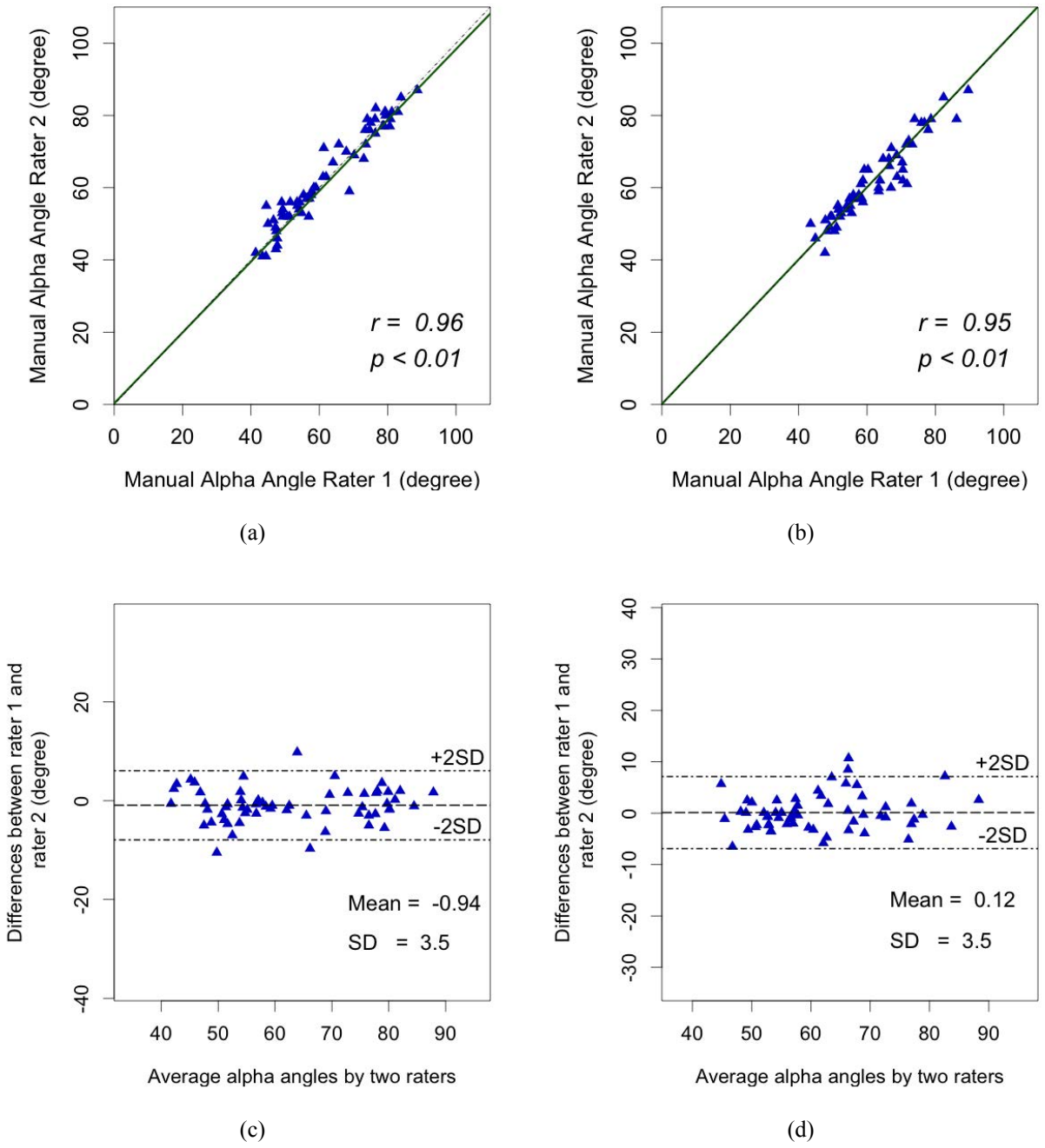

Figure 4.4: Statistical analyses of manual alpha angle measures at the (a, c) anterosuperior and (b, d) anterior positions between Rater 1 and Rater 2 based on automatic image reformation process in the dataset of 30 bilateral DESS images for hip joints of both sides: (a-b) are the scatter plots with the regression lines (r is the Pearson's correlation coefficient), (c-d) are the Bland-Altman plots.

Figure 4.5 to illustrate the accuracy of the segmented femur surfaces, particularly at the femoral head and neck, and view the distribution of segmentation errors across various anatomical regions. The average Hausdorff distance for the femoral head and neck was under 0.8 mm with a very small variance, which indicates accurate bone delineation within the region achieved by the automatic segmentation scheme.

Alpha angle measurements: There were very strong positive, statistically significant correlations between the manual and automatic alpha angle measures obtained from the DESS images for both the

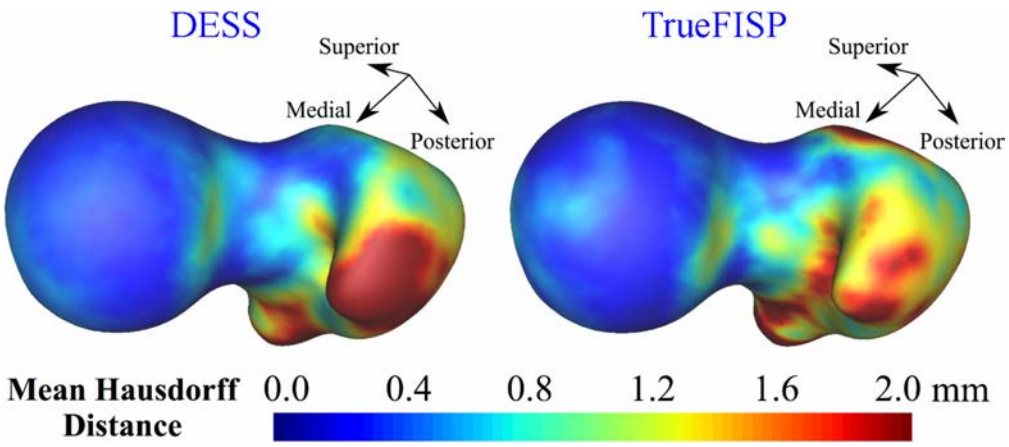

(a)

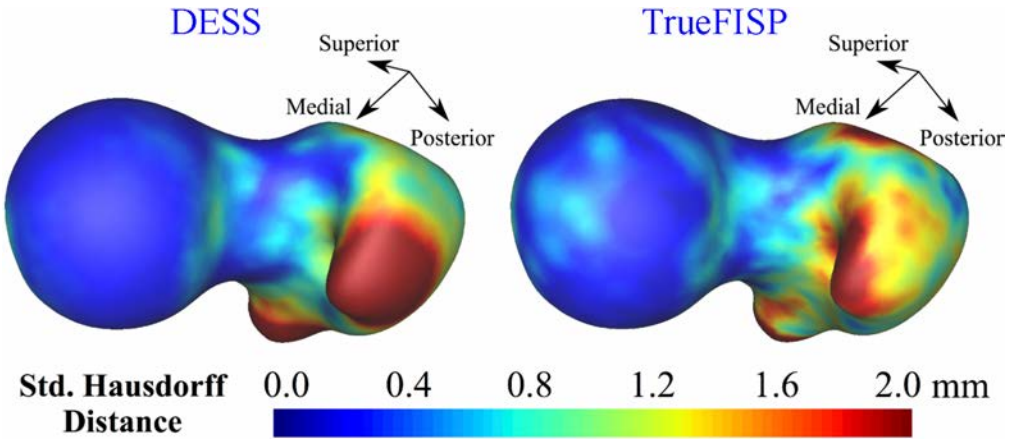

(b)

Figure 4.5: (a) Mean and (b) standard deviation maps of directed Hausdorff distances computed from validation results of the bilateral DESS (N = 30) and unilateral TrueFISP (N = 18) examinations.

anterosuperior ($r = 0.84, p < 0.01$) and anterior ($r = 0.92, p < 0.01$) positions (Figure 4.6a and 4.6b). The Bland-Altman plots (Figure 4.6c and 4.6d) indicated average angular differences of -2.49° (SD: 7.34°) and -4.01° (SD: 3.98°) between the manual and automatic alpha angle measurements at the anterosuperior and anterior positions of the FHN junction, respectively.

4.3.3 Comparisons between automatic measures of alpha angles from DESS and TrueFISP images

Comparisons of the constructed coordinate systems using automated bone segmentations from the matched 3D DESS and TrueFISP scans (18 individuals, right hips) showed a mean RMS error of 0.83 mm (SD: 0.72 mm) for the FHC location and mean angular differences of 2.11° (SD: 0.94°) and 0.43° (SD: 0.49°) for the FN and FS axes, respectively. Figure 4.7 shows representative examples of the reformatted 2D radial plane slices at five different positions within the upper anterior quadrant of the FHN junction extracted from DESS and TrueFISP scans in cases having larger alpha angle (e.g., > 60°) consistent with cam-type lesions and smaller alpha angles (e.g., < 50°) without cam-type lesions. Figure 4.7 also illustrates that despite differences in the contrast (characteristics) between the DESS and TrueFISP images, the automatic image reformation process is consistent based on the proposed

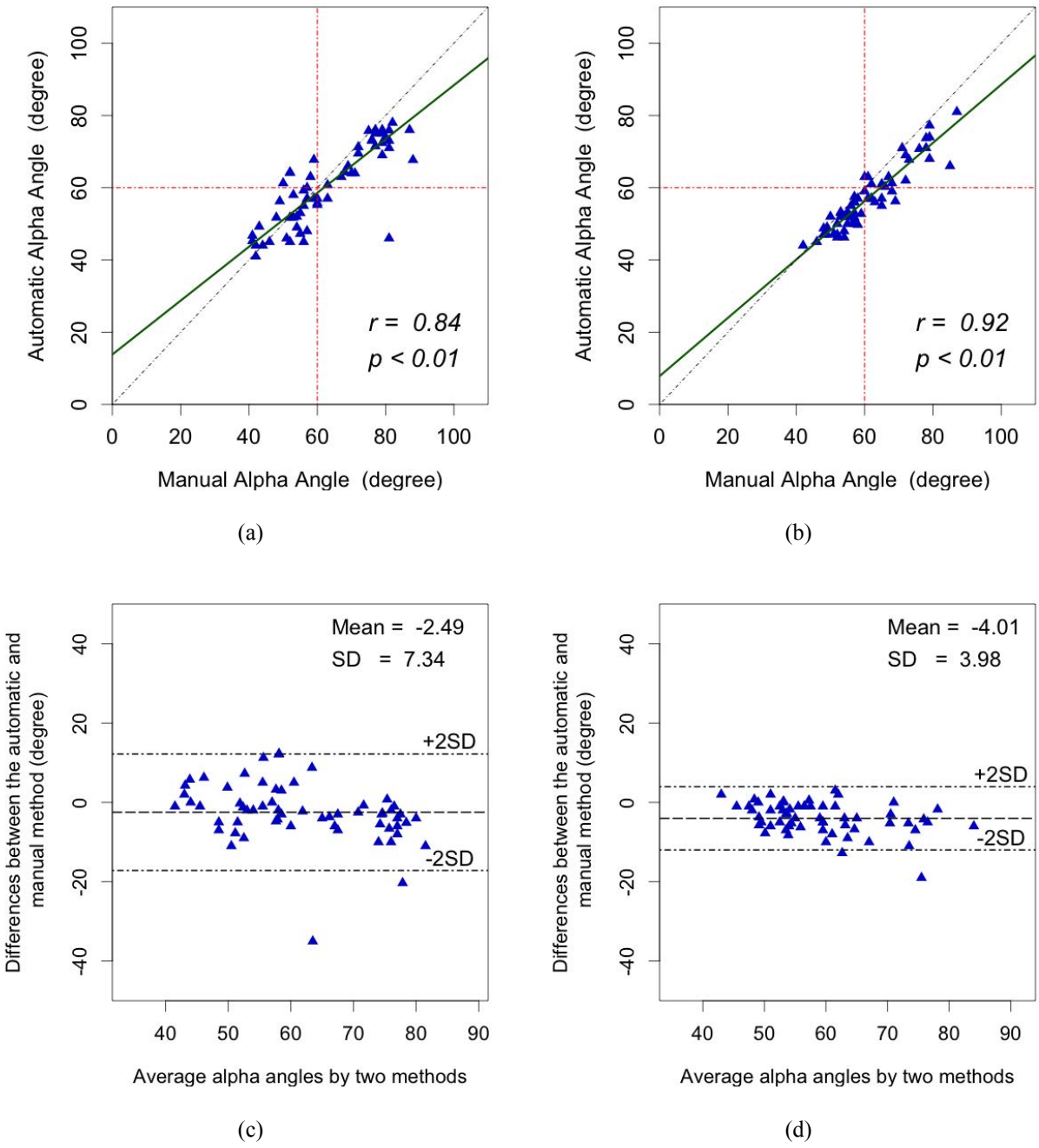

Figure 4.6: Statistical analyses of alpha angles at the positions of (a,c) 45° and (b,d) 90° of the FHN junction measured between the manual method based on automatic image reformation process and the proposed automated assessment scheme from 30 bilateral DESS images: (a-b) are the scatter plots with the regression lines (r is the Pearson's correlation coefficient), (c-d) are the Bland-Altman plots.

3D local reference coordinate systems constructed from these two MR sequences.

Figure 4.8a shows the mean ($\pm$ 95% CI) alpha angle curves computed from the automatic measures between the DESS and TrueFISP images. There was good agreement of alpha angles varying across all the locations 1° 180° of the FHN junction obtained using our method, where the largest alpha angle was likely to be located within the upper anterior quadrant between 45° and 75° positions of the FHN junction. In Figure 4.8b, for four different pre-selected positions particularly at 30°, 45°, 60° and 90°, there were strong correlations with Pearson's correlation coefficients r = 0.86, 0.78,

0.83 and 0.94 ($p < 0.01$) achieved between alpha angle measures from these two MR sequences and boxes of these alpha angles are also largely overlapped. The two-way repeated measures ANOVA test also showed no significant effects of the MR sequences (i.e., DESS and TrueFISP) on the automatic alpha angle measures ($F < 0.01$, $p = 0.98$), but presumably there was a main effect for measurement position ($F = 14.36$, $p < 0.01$). There was no significant interaction between MR sequences and measurement positions of the FHN junction ($F = 1.5$, $p = 0.21$).

4.4 Discussion

We have successfully developed a quantitative assessment method for MR images of the hip joint which automatically evaluates 3D bone morphology and provides 360° calculation of alpha angles around the FHN junction. At the anterosuperior and anterior FHN positions, as investigated in previous clinical studies (Dudda et al. 2009; Pfirrmann et al. 2006; Rakhra et al. 2009), there were very strong correlations ($r > 0.8$, $p < 0.01$) between the manual (ground truth) and automatic alpha angle measures as derived from the ASM-based 3D segmentations of the proximal femur. Similarly, there were strong correlations ($r > 0.78$, $p < 0.01$) between the automatic alpha angle measures derived from paired DESS and TrueFISP images acquired across multiple sites in the upper anterior quadrant of the FHN junction.

Universally, the automated method required under 15 minutes to calculate alpha angles around the FHN circumference and allowed detailed analysis of alpha angle sized and distribution characteristics for assessing the full extent and shape of cam lesions (e.g., see the 2D shape map in Figure 4.3c; polar plots in Figure 4.9). In previous studies on cam-type FAI, manual alpha angle measures from one or two locations of the FHN junction were always substantially overlapped between asymptomatic and symptomatic hips (Jung et al. 2011; Sutter et al. 2012). In a recent study of Lepage-Saucier et al. (2014), the ranges of anterosuperior and anterior alpha angles in asymptomatic hips were found far beyond the current morphometric definitions (i.e., 50°/55°/60° cut-off thresholds for cam-type FAI). Our assessment method, which automatically provides 3D visualization of the bone morphology and 360° measurement of alpha angles around the FHN junction (Figure 4.9), could assist the redefinition of this morphometric parameter (alpha angle) that can be used in the diagnosis of cam-type FAI.

For the bilateral DESS images, the manual measurements of alpha angles from the auto-extracted radial slices at the anterosuperior and anterior positions of the FHN junction showed very high intra- and inter-rater reliability (ICCs > 0.95). The excellent reliability of these ground truth measures was, in large part, attributed to the standardized, auto-extraction of the radial slices (see Figure 4.2), which avoided the intra/inter-rater inconsistencies (subjective biases) associated with traditional manual image reformation processes. Although direct visualization of the auto-extracted 2D radial slices (Figure 4.3b) is not necessary for the automated measurement of alpha angles from the current assessment scheme, all images are readily obtained to allow further evaluation or review by expert observers.

For the large range of alpha angles (41° to 88°) from the anterosuperior and anterior positions obtained in the current study, the fully automated and manual measures compared very favourably. The exceptionally robust performance of the automatic measurement approach using a 2D shape map of

the femoral head for determining alpha angles across individuals with "normal" values (e.g., < 50°-55° (Nouh et al. 2008; Nötzli et al. 2002)), "high" values (60-70°) and "very high" values (> 70°) attested the effectiveness of this method to analyse a wide variety of bone morphologies occurring at the anterosuperior and anterior positions of the FHN junction. Similarly, the very strong correlations between the manual and automated alpha angle measures for the anterosuperior ($r = 0.84$) and anterior ($r = 0.92$) positions were obtained across these two different locations where typically the anterosuperior slice profile demonstrated a greater concavity of the FHN junction (Figure 4.7).

In the current study, a focal ossification within a lateral segment of the anterosuperior femoral cartilage in an isolated case (Figure 4.10a) produced a very large discrepancy between the manual and automatic alpha angle measures at the anterosuperior position (Figure 4.6a, see the extreme outlier). This "abnormality" was not consistent with a classic protuberance (exostosis) of bone typically associated with a cam-type lesion but rather was "confined" within the regular cartilage profile. At review, the automated analyses of the alpha angle (∼40°) was considered to be "definitionally correct" although both raters used the medical edge of this abnormal bone "lesion" to determine their manual measures (∼80°). Further investigation of such intra-chondral bone lesions would be of interest in terms of the development of an algorithmic approach for automated analyses of various pathoanatomical characteristics and for more detailed consideration of possible *in vivo* impingement or associated damage to joint structures.

Application of the automated 3D bone reconstruction process to unilateral TrueFISP images, in comparison with matched DESS images, showed good reproducibility with relatively small biases reported for the location of the FHC and directions of the FN and FS axes in the constructed local coordinate system for the proximal femur. In terms of automated measurement of alpha angles between paired DESS and TrueFISP images, there were strong correlations for these angles analysed for a series of positions across the upper anterior quadrant of the FHN junction ranging from $r = 0.78$ for the anterosuperior (45°) to $r = 0.94$ for the anterior (90°) positions (see Figure 4.8b).

To facilitate clinical application of the current work, future investigations involving fuller evaluation of the automated measurement method with larger subject cohorts with varied demographics (e.g., asymptomatic and symptomatic, males and females, different age groups) and clinical MR sequences (e.g., 2D or 3D fast spin-echo) would be beneficial. Similarly, further work to include and validate the automatic measurement of a suite of parameters such as the FHN offset (Tannast et al. 2007), triangular index (Gosvig et al. 2007) and 3D head-neck ratios (Masjedi et al. 2013b) along with the alpha angle measures as validated in the current assessment scheme would enhance efforts targeting morphometric quantification of cam lesions. Moreover, our automated assessment method can be extended in future work to provide simultaneous 3D measurements from the acetabulum for parallel analysis of pincer-type lesions in FAI (Dandachli et al. 2012; Tannast et al. 2007).

Our automatic approach is ideally suited for MR analyses of FHN alpha angles in both individual patients and in population-based investigations of asymptomatic (apparently healthy) and FAI cohorts. On a patient-specific basis, the automated 3D method offers 360° alpha angles for detecting and characterizing the variable presentations and locations of cam lesions around the FHN junction (e.g., epicentre and extent of these osseous protrusions) for clinical evaluation and treatment purposes.

In larger scale studies, the fully automated approach offers the capacity to provide comprehensive 3D morphometric assessment and alpha angles for the FHN junction to better understand the development of cam lesions in relation to various age, activity and anatomical characteristics.

4.5 Conclusion

This chapter presented a novel quantitative assessment and measurement method to automatically evaluate 3D bone morphology and determine the alpha angles circumferentially around the FHN junction from MR images of the hip joint. Our developed automatic 3D method generated alpha angle measures circumferentially for the FHN junction with very good reliability and reproducibility for two different MR images (i.e., DESS and TrueFISP sequences). This work therefore has the potential to facilitate dedicated analyses of cam-type lesions of the FHN junction and, more generally, large-scale morphometric and clinic MR investigations into the human hip region.

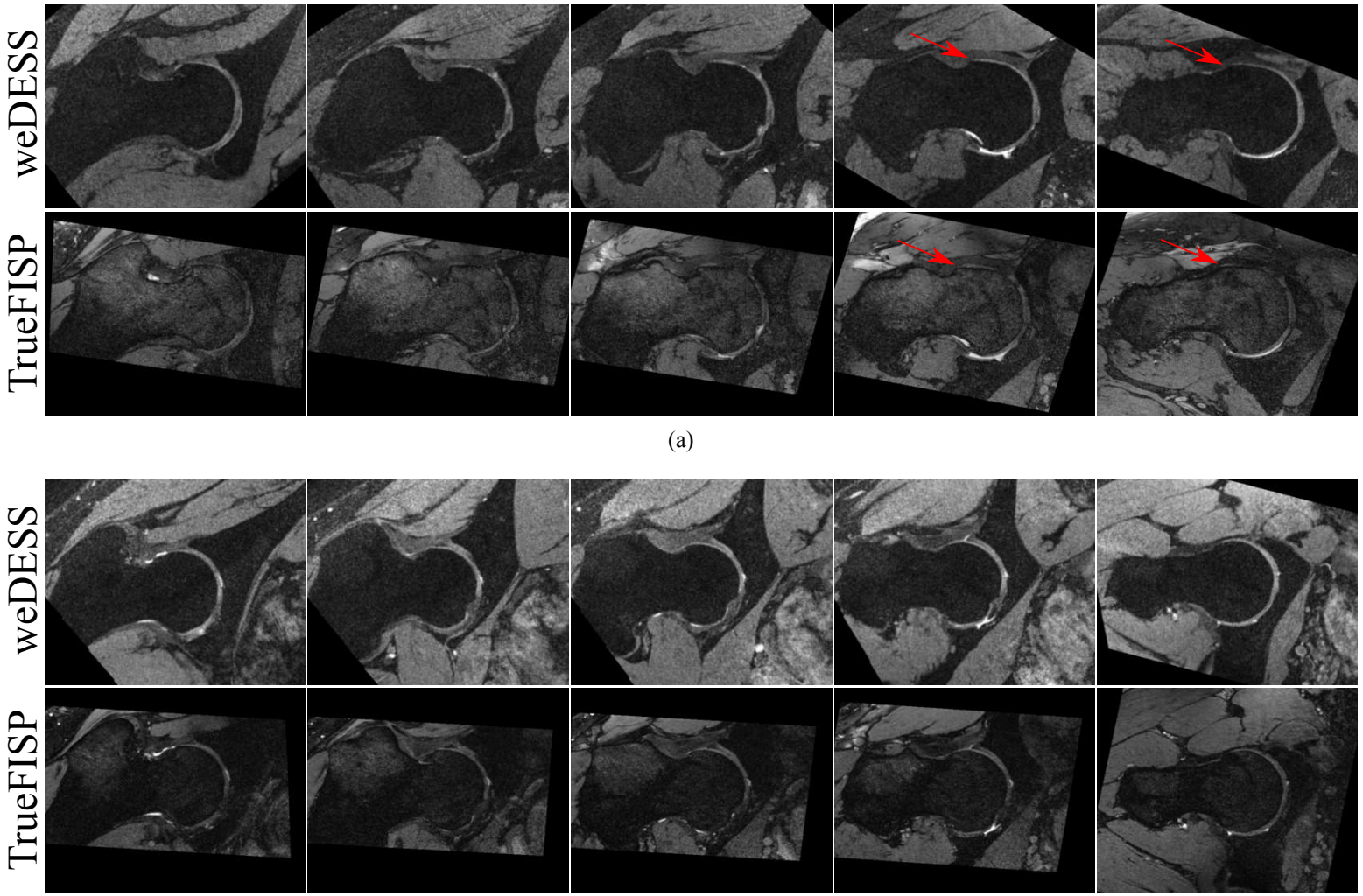

Figure 4.7: Representative auto-extracted 2D radial slices at five different positions in the upper anterior quadrant of the FHN junction (from left to right, 0°, 30°, 45°, 60°, 90°) from (top) DESS and (bottom) TrueFISP examinations of the right hip joints with (a) big and (b) small alpha angles (Red arrows indicating the perceptible cam-type lesion).

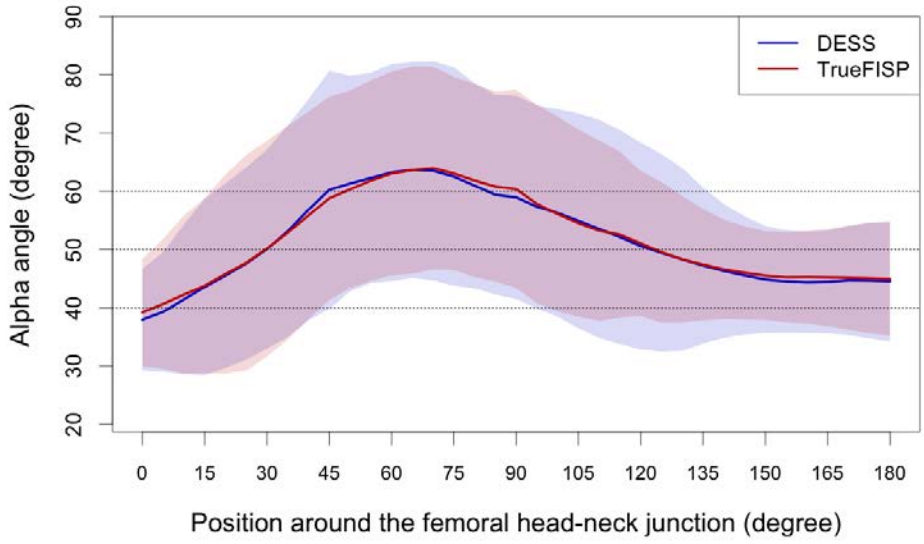

(a)

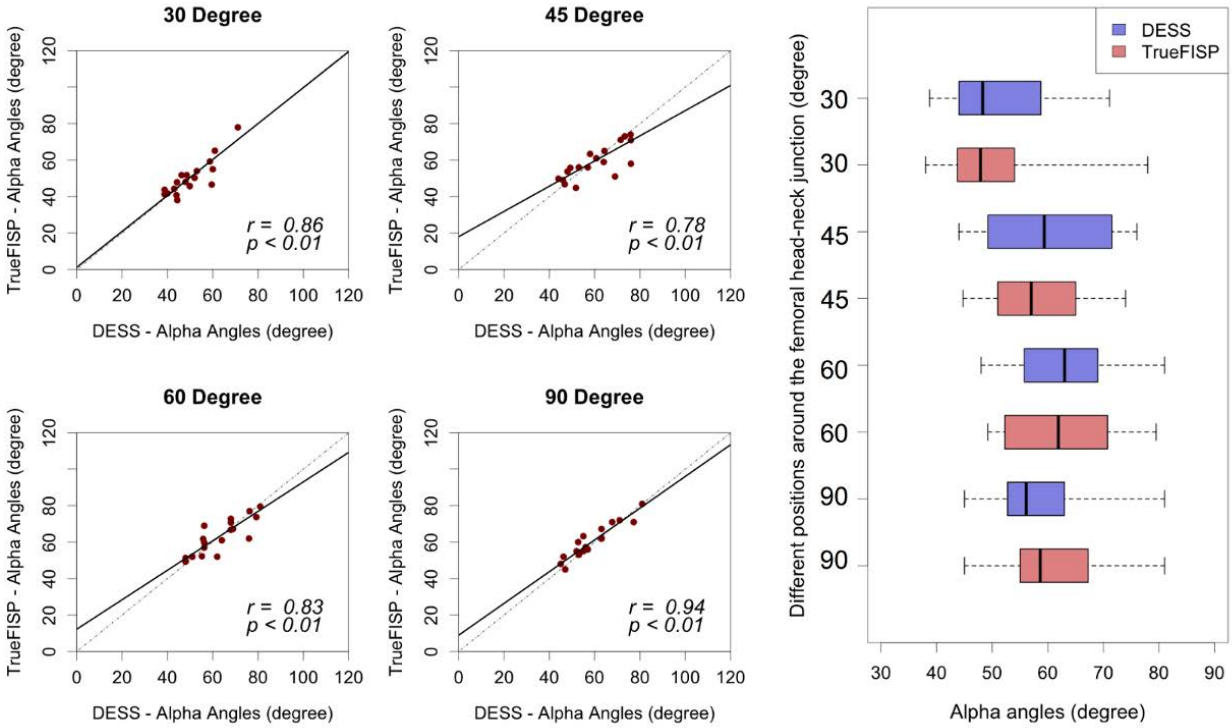

(b)

Figure 4.8: (a) Average alpha angle curves with regions of 95% CI across all positions 0° - 180° of the FHN junction and (b) linear correlation plots and boxplots of alpha angles at four pre-selected positions (30°, 45°, 60°, 90°) in the upper anterior quadrant of the FHN junction in the reproducibility test between paired DESS and TrueFISP scans from 18 subjects.

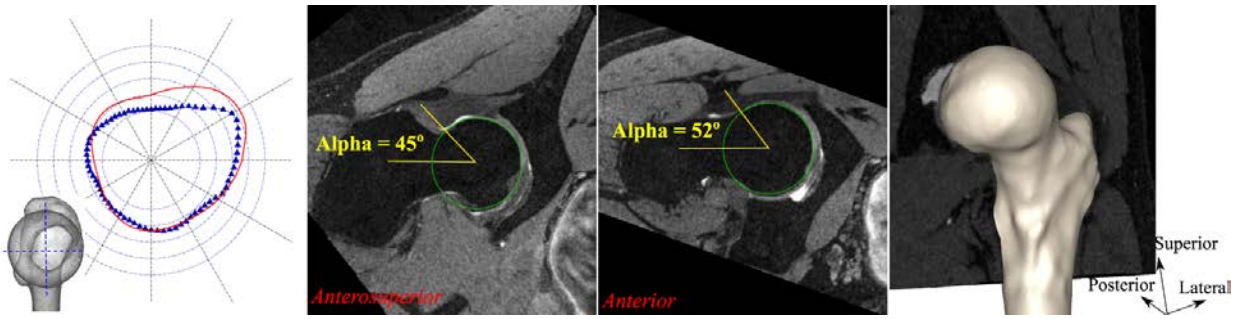

(a)

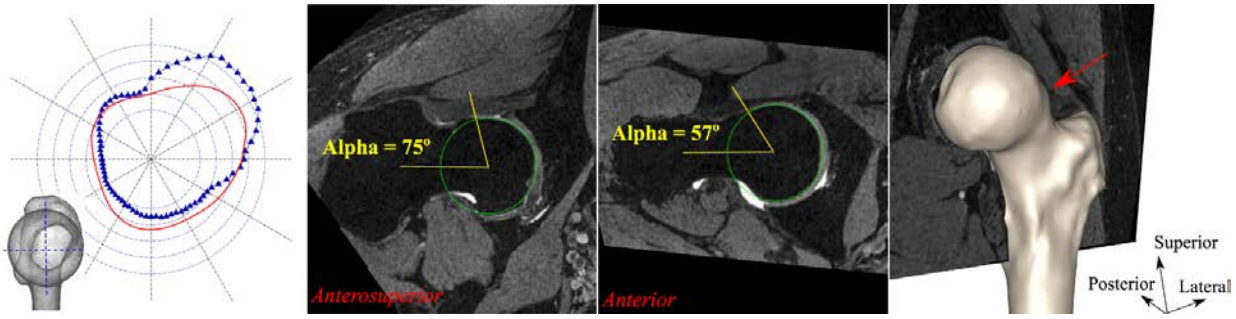

(b)

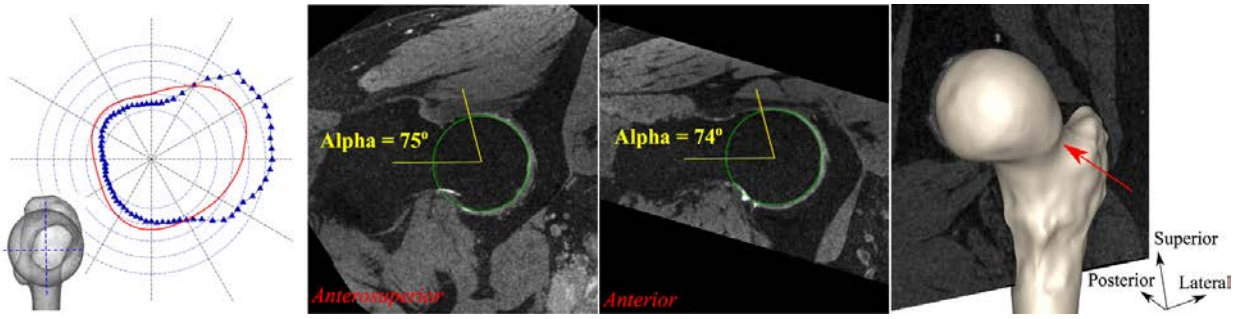

(c)

Figure 4.9: Example assessment results for hip joints having (a) smaller anterosuperior and anterior alpha angles, (b) a larger anterosuperior alpha angle, (c) larger anterosuperior and anterior alpha angles: (from left to right) diagrams of alpha angles (blue dots) around the FHN junction (The red line indicates the average alpha angle contour computed from the bilateral DESS images (i.e., 60 hips).), anterosuperior radila slices, anterior radial slices and 3D visualization of the segmented femur surfaces.

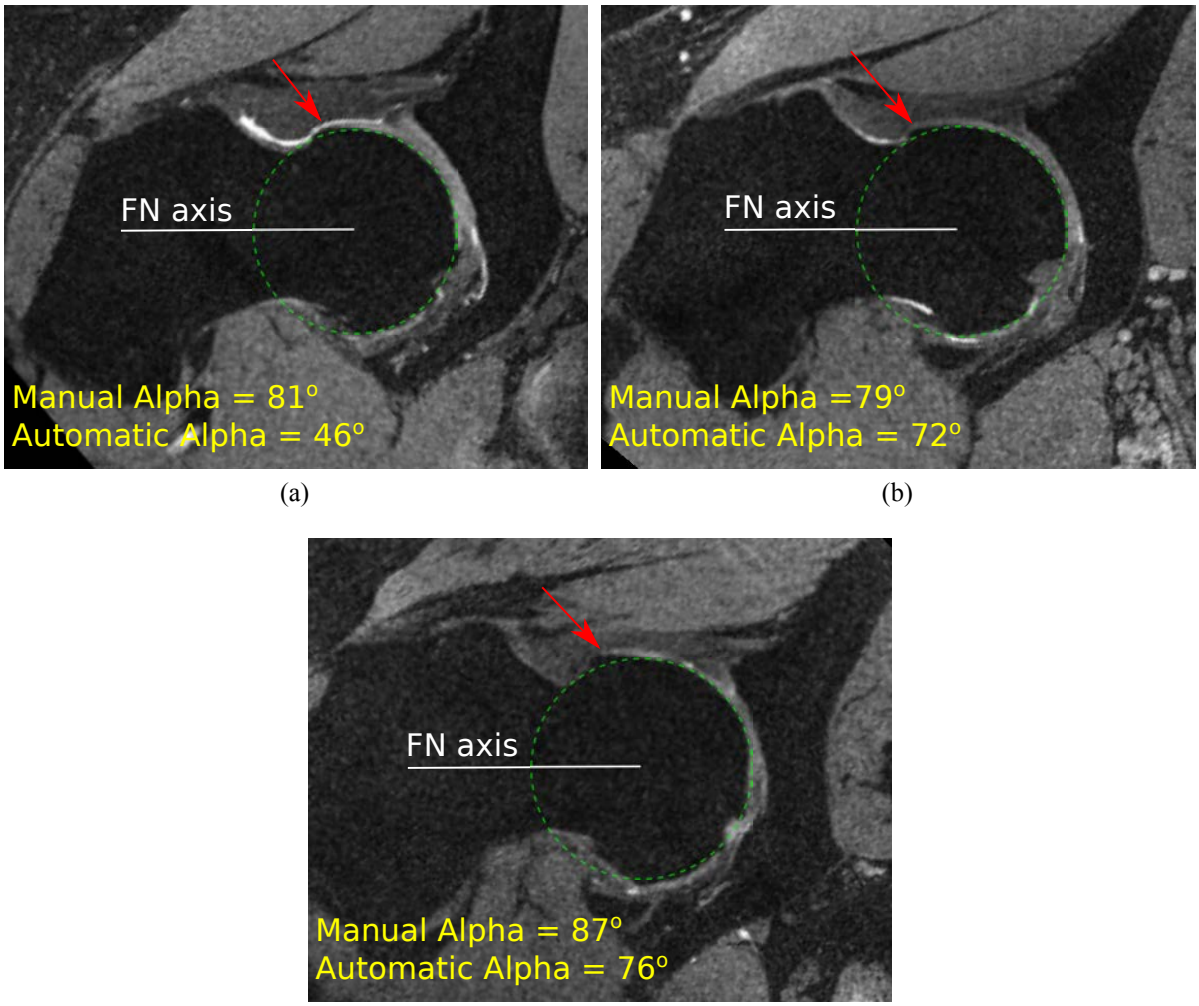

(a) (b)

(c)

Figure 4.10: Comparisons of manual and automatic alpha angle measures in cases having varying presence of osteophytes at the anterosuperior position of the FHN junction.

5

AUTOMATIC CARTILAGE SEGMENTATION FROM HIGH-RESOLUTION 3D MR IMAGES OF THE HIP JOINT

This chapter presents the work to attain **Aim 1.2**, which is to develop and evaluate the 3D autoamtic method for segmenting the hip joint cartilages from high-resolution MR images. To this end, a hybrid segmentation scheme was introduced here to provide automatic segmentations of the femoral and acetabular cartilages from MR images acquired without joint distraction or contrast agents. This developed scheme builds on the ASM-based bone segmentation algorithm (Chapter 3), which proved to have good accuracy particularly within the likely BCI regions. Automatic cartilage segmentation is performed using an improved graph search framework with an integration of an arc-weighted graph representation and varying surface feasibility constraints in order to allow reliable delineation of two cartilage plates despite weak or no separation between cartilage boundaries. These segmented cartilage volumes are then carefully validated against expert manual segmentations from TrueFISP MR examinations of volunteers with no apparent OA or clinically reported hip pain.

The presentation of this novel automatic cartilage segmentation approach was also included in the accepted manuscript in *Physics in Medicine and Biology* (Xia et al. 2014). At the current stage, manual segmentations of the individual femoral and acetabular cartilage plates have all been obtained from the full dataset of 46 TrueFISP images. The results for training of the articular cartilage model and validation of automatic cartilage segmentations are thereby updated accordingly in this thesis. In addition, a comparative study is also conducted to evaluate the segmentation accuracy between our proposed method and a multi-atlas-based algorithm (state-of-the-art) that has been successfully applied to segment the bones of the hip joint in Chapter 3.

Related publication details

Xia, Y., Chandra, S. S., Engstrom, C., Strudwick, M. W., Crozier, S., and Fripp, J. (2014). Automatic hip cartilage segmentation from 3D MR images using arc-weighted graph searching. *Physics in Medicine and Biology*, 59(23):7245. http://stacks.iop.org/0031-9155/59/i=23/a=7245 (Xia et al. 2014)

Manuscript revision history

Submitted to *Physics in Medicine and Biology*	11 April 2014
Interim decision (moderate revision)	19 August 2014
Revision submitted	15 September 2014
Accepted	3 October 2014
Published	10 November 2014

5.1 Introduction

Accurate segmentation of the articular cartilage in the hip joint can provide a basis for quantitative radiological analyses (e.g., cartilage volume, thickness, curvature and joint surface coverage) of pathoanatomical conditions such as OA. Quantitative assessment of cartilage using recent biochemical MR imaging techniques (e.g., *d*GEMRIC (Bittersohl et al. 2009; Mamisch et al. 2011), T1ρ (Carballido-Gamio et al. 2008b), T2 (Nishii et al. 2010; Watanabe et al. 2007) and T2* (Bittersohl et al. 2012) mapping) also relies on the provision of ROIs, i.e., the segmentation volumes, to evaluate water, collagen and proteoglycan content of articular cartilages.

Currently, due to anatomical and imaging challenges particularly for the hip joint (Section 1.3), MR-based quantitative analyses for hip joint cartilages have not paralleled advances in comparable work with the knee joint (Fripp et al. 2010; Tamez-Pena et al. 2012; Yin et al. 2010). Compared with the knee joint, the highly curved hip cartilages are much thinner with an average thickness of 1.4 and 1.2 mm for the femoral head and acetabular plates, respectively (Hodler et al. 1992). Contemporary 3T MR sequences for the hip joint have a maximum in-plane resolution of 0.312 $\times$ 0.312 mm with 1.5 mm slice thickness (Carballido-Gamio et al. 2008b) although scans of 0.6 $\times$ 0.6 mm with larger slice thickness are usually acquired in clinical examinations (Kijowski 2010). Consequently, a large portion of image voxels are subject to considerable PVE making reliable cartilage segmentation difficult for manual and more automated methods (Cicuttini et al. 2000; Hodler et al. 1992; Li et al. 2008; Naish et al. 2006; Zhai et al. 2005). Furthermore, the distinction between the individual femoral and acetabular cartilage plates is particularly difficult to discern in weight-bearing areas of these closely apposed plates (Nishii et al. 1998). In response to these issues, previous studies have employed approaches using leg traction devices (Cheng et al. 2013; Nishii et al. 2004; Sato et al. 2001) or contrast agents/mechanisms (Baniasadipour et al. 2007) for segmentation of the hip joint cartilages in the presence of weak boundaries, i.e., poor separation between the femoral and acetabular plates (see Figure 5.1).

In this chapter, we present a hybrid segmentation scheme that incorporates an improved multi-object multi-surface graph search framework for fully automatic segmentation of the articular cartilages from high-resolution 3D MR images of the hip joint. This developed scheme relies on the following processes: bone pre-segmentation using a 3D ASM algorithm introduced in Chapter 3, extraction of the BCI and segmentation of the hip joint cartilage using an improved multi-layered graph search algorithm (Yin et al. 2010).

The improvements to the earlier graph search framework (Yin et al. 2010) are made by a novel

integration of an arc-weighted graph representation (Song et al. 2013) incorporating varying surface feasibility constraints learned from prior knowledge of the articular cartilage within the hip joint. These specified segmentation properties and constraints are encoded by both node weights and arc costs. This will allow fully automatic and reliable segmentation of the individual femoral and acetabular cartilage plates from 3D MR images with weak or no separation between cartilage boundaries, which were usually solved by continuous leg traction or contrast agents during the acquisition. To our best knowledge, this is the first method that allows to do this. This method has been validated against expert manual segmentations for the combined and individual cartilage plates from MR examinations of 46 healthy volunteers, and is further compared with a multi-atlas-based method similar to (Chandra et al. 2012a; Siversson et al. 2013).

5.2 Previous work

5.2.1 Manual and semi-automatic segmentation of hip joint cartilage

Presently, quantitative radiological investigations on the hip joint cartilage mostly rely on manual or semi-automatic segmentation approaches (Cicuttini et al. 2000; Hodler et al. 1992; Li et al. 2008; Naish et al. 2006; Zhai et al. 2005). Cicuttini et al. (2000) and Zhai et al. (2005) measured the hip cartilage volume by manually contouring cartilage boundaries on individual 2D images of MR scans from OA patients. Naish et al. (2006) utilized a semi-automatic livewire algorithm to evaluate thickness distribution maps of the combined hip cartilage from 3D gradient-echo MR images. Li et al. (2008) reported semi-automatic segmentation of the individual acetabular and femoral cartilage plates (using active contours) in 2D MEDIC MR images without the use of continuous leg traction. The use of these manual and semi-automatic approaches for cartilage segmentation typically requires skilled analysts with considerable experience and is time-consuming, e.g., 1 hour per image for semi-automatic analysis (Naish et al. 2006) and 3 hours for manual delineation of the cartilages on each SPACE image (Chandra et al. 2015b); consequently the development of an accurate automatic scheme for hip joint cartilage segmentation would be beneficial for large-scale clinical and research studies focusing on morphometric evaluations.

5.2.2 Automatic segmentation of hip joint cartilage

There has been limited development of approaches for fully automated segmentation of hip cartilage from CT and MR images. Several studies have employed edge detection algorithms for segmentation of the combined hip cartilages from MR (Nishii et al. 2004; Sato et al. 2001) and CT (Baniasadipour et al. 2007) images; however, only rudimentary validation was reported in these studies. Siversson et al. (2013) validated automated segmentations of the combined hip cartilage volume from a multi-atlas label fusion method against manual measures reporting a mean DSC of 0.84 from 3D TrueFISP images (isotropic 0.6 mm) acquired from ten patients with cartilage degeneration, although this work did not generate segmentations for the individual femoral and acetabular cartilage plates. Recently, Cheng et al. (2013) proposed a mathematical model of two adjacent sheet structures to simulate the

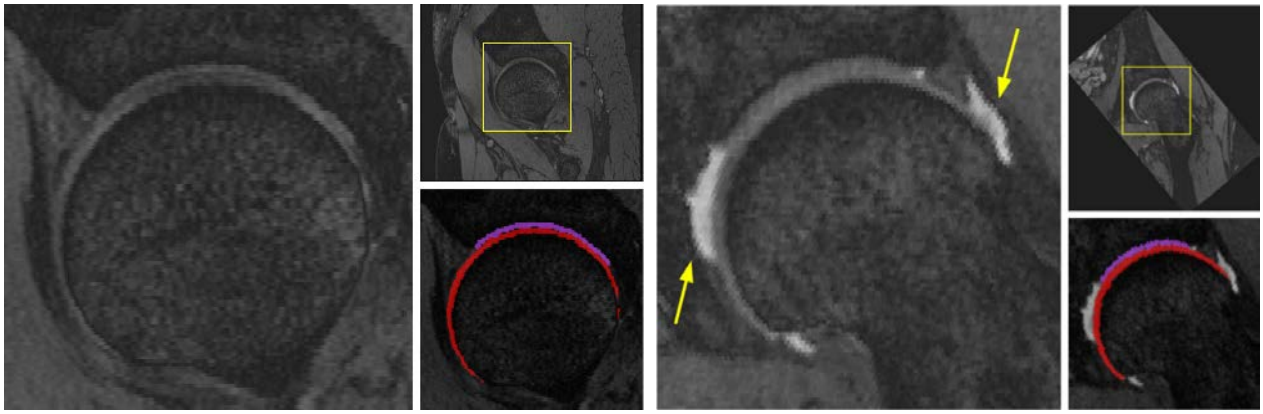

(a) (b)

Figure 5.1: Example (a) sagittal and (b) oblique coronal reformatted MR slice (top right, in-plane resolution: 0.234 mm, slice thickness: 0.490 mm) with manual labels (bottom right, red: femoral cartilage, purple: acetabular cartilage) overlaid on the zoomed region of the hip joint (left), with weak to non-existent boundaries between the femoral and acetabular cartilage plates (arrows show the bright signal of synovial fluid).

femoral and acetabular cartilages to evaluate the accuracy limits on thickness measurements. This approach, however, requires a distinct discrimination of two cartilage layers as might be obtained in MR imaging using physical separation of the hip joint via continuous leg traction (Cheng et al. 2013; Nishii et al. 2004; Sato et al. 2001).

To the best of our knowledge, no fully automated algorithm for segmenting individual femoral and acetabular cartilage layers has been reported for 3D MR images of the hip joint without the use of joint distraction or contrast agents. In comparison, a number of MR studies on the knee joint have reported automatic segmentation approaches for morphometric analyses of femoral, tibial and patellar cartilage plates (Dodin et al. 2010; Folkesson et al. 2007; Fripp et al. 2010; Lee et al. 2011; Tamez-Pena et al. 2012; Yin et al. 2010). Amongst these approaches, the BCI has been used regularly as an underlying frame of reference for subsequent cartilage segmentation (Dodin et al. 2010; Fripp et al. 2010; Lee et al. 2011; Yin et al. 2010). Though promising results have been obtained for individual knee cartilages, adapting these existing methods to the hip joint faces considerable challenges given the issues of substantial PVE and signal intensity similarities between the closely apposed articulating cartilage interfaces of the femoral and acetabular layers.

5.2.3 Optimal 3D graph search framework

The optimal 3D graph search framework has been successfully applied in MR studies of cartilage segmentation in the knee (Yin et al. 2010) and ankle (Li et al. 2005), where an object-specific graph was constructed from the pre-segmented triangulated mesh of the articulating bones within these joints. This work was performed using the node-weighted graph representation, where the connectedness from one node to the other was simply of equal importance under the defined surface feasibility constraints. However, this approach is not readily applicable to the delineation of multiple surfaces with poor separation of boundaries, e.g., the femoral and acetabular cartilage plates. More recently, an

arc-weighted graph representation using weights of graph arcs to linearly penalize shape changes has been used for segmentation of the closely opposed bladder and prostate in CT images (Song et al. 2010). Song et al. (2013) have developed a more sophisticated graph construction scheme for the intra-rentinal layer segmentation from optical coherence tomography images of the eyes, which incorporated both shape and context prior penalties in the graph to make greater use of prior information for separation of apposed layers.

In this MR study of the hip cartilages, our newly proposed hybrid graph search framework coalesces the discrete works of Yin et al. (2010) and Song et al. (2013) to enable simultaneous segmentation for the individual femoral and acetabular cartilage plates of the hip joint in the presence of weak boundaries.

5.3 Materials and Methods

5.3.1 MR image acquisition

A set of unilateral TrueFISP images with a small FOV of the right hip joint were used in this work, which were acquired from from 46 volunteers with no apparent OA or clinically reported hip pain (aged 31.7 $\pm$ 9.6 (18 - 60) years, 31 males and 15 females, BMI: 23.9 $\pm$ 4.9 kg/m^2). The parameters for unilateral TrueFISP sequence are listed in Table 2.1. Slice interpolation (K-space) was enabled for a subset of 41 subjects to obtain an in-plane image resolution of 0.234 mm spacing. Example TrueFISP images are shown in Figure 5.1 illustrating a typically indistinct separation between the femoral and acetabular cartilages.

Manual segmentation

The articular cartilages within the hip joint were manually segmented by Dr. Mark W Strudwick (Rater 1, an experienced radiographer) using ITK-SNAP (Yushkevich et al. 2006) to produce cartilage plate labels across all the MR images.

The cartilages in the initial 22 MR examinations were segmented as a combined cartilage volume, i.e., no partitioning into the individual femoral or acetabular plates. MR images from 9 randomly selected subjects were segmented by Dr. Craig Engstrom (Rater 2, an experienced MSK analyst) to investigate the inter-rater reliability for manual segmentations of the combined cartilage volume. In a blinded fashion, MR scans from 3 of these 9 subjects were re-segmented by both raters to assess the intra-rater reliability.

The individual femoral and acetabular cartilage plates were manually labelled by Rater 1 from all MR images (N = 46), which also included the first 22 MR scans whose combined cartilage volumes were further manually delineated into two individual cartilage partitions at a later stage. MR images of 5 subjects (randomly selected) were re-segmented for intra-rater reliability analyses of each cartilage partition.

In this study, the set of manual segmentations (N = 46) with the individual femoral and acetabular

cartilage partitions from Rater 1 was used in the training process of the hip articular cartilage model as well as the validation against automatic cartilage segmentation results.

5.3.2 Multi-atlas based cartilage segmentation

In this chapter, a multi-atlas-based segmentation method (state-of-the-art) was implemented for a validational comparison with our newly proposed segmentation scheme, which has been successfully applied for segmentation of the bone elements in the hip joint region in Chapter 3. In this method, the multi-atlas set is composed of preprocessed TrueFISP images (N4 bias field correction (Tustison et al. 2010) and smoothing using gradient anisotropic diffusion detailed in Chapter 3) with corresponding manual data with different labels for the individual femoral and acetabular cartilage partitions as well as the subchondral bones (proximal femur, acetabulum) (N = 46 or N = 45 if a leave-one-out cross-validation was used).

To automatically segment an image, the image is firstly preprocessed in the same way as the training images and cropped into a small FOV, focusing on the articular cartilages within the hip joint, based on the size and center of the femoral head detected by a joint center locator (Nishii et al. 2004). The extracted ROI of the input image is then used in order to reduce the heavy computational burdens in the pairwise NRR with the atlases using the Nifty-Reg package (Modat et al. 2010). The most similar atlases are chosen based on a similarity metric NMI that was defined in (3.1) (A threshold $\phi = 0.8$ was used here), whose corresponding manual segmentations are fused via majority voting (Artaechevarria et al. 2009) to obtain automatic segmentations of the individual femoral and acetabular cartilages.

5.3.3 Our approach: model generation and graph-based cartilage segmentation

The proposed segmentation scheme for the hip cartilage can be summarized in two phases (see Figure 5.2): *i*) bone pre-segmentation and BCI extraction and *ii*) graph-based cartilage segmentation. Based on bone pre-segmentation for the hip joint, the BCI can be identified as the ROI on each individual bone surface in order to locate the articular cartilage for the subsequent graph-based cartilage segmentation phase. In the proposed graph search framework, the femoral and acetabular cartilage plates are simultaneously segmented using an arc-weighted graph representation that incorporates multiple surface feasibility constraints (e.g., surface smoothness, inter-surface distance and inter-object separation) learned from prior knowledge of cartilage morphology. In the following section, we first describe the model training process then introduce the proposed optimal graph search framework for the hip joint.

Training of the articular cartilage model

In order to obtain the prior knowledge required as a basis for the BCI extraction and subsequently for the graph-based cartilage segmentation, an articular cartilage model is generated using a training set of manual segmentations where the computed statistical properties of each cartilage plate (e.g., cartilage location, likelihood and thickness) are directly mapped to each vertex on the mean surface of

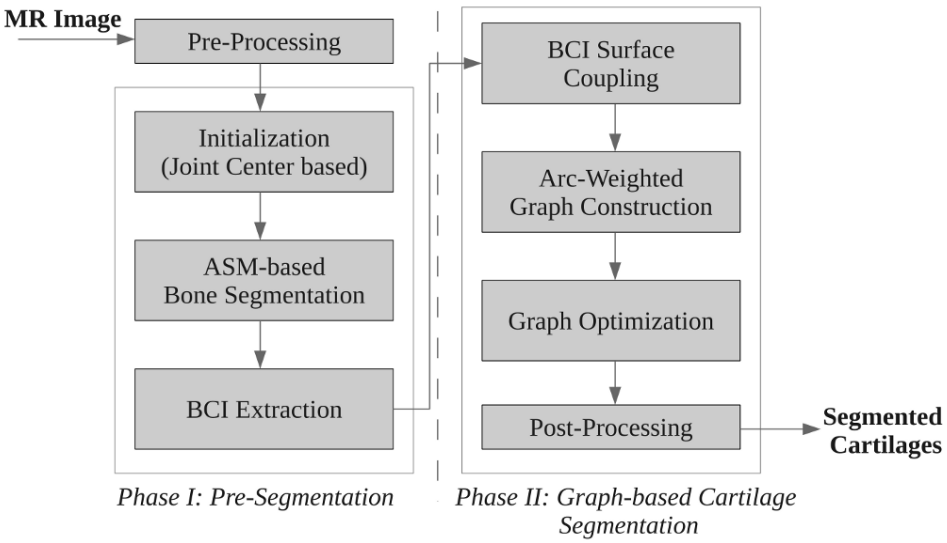

Figure 5.2: Automatic segmentation scheme for the articular cartilage from MR images of the hip joint.

a SSM of the articulating bone. In this chapter, manual segmentations of the individual femoral and acetabular cartilage plates (N = 46 or N = 45 if leave-one-out validation was used) were used for the model generation (Figure 5.3). The following statistical properties were included:

- *Cartilage Probability*: The probability (0 - 1) at each vertex of cartilage tissue being present (see Figure 5.3a). This is used to initialize the extraction of the BCI from bone segmentations.
- *Cartilage Thickness*: The mean and SD of the cartilage thickness (mm) on each vertex indicates the range of possible thickness changes for each plate as shown in Figures 5.3b and 5.3c. This is used to enforce the distance constraints between each pair of the cartilage inner (i.e., the BCI) and outer interface (i.e., articulating surface) in the graph representation.
- *Joint Spacing*: The mean and SD of the joint spacing between the articulating surfaces of the femoral and acetabular cartilage plates indicates the range of the possible separation distance at each vertex in the interacting region. This is used to enforce the separation constraints between the two articulating cartilage interfaces in the graph representation. Note: the distance values are only measured at the vertices in the interacting region (see Figure 5.4) of the bone surfaces along the same direction as the cartilage thickness.

In addition to the above statistical properties, the mean and SD of the *thickness difference between pairs of neighbouring vertices* is computed from the training set to provide the prior information used for the surface smoothness constraints to the outer interface of each cartilage plate.

As per the ball-and-socket-like 3D geometry of the hip joint, the *cartilage thickness* used in this work was defined with reference to the center of the femoral head(∼joint center), following previous studies (Li et al. 2008; Naish et al. 2006; Sato et al. 2001). At each vertex within the BCI regions on the bone surface, the thickness was calculated as the distance of the intersection points with the inner and outer interface of the (femoral or acetabular) cartilage plate along the radial direction from the joint center.

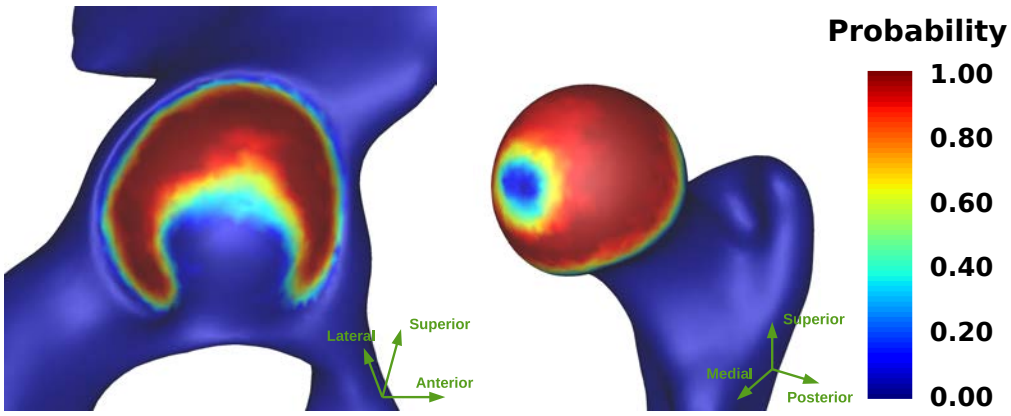

(a)

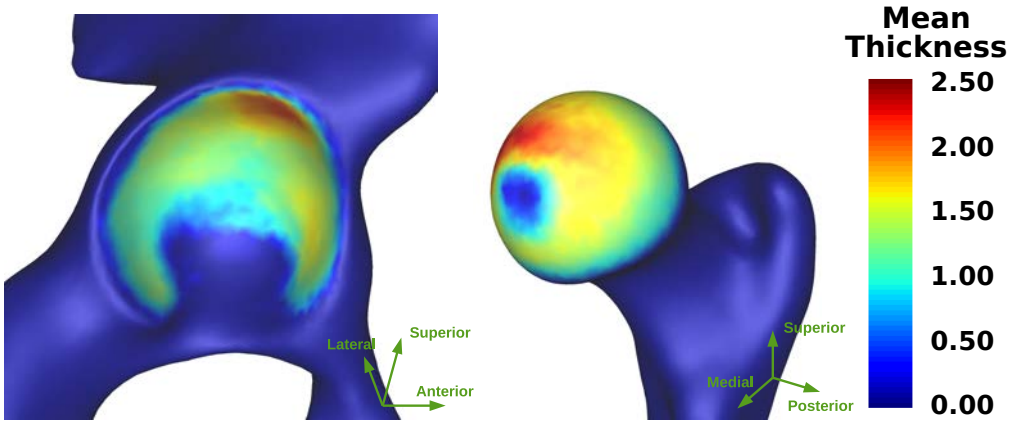

(b)

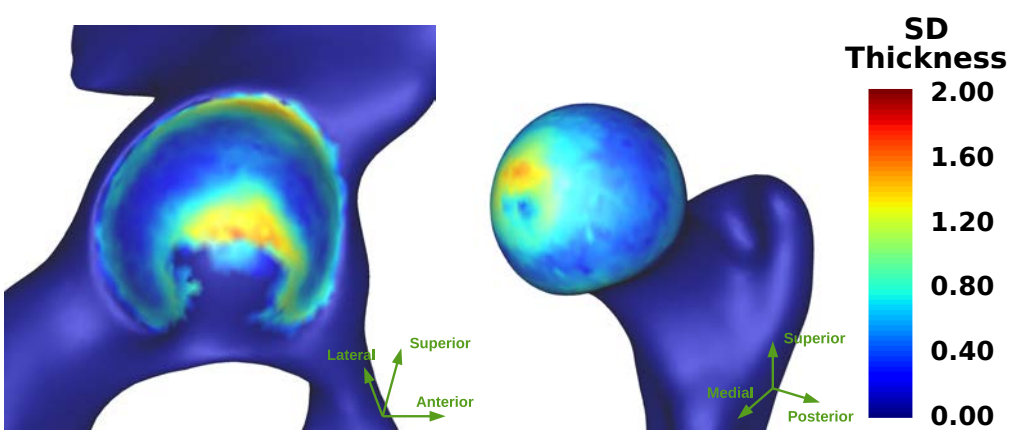

(c)

Figure 5.3: Cartilage probability and thickness measures of the acetabular (left) and the femoral head (right) cartilage models of the hip joint based on manual segmentations from the training dataset of 46 subjects: (a) probability of segmented cartilage tissue being present (valued 0 to 1), (b) average and (c) standard deviation of cartilage thickness (in mm) mapped to the atlas bone surfaces of the acetabulum and femoral head.

Bone pre-segmentation and BCI extraction

The bone segmentation approach used in this chapter has been previously presented in Chapter 3 (Xia et al. 2013). This approach is based on 3D ASMs, built from a training set of triangulated surface representations of each of the articulating bones in the hip joint with a hierarchical approach similar to previous studies (Chandra et al. 2012b; Yokota et al. 2009). To adapt this segmentation method to

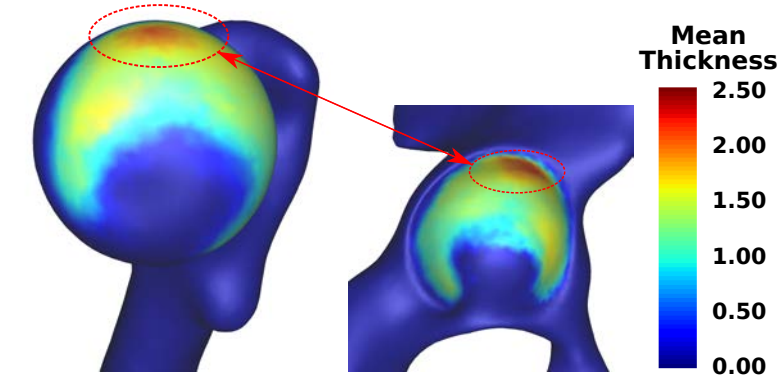

(a)

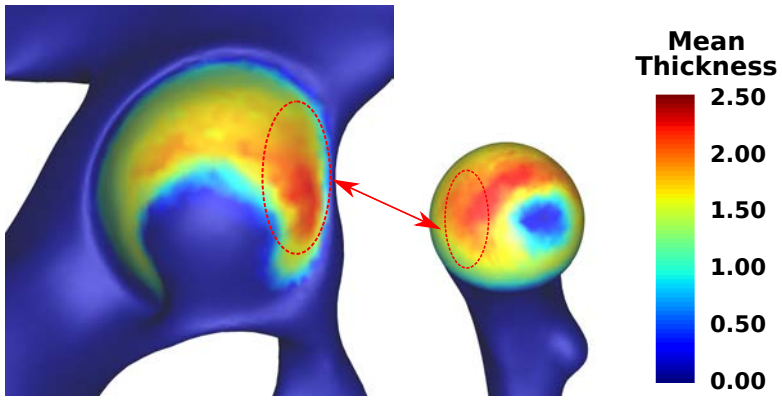

(b)

Figure 5.4: Articular interacting regions on the femoral head and acetabulum with the projection from the average thickness map of the (a) acetabular and (b) femoral cartilage plates using one-to-one correspondences built from BCI surface coupling. Dashed circles show the corresponding regions between (left) the articular interacting regions and (right) reference average cartilage thickness maps in the articular cartilage model.

TrueFISP images of the unilateral hip joint (i.e., small FOV), initialization of 3D ASM is performed based on a joint center locator (Nishii et al. 2004) and is then followed by coarse bone segmentation using a unilateral hip joint SSM and segmentation refinement using SSMs of individual bone elements, i.e., the proximal femur and acetabulum.

Instead of using the entire bone surface as the base graph for graph construction (Li et al. 2005; Yin et al. 2010), the predicted BCIs are extracted from the segmented bone surfaces using the approach of Fripp et al. (2007), which is based on the trained articular cartilage model and the estimated tissue properties of the cartilage.

Graph-based cartilage segmentation

Given the extracted BCIs, the segmentation task in this study can be represented as a multiple surface detection problem, which is to simultaneously detect four interfaces from two closely apposed cartilage plates and to co-optimize the inner and outer interfaces of the femoral and acetabular cartilage plates. The background information of the optimal graph search approach for solving this problem is given in Section 2.4.4.

As shown in Figure 5.5, a directed multi-object graph G including four subgraphs $\{G_i = (N_i, A_i) :$

$i = 0, 1, 2, 3\}$ is constructed, where G_0, G_1, G_2 and G_3 are the subgraphs respectively for the femoral inner interface, acetabular inner interface, femoral outer interface and acetabular outer interface in the hip joint. N_i and A_i are the node set and arc set for the subgraph G_i, respectively. $G_F = G_0 \cap G_2$ denotes a dual-surface graph for the femoral cartilage, which is constructed from the base graph $M_F = (V_F, E_F)$, i.e.the femoral BCI surface, and $G_A = G_1 \cap G_3$ denotes a dual-surface graph for the acetabular cartilage constructed from the base graph $M_A = (V_A, E_A)$, i.e., the acetabular BCI surface. In order to integrate the two dual-surface graphs, i.e., G_F and G_A, into a multi-object graph, inter-object graph separation constraints are implemented via inter-object arcs (see Figure 5.5).

1) BCI surface coupling

To construct a multi-object graph, the femoral and acetabular BCIs should be coupled to build one-to-one correspondences in interacting regions between these two base graphs with different surface topologies. Compared with the work of Yin et al. (2010) introducing a nonlinear cross-object surface mapping algorithm using electric field lines of force, our proposed coupling process is modified based on the anatomical "ball-and-socket" structure of the hip joint. Assuming both the femoral and acetabular BCIs as partial sphere-like surfaces, each vertex on one BCI surface is mapped to the other BCI surface if the line connecting the detected center of the femoral head and this vertex intersects with the other BCI surface. The intersection point is then included in the vertex collection of the other BCI surface. This results in the two base graphs "sharing" common vertices in the interacting regions, which allows the construction of inter-object arcs between the two corresponding columns from two objects' graphs. This surface coupling method is also applied to the training process of the articular cartilage model (see Figure 5.4).

2) Arc-weighted graph construction

We firstly consider the construction of a single arc-weighted dual-surface graph $G = G_0 \cap G_1$ for one of the cartilage plates, where $G_0 = (N_0, A_0)$ and $G_1 = (N_1, A_1)$ are the subgraphs for the inner and outer cartilage interfaces, from the related BCI surface, i.e., the base graph $M = (V, E)$. At each vertex on the BCI, two spatially coincident columns of equidistant nodes are constructed along its "normal" direction, which is re-computed as the direction from the femoral head center to this vertex. The two columns of nodes constructed at $v_p \in V$ with the length K can be denoted by $N_0(v_p) \equiv \{n_0(p, k) \in N_0 : k = 0, 1, \ldots, K-1\}$ and $N_1(v_p) \equiv \{n_1(p, k) \in N_1 : k = 0, 1, \ldots, K-1\}$. The length K is determined by the required node spacing and the expected maximum cartilage thickness, which is computed based on the maximum distance between the two BCI surfaces.

In order to enforce multiple surface feasibility constraints, different graph arcs are constructed in the arc-weighted dual-surface graph as follows:

- *Intra-Column Arcs*: To ensure that the optimal surface intersects with each column exactly once, along every column $N_i(v_p)$, $i \in \{0, 1\}$, every node $n_i(p, k)$ has a directed arc with $+\infty$ weight to the node $n_i(p, k-1)$, $k = 1, 2, \ldots, K-1$.
- *Inter-Column Arcs*: To control the stiffness of output surfaces, surface smoothness constraints are implemented by inter-column arcs, which are imposed between each pair of adjacent columns

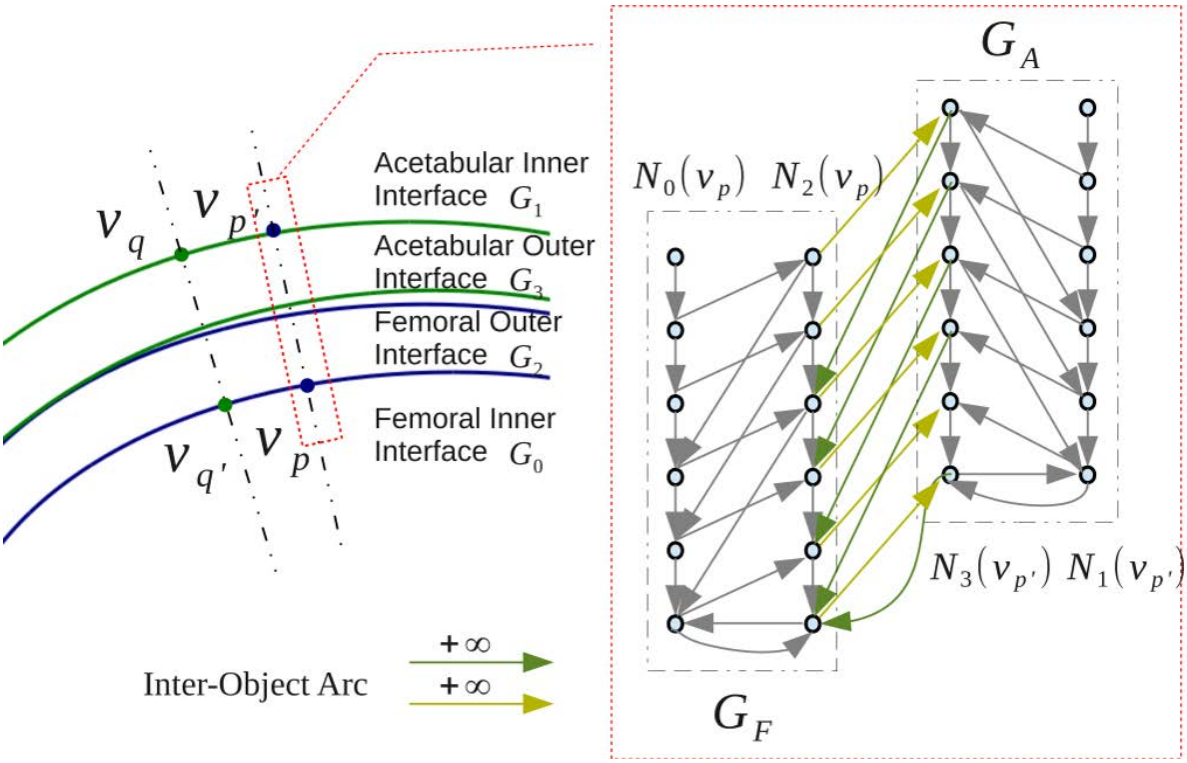

Figure 5.5: Examples showing the construction of the multi-object graph with inter-object arcs at the interacting regions within the hip joint. G_F is the dual-surface graph constructed from the femoral BCI and G_A is the dual-surface graph constructed from the acetabular BCI.

in the graph. Let $N_i(v_p)$ and $N_i(v_q)$ be two adjacent columns ($p \neq q$, $\langle v_p, v_q \rangle \in E$), and $\Delta_{p,q}$ is the index difference of the nodes $n_i(p,*)$ and $n_i(q,*)$ where the optimal surface intersects with the column $N_i(v_p)$ and $N_i(v_q)$. Two smoothness constraint parameters $\overline{\Delta}_{p,q}$ and $\sigma_{p,q}$ learned from the prior information are used to define the allowed possible range of surface changes between neighbouring columns $N_i(v_p)$ and $N_i(v_q)$, i.e., the *hard constraint term* $|\Delta_{p,q} - \overline{\Delta}_{p,q}| \leq \alpha_1 \sigma_{p,q}$ (α_1 is a constant factor, $\alpha_1 = 2.5$ was used here), and to penalize the surface deformation inside the allowed range using a prior penalty function $f_s(\Delta_{p,q} - \overline{\Delta}_{p,q})$. An example for the construction of inter-column arcs is illustrated in Figure 5.6a.

- *Hard constraint term*: The possible range is defined as $[\overline{\Delta}_{p,q} - \alpha_1\sigma_{p,q}, \overline{\Delta}_{p,q} + \alpha_1\sigma_{p,q}]$. Along the column $N_i(v_p)$, a directed arc with $+\infty$ weight is constructed from each node $n_i(p,k)$ to the node $n_i(q,k')$ in the column $N_i(v_q)$, $k' = \max(0, k - (\overline{\Delta}_{p,q} - \alpha_1\sigma_{p,q}))$. Simultaneously, along the column $N_i(v_q)$, a directed arc $(+\infty)$ is constructed from each node $n_i(q,k)$ to the node $n_i(p,k')$ in the column $N_i(v_p)$, $k' = \max(0, k - (\overline{\Delta}_{p,q} + \alpha_1\sigma_{p,q}))$.
- *Prior penalty term*: In order to "distribute" the smoothness penalty within the allowed range, for every pair of nodes, say $n_i(p,k)$ and $n_i(q,k')$, $\Delta_{p,q} = k' - k$, a weighted arc is added using the second derivative of the prior penalty function $f_s(\cdot)$ if $(\overline{\Delta}_{p,q} - \alpha_1\sigma_{p,q}) \leq \Delta_{p,q} \leq (\overline{\Delta}_{p,q} + \alpha_1\sigma_{p,q})$. Suppose $h = \Delta_{p,q} - \overline{\Delta}_{p,q}$, the second derivative for $f_s(h)$ is computed as: $f_s''(h) = [f_s(h+1) - f_s(h)] - [f_s(h) - f_s(h-1)]$.
  For each pair of the node $n_i(p,k)$ and $n_i(q,k')$, $k' = k + \overline{\Delta}_{p,q} + h$,
  * When $h < 0$, an arc is added from $n_i(p,k)$ to $n_i(q,k')$ with the weight $f_s''(h)$;

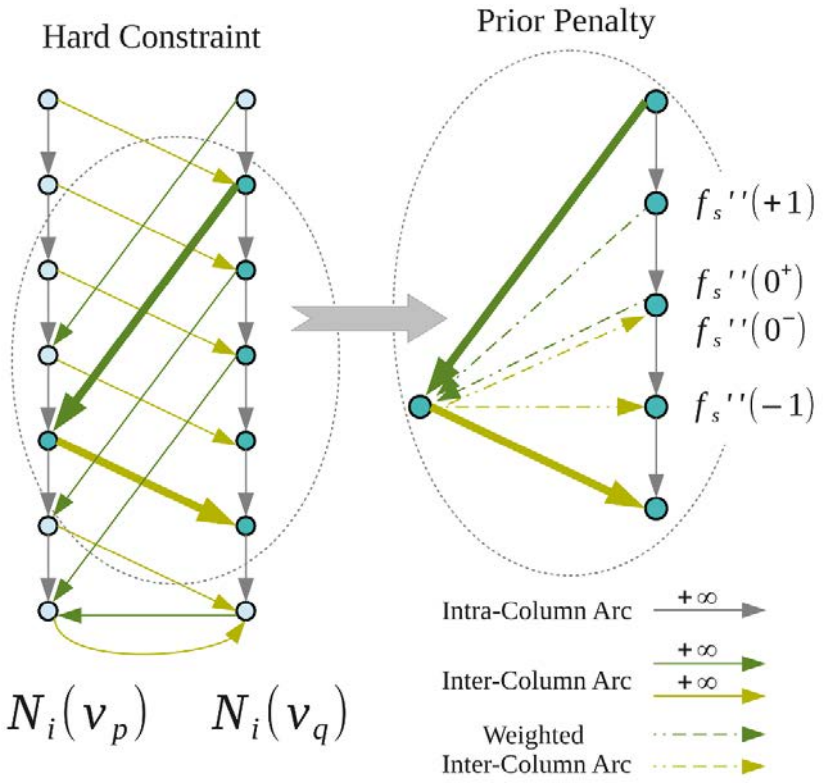

(a)

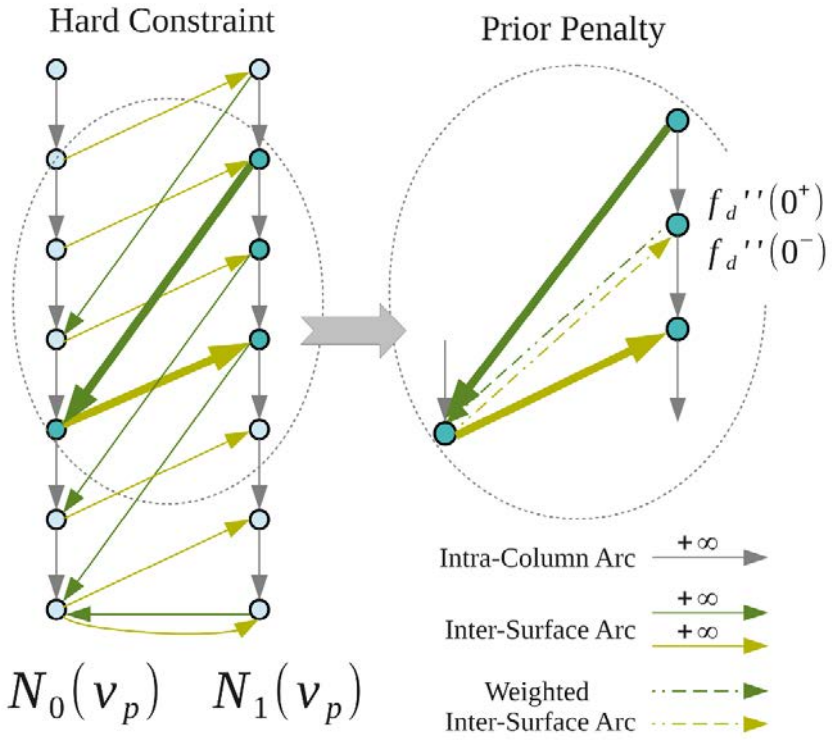

(b)

Figure 5.6: The construction of an arc-weighted graph for example showing (a) surface smoothness constraints between the neighboring column $N_i(v_p)$ and $N_i(v_q)$, $\overline{\Delta}_{p,q} = 1$, $\sigma_{p,q} = 2$, $\alpha_1 = 1$; (b) inter-surface distance constraints between two columns $N_0(v_p)$ and $N_1(v_p)$ at the vertex v_p, $\overline{\Lambda}_p = 2$, $\phi_p = 1$, $\alpha_2 = 1$.

* When $h > 0$, an arc is added from $n_i(q, k')$ to $n_i(p, k)$ with the weight $f_s''(h)$;
* When $h = 0$, an arc $\langle n_i(q, k'), n_i(p, k)\rangle$ is added with the weight $f_s''(0^+) = f_s(1) - f_s(0)$ and its reverse arc $\langle n_i(p, k), n_i(q, k')\rangle$ is also constructed with the weight $f_s''(0^-) = f_s(-1) - f_s(0)$.

- *Inter-Surface Arcs*: To define the distance between the inner and outer cartilage interface (i.e., the cartilage thickness), inter-surface distance constraints are implemented by inter-surface arcs, which are imposed between each pair of columns constructed at the same vertex. Let $N_0(v_p)$ and $N_1(v_p)$ be the columns at the vertex $v_p \in V$, and Λ_p is the distance of the two surfaces at this vertex. For inter-surface distance constraints, $\overline{\Lambda}_p$ and ϕ_p are parameters learned from the priors, which defines the possible range of cartilage thickness changes at the vertex $v_p \in V$, i.e., $|\Lambda_p - \overline{\Lambda}_p| \leq \alpha_2\phi_p$, where α_2 is a constant factor ($\alpha_2 = 2.5$ was used here), and also penalizes cartilage thickness changes inside the allowed range with a prior penalty function $f_d(\Lambda_p - \overline{\Lambda}_p)$. Figure 5.6b shows an example of the inter-surface arc construction.
  - *Hard constraint term*: The possible range $[\Lambda_{\text{min}}, \Lambda_{\text{max}}]$ of the thickness at the vertex v_p is defined by the two prior parameters, where $\Lambda_{\text{min}} = \max(0, \overline{\Lambda} - \alpha_2\phi_p)$ and $\Lambda_{\text{max}} = \overline{\Lambda} + \alpha_2\phi_p$. Along the column $N_0(v_p)$, a directed arc with $+\infty$ weight is constructed from each node $n_0(p, k)$ to the node $n_1(p, k + \Lambda_{\text{min}})$ in the column $N_1(v_p)$. Simultaneously, along the column $N_1(v_p)$, a directed arc $(+\infty)$ is constructed from each node $n_1(p, k)$ to the node $n_0(p, \max(0, k - \Lambda_{\text{max}})$ in the column $N_0(v_p)$.
  - *Prior penalty term*: In order to penalize the preferred thickness learned from the prior information, for every pair of nodes, say $n_0(p, k)$ in $N_0(v_p)$ and $n_1(p, k')$ in $N_1(v_p)$, $\Lambda_p = k' - k$, a weighted arc is added using the second derivative of the prior penalty function $f_d(\cdot)$ if Λ_p is within the interval of $[\Lambda_{\text{min}}, \Lambda_{\text{max}}]$. Let $h = \Lambda_p - \overline{\Lambda}_p$ and the second derivative for $f_d(h)$ is computed similarly to $f_s''(h)$.
    For each pair of the node $n_0(p, k)$ and $n_1(p, k')$, $k' = k + \overline{\Lambda}_p + h$,
    * When $h < 0$, an arc is added from $n_0(p, k)$ to $n_1(p, k')$ with the weight $f_d''(h)$;
    * When $h > 0$, an arc is added from $n_1(p, k')$ to $n_0(p, k)$ with the weight $f_d''(h)$;
    * When $h = 0$, an arc $\langle n_1(p, k'), n_0(p, k)\rangle$ is added with the weight $f_d''(0^+) = f_d(1) - f_d(0)$ and its reverse arc $\langle n_0(p, k), n_1(p, k')\rangle$ is also constructed with the weight $f_d''(0^-) = f_d(-1) - f_d(0)$.
- *Inter-object Arcs*: The inter-object arcs are used to enforce multi-object separation constraints between two interacting objects, i.e., G_F and G_A. After coupling the two BCI surfaces, one-to-one correspondences between these two base graphs are built at the interacting regions. Suppose $V_1{}'$ is the collection of the interacting vertices on the femoral BCI and $V_2{}'$ is the collection of the interacting vertices on the acetabular BCI. For every pair of coupled vertices in the interacting regions, e.g., in Figure 5.5, $v_p \in V_1{}'$ and $v_{p'}$ that is its corresponding point found on the acetabular BCI, two columns $N_0(v_p)$ and $N_2(v_p)$ are constructed at the vertex v_p along the line between v_p and $v_{p'}$, while $N_1(v_{p'})$ and $N_3(v_{p'})$ are constructed at $v_{p'}$. The inter-object arcs are added between the column $N_2(v_p)$ and $N_3(v_{p'})$ in the same way as the inter-surface arcs with the hard constraint $|\Gamma_p - \overline{\Gamma}_p| \leq \alpha_3\psi_p$ (α_3 is a constant factor, $\alpha_3 = 1.0$ was used here) and the

prior penalty function $f_t(\Gamma_p - \overline{\Gamma}_p)$.

3) Cost function design

The overall energy of the set $\mathcal{S}$ of surfaces S_i ($i = 0, 1, 2, 3$) shown in (5.1) contains four terms involving:

$$E(\mathcal{S}) = \underbrace{\sum_{i=0}^{3} \sum_{n_i(p,k) \in S_i} c_i(p,k)}_{\text{boundary energy term}} + \underbrace{\sum_{i=0}^{3} \sum_{(v_p, v_q) \in E_i} f_s(\Delta_{p,q} - \overline{\Delta}_{p,q})}_{\text{smoothness prior penalty term}} + \underbrace{\sum_{i=0}^{1} \sum_{v_p \in V_i} f_d(\Lambda_p - \overline{\Lambda}_p)}_{\text{inter-surface prior penalty term}} + + \underbrace{\sum_{v_p \in V_1{}' \cup V_2{}'} f_t(\Gamma_p - \overline{\Gamma}_p)}_{\text{inter-object prior penalty term}} \tag{5.1}$$

- *Boundary energy term* defined as the summation of the on-surface costs associated with all nodes on the surface S_i. For each column in G_i, e.g., $N_i(v_p)$, $v_p \in V_i$, the on-surface cost $c_i(p,k)$ associated with the graph node $n_i(p,k)$ is computed using a nonedge-based cost function (5.2) as described in (Li et al. 2006) and its node weight $w_i(p,k)$ is then assigned according to (5.3):

$$c_i(p,k) = \sum_{k'=0}^{k-1} (\mathcal{I}(n_i(p,k')) - a_1)^2 + \sum_{k'=k+1}^{K-1} (\mathcal{I}(n_i(p,k')) - a_2)^2 \tag{5.2}$$

where $\mathcal{I}(\cdot)$ is the intensity value of the node. a_1 and a_2 are the intensity mean of nodes $n_i(p,k')$ within the range of $k' \in [0,k)$ and $k' \in (k, K-1]$.

$$w_i(p,k) = \begin{cases} c_i(p,k) & \text{if } k = 0 \\ c_i(p,k) - c_i(p,k-1) & \text{otherwise} \end{cases} \tag{5.3}$$

- *Prior penalty term* of surface smoothness constraints with the prior penalty function (5.4).

$$f_s(\Delta_{p,q} - \overline{\Delta}_{p,q}) = \frac{(\Delta_{p,q} - \overline{\Delta}_{p,q})^2}{2\sigma_{p,q}^2} \tag{5.4}$$

Assuming that the extracted BCIs are close to actual bone boundaries, $\overline{\Delta}_{p,q} = 0$ is used and $\sigma_{p,q}$ is set as a constant in the subgraph G_0 and G_1 for the inner cartilage interfaces. In the subgraph G_2 and G_3 for the outer cartilage interfaces, $\overline{\Delta}_{p,q}$ and $\sigma_{p,q}$ are the mean and SD of *thickness difference between pairs of neighboring vertices* in the articular cartilage model of the hip joint.

- *Prior penalty term* of inter-surface distance constraints with the prior penalty function (5.5)

$$f_d(\Lambda_p - \overline{\Lambda}_p) = \frac{(\Lambda_p - \overline{\Lambda}_p)^2}{2\phi_p^2} \tag{5.5}$$

The prior parameters $\overline{\Lambda}_p$ and ϕ_p are the mean and SD of the *cartilage thickness* at the vertex v_p

in the articular cartilage model.

- *Prior penalty term* of multi-object separation constraints with the prior penalty function (5.6)

$$f_t(\Gamma_p - \overline{\Gamma}_p) = \frac{(\Gamma_p - \overline{\Gamma}_p)^2}{2\psi_p^2} \tag{5.6}$$

The prior parameters $\overline{\Gamma}_p$ and ψ_p are the mean and SD of the *joint spacing* at the vertex v_p obtained from the articular cartilage model.

4) Graph optimization

With this constructed graph $G = (N, A)$, we can find an optimal cut $\mathcal{C}^* = (\mathcal{N}^*, \overline{\mathcal{N}}^*)$ ($\mathcal{N}^* \cup \overline{\mathcal{N}}^* = N$), minimizing total weights of nodes in $\mathcal{N}^*$ plus total arc weights of $\mathcal{C}^*$, which can be solved by using a minimum $s-t$ cut algorithm (Hochbaum 2001; Wu and Chen 2002). A min-cut/max-flow algorithm proposed by Boykov and Kolmogorov (2004) was used in this work.

5) Post-processing

After graph optimization, the segmented cartilage volumes are post-processed using the estimated cartilage tissue properties by removing segmentation voxels of synovial fluid, which likely have the image intensity higher than the average intensity of the cartilage tissue plus three times its corresponding SD (see as the bright signal in Figure 5.1b).

5.3.4 Validation method

The validation of automated cartilage segmentations is reported using five volume/distance-based measures: sensitivity, DSC (Dice 1945), RAVD (Van Ginneken et al. 2007) and MASD (Gerig et al. 2001) and 95% Hausdorff distance (Fedorov et al. 2008; Litjens et al. 2014). Let TP, FP and FN respectively denote true positive, false positive and false negative counts for the voxels, then sensitivity = TP / (TP + FN) is the true positive fraction and the DSC = 2TP / (2TP + FP + FN). The RAVD is given in percentage terms, RAVD (%) = 100 × |A - M|/M, where A and M are automatic and manual segmentation volumes, respectively. The MASD (mm) is defined as:

$$d_{\text{MASD}} = [d_{\text{avg}}(S_A, S_M) + d_{\text{avg}}(S_M, S_A)]/2,$$

where $d_{\text{avg}}(S_A, S_M)$ is the average directed surface distance from all points on the automated surface S_A to the manual surface S_M. The 95% Hausdorff distance (mm) (Fedorov et al. 2008; Litjens et al. 2014) is the 95th-percentile value of the Hausdorff distances in order to estimate the accuracy of the alignment between two segmentation volumes. The regular Hausdorff distance is defined as:

$$d_{\text{Hausdorff}} = \max\{\max\{d(v_A, S_M), v_A \in S_A\}, \max\{d(v_M, S_A), v_M \in S_M\}\}.$$

5.4 Results

Each MR image of the hip joint was automatically segmented for all 46 TrueFISP examinations using the described hybrid scheme. A leave-one-out cross-validation approach was performed, whereby a new articular cartilage model was generated from the remaining 45 cases when the case to be segmented was included in the training set. No user-interaction was required for any of the automatic segmentation steps or for any *post-hoc* manual editing of resulting surfaces.

5.4.1 Inter- and intra-rater reliability

As summarized in Table 5.1, reliability analyses for manual segmentations of the combined cartilage volumes show mean DSC values of 0.82 and (0.86, 0.88) for the inter- and intra-rater (Rater 1, Rater 2) reliability, while mean RAVD values were 11.61% and (4.58%, 2.18%). For the manual partitioning of each cartilage plate, the intra-rater reliability of Rater 1 had mean DSC and RAVD values of 0.85 and 2.50% for the femoral partition and 0.80 and 5.07% for the acetabular partition.

5.4.2 Segmentation accuracy

A summary of the comparative volumetric and distance-based validation metrics is presented in Table 5.2. Comparisons between automatic and manual segmentation methods for the combined cartilage volumes showed a mean DSC value of 0.81 ($\pm$ 0.03) and a RAVD of 7.54% ($\pm$ 5.77), while, for segmentation of the individual femoral and acetabular cartilage plates, they showed mean ($\pm$ SD) DSC values of 0.77 ($\pm$ 0.03) and 0.73 ($\pm$ 0.05), and RAVD values of 8.86% ($\pm$ 8.19) and 8.63% ($\pm$ 6.23). Figure 5.7 shows boxplots for DSC values between manual and automatic segmentations for the cartilage volume data where the interquartile ranges of DSC values were 0.79 - 0.83 for the combined, 0.75 - 0.79 for the femoral and 0.70 - 0.76 for the acetabular plate.

Representative examples of validation results of the combined, femoral and acetabular cartilage plates with maximum, median and minimum DSC values are shown in Figure 5.7. Overall, there was good consistency between automatic and manual segmentations of the cartilages across the majority of the articulating surfaces of the femoral and acetabular plates. There were, however, specific areas where differences between automated and manual segmentations were consistently more apparent such as around the femoral head fovea, the acetabular fossa and the more peripherally located, thinner regions of cartilage coverage (see yellow regions in B2, B3, C3 example slices of Figure 5.7). Examples of automated segmentation results for cases with average DSC values are provided in Figure 5.8a, which shows a typical reliable delineation between the femoral and acetabular cartilage plates within the hip joint. Figure 5.8b presents corresponding 3D visualizations of the segmented cartilage plate volumes with the reference of the (proximal femur, acetabular) bone structures, which indicates great potential for provision of morphometric data in the subsequent research and clinical studies related to articular cartilages of the hip joint that will be further investigated in the next chapter.

In order to investigate the effect of the prior penalization used in our new hybrid segmentation scheme, a comparison was performed against a node-weighted graph representation, which was still

Table 5.1: Inter- and intra-rater reliability of manual segmentations for the combined, femoral and acetabular cartilage volumes.

		No. of subjects	DSC		RAVD* (%)		95% Hausdorff (mm)	
			Mean	SD	Mean	SD	Mean	SD
Combined	Inter Rater 1vs2	9	0.82	0.03	11.61	7.68	1.36	1.19
	Intra Rater 1	3	0.86	0.05	4.58	3.97	1.37	1.02
	Intra Rater 2	3	0.88	0.01	2.18	2.67	0.49	0.00
Femoral	Intra Rater 1	5	0.85	0.01	2.50	6.19	0.52	0.05
Acetabular	Intra Rater 1	5	0.80	0.02	5.07	8.74	1.58	0.79

* MASD = $100 \times 2\,|M_1 - M_2|/(M_1 + M_2)$, M_1 and M_2 are two manually segmented volumes.

encoded with hard surface constraints but no prior penalization via weighted arcs; it yielded mean (± SD) DSC values of 0.81 (± 0.02), 0.76 (± 0.03) and 0.71 (± 0.05) for the combined, femoral and acetabular cartilage volumes, respectively. Comparatively, the hybrid segmentation scheme showed statistically significant improvements in DSC scores for segmentation of the femoral ($t(45) = 7.98$, $p < 0.001$) and acetabular ($t(45) = 10.12$, $p < 0.001$) cartilage volumes, while no significant difference was found for segmentation of the combined cartilage volumes ($t(45) = 1.23$, $p = 0.223$).

5.4.3 Comparison with the multi-atlas-based method

The multi-atlas-based algorithm was also applied to all 46 TrueFISP images, which obtained mean (± SD) DSC values of 0.80 (± 0.05), 0.77 (± 0.05) and 0.73 (± 0.06), and RAVD of 9.01% (± 7.61), 8.76% (± 7.00) and 13.02% (± 9.66) for segmentation of the combined, femoral and acetabular cartilage volumes (see Table 5.2). Using paired t-test analyses, no significant difference was found in DSC values for validation results of the combined ($t(45) = -1.232$, $p = 0.224$), femoral ($t(45) = -0.260$, $p = 0.796$) and acetabular ($t(45) = 0.084$, $p = 0.934$) cartilage segmentations.

Figure 5.10 illustrates a case-by-case comparison between the multi-atlas-based and our proposed method in DSC scores of validation results for the combined, femoral and acetabular cartilage segmentations, respectively. For each cartilage partition, a similar trend across the cases can be observed while there are a few cases, e.g., case 11 and 18, having an evident drop in the DSC value when using the multi-atlas-based approach (see asterisk symbols in Figure 5.10). This resulted from the poor image quality, particularly low or no contrast at the BCIs and articulating cartilage (cartilage-synovial fluid) interfaces, which was especially true for case 18 shown in Figure 5.10a with a segmentation failure (DSC < 0.6) using the multi-atlas-based algorithm. In contrast, our method shows comparatively robust performance on this image, although segmentation errors can still be noticed for delineation of interfaces between the bone and cartilage layer. Figure 5.10b indicates superior delineation performance between the individual femoral and acetabular cartilage plates with our method in case 11, where the acetabular cartilage volume was largely underestimated using the state-of-the-art. For case 45, the multi-atlas-based approach achieved higher DSC values than the proposed segmentation method; however, both methods demonstrated qualitatively high levels of accuracy at the region of significance for both the femoral and acetabular cartilages (Figure 5.10c).

5.5 Discussion

We have presented a new, fully automatic approach for successful segmentation of the combined and the individual femoral and acetabular cartilage plates in the hip joint from high-resolution 3D MR images. This multi-stage approach is based on pre-segmentation of bone surfaces using a 3D ASM algorithm (Chapter 3) followed by implementation of an improved optimal multi-object multi-surface graph search framework, which employed an arc-weighted graph representation with varying surface feasibility constraints learned from prior knowledge of cartilage morphometry. In the present study, this hybrid scheme automatically segmented the individual femoral and acetabular cartilage plates from TrueFISP MR images without employing auxiliary approaches such as continuous leg traction for hip joint distraction or contrast agents during image acquisition.

In comparison with traditional manual segmentation of the combined hip joint cartilage volume, used as the "benchmark" in the present work and for previous quantitative research and clinical studies focusing on morphometric analyses of cartilage (Li et al. 2008; Naish et al. 2006), our automated approach achieved a good mean DSC value of 0.81 in the context of mean inter-rater and intra-rater manual segmentation DSC scores of 0.82 and 0.86 to 0.88. Similarly, the automated approach provided good overall cartilage segmentations compared with the time- and expertise-intensive manual segmentations of MR images for the individual femoral (mean DSC score of 0.77) and acetabular (mean DSC score of 0.73) cartilage volumes. These outcomes compared favourably with the intra-rater reliability DSC values of 0.85 and 0.80 for repeated manual measurements of the individual femoral and acetabular cartilage plates.

In comparison with an in-house implementation of the original layered optimal graph image segmentation of multiple objects and surfaces (LOGISMOS) algorithm (Yin et al. 2010), the current hybrid approach, with integration of prior penalty terms (Song et al. 2013) in the graph representation, achieved significantly higher DSC values for segmentation of the individual femoral and acetabular cartilage volumes (see Section 5.4.2). For these partitioned cartilage plates, the smaller volumes and higher surface-to-volume ratios of these individual plates and boundary separation difficulties between the closely apposed cartilage surfaces readily explain the lower DSC values in comparison with the combined hip cartilage segmentations. Further, delineation errors associated with both manual and automated segmentations could be readily apportioned to the substantial PVE occurring around the tapered edges and/or thinner regions of the highly curved cartilage tissue in the hip joint (Figure 5.7).

Furthermore, there is no significant difference in DSC values obtained between our developed automatic segmentation scheme and the multi-atlas-based method (state-of-the-art). However, our proposed method demonstrated comparative robust performance on MR examinations with the poor image quality, particularly no or low tissue contrast for the BCIs and articulating cartilage interfaces (Figure 5.10a). Even though improvements could be made to the multi-atlas-based method by incorporating a larger number of atlases with more variation, heavy computational burdens are an important concern for its potential clinical applications, particularly with consideration of timeliness and patient throughput. Therefore, our proposed method offers a good level of both segmentation precision and time-efficiency and has more potential for prospective research and clinical utilities.

Our current segmentation scheme offers the potential for quantitative assessment of the *in vivo* morphological characteristics of the individual femoral and acetabular cartilage plates from 3D MR images of the hip joint. Combined with biochemical MR imaging, this automated approach presents exciting avenues to systematically evaluate potential imaging biomarkers in large MR datasets of pre-OA and early OA studies for application to radiological examinations for disease diagnosis and clinical trials investigating therapeutic interventions.

There are a number of limitations in the present study. The evaluation of our newly developed method was performed on high-resolution 3T MR (TrueFISP) images of the hip from relatively young, healthy participants. Further, the current bone segmentation scheme was developed within a framework of a water excited or FS MR sequence with "dark" bones and bright cartilage and fluid; the automated approach will likely transfer to images with similar contrast characteristics (DESS, MEDIC, FS SPACE) although such validation needs to be undertaken. Moreover, future work involving MR images from non-FS sequences, from lower-resolution routine clinical sequences (e.g., 2D or 3D fast spin-echo) across different scanner field strengths (including scan-rescan reliability analyses involving different positioning, image sequences and in-plane resolutions) and in individuals with a spectrum of hip joint pathology will be required for a fuller evaluation of our current automated framework. Clinically, our approach is likely to be applicable for the hip joint in early and/or less severe OA conditions. For more severe disease states involving changes to the femoral head (currently modelled as a sphere-like structure with its center serving as a reference landmark for the BCI surface coupling and cartilage thickness measurements), dedicated analyses will be needed for evaluating potential segmentation errors.

5.6 Conclusion

We have presented a fully automatic approach for successful cartilage segmentation from 3D MR images of the hip joint based on improvements to the optimal graph search framework incorporating prior knowledge of cartilage morphometry to simultaneously segment the femoral and acetabular plates despite their closely apposed surfaces (narrow joint spacing) and weak boundaries between these articulating structures. The proposed scheme provided an overall high level of validity and reliability of automated segmentations of the femoral and acetabular cartilage volumes in comparison with benchmark manual segmentations. Hence, the developed scheme has the capacity to provide automated reproducible quantitative volumetric data on the hip cartilages, without reliance on time- and expertise-intensive manual approaches, for potential use in large prospective pre-OA and early OA studies. The feasibility of this developed segmentation scheme for use in subsequent quantitative measurements will be then investigated in Chapter 6.

Table 5.2: Comparative volumetric and distance-based validation metrics for comparisons between manual and automatic segmentations of the combined, femoral and acetabular cartilage plates. The obtained automatic cartilage segmentations were obtained using the multi-atlas-based (state-of-the-art) and our proposed segmentation method, respectively.

	Sensitivity	DSC		RAVD (%)		95% Hausdorff (mm)		MASD (mm)	
	Mean ± SD	Mean ± SD	Min - Max	Mean ± SD	Min - Max	Mean ± SD	Min - Max	Mean ± SD	Min - Max
State-of-the-Art									
Combined	0.79 ± 0.07	0.80 ± 0.05	0.60 - 0.86	9.01 ± 7.61	0.39 - 34.20	1.45 ± 0.95	0.54 - 6.10	0.32 ± 0.13	0.20 - 1.03
Femoral	0.76 ± 0.07	0.77 ± 0.05	0.54 - 0.84	8.76 ± 7.00	0.22 - 32.76	1.62 ± 1.14	0.52 - 6.69	0.31 ± 0.18	0.18 - 1.38
Acetabular	0.71 ± 0.10	0.73 ± 0.06	0.51 - 0.81	13.02 ± 9.66	1.10 - 44.28	2.06 ± 1.47	0.59 - 5.83	0.33 ± 0.16	0.16 - 0.89
Our Method									
Combined	0.80 ± 0.05	0.81 ± 0.03	0.74 - 0.85	7.54 ± 5.77	0.05 - 21.77	1.73 ± 0.77	0.68 - 3.85	0.38 ± 0.08	0.23 - 0.58
Femoral	0.76 ± 0.06	0.77 ± 0.03	0.70 - 0.84	8.86 ± 8.19	0.21 - 36.12	2.20 ± 1.10	0.70 - 4.81	0.35 ± 0.10	0.20 - 0.61
Acetabular	0.73 ± 0.07	0.73 ± 0.05	0.62 - 0.83	8.63 ± 6.23	0.32 - 26.07	2.48 ± 1.59	0.66 - 7.67	0.38 ± 0.15	0.18 - 0.80

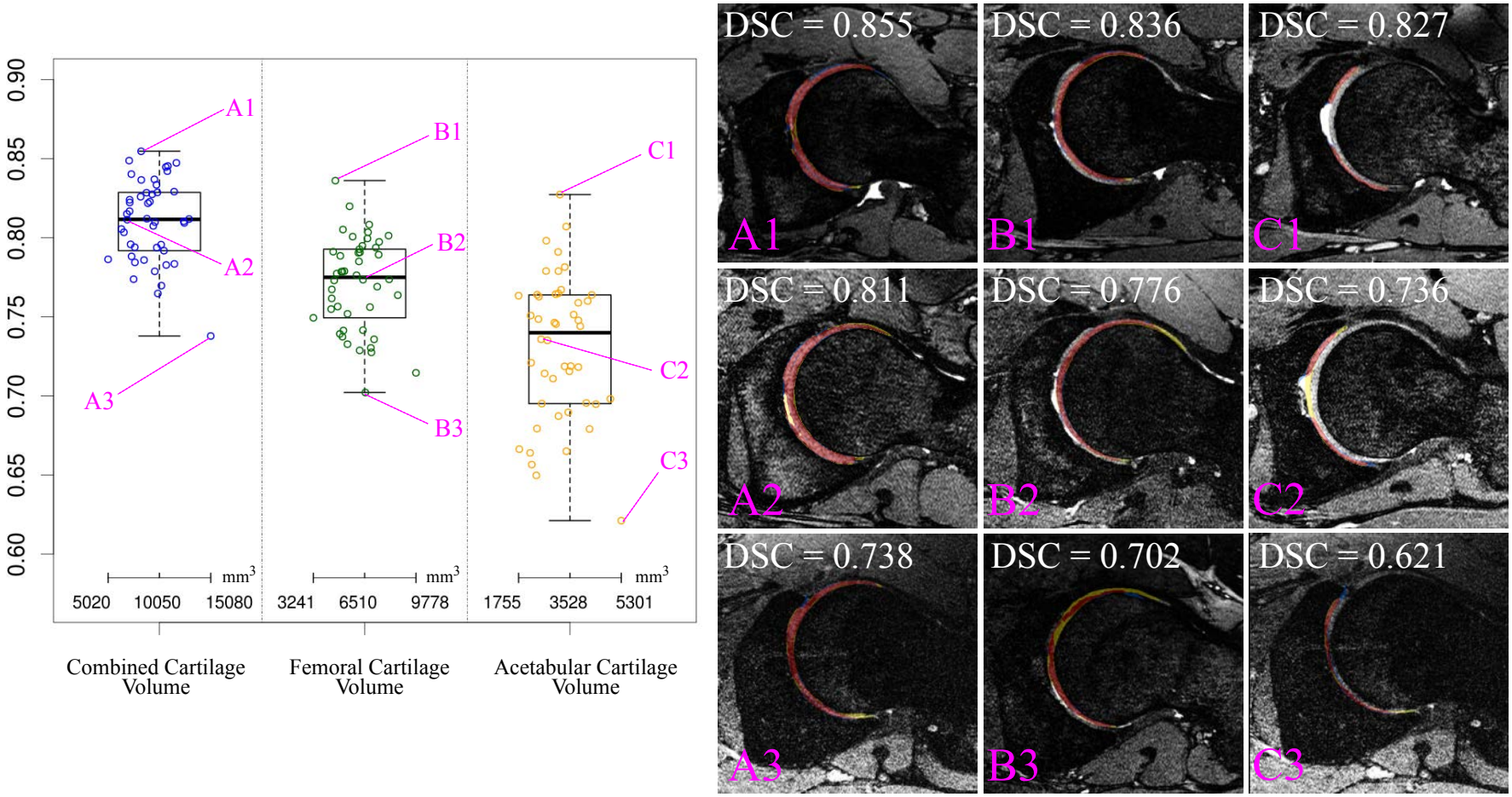

Figure 5.7: Boxplots of validation results with example slices for maximum, median, minimum DSC values for the combined, femoral and acetabular cartilage volumes (red - region in common, yellow - only in manual segmentations, blue - only in automatic segmentations).

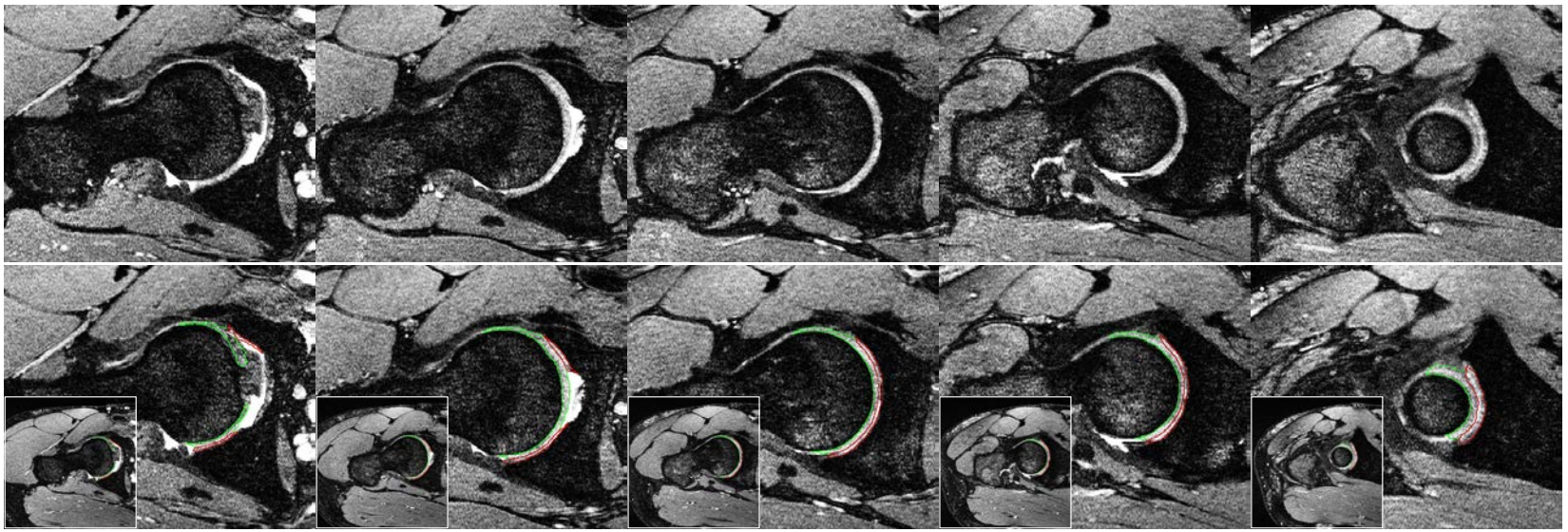

(a)

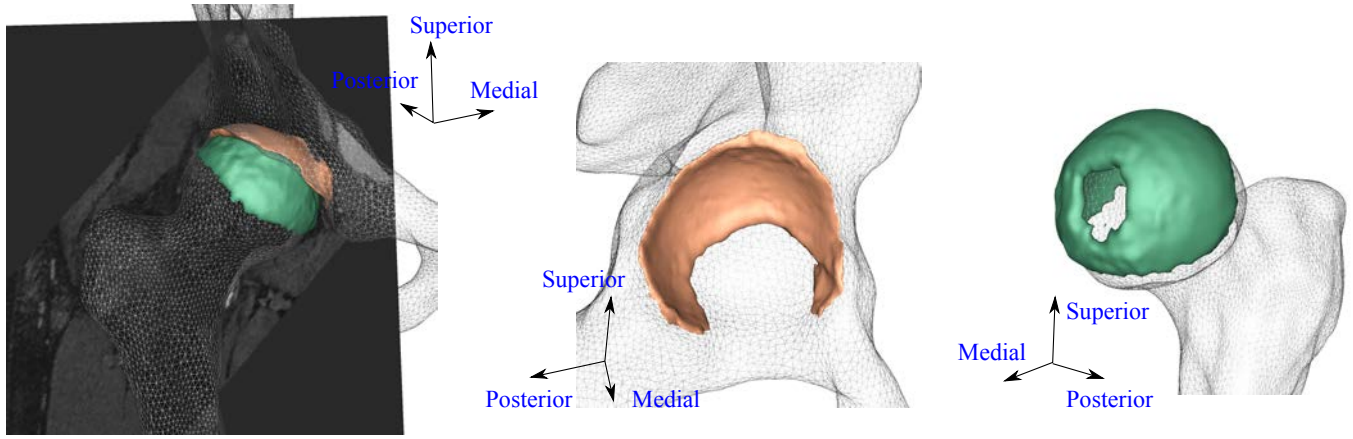

(b)

Figure 5.8: (a) 2D MR slices (top) with overlaid cartilage segmentations (bottom) (green - femoral cartilage, red - acetabular cartilage) and (b) 3D visualization of smoothed cartilage volumes (green - femoral cartilage, orange - acetabular cartilage) with the reference of (proximal femur, acetabulum) bone surfaces obtained from an example automatic segmentation results around the mean DSC of (0.79, 0.76, 0.74) for the (combined, femoral, acetabular) cartilage.

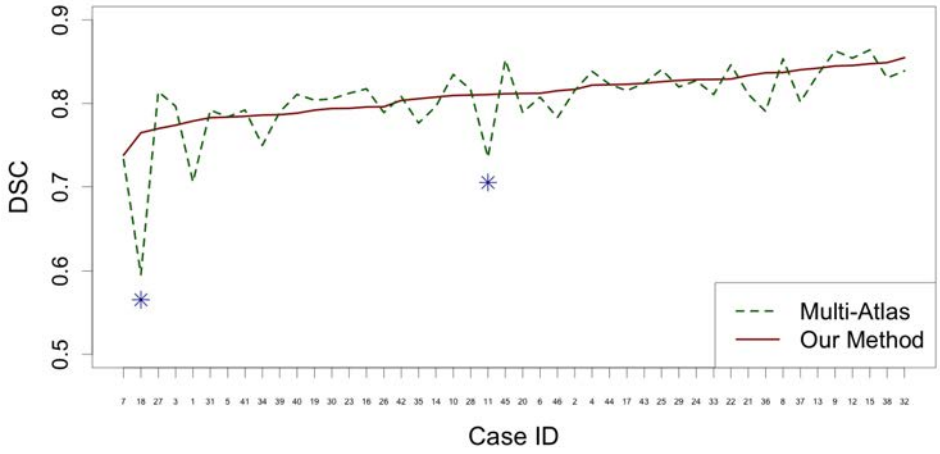

(a)

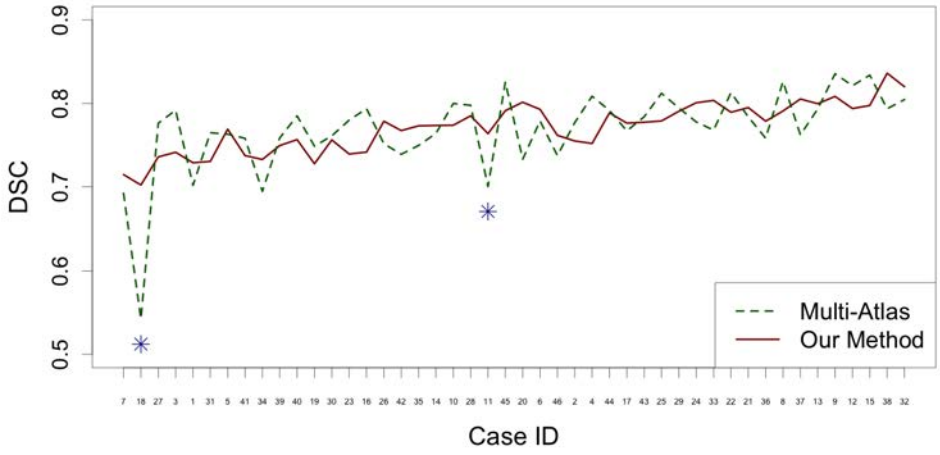

(b)

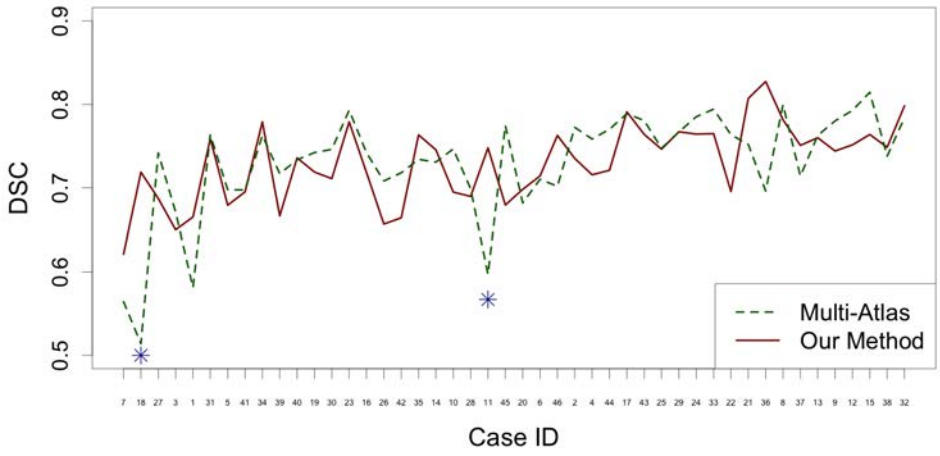

(c)

Figure 5.9: DSC results for segmentation of the (a) combined, (b) femoral and (c) acetabular cartilages obtained using the multi-atlas-based method (dashed line) and our proposed method. The results are sorted based on DSC scores of the combined cartilage segmentations from our approach (Asterisk symbols indicate cases with an evident drop of the DSC value using the multi-atlas-based method).

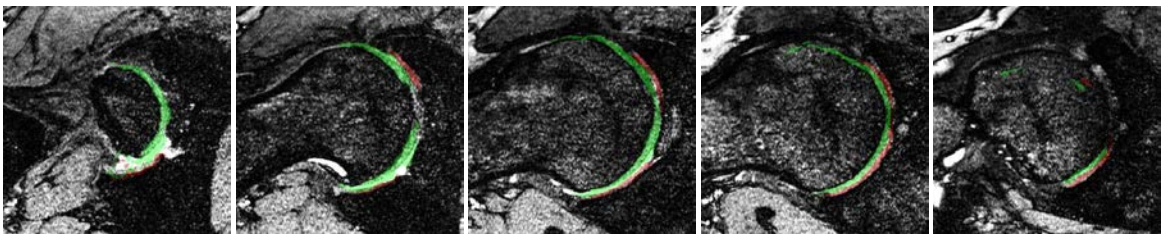

DSC(Combined, Femoral, Acetabular) = (0.60, 0.54, 0.51)

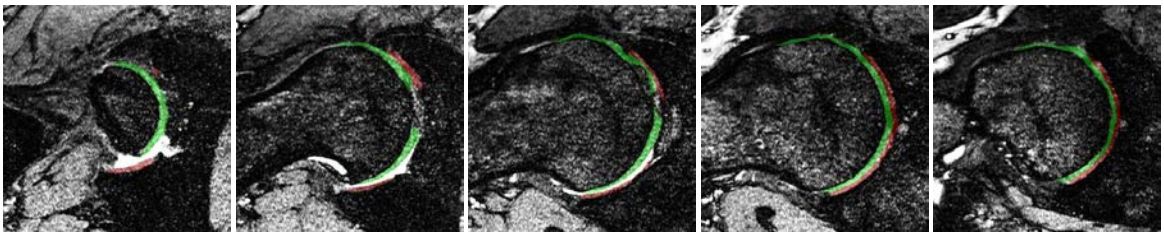

DSC(Combined, Femoral, Acetabular) = (0.76, 0.70, 0.72)

(a) Case 18

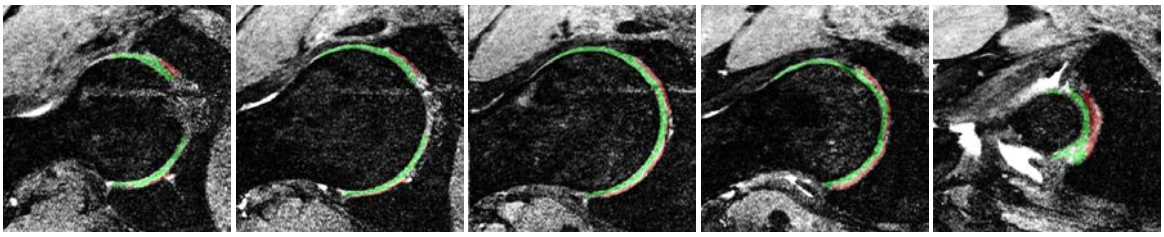

DSC(Combined, Femoral, Acetabular) = (0.74, 0.70, 0.60)

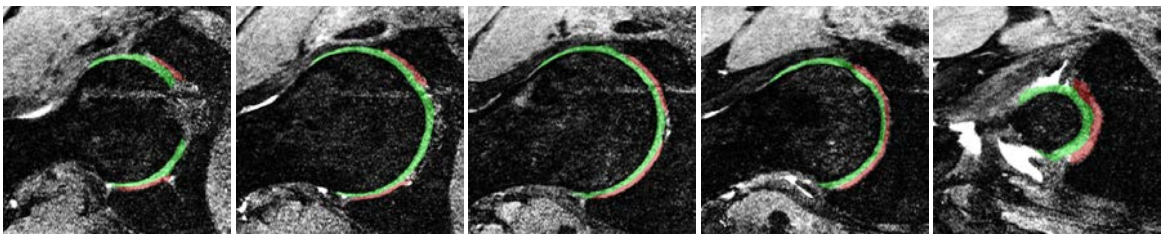

DSC(Combined, Femoral, Acetabular) = (0.81, 0.76, 0.75)

(b) Case 11

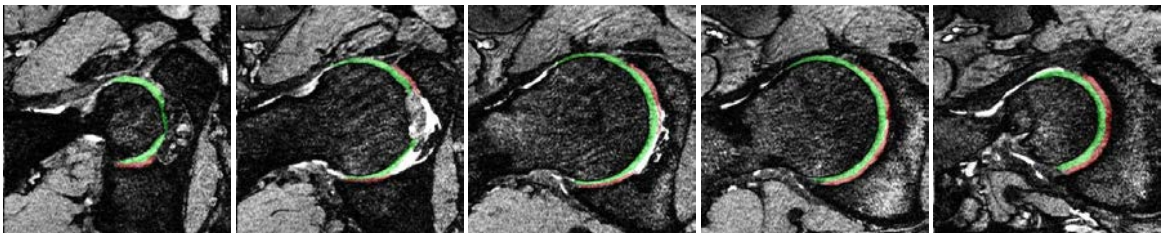

DSC(Combined, Femoral, Acetabular) = (0.85, 0.83, 0.77)

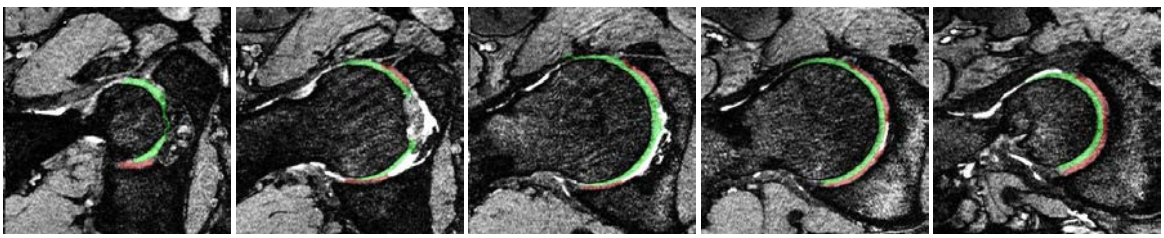

DSC(Combined, Femoral, Acetabular) = (0.81, 0.79, 0.68)

(c) Case 45

Figure 5.10: Overlaid segmentations for (a) case 18, (b) case 11 and (c) case 45 obtained using (top) the multi-atlas-based method and (bottom) our proposed method.

6

QUANTITATIVE ANALYSES OF THE CARTILAGES AND ITS REPRODUCIBILITY

This chapter presents the work to attain **Aim 2.2**, which is to perform quantitative measurements of the segmented femoral and acetabular cartilages within the hip joint from high-resolution 3D MR images.

Quantitative measurements and subregional analyses for the cartilage morphology (i.e., volume, thickness) is performed based on automatic cartilage segmentation volumes obtained from MR images of the hip joint using the graph-based segmentation scheme in Chapter 5. Quantitative results are compared between manual and automatic cartilage segmentation results of 3D TrueFISP images from 46 volunteer subjects. Subregional analyses are performed within the majority of the weight-bearing regions for the individual femoral and acetabular cartilage plates, where seven clinically-defined subregions were automatically identified and evaluated using quantitative volume and thickness measurements. In addition, the reproducibility of quantitative analyses is evaluated using unilateral 3D DESS and SPACE examinations from the subset of 18 subjects.

In this chapter, the work on volume and thickness measurements was included in the publication of (Xia et al. 2014), which presented initial quantitative measurement results based on a subset of TrueFISP images from 26 subjects.

Related publication details

Xia, Y., Chandra, S. S., Engstrom, C., Strudwick, M. W., Crozier, S., and Fripp, J. (2014). Automatic hip cartilage segmentation from 3D MR images using arc-weighted graph searching. *Physics in Medicine and Biology*, 59(23):7245. http://stacks.iop.org/0031-9155/59/i=23/a=7245 (Xia et al. 2014)

Manuscript revision history

Submitted to *Physics in Medicine and Biology*	11 April 2014
Interim decision (moderate revision)	19 August 2014
Revision submitted	15 September 2014
Accepted	3 October 2014
Published	10 November 2014

6.1 Introduction

Quantitative analyses of the cartilage morphology (i.e., thickness, volume, surface areas) that fully exploit the 3D nature of MR imaging techniques, represent a powerful tool in cartilage and OA investigations (Li et al. 2008; Nishii et al. 2004). Compared with clinically used radiographic scoring methods, quantitative analyses of the hip joint cartilage can be more objective and less observer-dependent (Roemer et al. 2011). This allows relatively small structural alterations in the cartilage to be detected over time while these changes might not be apparent to the human eye. In particular, subregional morphological analyses of cartilage can detect and monitor subtle structural changes during the pathological process with better sensitivity and specificity, which therefore provide an indepth understanding of the cartilage degeneration across different subregions (Carballido-Gamio et al. 2008b; Subburaj et al. 2013).

However, to be of value in clinical applications, the fulfilment of quantitative analyses requires the cartilage to be segmented with a high level of reliability and reproducibility, which was previously achieved using manual and semi-automatic approaches (Cicuttini et al. 2000; Li et al. 2008; Mechlenburg et al. 2007; Naish et al. 2006; Zhai et al. 2005). The cartilage thickness of the hip joint was initially measured in (Hodler et al. 1992) from 1.5T coronal and sagittal fat-suppression spin-echo MR images of ten cadavers. Due to problems encountered with an imprecise delineation of the BCI, limited spatial resolution (0.46 mm with slice thickness 3 mm) and insufficient tissue contrast between the cartilage and joint fluid, the method was insufficiently accurate to be of value in clinical practice. Cicuttini et al. (2000) measured the volume of the femoral head cartilage based on 3D rendering from disarticulation contours that were manually delineated on each slice of 1.5T 3D fat-suppressed SPGR images. In the dataset of 10 hip specimens, the cartilage volume was found ranged from 1.8 ml to 7.8 ml, which had the average 12% over- or under-estimation in comparison to the results measured by the dissection and volume displacement. A similar technique was used to manually determine the volume and thickness of the femoral head cartilage from MR images of 151 subjects randomly selected from an older adult cohort study (Zhai et al. 2005). Moreover, Mechlenburg et al. (2007) evaluated three stereologic methods of manual thickness measurement for the hip joint cartilage on 3D FLASH images, and indicated the superiority of the measurement method based on the center of the femoral head.

Nakanishi et al. (2001) utilized semi-automatic 3D visualization techniques to measure the cartilage thickness and to evaluate the entire femoral cartilage between SPGR images of 10 normal volunteers and 5 patients with advanced OA or osteonecrosis. Naish et al. (2006) reported a good test-retest coefficient of variation (CoV) of 2.5% using a semi-automatic livewire-based method to determine the thickness of the combined hip joint cartilage, which was promising for reproducible quantitative assessment of hip cartilage thickness in longitudinal studies. More recently, semi-automatic segmentation of the individual acetabular and femoral cartilage plates of the hip was first reported on 1.5T MR images (in-plane resolution 0.5 mm, 3 mm slice thickness) using a 2D MEDIC sequence with no use of continuous leg traction (Li et al. 2008). In this noninvasive system, good reproducibility was obtained for the global, femoral and acetabular cartilage volume with the root mean square CoV of

3.3%, 3.6% and 5.6% comparable to the data in the literature; however, for the hip cartilage subregion (inferior, anterior, superior and posterior) analysis, less repeatability was noted with the F statistic (ANOVA) of 0.969 ($p = 0.38$) for independent effects and 0.736 ($p = 0.78$) for interaction effects.

The disadvantages of these manual and semi-automatic approaches are that they are time-consuming (e.g., 1 hour per image for the livewire-based semi-automatic method (Naish et al. 2006), 3 hours per SPACE scan for manual cartilage segmentation (Chandra et al. 2015b)) and require skilled operators with significant experience. These would become problematic for potential research and clinical application in large prospective early and pre-OA studies to evaluate potential imaging biomarkers.

In this chapter, it is assumed that 3D MR image is an accurate representation of the cartilages and allows reliable and reproducible quantitative analyses (e.g., volume, thickness) to be performed using automatic segmentations of the individual femoral and acetabular cartilage plates. Therefore, we aim:

1. to perform quantitative volume and thickness measurements based on automatic cartilage segmentations from 3D TrueFISP examinations of 46 subjects, which are compared with measurements from the corresponding manual segmentations;
2. to carry out preliminary analyses of the subregional cartilage morphology, particularly at the weight-bearing regions of the individual acetabular and femoral cartilage plates;
3. to evaluate the reproducibility of the proposed segmentation and quantitative analysis scheme for the hip joint using various MR acquisition protocols. This is achieved using MR examinations with 3D DESS and SPACE sequences in a subset of 18 subjects.

6.2 Materials and Methods

6.2.1 Data acquisition

TrueFISP, DESS, SPACE images

An MR dataset of 3D high-resolution TrueFISP examinations acquired from 46 volunteer subjects introduced in Chapter 5 was used for the subsequent quantitative analyses of the hip joint cartilage. Additionally, a subset of 18 subjects were imaged using another two different MR sequences,3D T2w DESS and 3D fat-suppressed proton density weighted (PDw) SPACE, with a lower image resolution to investigate the reproducibility of our proposed MR-based segmentation and quantitative analysis scheme. The parameters for each imaging sequence are listed in Table 2.1. Example coronal slices of TrueFISP, DESS and SPACE images acquired from the same subject are shown in Figure 6.1.

SPRI clinical SPACE and T2 mapping images

Another MR dataset provided by the Steadman Philippon Research Institute (SPRI) (Vail, Colorado, USA) as per Chandra et al. (2015b); Ho et al. (2014), was used in this chapter to obtain the prior information of clinically-defined anatomical subregions for the individual femoral and acetabular cartilage plates. This dataset consists of 24 anonymized volunteers (12 males and 12 females, aged 23-34 years, body masses 53-151 kg) enrolled in an asymptomatic study after subjective scoring, objective

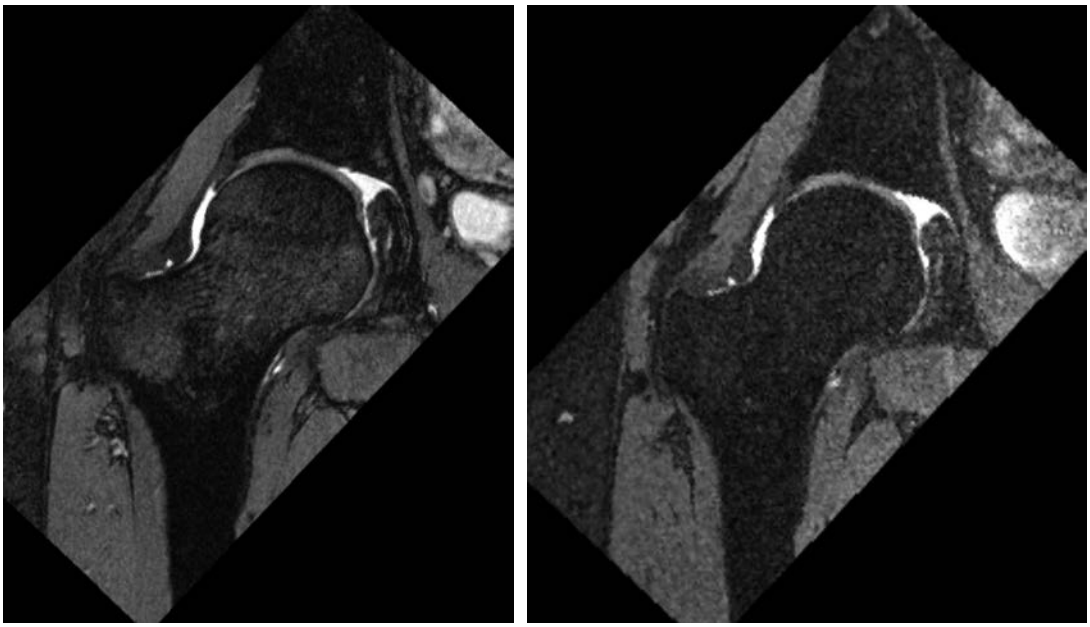

(a) (b)

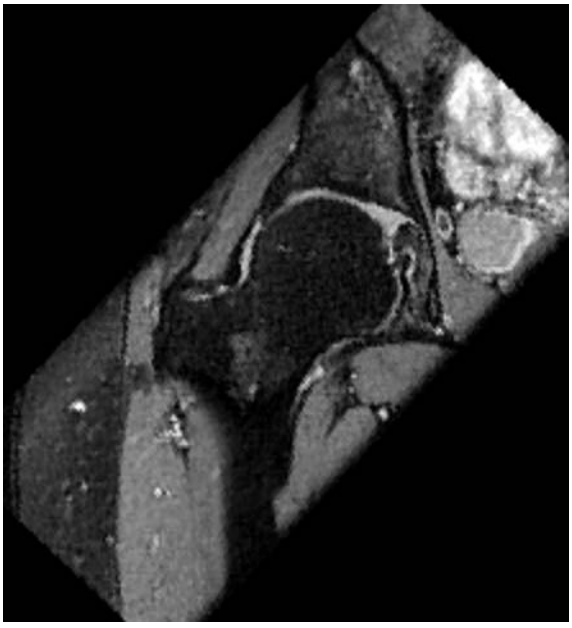

(c)

Figure 6.1: Example coronal slices of MR images acquired from the right-side hip joint of the same subject with three different sequences: (a) TrueFISP, (b) DESS and (c) SPACE.

clinical examinations and radiological evaluation using the Hip Osteoarthritis MRI Scoring System (HOAMS) (Roemer et al. 2011). MR acquisition was performed on a clinical 3T scanner (Magnetom Verio, Siemens Healthcare, Germany) using a large 4-channel matrix coil with volunteers positioned supine during scanning.

All the volunteers were imaged using a 3D fat-suppressed PDw SPACE sequence (acquisition time: 8 min, TR/TE: 1500/44 ms, flip angle: 120°, voxel size: 0.75 × 0.75 × 0.9 mm, acquisition matrix: 256 × 256 and FOV: 19.2 × 19.2 cm) and a multi-echo spin-echo T2 mapping sequence (MESE T2 Map SAG; acquisition time: 6.45 min TR/TE: 2080/18-90 ms, flip angle: 180°, voxel size: 0.78 ×

0.78 × 2.0 mm, FOV: 20 × 20 cm).

Manual segmentation and analyses

All TrueFISP examinations acquired from 46 volunteers were manually segmented by Dr. Mark W Strudwick (an experienced radiographer) to produce labelled images for the individual femoral and acetabular cartilage plates (see Chapter 5). No manual segmentation was performed on the DESS and SPACE scans due to segmentation difficulties related to the decrease in SNR and insufficient image contrast, particularly poor/no delineation between the two cartilage plates (see Figure 6.1).

In the SPRI dataset, all MR examinations (N = 24) using the T2 mapping sequence were manually segmented on a slice-by-slice basis using a stylus and touch screen monitor and Mimics software (Materialise, MI, USA) by a trained musculoskeletal radiologist under the expert supervision of Dr. Charles Ho. Manual segmentation was performed only on the regions of high confidence for both the femoral and acetabular cartilage plates. Meanwhile, the corresponding 3D SPACE images were simultaneously examined on an adjacent monitor in order to identify areas of synovial fluid and chemical shift artefact. All manual segmentations of cartilage were imported into a custom Matlab program (Mathworks, MA, USA) to generate regional analyses for 12 anatomical partitions using manually defined landmarks considered clinically noteworthy (see Figure 6.2a). In this study, seven high confidence superior regions within the weight-bearing regions of the articulating surfaces were chosen from these partitions for quantitative analyses, which include three acetabular and four femoral partitions (the femoral superior neck partition was further divided into two regions). The inferior regions of both femoral and acetabular plates were omitted from the current analyses, which are likely to be inconsistent in T2 manual delineations across the current dataset due to the large slice thickness and variability of the thinner cartilages in these regions. An example of manual cartilage segmentations from the T2 mapping scans is shown in Figure 6.2b with the color map indicating the coverage of each superior region of high confidence that will be considered in this chapter.

6.2.2 Quantitative analyses

Cartilage volume

The cartilage volume is commonly measured as a direct numerical integration of the voxels attributed to each segmented cartilage partition, which are used to indicate the global cartilage loss to a certain degree. The volume calculation is performed on the raw voxelization of the segmented 3D volumes for the combined, femoral and acetabular cartilages, respectively.

Cartilage thickness

The cartilage thickness for each cartilage plate is commonly defined as the distance between its bone-cartilage (inner) interface and cartilage-synovial (outer) interface (Li et al. 2008). In this chapter, the center of the femoral head is firstly estimated using a joint locator (Nishii et al. 2004) and serves as a reference landmark for measuring the cartilage thickness at each vertex of the BCI surface, which aims to mitigate PVE since the cartilage surface is intersected perpendicularly with the line from the femoral

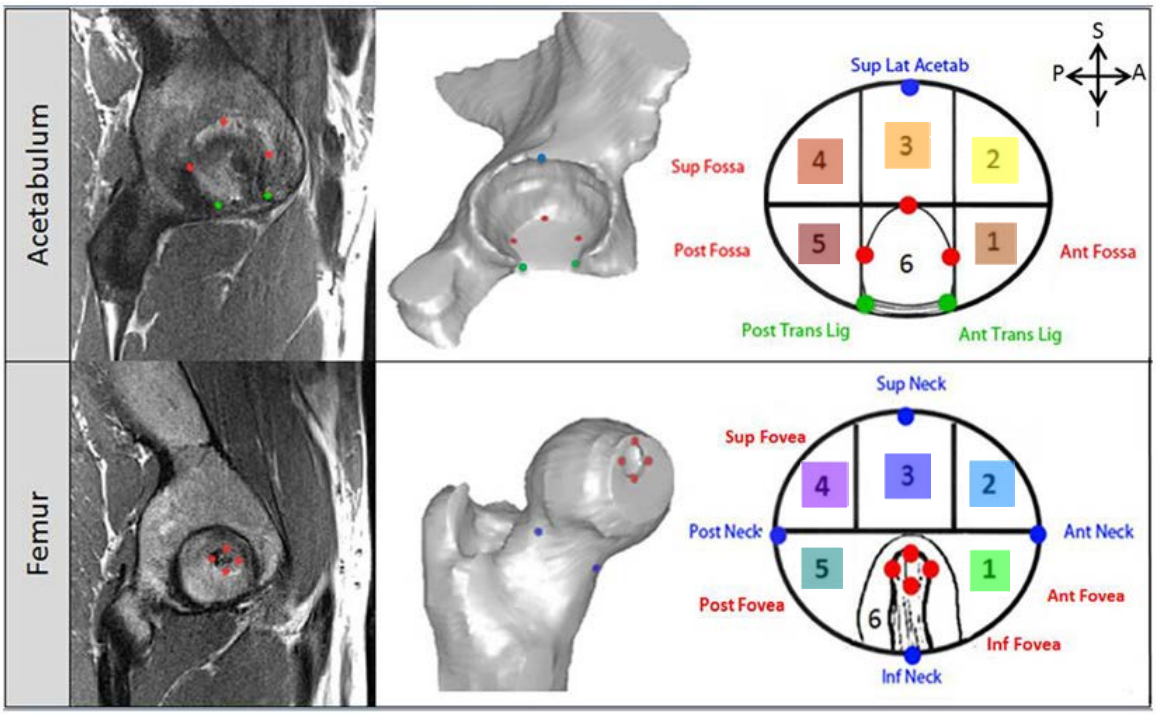

(a)

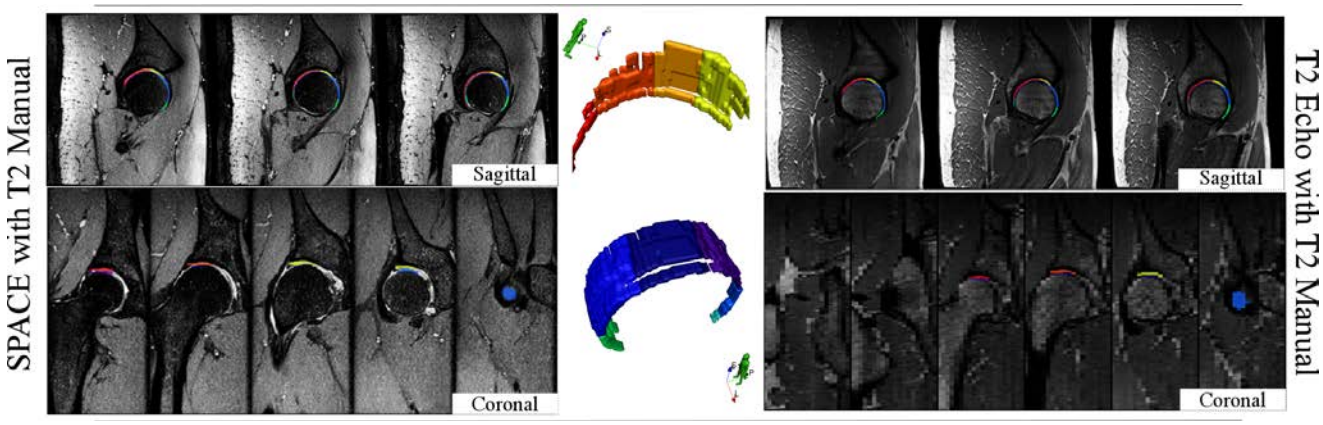

(b)

Figure 6.2: (a) Partitioned regions with associated regional descriptors for the (top) acetabular and (bottom) femoral cartilages of the hip joint based on manual landmarks (red dots), which were illustrated using a 3D innominate bone volume from the left-side hip joint and a bone volume of proximal femur from the right-side hip joint, respectively; (b) Example manual cartilage segmentation overlaid on both the (left) 3D SPACE and (right) T2 echo as slices of the 3D image volume. (Used with permission from (Chandra et al. 2015b; Ho et al. 2014))

head center (Mechlenburg et al. 2007). At each BCI vertex, a one-directional grey-value profile with the sampling spacing of 0.125 mm is extracted from the voxelization of cartilage segmentations along the direction from the femoral head center to this vertex (see Figure 6.3). The cartilage thickness of each cartilage plate at this vertex can be measured as the distance of intersection positions with the corresponding outer and inner interfaces (i.e., the distance between A and B, the distance between B and C in Figure 6.3), which are found by one-directional profile searching in the labelled image of cartilage segmentations.

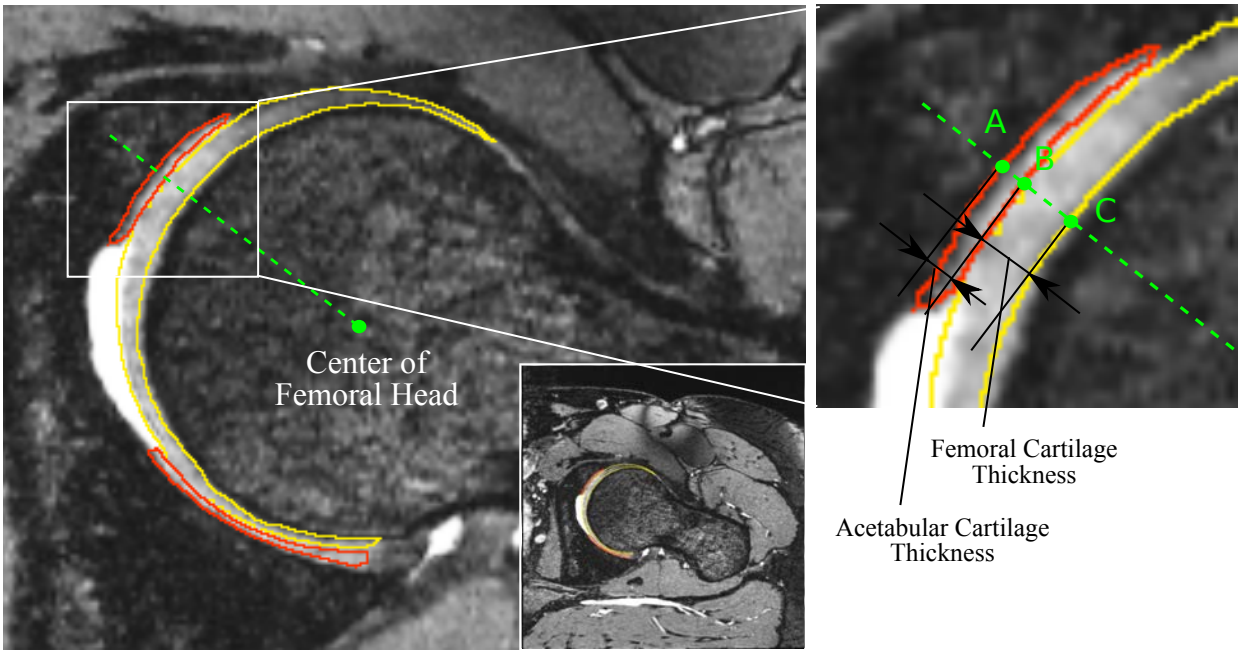

Figure 6.3: Cartilage thickness measurement illustrated on an example 2D slice overlaid with manual cartilage contours. The example slice is assumed to go through the estimated center of the femoral head. Point A, B and C are the intersection points on the dashed line from the femoral head center with the inner acetabular cartilage interface, the outer acetabular cartilage interface (or outer femoral cartilage interface) and the inner femoral cartilage interface, respectively. The cartilage thickness is measured as the distance between A and B for the acetabular cartilage plate, between B and C for the femoral cartilage plate.

Subregional analyses

Atlases with a scalar field of maximum likelihood for each cartilage subregion are firstly trained for the individual femoral and acetabular cartilage plates using the SPRI 3D SPACE dataset with the related manual cartilage delineation and partitioning. This offline training process has been detailed in the work of Chandra et al. (2015b). Briefly, 3D-SPACE images were first automatically segmented to obtain triangulated surfaces of the proximal femur and innominate bone with the point-wise correspondences using the ASM-based bone segmentation method (Chapter 3). On the other hand, T2 map manual delineations of the acetabular and femoral cartilage plates were rigidly aligned to the corresponding 3D SPACE images. The spatial statistics and extents of the individual partitioned regions from these propagated manual segmentations were determined using surface registration with the contoured regions being extracted from the propagated T2 maps as scalar fields using a closed form registration algorithm (Gower 1975). The regional scalar fields were then superimposed to the segmented bone surfaces and averaged to obtain the partition map of maximum likelihood for each subregion, which is used to segment the individual subregions of the cartilages.

In this chapter, the trained cartilage partition maps of the femoral and acetabular cartilage plates are used to further partition automatic segmentation volumes from TrueFISP images into 12 clinically-defined subregions. As the cartilage coverage of manual segmentations from TrueFISP images (see Chapter 5) is different from manual delineations of SPRI T2 mapping scans and the partitioned inferior regions of both cartilage plates in T2 mapping delineations are highly inconsistent, only seven

high-confidence cartilage regions at the weight-bearing regions are investigated, which included the anterior-superior (*AceAntSupFossa*), mid-superior (*AceSupLat*) and posterior-superior (*AcePostSupFossa*) zones of the acetabular cartilage plate, and the anterior-superior (*FemSupAntFovea*), mid-superior-anterior (*FemSupNeckAnt*), mid-superior-posterior (*FemSupNeckPost*) and posterior-superior (*FemSupPostFovea*) zones of the femoral cartilage plate.

For all these seven subregions, cartilage volume and thickness measurements are both performed in subregional analyses of automatic cartilage segmentations from 46 TrueFISP images. The significance of differences in thickness measurements for various subregions of each individual cartilage plate is investigated using one-way ANOVA analyses followed by Tukey's honestly significant difference (HSD) tests.

6.3 Results

6.3.1 Quantitative analyses on TrueFISP images

Quantitative analyses (i.e., volume, thickness and subregional analyses) were performed using automatic segmentations of the individual femoral and acetabular cartilages obtained from 46 3D TrueFISP images using the proposed graph-based segmentation scheme (see in Chapter 5). Although there was no ground truth available for direct validation of these cartilage volume and thickness measurements, the morphological data obtained from the related manual cartilage segmentations were considered as ground truth for validation of the volume and thickness measurements.

Cartilage volume

The mean volumes for manual and automatic segmentations of the combined cartilage within the hip joint from all TrueFISP examinations of 46 subjects were 9572 and 9182 mm^3. For each individual cartilage plate, the mean volumes of manual and automatic segmentations were 6354 and 6018 mm^3 for the femoral cartilage, and 3218 and 3164 mm^3 for the acetabular cartilage.

There were strong positive correlations between manual and automatic segmentation volumes for the combined (Pearson's correlation coefficient $r = 0.92$, $p < 0.001$), femoral ($r = 0.86$, $p < 0.001$) and acetabular ($r = 0.92$, $p < 0.001$) cartilages (Figure 6.4a-6.4e). From the Bland-Altman analyses in Figure 6.4b-6.4f, the automated data for the combined, femoral and acetabular cartilage volumes had a mean ($\pm$ SD) volume difference error of -3.03% ($\pm$ 9.05), -3.97% ($\pm$ 11.46) and -0.45% ($\pm$ 10.72) indicating a slight under-segmentation of the femoral cartilage volume and thereby the combined cartilage volume.

Cartilage thickness

Figure 6.5a illustrates the average thickness maps for the femoral and acetabular cartilage plates obtained from automatic segmentations of 3D TrueFISP images in 46 subjects. Compared to Figure 5.3b, the absolute thickness difference maps against manual cartilage segmentations demonstrate highly

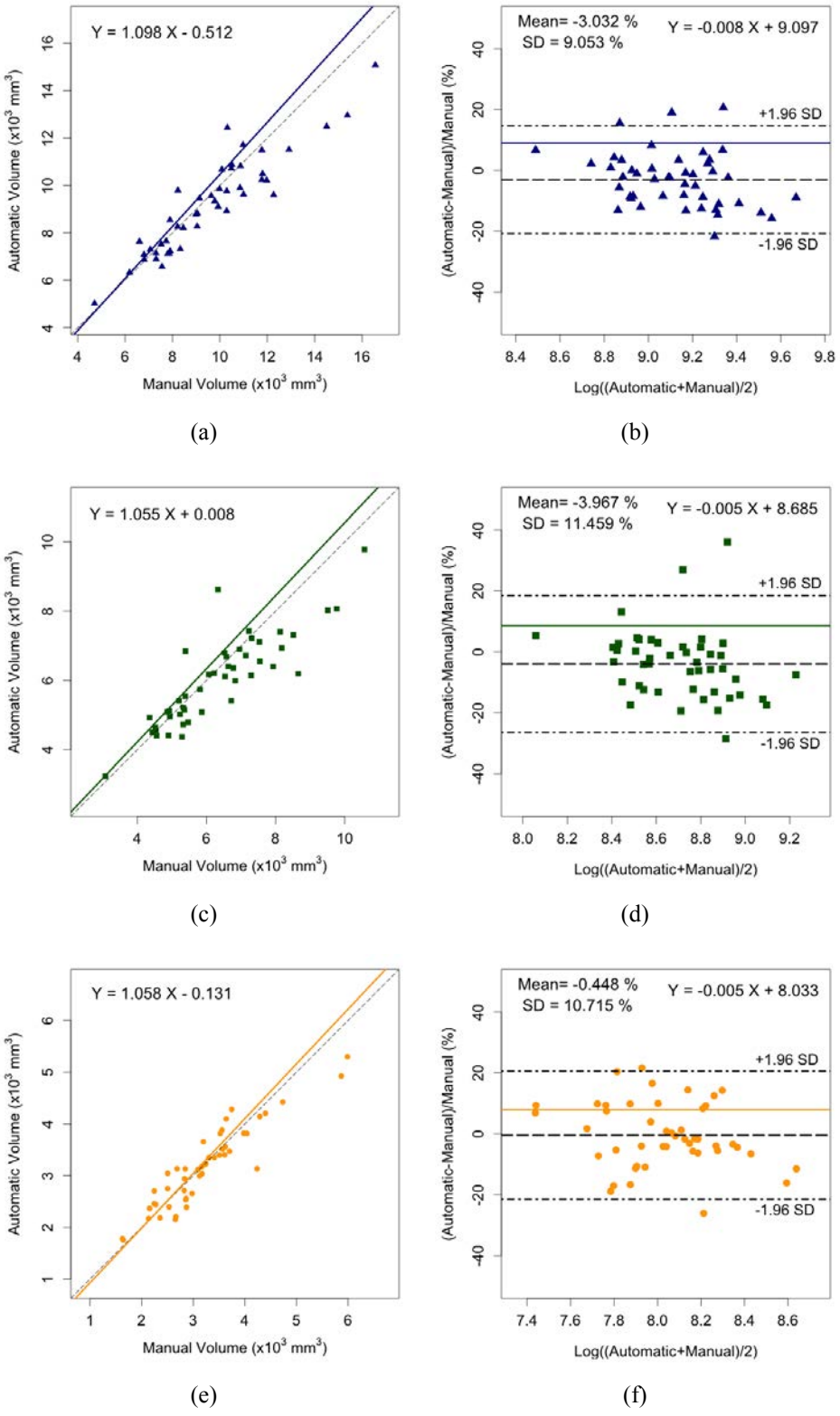

Figure 6.4: Comparative analyses between automatic and manual cartilage volume data:(left) scatter plots with linear regression lines and (right) Bland-Altman plots of volume segmentations for the (a, b) combined, (c, d) femoral and (e, f) acetabular cartilages. Segmentations of the combined and individual femoral and acetabular cartilage volumes were from all TrueFISP images of 46 subjects.

consistent thickness patterns (i.e., the absolute difference < 0.2 mm) within the majority of the articulating surfaces of the femoral and acetabular plates (see Figure 6.5b). However, the cartilage areas

near the fovea of the femoral head and the fossa of the acetabulum were mis-classified with an absolute thickness difference above 0.4 mm, which correspond to the attachment site of the ligamentum teres; this anatomically variable intra-capsular ligament has a similar signal intensity profile to the adjacent cartilage tissue.

A quantitative comparison of the computed average cartilage thickness maps (Figure 6.5) was performed within the majority of the articulating surfaces for both cartilage plates (defined as the vertices with probabilities of having the cartilage tissue > 90% in the articular cartilage model, see Figure 5.3a). Within the defined ROI, the thickness statistics were in a good agreement between manual and automatic segmentations for both cartilage plates with a mean ($\pm$ SD) thickness of 1.53 mm ($\pm$ 0.32) and 1.51 mm ($\pm$ 0.32) for the femoral plate, and of 1.40 mm ($\pm$ 0.25) and 1.40 mm ($\pm$ 0.24) for the acetabular plate (Table 6.1). The absolute mean differences between the manual and automatic thickness values were 0.13 mm ($\pm$ 0.12) and 0.09 mm ($\pm$ 0.06) for the femoral and acetabular cartilages, respectively. Strong positive correlations were found between manual and automatic thickness maps within the ROI for the femoral ($r = 0.85$) and acetabular ($r = 0.89$) thickness distribution.

Subregional analyses

An example of automatic segmentation volumes in various subregions for the acetabular and femoral cartilage plates are provided in Figure 6.6. Table 6.2 summarizes subregional quantitative results of volume and thickness measurements for all seven clinically-defined partitions at the weight-bearing regions of the acetabular and femoral cartilage plate using automatic cartilage segmentations from the 3D TrueFISP dataset. For the acetabular cartilage plate, the anterior-superior subregion (*AceAntSupFossa*) was found to have the largest cartilage volume (an average volume of 869.82 mm^3) and the thickest cartilage layer (an average thickness of 1.18 mm), which is sequentially followed by the mid-superior (*AceSupLat*) (an average volume: 632.66 mm^3, an average thickness: 1.13 mm) and posterior-superior (*AcePostSupFossa*) subregions (an average volume: 581.52 mm^3, an average thickness: 0.93 mm). The anterior-superior (*FemSupAntFovea*) zone of the femoral cartilage plate had a larger cartilage volume size (1906.29 $\pm$ 357.49 mm^3) and a thicker cartilage layer (1.30 $\pm$ 0.12 mm) than the other three subregions. Due to further subdivisions of the mid-superior subregion (i.e., mid-superior-anterior and mid-superior-posterior), the volumes for these two subdivided partitions, *FemSupNeckAnt* and *FemSupNeckPost*, were relatively small with average sizes of 539.99 and 669.73 mm^3, respectively. An average thickness difference of 0.2 mm was found between these two subregions of *FemSupNeckAnt* (1.26 $\pm$ 0.20 mm) and *FemSupNeckPost* (1.04 $\pm$ 0.17 mm). The cartilage layer at the posterior-superior (*FemSupPostFovea*) subregion was thinnest among these four femoral subregions, which had an average thickness of 0.95 mm ($\pm$ 0.12).

Figure 6.7 shows boxplots for average cartilage thickness values for all 46 cases at different subregions of the acetabular and femoral cartilage plates measured from automatic segmentations of unilateral TrueFISP images. Significant differences were found when comparing the partitioned subregions for the individual femoral (one-way ANOVA, $F = 52.58$, $p < 0.001$) and acetabular (one-way ANOVA, $F = 21.73$, $p < 0.001$) cartilage plate. The anterior-superior subregion (*Region-4* in Figure 6.7a) had a significantly thinner cartilage layer (Tukey's HSD $p < 0.001$) than the other two

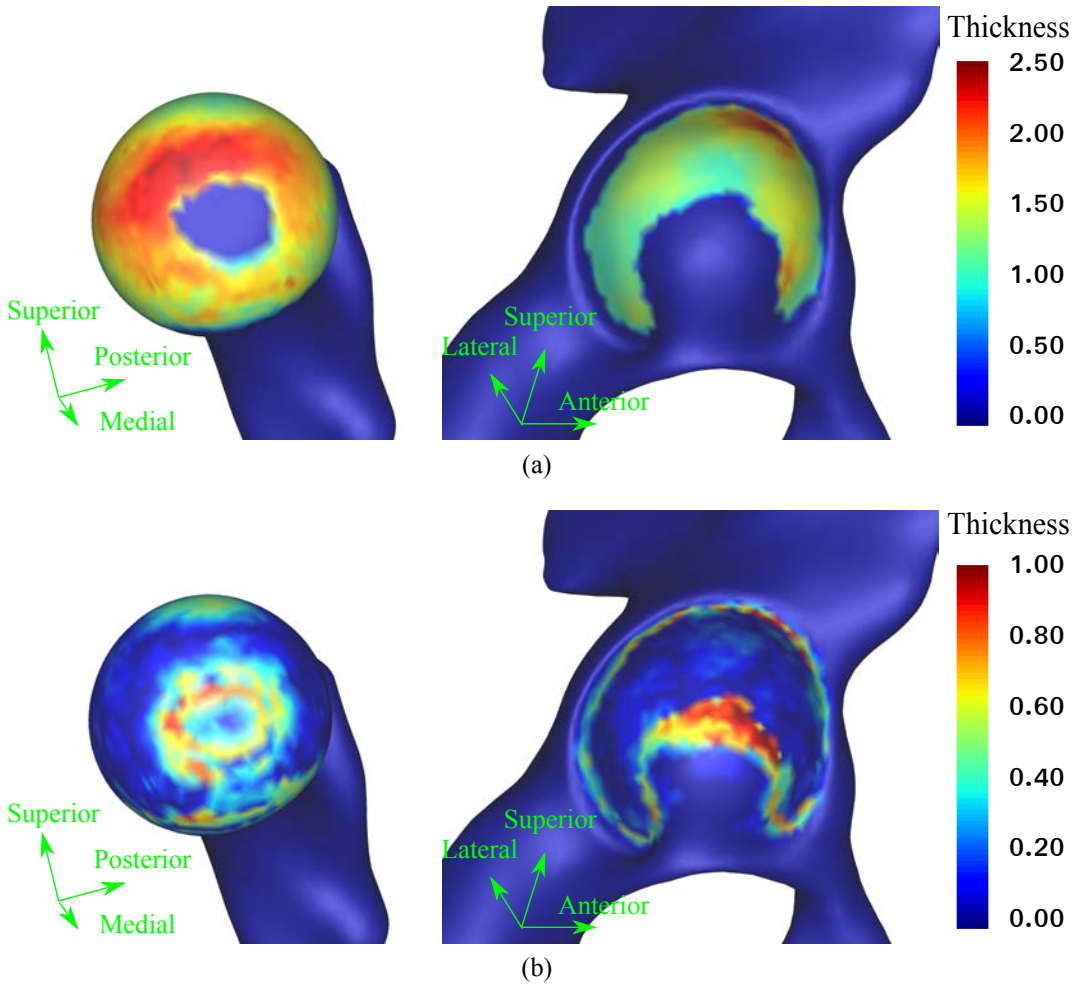

Figure 6.5: Cartilage thickness maps:(a) average thickness with color scale (0 - 2.5 mm) for automatic segmentations and (b) absolute thickness difference against manual segmentations from the set of 46 TrueFISP images with color scale (0 - 1.0 mm) for the femoral and acetabular cartilage.

subregions (*Region-2* and *Region-3* in Figure 6.7a) of the acetabular cartilage plate. For the femoral cartilage plate, the cartilage layer at both the anterior-superior and mid-superior-anterior partitions (*Region-2* and *Region-3a* in Figure 6.7b) was significantly thicker (Tukey's HSD, $p < 0.001$) than that of the mid-superior-posterior and posterior-superior partitions (*Region-3b* and *Region-4* in Figure 6.7b). Moreover, the cartilage thickness at the mid-superior-posterior subregion was found to be significantly larger (Tukey's HSD, $p < 0.001$) than that of the posterior-superior subregion.

6.3.2 Reproducibility: DESS and SPACE images

To investigate the reproducibility of our proposed cartilage segmentation and quantitative analysis scheme in various MR sequences and relatively lower image resolution quantitative (volume, thickness) measures for unilateral DESS and SPACE scans of the same subject were calculated using the related automatic segmentation volumes of the femoral and acetabular cartilages. Figure 6.8 provides a qualitative comparison of automatic segmentations from different MR examinations of the same subject using TrueFISP, DESS and SPACE sequences, which demonstrates similar delineation results of the individual femoral and acetabular cartilage plates for these MR scans. However, due to a

Table 6.1: Cartilage thickness (mm) statistics within the majority of the articulating surfaces for the femoral and acetabular cartilage plates obtained from manual and automatic segmentations of all 46 TrueFISP images.

	Femoral			Acetabular		
	Manual	Automatic	Difference*	Manual	Automatic	Difference*
Mean	1.530	1.509	-0.020	1.400	1.396	-0.004
SD	0.320	0.322	0.177	0.249	0.238	0.112
Min	0.875	0.845	-0.573	0.970	1.008	-0.248
Max	2.377	2.413	0.671	2.190	2.432	0.291

*The thickness difference is calculated at each vertex as the value of the automatic thickness subtracted from the manual measure.

lower resolution of 0.625 mm and 0.75 mm used for DESS and SPACE sequences, unfilled gaps were observed in 3D visualizations of segmentation volumes for these two sequences, particularly for 3D SPACE images and for the relatively thinner cartilage partitions, e.g., the acetabular posterior-superior and femoral posterior-superior subregions (see Figure 6.9).

Figure 6.10 illustrates a case-by-case comparison in volume measurements of the cartilage based on automatic segmentations of the combined, femoral and acetabular cartilages using three different MR sequences in the dataset of 18 subjects, where manual cartilage segmentation volumes of TrueFISP images were treated as the ground truth. For each cartilage partition, a similar trend across all 18 cases was observed, while in some cases, cartilage volumes were likely to be under-estimated using the SPACE sequence, e.g., case 5, 7 and 13, and to be over-estimated using the DESS sequence, e.g., case 10 and 18, in Figure 6.10. Similar findings were also observed in Figure 6.11, where, in the computed average thickness maps for the individual femoral and acetabular cartilage plates, the measured cartilage thickness values were comparatively largest using the DESS sequence and smallest using the SPACE sequence (see dashed circles in Figure 6.11).

6.4 Discussion

In this chapter, we have presented the work based on automatic segmentations of the individual femoral and acetabular cartilage plates within the hip joint, which aimed to deliver reliable and reproducible morphometric data in terms of the volume and thickness of the hip joint cartilage. The quantitative measurements obtained from automatic cartilage segmentation volumes in the TrueFISP MR dataset showed a good agreement with the results obtained using the corresponding manual segmentations. The Pearson's correlation coefficients were both over 0.86 for volume measurements of individual femoral and acetabular cartilage plates, and the absolute mean thickness differences of 0.13 and 0.09 mm within the majority of the articulating surfaces for the femoral and acetabular cartilage, respectively.

In the right-side hip joints from 46 healthy male subjects, the mean volumes of (9572, 6354, 3218) mm^3 and (9182, 6018, 3164) mm^3 were obtained from manual and automatic segmentations for the (combined, femoral, acetabular) cartilage plates. These are in general agreement with the findings

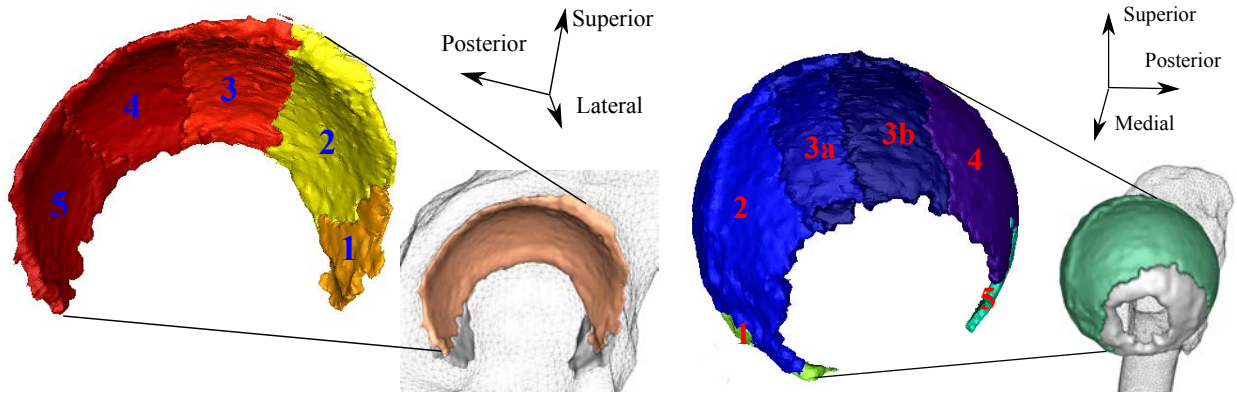

(a) (b)

Figure 6.6: Example 3D visualization of the segmented cartilage volumes with the partitioned regions (see Figure 6.2a) for the individual (a) acetabular and (b) femoral cartilage plates obtained from a 3D high-resolution TrueFISP image.

from the previous work using the state-of-the-art manual techniques despite study design differences in term of MR imaging protocols, sample sizes and disease state of participants. Zhai et al. (2005) reported a mean femoral head cartilage volume of 5.9 ml ($\pm$ 1.0) manually measured from 79 male subjects and 4.7 ml ($\pm$ 0.8) from 72 female subjects. In the recent work of Li et al. (2008), the average cartilage volumes were found to be 8106.3 ± 2370.9 mm^3, 3966.7 ± 1284.2 mm^3 and 4139.7 ± 1212.7 mm^3 respectively for the combined, femoral and acetabular cartilages.

For quantitative cartilage thickness measurements, high consistency was observed between the average thickness maps of manual and automatic cartilage segmentations within the majority of the articulating surfaces (see Figure 6.5). Within the defined ROI of cartilage tissue being present with high confidence (i.e., the probability > 90%), the average manual and automatic cartilage thickness measures were (1.53, 1.51) mm for the femoral and (1.40, 1.40) mm for the acetabular plate, where the mean absolute difference in cartilage thickness between manual and automated segmentations was $\sim$0.1 mm for both cartilage plates. In comparison, Li et al. (2008) reported that the cartilage thickness distribution (mean $\pm$ SD) was 0.93 ± 0.15 mm for the femoral and 1.09 ± 0.13 mm for the acetabular plates semi-automatically determined from 2D MEDIC MR images. In 3D FLASH MR images from 26 adult patients with dysplastic hips, Mechlenburg et al. (2007) calculated the cartilage thickness using three different manual measurement approaches reporting a mean thickness range of 1.18 – 1.78 mm for the femoral and 1.15 - 1.46 mm for the acetabular cartilage. Additionally, Cheng et al. (2013) performed a simulation study on accuracy limits of cartilage thickness measurement using OA patients and reported the biases between MR-based measured and model-based simulated thicknesses within 0.12 mm.

From subregional quantitative analyses within the weight-bearing regions of the cartilage plates, we observed that both anterior-superior subregions of the opposing acetabular and femoral cartilage plates were covered by the thickest cartilage layer (1.18 ± 0.22 mm for the acetabular and 1.30 ± 0.12 mm for the femoral cartilage), which tallies with the common anatomical knowledge of regional thickness variation for the acetabular and femoral cartilages (Fagerson 1998) (see Figure 2.2). Significant differences in the cartilage thickness were found between different subregions of the individual

cartilage plate. For example, the cartilage thickness at the anterior-superior partition of the acetabular cartilage plate was significantly larger than that at the posterior-superior partition. Between the two partitions of the mid-superior region for the femoral cartilage plate, the mid-superior-anterior subregion had a thicker cartilage layer than the mid-superior-posterior subregion (see Figure 6.7).

Currently, more advanced techniques have been developed for the knee joint allowing point-wise intra- and inter-subject comparisons of the cartilage and further detect localized morphological changes in the knee cartilage (Carballido-Gamio et al. 2008a;c; Guo et al. 2015; Williams et al. 2003). For the hip joint, our preliminary work on subregional analyses of the hip joint cartilages showed great potential to effectively detect focal cartilage defects, to elucidate spatial pattern of cartilage thinning and to potentially identify subregions with increased rates of (and sensitivity to) cartilage loss in intervention trials. Furthermore, these subregional analyses can also be used jointly with biochemical MR imaging techniques (such as *d*GEMRIC, T1ρ, T2 and T2* mapping) allowing both morphological and biochemical MR evaluation of the hip joint cartilages in a region-wise fashion (Carballido-Gamio et al. 2008b; Subburaj et al. 2013). The SPRI dataset introduced in this chapter has also been used in another concurrent work in our project by Chandra et al. (2012a), which validated the proposed cartilage segmentation scheme to extract biochemical information of the hip joint cartilages from MR T2 mapping images.

The current work has qualitatively demonstrated a good reproducibility with another two MR sequences (DESS and SPACE) featuring a lower image resolution. Promising consistency was observed in quantitative volume and thickness measurements using automatic cartilage segmentations from the paired TrueFISP, DESS and SPACE images (see Figure 6.10 and 6.11). However, due to significant PVE affecting most cartilage voxels (particularly at the thinner regions of the highly curve cartilage layer) in the latter two MR examinations to different degrees, the volume and thickness measurement results showed slight over-estimation using the DESS sequence and under-estimation using the SPACE sequence. Further improvements can be possibly made by incorporating advanced MR image upsampling techniques such as super-resolution algorithms (Van Reeth et al. 2012). Nevertheless, as reported in the work of hip cartilage T2 mapping assessment (Chandra et al. 2012a), automatic cartilage volumes from 3D low-resolution SPACE images were sufficiently accurate to deliver good agreement (a relative difference error $< 10\%$) between manual and automatic analyses of T2 values.

There are a number of limitations in the present study. Quantitative analyses were performed on MR images of the hip joint acquired from relatively young, healthy participants, which are similar to the limitations of the proposed automatic cartilage segmentation method discussed in Chapter 5. Future studies on individuals with a spectrum of hip joint pathologies (e.g., early or pre-OA) will be required for a fuller evaluation of our current segmentation and quantitative analysis scheme for the hip joint. Current quantitative analyses were successfully applied to three different MR sequences, TrueFISP, DESS and SPACE, which had similar contrast characteristics ("dark" bones and bright cartilage and fluid) although a more detailed validation needs to be undertaken. More MR examinations involving non-fat-suppressed sequences, lower-resolution routine clinical sequences (e.g., 2D or 3D fast spin-echo) across different scanner field strength, should be also investigated and carefully validated. Clinically, the proposed thickness measurement is more likely to be applicable for the hip joint

with the spherical-like femoral head, which could be in early and/or less severe OA conditions without bony deformities of the femoral head. For the hip joint with the non-spherical femoral head such as in more severe OA states, a more dedicated model for the femoral head, e.g., an ellipsoid model (Liu et al. 2014), will be needed to reduce the potential measurement errors.

6.5 Conclusion

This chapter demonstrated the feasibility of extracting reliable and reproducible quantitative measurements of the cartilage morphology from the automatically segmented cartilage volumes from high-resolution MR images of the hip joint. A good agreement was achieved in the morphometric data of volume and thickness measurements obtained from manual and automatic cartilage segmentations for both the femoral and acetabular cartilage plates. This can be of great use for provision of morphometric data in large-scale research and clinical studies on morphological evaluation of hip joint cartilages, without reliance of time- and expert-intensive manual methods. The subregional analyses have also demonstrated significant morphological differences of the cartilage layer across different subregions. This indicates the potential application of our method as an advanced surrogate measure allowing small cartilage changes, e.g., focal cartilage lesions, to be captured for dedicated use in prospective research and clinical studies on morphological evaluation of the hip joint cartilages related to hip OA.

Table 6.2: Quantitative volume and thickness measurements of the partitioned subregions for the individual femoral and acetabular cartilage plates.

	Region ID	Cartilage Volume (mm^3)				Average Cartilage Thickness (mm)			
		Mean	SD	Min	Max	Mean	SD	Min	Max
Acetabular Cartilage Plate									
AceAntSupFossa	2	869.82	230.61	512.98	1518.74	1.18	0.22	0.81	1.65
AceSupLat	3	632.66	199.42	272.01	1129.77	1.13	0.22	0.72	1.49
AcePostSupFossa	4	581.52	161.15	301.13	972.22	0.93	0.13	0.59	1.17
Femoral Cartilage Plate									
FemSupAntFovea	2	1906.29	357.49	1184.56	2710.41	1.30	0.12	1.06	1.59
FemSupNeckAnt	3a	539.99	119.80	285.09	789.72	1.26	0.20	0.88	1.76
FemSupNeckPost	3b	669.73	168.78	321.72	1162.03	1.04	0.17	0.74	1.55
FemSupPostFovea	4	858.82	239.78	407.23	1690.80	0.95	0.12	0.66	1.25

(Ant: Anterior, Sup: Superior, Post: Posterior, Lat: Lateral)

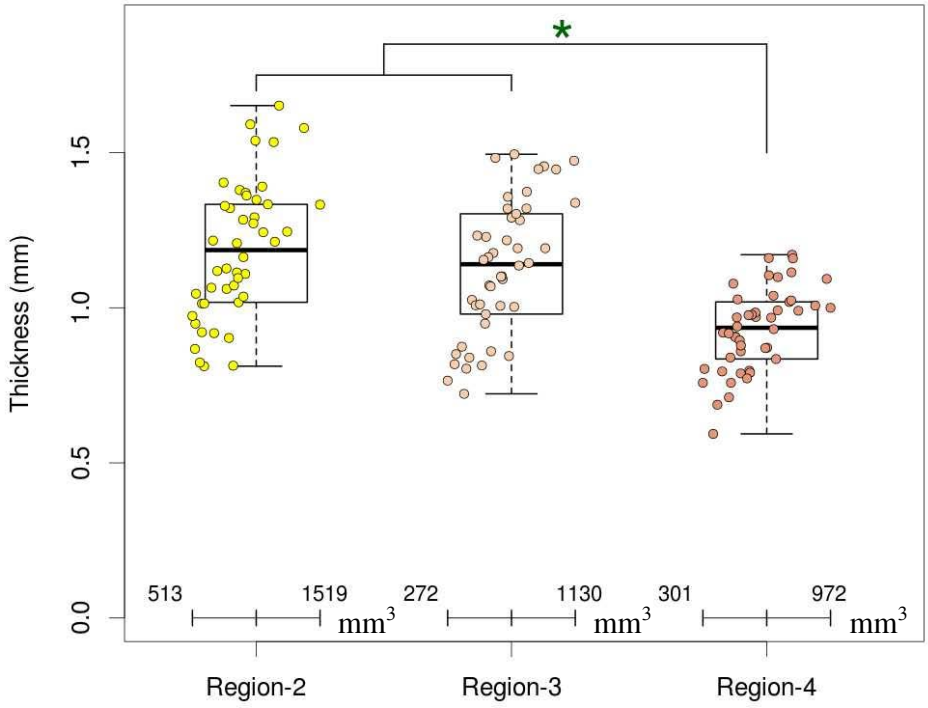

(a)

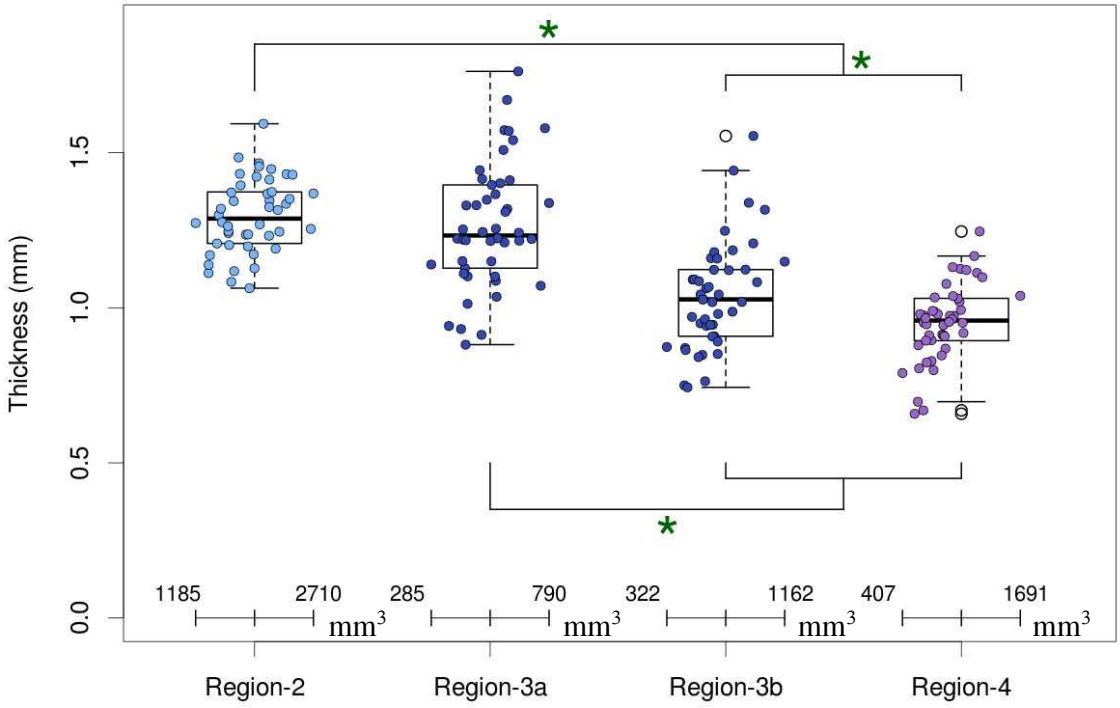

(b)

Figure 6.7: Boxplots display the average thickness in each partitioned subregion of the individual (a) acetabular and (b) femoral cartilage plates calculated from automatic segmentations of 46 TrueFISP images. Asterisks indicate significant differences between the partitioned subregions.

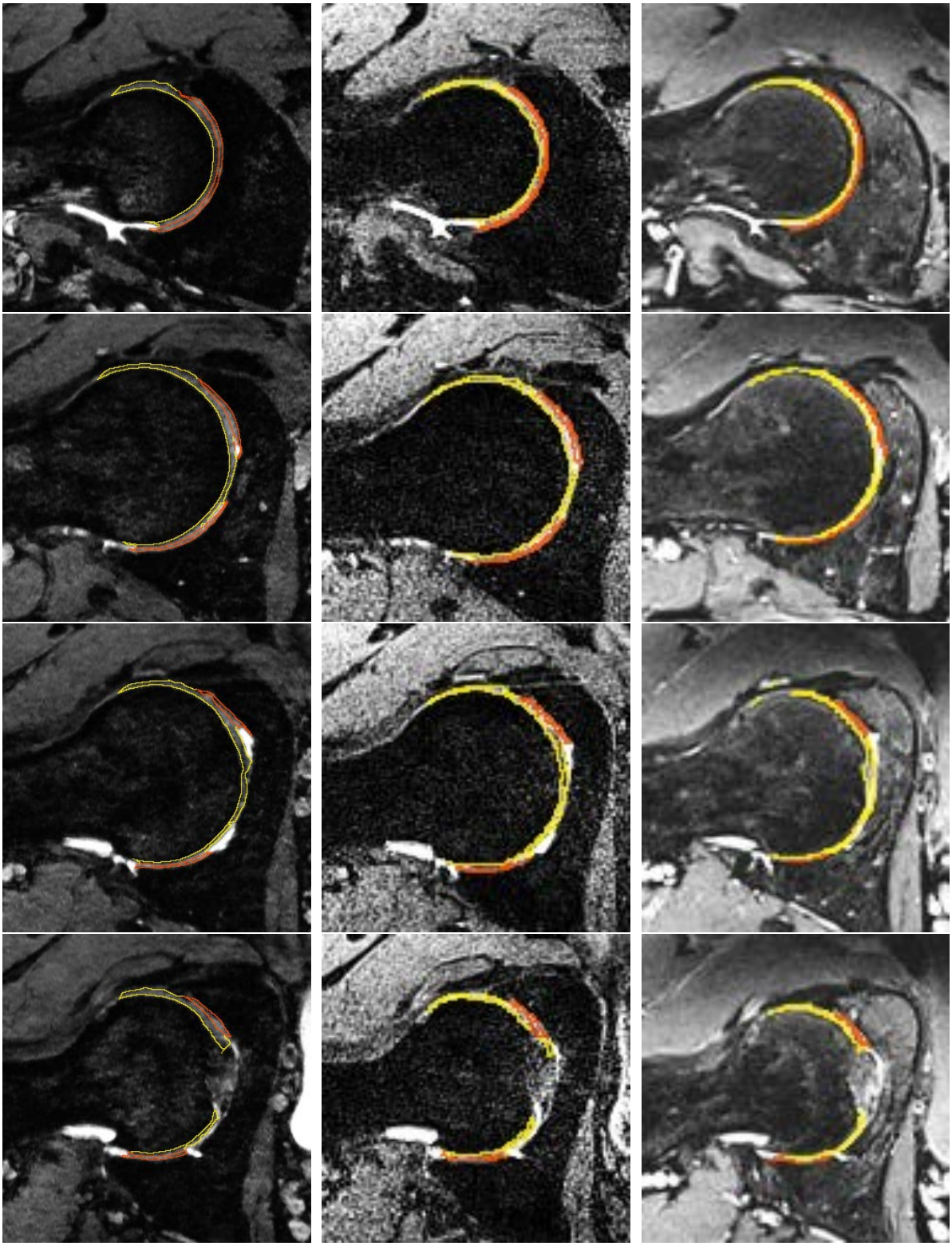

(a) (b) (c)

Figure 6.8: Example 2D axial MR slices with overlayed cartilage segmentation contours obtained from MR examinations of case 11 using three different acquisition sequences: (a) TrueFISP, (b) DESS and (c) SPACE.

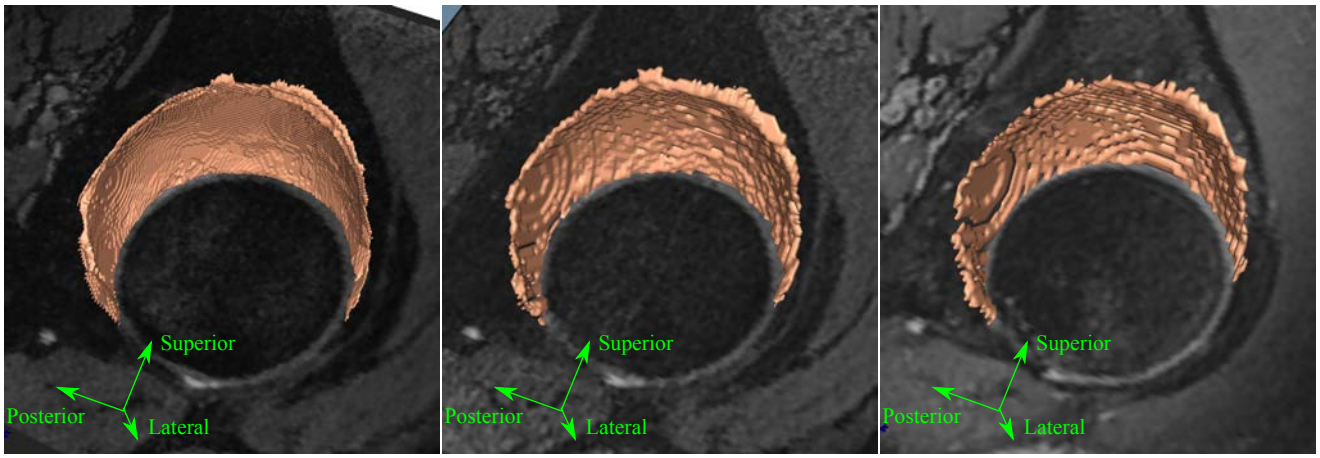

(a)

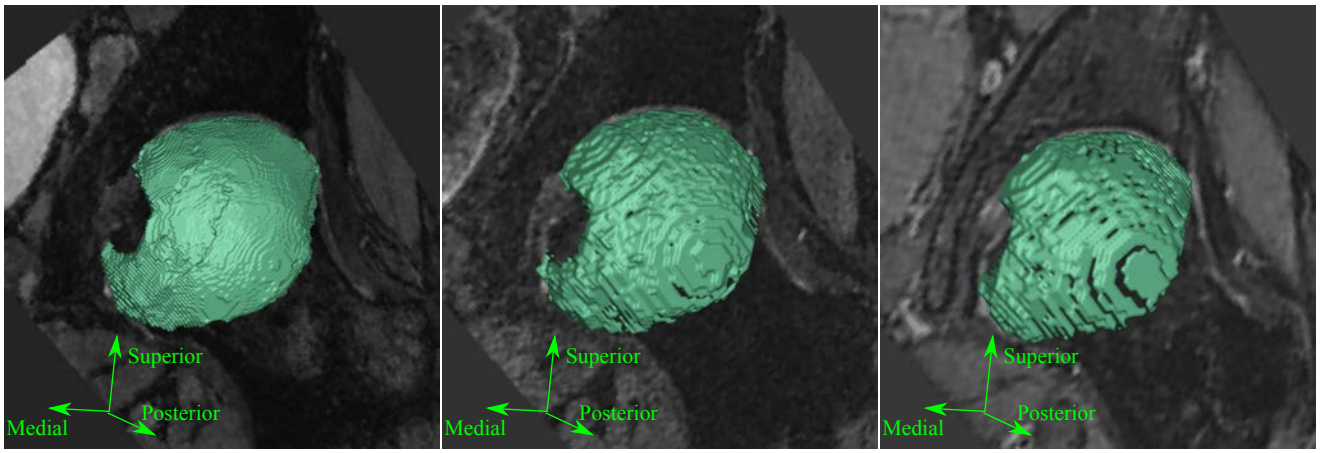

(b)

Figure 6.9: 3D visualizations of the (a) acetabular and (b) femoral cartilage volumes automatically segmented from three different MR examinations of case 11: (from *left* to *right*) TrueFISP, DESS, SPACE.

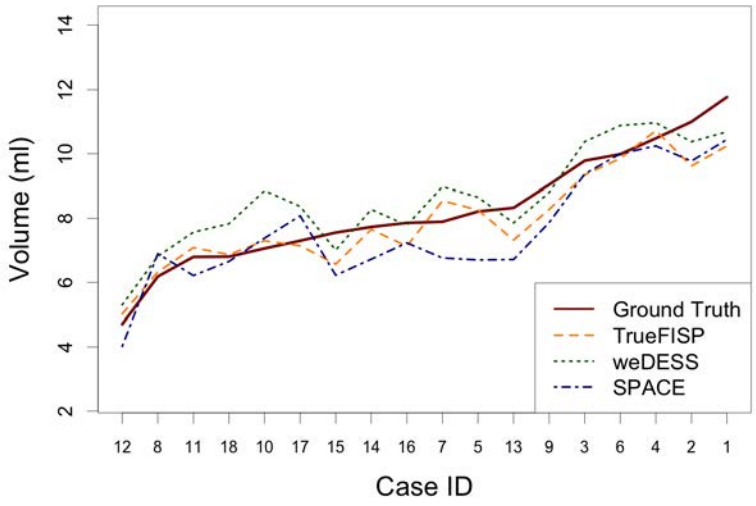

(a)

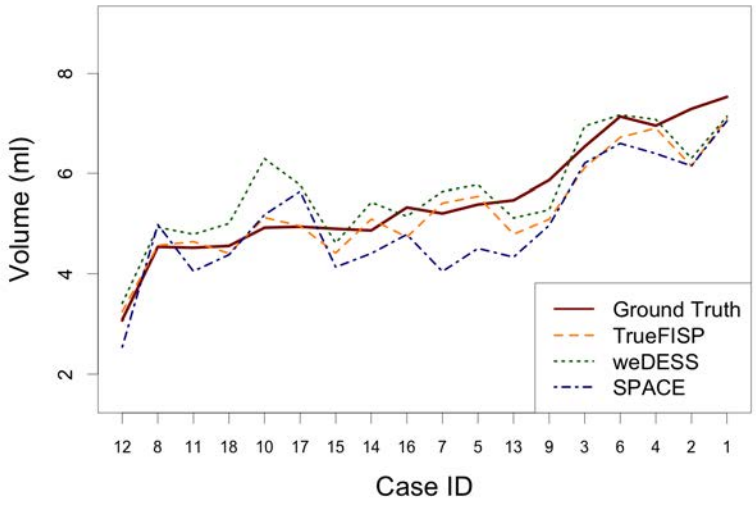

(b)

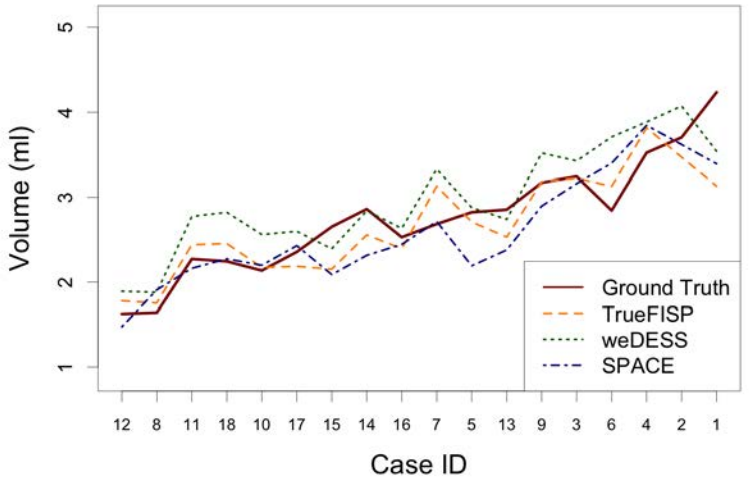

(c)

Figure 6.10: Volume measurements of the (a) combined, (b) femoral and (c) acetabular cartilages for each case obtained from automatic segmentations of TrueFISP, DESS and SPACE scans as well as manual segmentations from TrueFISP images in the dataset of 18 subjects.

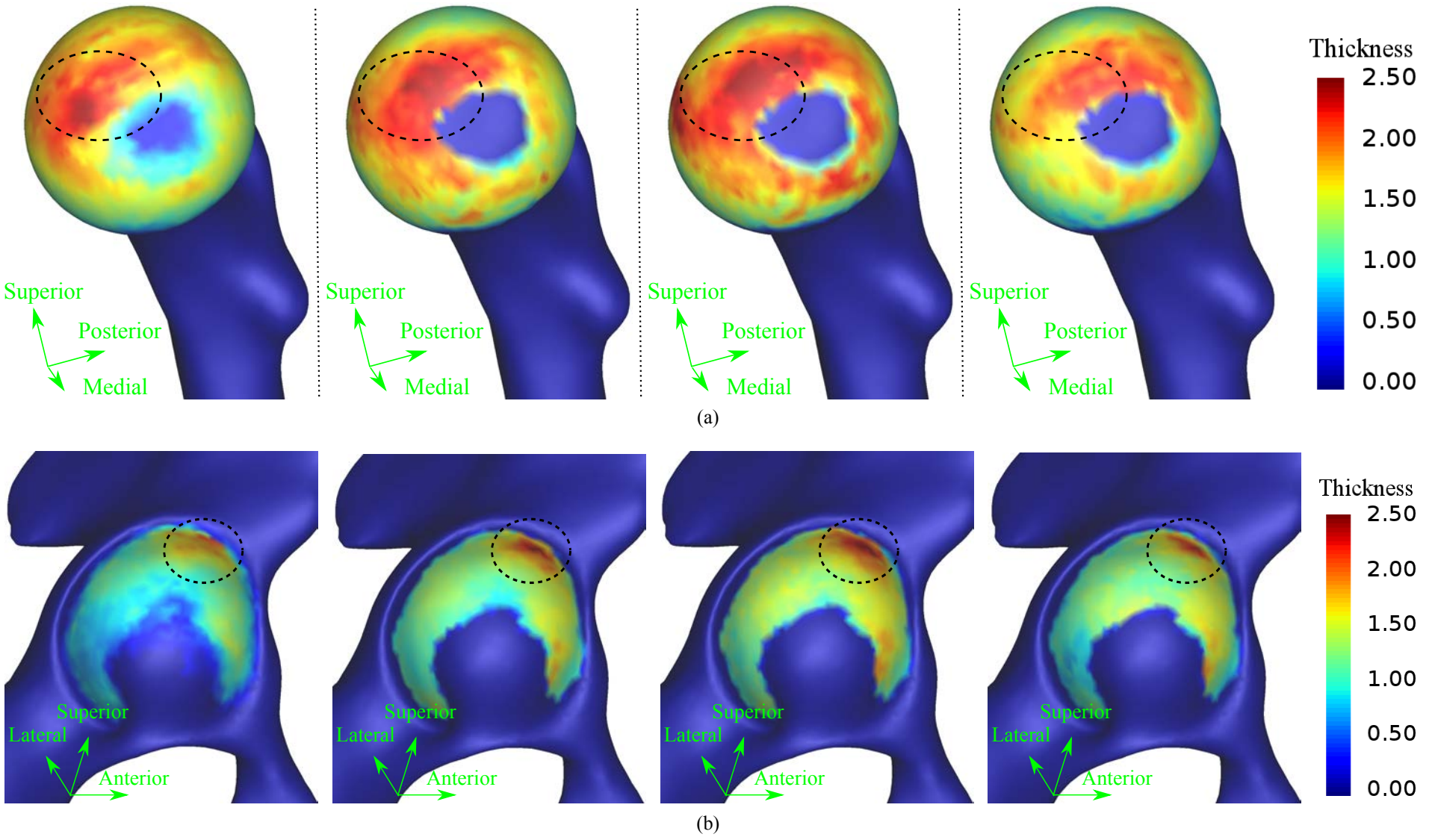

Figure 6.11: Average thickness maps with color scale (0 - 2.5 mm) for automatic segmentations of the (a) femoral and (b) acetabular cartilage plates obtained from manual or automatic segmentations of MR examinations in 18 volunteers: (from *left* to *right*) manual segmentations (ground truth), TrueFISP, DESS, 3D SPACE.

7 GENERAL DISCUSSION AND CONCLUSION

Quantitative measurements of the bones and articular cartilages can provide useful morphometric data from the large volume of complex MR data for potential use in research and clinical studies about pathoanatomcial conditions such as early hip OA and FAI. Accurate detection and quantification of structural changes in the bones and cartilages at an early stage may assist initiating appropriate therapy and reducing subsequent irreversible damages to the articular cartilages and associated articulating structures before the onset of hip OA.

The segmentation of bones and cartilages from MR images is an essential prerequisite, which must be accurate, reliable and reproducible, for subsequent quantitative measurements. However, this has been difficult to perform previously for the hip joint because of anatomical (e.g., the deeply located joint structure and very thin, highly spherical articular cartilage) and imaging (e.g., the limited image resolution, complex tissue contrast and inhomogeneity in signal) challenges.

7.1 Key Contributions and Findings

This thesis has developed and validated several novel technologies in the proposed computer-aided system (Figure 1.1) that demonstrate the clinical feasibility of automatic segmentation and quantification of the osteochondral elements, i.e., the articulating bones and cartilages, from high-resolution 3D MR images of the hip joint.

This was achieved within two main aims:

1. To develop and evaluate a fully automated segmentation approach with advanced image segmentation techniques in order to deliver accurate and reproducible bone and cartilage segmentations from high-resolution 3D MR images of the hip joint and;

2. To automatically extract reliable and reproducible morphometric data based on the segmented subchondral bones and articular cartilages.

These two aims were accomplished in several stages (presented in Chapter 3-6):

- Chapter 3 developed and evaluated automatic segmentation of the bone elements within the hip joint region from high-resolution large FOV MR images using two state-of-the-art methods, i.e., the multi-atlas and ASM based algorithms (**Aim 1.1**);

- Chapter 4 automatically performed quantitative measurement and assessment (i.e., alpha angles) of 3D bone morphology at the FHN junction of the proximal femur for potential use in accurate detection and quantification of cam-type lesions (**Aim 2.1**);

- Chapter 5 developed a novel hybrid cartilage segmentation scheme, which allowed fully automatic and reliable delineation of the individual femoral and acetabular cartilage plates from MR images acquired without continuous leg traction or the use of contrast agents (**Aim 1.2**);

- Chapter 6 performed reliable and reproducible quantitative measurements (i.e., volume, thickness) of the segmented femoral and acetabular cartilages from MR images using three different imaging sequences, i.e., TrueFISP, DESS and 3D SPACE (**Aim 2.2**). Subregional analyses of quantitative measurements were also performed to investigate a morphological pattern of volume and thickness variation across different partitioned subregions for each cartilage plate.

The main findings are summarized below.

In Chapter 3, the multi-atlas and ASM based methods both proved to be effective and robust achieving good segmentations of the femoral and innominate bones within the hip joint region from high-resolution 3D nearly isotropic MR images (DESS and MEDIC), which were acquired from volunteer subjects with varying FHN junction geometries. The results indicated accurate and robust segmentation performance, including when cam lesions were present, which showed the capacity of both methods for 3D morphometric analyses of cam-type deformities. Based on Hausdorff distance metrics, the likely femoral and acetabular BCIs were well delineated using these methods, which both achieved the average Hausdorff distance mostly < 0.5 mm (corresponding to the in-plane resolution of 0.65 mm and 0.67 mm for MEDIC and DESS images). These likely BCI surfaces could be readily used providing a reference frame for subsequent cartilage segmentation. Although the multi-atlas method showed slight advantages in terms of DSC and MASD metrics regarding the accuracy performance, the ASM-based approach was significantly more time-efficient than the multi-atlas method (13 minutes versus 6 hours), which would be favourable for potential clinical utility (e.g., timeliness, patient throughput).

The proposed 3D method for automatic measurement and assessment of the FHN junction (Chapter 4) achieved strong correlations (Pearson's correlation coefficient $r > 0.8$, $p < 0.01$) between manual and automatic alpha angle measures at both anterosuperior and anterior positions of the FHN junction (where cam lesions often appear) from a set of 30 DESS images encompassing both hip joints. The preliminary study on the reproducibility of the proposed method revealed a high consistency in alpha angle measures across different positions within the upper anterior quadrant of the FHN junction obtained from bilateral DESS images and unilateral TrueFISP images.

A novel hybrid cartilage segmentation scheme (Chapter 5) was developed based on an improved multi-object multi-surface graph search framework with a novel integration of the arc-weighted graph representation and varying surface feasibility constraints learned from prior knowledge of the cartilage morphology. The proposed method successfully segmented the individual cartilage plates from MR images with weak or no separation between cartilage boundaries and provided an overall high level of validity and reliability of automated segmentation of the femoral and acetabular cartilage volumes in comparison with benchmark manual segmentations, which had mean DSC values of (0.81, 0.77, 0.73) for segmentation of (combined, femoral, acetabular) cartilage volumes in the validation dataset of 46 high-resolution TrueFISP images. Moreover, compared with the multi-atlas-based method (state-of-the-art), this scheme showed comparative robustness for MR images with poor image quality, particularly when there was low or no tissue contrast for the BCIs and cartilage-synovial fluid interfaces.

In Chapter 6, a very good agreement was obtained for both volume and thickness measurements between automatic and manual segmentations of the femoral and acetabular cartilage plates in the dataset of 46 TrueFISP images. In subregional analyses of each individual cartilage plate, the anterior-superior subregion was found having the thickest cartilage layer, which tallies with common knowledge of regional thickness variation for the femoral and acetabular cartilages (Fagerson 1998). Significant differences in the cartilage thickness were found across different subregions of the individual cartilage plate, which indicated the significance of subregional morphological analyses that may improve the sensitivity of cartilage thickness measurement and allow small cartilage changes to be captured. Furthermore, even when partial volume effects were pronounced, moderate reproducibility was nevertheless obtained for the proposed volume and thickness measurements based on automatic cartilage segmentations from high-resolution TrueFISP, low-resolution DESS and low-resolution 3D SPACE examinations of the same participant.

7.2 Implications of Findings

The innovative developments presented in this thesis provide a series of effective tools to perform quantitative assessment of the osteochondral elements (e.g., the subchondral bones, articular cartilages) within the hip joint from high-resolution 3D MR images. These approaches deliver reliable and reproducible morphometric data of these joint structures of interest without reliance of time- and expertise-intensive manual methods, which have great potential to be used in large-scale research and clinical studies on pathoanatomical conditions such as early hip OA and FAI. Additionally, these algorithms with an overall good level of reliability, robustness and time-efficiency can be favourably implemented to the software platform of MR systems for potential clinical utility (e.g., timeliness, patient throughput).

The preliminary evaluation on automatic quantification of 3D bone morphology at the FHN junction has demonstrated the feasibility to accurately locate the epicenter of a cam lesion and quantify the severity of cam-type deformities from MR images of the hip joint (Figure 4.9). This may therefore assist initiating appropriate therapy for cam-type FAI and predicting the subsequent cartilage damage potentially leading to the onset of hip OA (Beaulé et al. 2012). As there is limited consensus on al-

pha angle measures from 2D plain radiographs and reformatted MR radial views (Clohisy et al. 2009; Meyer et al. 2006; Sutter et al. 2012), our method based on 3D reconstructions of the proximal femur offers great advantages in providing 360° alpha angle measurements for detecting and characterizing the variable presentations and locations of cam lesions on a patient-specific basis. Moreover, the proposed ASM-based bone segmentation method with fast, accurate and robust performance, including when cam lesions were present, lays the foundation to automate this quantification process, which enables its application in prospective large-scale research and clinical studies on cam-type FAI.

The developed hybrid cartilage segmentation scheme will be of great use for providing quantitative measures of the cartilage morphology in prospective large-scale research and clinical investigations about hip OA. These quantitative measurements based on automatic cartilage segmentations can be comparable to the results obtained from the segmentation data using time-consuming and expert-intensive manual approaches, as presented in Chapter 6. The subregional analyses of the cartilage morphology deliver advanced surrogate measures to detect small changes of the cartilage initialized in independent subregions, particularly within the weight-bearing region. These partitioned subregion volumes of the cartilage can automatically offer the extracted ROIs for biochemical evaluation using advanced MR technologies such as *d*GEMRIC (Siversson et al. 2014), T2 mapping (Chandra et al. 2015b; Ho et al. 2014), T1ρ (Rakhra et al. 2012). Ideally, these developments can greatly help to obtain a thorough morphological and biochemical patterns of cartilage degeneration within the hip joint, which is significantly important for diagnosis and intervention of hip OA at a very early stage.

7.3 Limitations of the Study

In this thesis, there are several limitations mainly around four aspects:

1. *Clinical Application:* The evaluation of the developed bone and cartilage segmentation methods was based on high-resolution 3 T MR images of the hip joint. In order to allow the prospective clinical application, a fuller evaluation of the current automated segmentation framework is required on a larger dataset of MR images from lower-resolution routine clinical sequences (e.g., 2D or 3D FSE, SPGR) across different scanner field strengths (e.g., 1.5 T), imaging positioning, image sequences and in-plane resolutions. The current framework demonstrated a promising reproducibility in lower-resolution DESS (in-plane spacing: 0.63 mm, slice thickness: 0.70 mm) and SPACE (in-plane spacing: 0.75, slice thickness 0.90) images with a good consistency of the obtained quantitative volume and thickness measurements in Chapter 6 although a more detailed validation needs to be undertaken.

2. *Algorithm Generalization:* The proposed bone segmentation scheme was developed within the framework of a water excited or fat suppressed MR sequence with 'dark' bones and bright cartilage and fluid. Our automated approach has been successfully transferred to water excitation DESS, MEDIC, fat-suppressed SPACE images with similar contrast characteristics, although non-fat-suppressed MR sequences need to be further evaluated with certain adjustments to the segmentation algorithms.

3. *Demographics:* The training database for creation of bone SSMs in Chapter 3 was restricted to male cases. Consequently, this affected the performance of the SSM to robustly describe the anatomical variation among female subjects especially for the (irregular) innominate bone structure. However, this factor may have less impact on segmentation accuracy of the proximal femur and subsequent quantitative assessment of cam-type lesions. A larger training dataset, possibly with specific male and female models, will be necessary to better encode shape variation and handle different anatomical bone structures.

4. *Cartilage Pathology:* The validation dataset of TrueFISP images in Chapter 5 was obtained from relatively young, healthy participants. Although a variety of the FHN junction geometries (including very larger alpha angles $> 70°$) was included in this dataset, no subject was clinically diagnosed with cartilage degeneration conditions. A comprehensive validation on symptomatic patients with a wide spectrum of the hip joint pathology including hip OA with varying degrees of severity is required before a wide employment in the clinical setting is possible. Nevertheless our approach is likely to be applicable for the hip joint in early and/or less severe OA conditions.

7.4 Opportunities and Future Directions

7.4.1 Bone and cartilage segmentation

The training process of the SSM and articular cartilage model can be improved by incorporating a large and targeted demographic (e.g., male and female, different age groups). This is important because of the inherent anatomical variety in the bones and cartilages of the hip joint between males and females, subjects in different age groups.

More advanced preprocessing techniques can be incorporated into the current segmentation framework in order to improve the image quality and handle various MR artefacts for the later automatic segmentation process. As significant PVE affecting most cartilage voxels is the primary concern about adapting our methods to low-resolution routine clinical scans, advanced image upsampling techniques such as super-resolution algorithms (Van Reeth et al. 2012) can be explored in the future. Additionally, a spectrum of techniques focusing on contrast enhancement and denoising can be also investigated.

Future improvements to the cartilage segmentation method can be made to minimize segmentation errors that were obviously observed near the femoral fovea and acetabular fossa or at other peripheral articulating regions outside the weight-bearing areas (Figure 5.7). Due to the anatomical variety (e.g., different location and appearance) of the femoral fovea, the extraction of BCI surfaces can be further improved with some particular refinement steps to automatically locate the femoral fovea and acetabular fossa based on the joint morphology and other image-based features. More sophisticated classification methods such as Markov random field (MRF) techniques (Lee et al. 2011; Park et al. 2013), can be used to better define the coverage of the BCI surfaces and handle the peripheral regions

with very thin cartilage and insufficient tissue contrast.

7.4.2 Quantitative analysis

More quantitative measurements such as the FHN offset (Tannast et al. 2007), triangular index (Gosvig et al. 2007) and 3D head-neck ratios (Masjedi et al. 2013b) can be incorporated into the current quantitative assessment scheme for a thorough and reliable evaluation of 3D bone morphology of the femoral head and neck. Another future research area can involve the evaluation of the abnormal bone morphology for the hip joint with pincer-type FAI to detect and quantify the overcoverage of the acetabulum since accurate 3D reconstruction of the innominate bone can be automatically obtained from MR images using our developed method.

With current biochemical MR techniques, there are possibilities to perform a comprehensive assessment of the hip joint cartilages in both morphological and biochemical ways, which may assist earlier detection of cartilage degenerative conditions. This has been initially investigated in another concurrent work in our project by Chandra et al. (2015b) for validating the capability of our segmentation scheme to automatically extract T2 mapping information across subregions of the femoral and acetabular cartilages. Similarly, more applications can be made to *d*GEMRIC and other biochemical MR imaging techniques.

Another obvious area to pursue is to investigate the clinical value of these results (volume, thickness, subregional analyses) by correlating them to health status, progression or other clinical findings. This can also demonstrate the applicability of the proposed automatic framework for use in prospective large-scale cross-sectional and longitudinal studies on hip OA.

7.5 Conclusion

In summary, this thesis presents an innovative computer-aided system involving a series of technological developments for automatic segmentation and quantitative assessment of the osteochondral elements within the hip joint from MR images. The developed algorithms provide automatic segmentations of the bones and cartilages with an overall high level of validity and reliability, in comparisons with benchmark manual segmentations. To our best knowledge, it is the first method for automatic and reliable segmentation of the individual femoral and acetabular cartilage plates from MR images despite weak or no separation between cartilage boundaries. The obtained segmentations were successfully used in quantitative measurements of the bone and cartilage morphology, which provide reliable and reproducible morphometric data allowing small structural changes of the bone and cartilage to be captured. The findings of this thesis provide great potential for dedicated use in prospective large-scale research and clinical studies focusing on morphometric evaluations of the hip joint in pathoanatomical conditions such as early OA and FAI.

BIBLIOGRAPHY

Ababneh, S. Y., Prescott, J. W., and Gurcan, M. N. (2011). Automatic graph-cut based segmentation of bones from knee magnetic resonance images for osteoarthritis research. *Medical Image Analysis*, 15(4):438--448, DOI:10.1016/j.media.2011.01.007. Special section on IPMI 2009. http://www.sciencedirect.com/science/article/pii/S1361841511000223.

AIHW (2014). *Arthritis and other musculoskeletal conditions across the life stages*. Arthritis series no. 18, Cat. no. PHE 173. AIHW, Canberra. http://www.aihw.gov.au/publication-detail/?id=60129547059.

Aliprandi, A., Di Pietto, F., Minafra, P., Zappia, M., Pozza, S., and Sconfienza, L. (2014). Femoro-acetabular impingement: what the general radiologist should know. *La radiologia medica*, 119(2):103--112, DOI:10.1007/s11547-013-0314-7. http://dx.doi.org/10.1007/s11547-013-0314-7.

Aljabar, P., Heckemann, R., Hammers, A., Hajnal, J., and Rueckert, D. (2009). Multi-atlas based segmentation of brain images: Atlas selection and its effect on accuracy. *NeuroImage*, 46(3):726--738, DOI:10.1016/j.neuroimage.2009.02.018. http://www.sciencedirect.com/science/article/pii/S1053811909001554.

Anderson, L. and Blake, D. (1994). The anatomy and biomechanics of the hip joint. *Journal of back and musculoskeletal rehabilitation*, 4(3):145--153, DOI:10.3233/bmr-1994-4305. http://dx.doi.org/10.3233/BMR-1994-4305.

Artaechevarria, X., Munoz-Barrutia, A., and Ortiz-de Solorzano, C. (2009). Combination Strategies in Multi-Atlas Image Segmentation: Application to Brain MR Data. *Medical Imaging, IEEE Transactions on*, 28(8):1266--1277, DOI:10.1109/TMI.2009.2014372.

Aspert, N., Santa Cruz, D., and Ebrahimi, T. (2002). Mesh: measuring errors between surfaces using the Hausdorff distance. In *ICME (1)*, pages 705--708.

Audenaert, E., Baelde, N., Huysse, W., Vigneron, L., and Pattyn, C. (2011). Development of a three-dimensional detection method of cam deformities in femoroacetabular impingement. *Skeletal*

Radiology, 40(7):921--927, DOI:10.1007/s00256-010-1021-2. http://dx.doi.org/10.1007/s00256-010-1021-2.

Bae, K., Shim, H., Tao, C., Chang, S., Wang, J., Boudreau, R., and Kwoh, C. (2009). Intra- and inter-observer reproducibility of volume measurement of knee cartilage segmented from the OAI MR image set using a novel semi-automated segmentation method. *Osteoarthritis and Cartilage*, 17(12):1589--1597, DOI:10.1016/j.joca.2009.06.003. http://www.sciencedirect.com/science/article/pii/S1063458409001629.

Baniasadipour, A., Zoroofi, R., Sato, Y., Nishii, T., Nakanishi, K., Tanaka, H., Sugano, N., Yoshikawa, H., Nakamura, H., and Tamura, S. (2007). A fully automated method for segmentation and thickness map estimation of femoral and acetabular cartilages in 3D CT images of the hip. In *Image and Signal Processing and Analysis, 2007. ISPA 2007. 5th International Symposium on*, pages 92--97. http://dx.doi.org/10.1109/ISPA.2007.4383670.

Barton, C., Salineros, M., Rakhra, K., and Beaulé, P. (2011). Validity of the alpha angle measurement on plain radiographs in the evaluation of cam-type femoroacetabular impingement. *Clinical Orthopaedics and Related Research®*, 469(2):464--469, DOI:10.1007/s11999-010-1624-x. http://dx.doi.org/10.1007/s11999-010-1624-x.

Bashir, A., Gray, M., Hartke, J., and Burstein, D. (1999). Nondestructive imaging of human cartilage glycosaminoglycan concentration by MRI. *Magnetic Resonance in Medicine*, 41(5):857--865, DOI:10.1002/(SICI)1522-2594(199905)41:5<857::AID-MRM1>3.0.CO;2-E. http://dx.doi.org/10.1002/(SICI)1522-2594(199905)41:5<857::AID-MRM1>3.0.CO;2-E.

Beaulé, P., Hynes, K., Parker, G., and Kemp, K. (2012). Can the alpha angle assessment of cam impingement predict acetabular cartilage delamination? *Clinical Orthopaedics and Related Research®*, 470(12):3361--3367, DOI:10.1007/s11999-012-2601-3. http://dx.doi.org/10.1007/s11999-012-2601-3.

Beaulé, P. E., Zaragoza, E., Motamedi, K., Copelan, N., and Dorey, F. J. (2005a). Three-dimensional computed tomography of the hip in the assessment of femoroacetabular impingement. *Journal of Orthopaedic Research*, 23(6):1286--1292, DOI:10.1016/j.orthres.2005.03.011.1100230608. http://dx.doi.org/10.1016/j.orthres.2005.03.011.1100230608.

Beaulé, P. E., Zaragoza, E., Motamedi, K., Copelan, N., and Dorey, F. J. (2005b). Three-dimensional computed tomography of the hip in the assessment of femoroacetabular impingement. *Journal of Orthopaedic Research*, 23(6):1286--1292, DOI:10.1016/j.orthres.2005.03.011.1100230608. http://dx.doi.org/10.1016/j.orthres.2005.03.011.1100230608.

Bedi, A., Dolan, M., Magennis, E., Lipman, J., Buly, R., and Kelly, B. T. (2012). Computer-assisted modeling of osseous impingement and resection in femoroacetabular impingement. *Arthroscopy: The Journal of Arthroscopic & Related Surgery*, 28(2):204--210, DOI:10.1016/j.arthro.2011.11.005. http://dx.doi.org/10.1016/j.arthro.2011.11.005.

Bergmann, G., Deuretzbacher, G., Heller, M., Graichen, F., Rohlmann, A., Strauss, J., and Duda, G. (2001). Hip contact forces and gait patterns from routine activities. *Journal of Biomechanics*, 34(7):859--871, DOI:10.1016/S0021-9290(01)00040-9. http://dx.doi.org/10.1016/S0021-9290(01)00040-9.

Bhosale, A. M. and Richardson, J. B. (2008). Articular cartilage: structure, injuries and review of management. *British Medical Bulletin*, 87(1):77--95, DOI:10.1093/bmb/ldn025. http://bmb.oxfordjournals.org/content/87/1/77.abstract.

Bittersohl, B., Hosalkar, H. S., Kim, Y.-J., Werlen, S., Siebenrock, K. A., and Mamisch, T. C. (2009). Delayed gadolinium-enhanced magnetic resonance imaging (dGEMRIC) of hip joint cartilage in femoroacetabular impingement (FAI): Are pre- and postcontrast imaging both necessary? *Magnetic Resonance in Medicine*, 62(6):1362--1367, DOI:10.1002/mrm.22166. http://dx.doi.org/10.1002/mrm.22166.

Bittersohl, B., Miese, F., Hosalkar, H., Herten, M., Antoch, G., Krauspe, R., and Zilkens, C. (2012). T2* mapping of hip joint cartilage in various histological grades of degeneration. *Osteoarthritis and Cartilage*, 20(7):653--660, DOI:10.1016/j.joca.2012.03.011. http://www.sciencedirect.com/science/article/pii/S1063458412007613.

Bland, J. M. and Altman, G. D. (1986). Statistical methods for assessing agreement between two methods of clinical measurement. *The Lancet*, 327(8476):307--310, DOI:10.1016/S0140-6736(86)90837-8. Originally published as Volume 1, Issue 8476. http://www.sciencedirect.com/science/article/pii/S0140673686908378.

Blezek, D. J. and Miller, J. V. (2007). Atlas stratification. *Medical Image Analysis*, 11(5):443--457, DOI:10.1016/j.media.2007.07.001. Special Issue on the Ninth International Conference on Medical Image Computing and Computer-Assisted Interventions - MICCAI 2006. http://www.sciencedirect.com/science/article/pii/S1361841507000722.

Boykov, Y. and Kolmogorov, V. (2004). An experimental comparison of min-cut/max- flow algorithms for energy minimization in vision. *Pattern Analysis and Machine Intelligence, IEEE Transactions on*, 26(9):1124--1137, DOI:10.1109/TPAMI.2004.60.

Broche, L. M., Ashcroft, G. P., and Lurie, D. J. (2012). Detection of osteoarthritis in knee and hip joints by fast field-cycling NMR. *Magnetic Resonance in Medicine*, 68(2):358--362, DOI:10.1002/mrm.23266. http://dx.doi.org/10.1002/mrm.23266.

Buckwalter, J. A., Mankin, H. J., and Grodzinsky, A. J. (2005). Articular cartilage and osteoarthritis. *INSTRUCTIONAL COURSE LECTURES-AMERICAN ACADEMY OF ORTHOPAEDIC SURGEONS*, 54:465.

Burstein, D., Bashir, A., and Gray, M. L. (2000). MRI techniques in early stages of cartilage disease. *Investigative radiology*, 35(10):622--638, DOI:10.1097/00004424-200010000-00008. http://dx.doi.org/10.1097/00004424-200010000-00008.

Carballido-Gamio, J., Bauer, J. S., Stahl, R., Lee, K.-Y., Krause, S., Link, T. M., and Majumdar, S. (2008a). Inter-subject comparison of MRI knee cartilage thickness. *Medical Image Analysis*, 12(2):120--135, DOI:10.1016/j.media.2007.08.002. http://www.sciencedirect.com/science/article/pii/S1361841507000783.

Carballido-Gamio, J., Link, T. M., Li, X., Han, E. T., Krug, R., Ries, M. D., and Majumdar, S. (2008b). Feasibility and reproducibility of relaxometry, morphometric, and geometrical measurements of the hip joint with magnetic resonance imaging at 3T. *Journal of Magnetic Resonance Imaging*, 28(1):227--235, DOI:10.1002/jmri.21411. http://dx.doi.org/10.1002/jmri.21411.

Carballido-Gamio, J., Link, T. M., and Majumdar, S. (2008c). New techniques for cartilage magnetic resonance imaging relaxation time analysis: Texture analysis of flattened cartilage and localized intra- and inter-subject comparisons. *Magnetic Resonance in Medicine*, 59(6):1472--1477, DOI:10.1002/mrm.21553. http://dx.doi.org/10.1002/mrm.21553.

Chabanas, L., LaVallee, S., Tonetti, J., Byrd, T., Kelly, B. T., and Larson, C. (2011). Method and system of automatic determination of geometric elements characterizing a bone deformation from 3D image. US Patent App. 13/704,218. http://www.google.com/patents/EP2583246A2?cl=en.

Chandra, S., Dowling, J., Shen, K.-K., Raniga, P., Pluim, J. P. W., Greer, P., Salvado, O., and Fripp, J. (2012a). Patient specific prostate segmentation in 3-D magnetic resonance images. *Medical Imaging, IEEE Transactions on*, 31(10):1955--1964, DOI:10.1109/TMI.2012.2211377. http://dx.doi.org/10.1109/TMI.2012.2211377.

Chandra, S. S., Dowling, J. A., Engstrom, C., Paproki, A., Neubert, A., Xia, Y., Rivest-Henault, D., Shen, K.-K., Salvado, O., Crozier, S., and Fripp, J. (2015a). Focused shape visualisation via the Simple Medical Imaging Library Interface. *Visualization and Computer Graphics, IEEE Transactions on*. (In Preparation).

Chandra, S. S., Surowiec, R., Ho, C., Xia, Y., Engstrom, C., Crozier, S., and Fripp, J. (2015b). Automated analysis of hip joint cartilage combining MR T2 and three-dimensional fast-spin-echo images. *Magnetic Resonance in Medicine*, DOI:10.1002/mrm.25598. http://dx.doi.org/10.1002/mrm.25598.

Chandra, S. S., Xia, Y., Engstrom, C., Crozier, S., Schwarz, R., and Fripp, J. (2014). Focused shape models for hip joint segmentation in 3D magnetic resonance images. *Medical Image Analysis*, 18(3):567--578, DOI:10.1016/j.media.2014.02.002. http://dx.doi.org/10.1016/j.media.2014.02.002.

Chandra, S. S., Xia, Y., Engstrom, C., Schwarz, R., Lauer, L., Crozier, S., Salvado, O., and Fripp, J. (2012b). Unilateral hip joint segmentation with shape priors learned from missing data. In *Biomedical Imaging (ISBI), 2012 9th IEEE International Symposium on*, pages 1711--1714. http://dx.doi.org/10.1109/ISBI.2012.6235909.

Chang, G., Deniz, C. M., Honig, S., Egol, K., Regatte, R. R., Zhu, Y., Sodickson, D. K., and Brown, R. (2014). MRI of the hip at 7T: Feasibility of bone microarchitecture, high-resolution cartilage, and clinical imaging. *Journal of Magnetic Resonance Imaging*, 39(6):1384--1393, DOI:10.1002/jmri.24305. http://dx.doi.org/10.1002/jmri.24305.

Cheng, Y., Guo, C., Wang, Y., Bai, J., and Tamura, S. (2013). Accuracy limits for the thickness measurement of the hip joint cartilage in 3-d mr images: Simulation and validation. *Biomedical Engineering, IEEE Transactions on*, 60(2):517--533, DOI:10.1109/TBME.2012.2230002. http://dx.doi.org/10.1109/TBME.2012.2230002.

Chu, C. R., Williams, A. A., Coyle, C. H., and Bowers, M. E. (2012). Early diagnosis to enable early treatment of pre-osteoarthritis. *Arthritis Research & Therapy*, 14(3):212, DOI:10.1186/ar3845. http://europepmc.org/articles/PMC3446496.

Cicuttini, F., Forbes, A., Morris, K., Woodford, N., and Stuckey, S. (2000). Determining the volume of hip cartilage by magnetic resonance imaging. *Radiography*, 6(2):79--82, DOI:10.1053/radi.2000.0239. http://www.sciencedirect.com/science/article/pii/S1078817400902396.

Clohisy, J., Carlisle, J., Trousdale, R., Kim, Y.-J., Beaule, P., Morgan, P., Steger-May, K., Schoenecker, P., and Millis, M. (2009). Radiographic evaluation of the hip has limited reliability. *Clinical Orthopaedics and Related Research*, 467(3):666--675, DOI:10.1007/s11999-008-0626-4. http://dx.doi.org/10.1007/s11999-008-0626-4.

Commandeur, F., Velut, J., and Acosta, O. (2011). A VTK algorithm for the computation of the Hausdorff distance. *VTK J*, 839. http://hdl.handle.net/10380/3322.

Conrozier, T., Jousseaume, C. A., Mathieu, P., Tron, A. M., Caton, J., Bejui, J., and Vignon, E. (1998). Quantitative measurement of joint space narrowing progression in hip osteoarthritis: a longitudinal retrospective study of patients treated by total hip arthroplasty. *Rheumatology*, 37(9):961--968, DOI:10.1093/rheumatology/37.9.961. http://rheumatology.oxfordjournals.org/content/37/9/961.abstract.

Conrozier, T., Lequesne, M., Favret, H., Taccoen, A., Mazières, B., Dougados, M., Vignon, M., and Vignon, E. (2001). Measurement of the radiological hip joint space width. an evaluation of various methods of measurement. *Osteoarthritis and Cartilage*, 9(3):281--286, DOI:10.1053/joca.2000.0386. http://www.sciencedirect.com/science/article/pii/S1063458400903868.

Cootes, T., Hill, A., Taylor, C., and Haslam, J. (1994). Use of active shape models for locating structures in medical images. *Image and Vision Computing*, 12(6):355--365, DOI:10.1016/0262-8856(94)90060-4. Information processing in medical imaging. http://www.sciencedirect.com/science/article/pii/0262885694900604.

Cootes, T., Taylor, C., Cooper, D., and Graham, J. (1992). Training models of shape from sets of examples. In Hogg, D. and Boyle, R., editors, *BMVC92*, pages 9--18. Springer London. http://dx.doi.org/10.1007/978-1-4471-3201-1_2.

Cootes, T., Taylor, C., Cooper, D., and Graham, J. (1995). Active shape models-their training and application. *Computer Vision and Image Understanding*, 61(1):38--59, DOI:10.1006/cviu.1995.1004. http://www.sciencedirect.com/science/article/pii/S1077314285710041.

Crawford, M. J., Dy, C. J., Alexander, J. W., Thompson, M., Schroder, S. J., Vega, C. E., Patel, R. V., Miller, A. R., McCarthy, J. C., Lowe, W. R., et al. (2007). The 2007 Frank Stinchfield Award: the biomechanics of the hip labrum and the stability of the hip. *Clinical orthopaedics and related research*, 465:16--22, DOI:10.1097/BLO.0b013e31815b181f. http://dx.doi.org/10.1097/BLO.0b013e31815b181f.

Dagenais, S., Garbedian, S., and Wai, E. (2009). Systematic review of the prevalence of radiographic primary hip osteoarthritis. *Clinical Orthopaedics and Related Research*, 467(3):623--637, DOI:10.1007/s11999-008-0625-5. http://dx.doi.org/10.1007/s11999-008-0625-5.

Dai, M., Newman, T. S., and Cao, C. (2007). Least-squares-based fitting of paraboloids. *Pattern Recognition*, 40(2):504--515, DOI:10.1016/j.patcog.2006.01.016. http://dx.doi.org/10.1016/j.patcog.2006.01.016.

Dandachli, W., Najefi, A., Iranpour, F., Lenihan, J., Hart, A., and Cobb, J. (2012). Quantifying the contribution of pincer deformity to femoro-acetabular impingement using 3d computerised tomography. *Skeletal Radiology*, 41(10):1295--1300, DOI:10.1007/s00256-012-1389-2. http://dx.doi.org/10.1007/s00256-012-1389-2.

Deniz, C. M., Brown, R., Lattanzi, R., Alon, L., Sodickson, D. K., and Zhu, Y. (2013). Maximum efficiency radiofrequency shimming: Theory and initial application for hip imaging at 7 tesla. *Magnetic Resonance in Medicine*, 69(5):1379--1388, DOI:10.1002/mrm.24377. http://dx.doi.org/10.1002/mrm.24377.

Dice, L. (1945). Measures of the amount of ecologic association between species. *Ecology*, 26(3):297--302.

Ding, C., Jones, G., Wluka, A. E., and Cicuttini, F. (2010). What can we learn about osteoarthritis by studying a healthy person against a person with early onset of disease? *Current Opinion in Rheumatology*, 22(5):520--527, DOI:10.1097/bor.0b013e32833b90e9. http://dx.doi.org/10.1097/BOR.0b013e32833b90e9.

Disler, D. (1997). Fat-suppressed three-dimensional spoiled gradient-recalled MR imaging: assessment of articular and physeal hyaline cartilage. *AJR. American journal of roentgenology*, 169(4):1117--1123, DOI:10.2214/ajr.169.4.9308475. http://intl.ajronline.org/cgi/reprint/169/4/1117.pdf.

Dodin, P., Pelletier, J.-P., Martel-Pelletier, J., and Abram, F. (2010). Automatic human knee cartilage segmentation from 3-D magnetic resonance images. *Biomedical Engineering, IEEE Transactions on*, 57(11):2699--2711, DOI:10.1109/TBME.2010.2058112. http://dx.doi.org/10.1109/TBME.2010.2058112.

Dougados, M., Gueguen, A., Nguyen, M., Berdah, L., Lequesne, M., Mazieres, B., and Vignon, E. (1996). Radiological progression of hip osteoarthritis: definition, risk factors and correlations with clinical status. *Annals of the Rheumatic Diseases*, 55(6):356--362, DOI:10.1136/ard.55.6.356. http://ard.bmj.com/content/55/6/356.abstract.

Dowling, J., Lambert, J., Parker, J., Greer, P., Fripp, J., Denham, J., Ourselin, S., and Salvado, O. (2010). Automatic MRI atlas-based external beam radiation therapy treatment planning for prostate cancer. In Madabhushi, A., Dowling, J., Yan, P., Fenster, A., Abolmaesumi, P., and Hata, N., editors, *Prostate Cancer Imaging. Computer-Aided Diagnosis, Prognosis, and Intervention*, volume 6367 of *Lecture Notes in Computer Science*, pages 25--33. Springer Berlin Heidelberg. http://dx.doi.org/10.1007/978-3-642-15989-3_4.

Dowling, J. A., Lambert, J., Parker, J., Salvado, O., Fripp, J., Capp, A., Wratten, C., Denham, J. W., and Greer, P. B. (2012). An atlas-based electron density mapping method for magnetic resonance imaging (MRI)-alone treatment planning and adaptive mri-based prostate radiation therapy. *International Journal of Radiation Oncology*Biology*Physics*, 83(1):e5--e11, DOI:10.1016/j.ijrobp.2011.11.056. http://www.sciencedirect.com/science/article/pii/S0360301611036145.

Drake, R., Vogl, A. W., and Mitchell, A. W. (2009). *Gray's anatomy for students*. Elsevier Health Sciences.

Duc, S. R., Koch, P., Schmid, M. R., Horger, W., Hodler, J., and Pfirrmann, C. W. A. (2007a). Diagnosis of articular cartilage abnormalities of the knee: prospective clinical evaluation of a 3D water-excitation True FISP sequence. *Radiology*, 243(2):475--482, DOI:10.1148/radiol.2432060274. http://intl-radiology.rsnajnls.org/cgi/reprint/243/2/475.pdf.

Duc, S. R., Pfirrmann, C. W. A., Schmid, M. R., Zanetti, M., Koch, P. P., Kalberer, F., and Hodler, J. (2007b). Articular cartilage defects detected with 3D water-excitation true FISP: prospective comparison with sequences commonly used for knee imaging. *Radiology*, 245(1):216--223, DOI:10.1148/radiol.2451060990. http://intl-radiology.rsnajnls.org/cgi/reprint/245/1/216.pdf.

Dudda, M., Albers, C., Mamisch, T., Werlen, S., and Beck, M. (2009). Do normal radiographs exclude asphericity of the femoral head-neck junction? *Clinical Orthopaedics and Related Research*, 467(3):651--659, DOI:10.1007/s11999-008-0617-5. http://dx.doi.org/10.1007/s11999-008-0617-5.

Eckstein, F., Hudelmaier, M., Wirth, W., Kiefer, B., Jackson, R., Yu, J., Eaton, C. B., and Schneider, E. (2006). Double echo steady state magnetic resonance imaging of knee articular cartilage at 3 tesla:

a pilot study for the osteoarthritis initiative. *Annals of the Rheumatic Diseases*, 65(4):433--441, DOI:10.1136/ard.2005.039370. http://ard.bmj.com/content/65/4/433.abstract.

Fagerson, T. L. (1998). *The hip handbook*. Butterworth-Heinemann Medical.

Farag, A., Ahmed, M., El-Baz, A., and Hassan, H. (2005). Advanced segmentation techniques. In Suri, J., Wilson, D., and Laxminarayan, S., editors, *Handbook of Biomedical Image Analysis*, International Topics in Biomedical Engineering, pages 479--533. Springer US. http://dx.doi.org/10.1007/0-306-48551-6_9.

Fedorov, A., Billet, E., Prastawa, M., Gerig, G., Radmanesh, A., Warfield, S., Kikinis, R., and Chrisochoides, N. (2008). Evaluation of brain mri alignment with the robust hausdorff distance measures. In Bebis, G., Boyle, R., Parvin, B., Koracin, D., Remagnino, P., Porikli, F., Peters, J., Klosowski, J., Arns, L., Chun, Y., Rhyne, T.-M., and Monroe, L., editors, *Advances in Visual Computing*, volume 5358 of *Lecture Notes in Computer Science*, pages 594--603. Springer Berlin Heidelberg. http://dx.doi.org/10.1007/978-3-540-89639-5_57.

Felson, D. T. (2006). Osteoarthritis of the knee. *New England Journal of Medicine*, 354(8):841--848, DOI:10.1056/NEJMcp051726. PMID: 16495396. http://www.nejm.org/doi/full/10.1056/NEJMcp051726.

Felson, D. T., Lawrence, R. C., Dieppe, P. A., Hirsch, R., Helmick, C. G., Jordan, J. M., Kington, R. S., Lane, N. E., Nevitt, M. C., Zhang, Y., Sowers, M., McAlindon, T., Spector, T. D., Poole, A. R., Yanovski, S. Z., Ateshian, G., Sharma, L., Buckwalter, J. A., Brandt, K. D., and Fries, J. F. (2000). Osteoarthritis: New Insights. Part 1: The Disease and Its Risk Factors. *Annals of Internal Medicine*, 133(8):635--646, DOI:10.7326/0003-4819-133-8-200010170-00016. http://dx.doi.org/10.7326/0003-4819-133-8-200010170-00016.

Ferguson, S., Bryant, J., Ganz, R., and Ito, K. (2003). An in vitro investigation of the acetabular labral seal in hip joint mechanics. *Journal of Biomechanics*, 36(2):171--178, DOI:10.1016/S0021-9290(02)00365-2. http://www.sciencedirect.com/science/article/pii/S0021929002003652.

Fife, R. S., Brandt, K. D., Braunstein, E. M., Katz, B. P., Shelbourne, K. D., Kalasinski, L. A., and Ryan, S. (1991). Relationship between arthroscopic evidence of cartilage damage and radiographic evidence of joint space narrowing in early osteoarthritis of the knee. *Arthritis & Rheumatism*, 34(4):377--382, DOI:10.1002/art.1780340402. http://dx.doi.org/10.1002/art.1780340402.

Fischler, M. A. and Bolles, R. C. (1981). Random sample consensus: A paradigm for model fitting with applications to image analysis and automated cartography. *Commun. ACM*, 24(6):381--395, DOI:10.1145/358669.358692. http://dx.doi.org/10.1145/358669.358692.

Folkesson, J., Dam, E., Olsen, O., Pettersen, P., and Christiansen, C. (2007). Segmenting articular cartilage automatically using a voxel classification approach. *Medical Imaging, IEEE Transactions*

on, 26(1):106--115, DOI:10.1109/TMI.2006.886808. http://dx.doi.org/10.1109/TMI.2006.886808.

Friedrich, K. M., Reiter, G., Kaiser, B., Mayerhöfer, M., Deimling, M., Jellus, V., Horger, W., Trattnig, S., Schweitzer, M., and Salomonowitz, E. (2011). High-resolution cartilage imaging of the knee at 3T: Basic evaluation of modern isotropic 3D MR-sequences. *European Journal of Radiology*, 78(3):398--405, DOI:10.1016/j.ejrad.2010.01.008. Undergraduate Teaching. http://www.sciencedirect.com/science/article/pii/S0720048X10000252.

Fripp, J., Crozier, S., Warfield, S., and Ourselin, S. (2010). Automatic segmentation and quantitative analysis of the articular cartilages from magnetic resonance images of the knee. *Medical Imaging, IEEE Transactions on*, 29(1):55--64, DOI:10.1109/TMI.2009.2024743. http://dx.doi.org/10.1109/TMI.2009.2024743.

Fripp, J., Crozier, S., Warfield, S. K., and Ourselin, S. (2007). Automatic segmentation of the bone and extraction of the bone–cartilage interface from magnetic resonance images of the knee. *Physics in Medicine and Biology*, 52(6):1617. http://stacks.iop.org/0031-9155/52/i=6/a=005.

Ganz, R., Parvizi, J., Beck, M., Leunig, M., Nötzli, H., and Siebenrock, K. A. (2003). Femoroacetabular impingement: a cause for osteoarthritis of the hip. *Clinical orthopaedics and related research*, 417:112--120. http://europepmc.org/abstract/MED/14646708.

Garvin, M. and Wu, X. (2014). Graph algorithmic techniques for biomedical image segmentation. In Saha, P. K., Maulik, U., and Basu, S., editors, *Advanced Computational Approaches to Biomedical Engineering*, pages 3--45. Springer Berlin Heidelberg. http://dx.doi.org/10.1007/978-3-642-41539-5_1.

Gerig, G., Jomier, M., and Chakos, M. (2001). Valmet: A New Validation Tool for Assessing and Improving 3D Object Segmentation. In Niessen, W. and Viergever, M., editors, *Medical Image Computing and Computer-Assisted Intervention – MICCAI 2001*, volume 2208 of *Lecture Notes in Computer Science*, pages 516--523. Springer Berlin Heidelberg. http://dx.doi.org/10.1007/3-540-45468-3_62.

Goldring, M. B. and Goldring, S. R. (2010). Articular cartilage and subchondral bone in the pathogenesis of osteoarthritis. *Annals of the New York Academy of Sciences*, 1192(1):230--237, DOI:10.1111/j.1749-6632.2009.05240.x. http://dx.doi.org/10.1111/j.1749-6632.2009.05240.x.

Gossec, L., Jordan, J., Lam, M.-A., Fang, F., Renner, J., Davis, A., Hawker, G., Dougados, M., and Maillefert, J. (2009). Comparative evaluation of three semi-quantitative radiographic grading techniques for hip osteoarthritis in terms of validity and reproducibility in 1404 radiographs: report of the oarsi-omeract task force. *Osteoarthritis and Cartilage*, 17(2):182--187, DOI:10.1016/j.joca.2008.06.009. http://www.sciencedirect.com/science/article/pii/S1063458408002069.

Gosvig, K. K., Jacobsen, S., Palm, H., Sonne-Holm, S., and Magnusson, E. (2007). A new radiological index for assessing asphericity of the femoral head in cam impingement. *Journal of Bone & Joint Surgery, British Volume*, 89-B(10):1309--1316, DOI:10.1302/0301-620X.89B10.19405. http://www.bjj.boneandjoint.org.uk/content/89-B/10/1309.abstract.

Gower, J. (1975). Generalized procrustes analysis. *Psychometrika*, 40(1).

Guo, C., Cheng, Y., Guo, H., Wang, J., Wang, Y., and Tamura, S. (2015). Surface-based rigid registration using a global optimization algorithm for assessment of MRI knee cartilage thickness changes. *Biomedical Signal Processing and Control*, 18(0):303--316, DOI:10.1016/j.bspc.2015.02.007. http://www.sciencedirect.com/science/article/pii/S1746809415000191.

Harris, M., Reese, S., Peters, C., Weiss, J., and Anderson, A. (2013a). Three-dimensional quantification of femoral head shape in controls and patients with cam-type femoroacetabular impingement. *Annals of Biomedical Engineering*, 41(6):1162--1171, DOI:10.1007/s10439-013-0762-1. http://dx.doi.org/10.1007/s10439-013-0762-1.

Harris, M. D., Datar, M., Whitaker, R. T., Jurrus, E. R., Peters, C. L., and Anderson, A. E. (2013b). Statistical shape modeling of cam femoroacetabular impingement. *Journal of Orthopaedic Research*, 31(10):1620--1626, DOI:10.1002/jor.22389. http://dx.doi.org/10.1002/jor.22389.

Harris, M. D., Kapron, A. L., Peters, C. L., and Anderson, A. E. (2014). Correlations between the alpha angle and femoral head asphericity: Implications and recommendations for the diagnosis of cam femoroacetabular impingement. *European Journal of Radiology*, 83(5):788--796, DOI:10.1016/j.ejrad.2014.02.005. http://dx.doi.org/10.1016/j.ejrad.2014.02.005.

Hayashi, D., Roemer, F., and Guermazi, A. (2012). Osteoarthritis year 2011 in review: imaging in OA – a radiologists' perspective. *Osteoarthritis and Cartilage*, 20(3):207--214, DOI:http://dx.doi.org/10.1016/j.joca.2011.12.016. http://www.sciencedirect.com/science/article/pii/S1063458412000313.

Heckemann, R. A., Hajnal, J. V., Aljabar, P., Rueckert, D., and Hammers, A. (2006). Automatic anatomical brain MRI segmentation combining label propagation and decision fusion. *NeuroImage*, 33(1):115--126, DOI:10.1016/j.neuroimage.2006.05.061. http://www.sciencedirect.com/science/article/pii/S1053811906006458.

Heimann, T. and Meinzer, H.-P. (2009). Statistical shape models for 3d medical image segmentation: A review. *Medical Image Analysis*, 13(4):543--563, DOI:10.1016/j.media.2009.05.004. http://www.sciencedirect.com/science/article/pii/S1361841509000425.

Henak, C. R., Ellis, B. J., Harris, M. D., Anderson, A. E., Peters, C. L., and Weiss, J. A. (2011). Role of the acetabular labrum in load support across the hip joint. *Journal of Biomechanics*, 44(12):2201--2206, DOI:10.1016/j.jbiomech.2011.06.011. http://www.sciencedirect.com/science/article/pii/S0021929011004568.

Ho, C. P., Surowiec, R. K., Ferro, F. P., Lucas, E. P., Saroki, A. J., Dornan, G. J., Fitzcharles, E. K., Anz, A. W., Smith, W. S., Wilson, K. J., and Philippon, M. J. (2014). Subregional anatomical distribution of T2 values of articular cartilage in asymptomatic hips. *Cartilage*, DOI:10.1177/1947603514529587. http://car.sagepub.com/content/early/2014/04/14/1947603514529587.abstract.

Hochbaum, D. S. (2001). An efficient algorithm for image segmentation, markov random fields and related problems. *J. ACM*, 48(4):686--701, DOI:10.1145/502090.502093. http://doi.acm.org/10.1145/502090.502093.

Hodler, J., Trudell, D., Pathria, M., and Resnick, D. (1992). Width of the articular cartilage of the hip: quantification by using fat-suppression spin-echo mr imaging in cadavers. *AJR. American journal of roentgenology*, 159(2):351--355, DOI:10.2214/ajr.159.2.1632354. http://intl.ajronline.org/cgi/reprint/159/2/351.pdf.

Ibanez, L., Schroeder, W., Ng, L., and Cates, J. (2003). The ITK software guide: the insight segmentation and registration toolkit. *Kitware Inc*, 5.

Ito, K., Minka-II, M.-A., Leunig, M., Werlen, S., and Ganz, R. (2001). Femoroacetabular impingement and the cam-effect: A mri-based quantitative anatomical study of the femoral head-neck offset. *Journal of Bone & Joint Surgery, British Volume*, 83-B(2):171--176, DOI:10.1302/0301-620X.83B2.11092. http://www.bjj.boneandjoint.org.uk/content/83-B/2/171.abstract.

Johnston, R. C. (1973). Mechanical considerations of the hip joint. *Archives of Surgery*, 107(3):411--417, DOI:10.1001/archsurg.1973.01350210047015. http://dx.doi.org/10.1001/archsurg.1973.01350210047015.

Johnston, T. L., Schenker, M. L., Briggs, K. K., and Philippon, M. J. (2008). Relationship between offset angle alpha and hip chondral injury in femoroacetabular impingement. *Arthroscopy: The Journal of Arthroscopic & Related Surgery*, 24(6):669--675, DOI:10.1016/j.arthro.2008.01.010. http://dx.doi.org/10.1016/j.arthro.2008.01.010.

Jolliffe, I. (2005). *Principal Component Analysis*. John Wiley & Sons, Ltd. http://dx.doi.org/10.1002/0470013192.bsa501.

Jung, K. A., Restrepo, C., Hellman, M., AbdelSalam, H., Morrison, W., and Parvizi, J. (2011). The prevalence of cam-type femoroacetabular deformity in asymptomatic adults. *Journal of Bone & Joint Surgery, British Volume*, 93-B(10):1303--1307, DOI:10.1302/0301-620X.93B10.26433. http://www.bjj.boneandjoint.org.uk/content/93-B/10/1303.abstract.

Kainmueller, D., Lamecker, H., Zachow, S., and Hege, H.-C. (2009). An articulated statistical shape model for accurate hip joint segmentation. In *Engineering in Medicine and Biology Society, 2009. EMBC 2009. Annual International Conference of the IEEE*, pages 6345--6351. http://dx.doi.org/10.1109/IEMBS.2009.5333269.

Kang, A. C. L., Gooding, A. J., Coates, M. H., Goh, T. D., Armour, P., and Rietveld, J. (2010). Computed tomography assessment of hip joints in asymptomatic individuals in relation to femoroacetabular impingement. *The American Journal of Sports Medicine*, 38(6):1160--1165, DOI:10.1177/0363546509358320. http://ajs.sagepub.com/content/38/6/1160.abstract.

Kang, X., Zhang, H., Garbuz, D., Wilson, D., and Hodgson, A. (2013). Preliminary evaluation of an MRI-based technique for displaying and quantifying bony deformities in cam-type femoroacetabular impingement. *International Journal of Computer Assisted Radiology and Surgery*, 8(6):967--975, DOI:10.1007/s11548-013-0837-3. http://dx.doi.org/10.1007/s11548-013-0837-3.

Karachalios, T., Karantanas, A. H., and Malizos, K. (2007). Hip osteoarthritis: What the radiologist wants to know. *European Journal of Radiology*, 63(1):36--48, DOI:10.1016/j.ejrad.2007.03.022. Hip Joint. http://dx.doi.org/10.1016/j.ejrad.2007.03.022.

Kavanagh, E., Read, P., Carty, F., Zoga, A., Parvizi, J., and Morrison, W. (2011). Three-dimensional magnetic resonance imaging analysis of hip morphology in the assessment of femoral acetabular impingement. *Clinical Radiology*, 66(8):742--747, DOI:10.1016/j.crad.2011.02.014. http://www.sciencedirect.com/science/article/pii/S0009926011001231.

Kijowski, R. (2010). Clinical cartilage imaging of the knee and hip joints. *American Journal of Roentgenology*, 195(3):618--628, DOI:10.2214/ajr.10.4661. http://intl.ajronline.org/cgi/reprint/195/3/618.pdf.

Kijowski, R., Davis, K. W., Woods, M. A., Lindstrom, M. J., De Smet, A. A., Gold, G. E., and Busse, R. F. (2009). Knee joint: comprehensive assessment with 3D isotropic resolution fast spin-echo MR imaging--diagnostic performance compared with that of conventional mr imaging at 3.0 t. *Radiology*, 252(2):486--495, DOI:10.1148/radiol.2523090028. http://intl-radiology.rsnajnls.org/cgi/content/full/252/2/486.

Kijowski, R. and Gold, G. E. (2011). Routine 3D magnetic resonance imaging of joints. *Journal of magnetic resonance imaging : JMRI*, 33(4):758--771, DOI:10.1002/jmri.22342. http://europepmc.org/articles/PMC3069719.

Kornaat, P., Reeder, S., Koo, S., Brittain, J., Yu, H., Andriacchi, T., and Gold, G. (2005). MR imaging of articular cartilage at 1.5t and 3.0t: Comparison of SPGR and SSFP sequences. *Osteoarthritis and Cartilage*, 13(4):338--344, DOI:10.1016/j.joca.2004.12.008. http://www.sciencedirect.com/science/article/pii/S1063458404002833.

Kurrat, H. J. and Oberländer, W. (1978). The thickness of the cartilage in the hip joint. *Journal of anatomy*, 126(Pt 1):145--155. http://europepmc.org/articles/PMC1235719.

Lane, N. E. (2007). Osteoarthritis of the hip. *New England Journal of Medicine*, 357(14):1413--1421, DOI:10.1056/NEJMcp071112. PMID: 17914042. http://www.nejm.org/doi/full/10.1056/NEJMcp071112.

Larson, C. M. (2012). Pincer-type femoroacetabular impingement. *Operative Techniques in Sports Medicine*, 20(4):273--280, DOI:10.1053/j.otsm.2012.08.004. Innovations in Hip Arthroscopy. http://dx.doi.org/10.1053/j.otsm.2012.08.004.

Lattanzi, R., Petchprapa, C., Ascani, D., Babb, J., Chu, D., Davidovitch, R., Youm, T., Meislin, R., and Recht, M. (2014). Detection of cartilage damage in femoroacetabular impingement with standardized dGEMRIC at 3 T. *Osteoarthritis and Cartilage*, 22(3):447--456, DOI:10.1016/j.joca.2013.12.022. http://www.sciencedirect.com/science/article/pii/S1063458414000120.

Laupacis, A., Bourne, R., Rorabeck, C., Feeny, D., Wong, C., Tugwell, P., Leslie, K., and Bullas, R. (1993). The effect of elective total hip replacement on health-related quality of life. *The Journal of Bone & Joint Surgery*, 75(11):1619--1626.

Lavigne, M., Parvizi, J., Beck, M., Siebenrock, K. A., Ganz, R., and Leunig, M. (2004). Anterior femoroacetabular impingement: part i. techniques of joint preserving surgery. *Clinical orthopaedics and related research*, 418:61--66. http://europepmc.org/abstract/MED/15043094.

Lee, S., Park, S. H., Shim, H., Yun, I. D., and Lee, S. U. (2011). Optimization of local shape and appearance probabilities for segmentation of knee cartilage in 3-D MR images. *Computer Vision and Image Understanding*, 115(12):1710--1720, DOI:10.1016/j.cviu.2011.05.014. Special issue on Optimization for Vision, Graphics and Medical Imaging: Theory and Applications. http://www.sciencedirect.com/science/article/pii/S1077314211001639.

Lepage-Saucier, M., Thiéry, C., Larbi, A., Lecouvet, F., Vande Berg, B., and Omoumi, P. (2014). Femoroacetabular impingement: normal values of the quantitative morphometric parameters in asymptomatic hips. *European Radiology*, 24(7):1707--1714, DOI:10.1007/s00330-014-3171-4. http://dx.doi.org/10.1007/s00330-014-3171-4.

Leunig, M., Beaulé, P., and Ganz, R. (2009). The concept of femoroacetabular impingement: Current status and future perspectives. *Clinical Orthopaedics and Related Research*, 467(3):616--622, DOI:10.1007/s11999-008-0646-0. http://dx.doi.org/10.1007/s11999-008-0646-0.

Levangie, P. K. and Norkin, C. C. (1992). *Joint structure and function: a comprehensive analysis*. Mosby inc.

Li, K., Millington, S., Wu, X., Chen, D., and Sonka, M. (2005). Simultaneous segmentation of multiple closed surfaces using optimal graph searching. In Christensen, G. and Sonka, M., editors, *Information Processing in Medical Imaging*, volume 3565 of *Lecture Notes in Computer Science*, pages 406--417. Springer Berlin Heidelberg. http://dx.doi.org/10.1007/11505730_34.

Li, K., Wu, X., Chen, D., and Sonka, M. (2006). Optimal surface segmentation in volumetric images-a graph-theoretic approach. *Pattern Analysis and Machine Intelligence, IEEE Transactions on*, 28(1):119--134, DOI:10.1109/TPAMI.2006.19. http://dx.doi.org/10.1109/TPAMI.2006.19.

Li, P. L. and Ganz, R. (2003). Morphologic features of congenital acetabular dysplasia: one in six is retroverted. *Clinical orthopaedics and related research*, 416:245--253. http://europepmc.org/abstract/MED/14646767.

Li, W., Abram, F., Beaudoin, G., Berthiaume, M.-J., Pelletier, J.-P., and Martel-Pelletier, J. (2008). Human hip joint cartilage: MRI quantitative thickness and volume measurements discriminating acetabulum and femoral head. *Biomedical Engineering, IEEE Transactions on*, 55(12):2731--2740, DOI:10.1109/TBME.2008.925679. http://dx.doi.org/10.1109/TBME.2008.925679.

Liess, C., Lüsse, S., Karger, N., Heller, M., and Glüer, C. (2002). Detection of changes in cartilage water content using MRI T2-mapping in vivo. *Osteoarthritis and cartilage / OARS, Osteoarthritis Research Society*, 10(12):907--913, DOI:10.1053/joca.2002.0847. http://dx.doi.org/10.1053/joca.2002.0847.

Ling, W., Regatte, R. R., Navon, G., and Jerschow, A. (2008). Assessment of glycosaminoglycan concentration in vivo by chemical exchange-dependent saturation transfer (gagCEST). *Proceedings of the National Academy of Sciences*, 105(7):2266--2270, DOI:10.1073/pnas.0707666105. http://www.pnas.org/content/105/7/2266.abstract.

Link, T. (2011). MRI of cartilage: Standard techniques. In Link, T. M., editor, *Cartilage Imaging*, pages 49--66. Springer New York. http://dx.doi.org/10.1007/978-1-4419-8438-8_6.

Link, T., Sell, C., Masi, J., Phan, C., Newitt, D., Lu, Y., Steinbach, L., and Majumdar, S. (2006). 3.0 vs 1.5 T MRI in the detection of focal cartilage pathology - ROC analysis in an experimental model. *Osteoarthritis and Cartilage*, 14(1):63--70, DOI:http://dx.doi.org/10.1016/j.joca.2005.08.002. http://www.sciencedirect.com/science/article/pii/S1063458405002244.

Litjens, G., Toth, R., van de Ven, W., Hoeks, C., Kerkstra, S., van Ginneken, B., Vincent, G., Guillard, G., Birbeck, N., Zhang, J., Strand, R., Malmberg, F., Ou, Y., Davatzikos, C., Kirschner, M., Jung, F., Yuan, J., Qiu, W., Gao, Q., Edwards, P., Maan, B., van der Heijden, F., Ghose, S., Mitra, J., Dowling, J., Barratt, D., Huisman, H., and Madabhushi, A. (2014). Evaluation of prostate segmentation algorithms for mri: The PROMISE12 challenge. *Medical Image Analysis*, 18(2):359--373, DOI:10.1016/j.media.2013.12.002. http://www.sciencedirect.com/science/article/pii/S1361841513001734.

Liu, B., Hua, S., Zhang, H., Liu, Z., Zhao, X., Zhang, B., and Yue, Z. (2014). A personalized ellipsoid modeling method and matching error analysis for the artificial femoral head design. *Computer-Aided Design*, 56(0):88--103, DOI:10.1016/j.cad.2014.06.009. http://www.sciencedirect.com/science/article/pii/S0010448514001274.

Lloyd-Roberts, G. C. (1955). Osteoarthritis of the hip: A study of the clinical pathology. *Journal of Bone & Joint Surgery, British Volume*, 37-B(1):8--47. http://www.bjj.boneandjoint.org.uk/content/37-B/1/8.abstract.

Lories, R. J. and Luyten, F. P. (2011). The bone-cartilage unit in osteoarthritis. *Nature reviews. Rheumatology*, 7(1):43--49, DOI:10.1038/nrrheum.2010.197. http://dx.doi.org/10.1038/nrrheum.2010.197.

Mamisch, T. C., Kain, M. S. H., Bittersohl, B., Apprich, S., Werlen, S., Beck, M., and Siebenrock, K. A. (2011). Delayed gadolinium-enhanced magnetic resonance imaging of cartilage (dGEMRIC) in femoacetabular impingement. *Journal of Orthopaedic Research*, 29(9):1305--1311, DOI:10.1002/jor.21371. http://dx.doi.org/10.1002/jor.21371.

Marín-Peña, O. (2012). Physical exam in fai. In Marín-Peña, □., editor, *Femoroacetabular Impingement*, pages 23--27. Springer Berlin Heidelberg. http://dx.doi.org/10.1007/978-3-642-22769-1_3.

Masjedi, M., Harris, S. J., Davda, K., and Cobb, J. P. (2013a). Mathematical representation of the normal proximal human femur: Application in planning of cam hip surgery. *Proceedings of the Institution of Mechanical Engineers, Part H: Journal of Engineering in Medicine*, 227(4):421--427, DOI:10.1177/0954411912466353. http://dx.doi.org/10.1177/0954411912466353.

Masjedi, M., Marquardt, C., Drummond, I., Harris, S., and Cobb, J. (2013b). Cam type femoroacetabular impingement: quantifying the diagnosis using three dimensional head-neck ratios. *Skeletal Radiology*, 42(3):329--333, DOI:10.1007/s00256-012-1459-5. http://dx.doi.org/10.1007/s00256-012-1459-5.

McConnell, S., Kolopack, P., and Davis, A. M. (2001). The Western Ontario and McMaster Universities Osteoarthritis Index (WOMAC): a review of its utility and measurement properties. *Arthritis Care & Research*, 45(5):453--461, DOI:10.1002/1529-0131(200110)45:5<453::AID-ART365>3.0.CO;2-W. http://dx.doi.org/10.1002/1529-0131(200110)45:5<453::AID-ART365>3.0.CO;2-W.

Mechlenburg, I., Nyengaard, J., Gelineck, J., and Soballe, K. (2007). Cartilage thickness in the hip joint measured by mri and stereology – a methodological study. *Osteoarthritis and Cartilage*, 15(4):366--371, DOI:10.1016/j.joca.2006.10.005. http://www.sciencedirect.com/science/article/pii/S1063458406002925.

Meyer, D. C., Beck, M., Ellis, T., Ganz, R., and Leunig, M. (2006). Comparison of six radiographic projections to assess femoral head/neck asphericity. *Clinical orthopaedics and related research*, 445:181--185, DOI:10.1097/01.blo.0000201168.72388.24. http://dx.doi.org/10.1097/01.blo.0000201168.72388.24.

Mintz, D. N., Hooper, T., Connell, D., Buly, R., Padgett, D. E., and Potter, H. G. (2005). Magnetic resonance imaging of the hip: Detection of labral and chondral abnormalities using noncontrast imaging. *Arthroscopy: The Journal of Arthroscopic & Related Surgery*, 21(4):385--393, DOI:10.1016/j.arthro.2004.12.011. http://www.sciencedirect.com/science/article/pii/S0749806304013994.

Modat, M., Ridgway, G. R., Taylor, Z. A., Lehmann, M., Barnes, J., Hawkes, D. J., Fox, N. C., and Ourselin, S. (2010). Fast free-form deformation using graphics processing units. *Computer Methods and Programs in Biomedicine*, 98(3):278--284, DOI:10.1016/j.cmpb.2009.09.002. HP-MICCAI 2008. http://www.sciencedirect.com/science/article/pii/S0169260709002533.

Mosher, T. J. and Pruett, S. W. (1999). Magnetic resonance imaging of superficial cartilage lesions: Role of contrast in lesion detection. *Journal of Magnetic Resonance Imaging*, 10(2):178--182, DOI:10.1002/(SICI)1522-2586(199908)10:2<178::AID-JMRI11>3.0.CO;2-W. http://dx.doi.org/10.1002/(SICI)1522-2586(199908)10:2<178::AID-JMRI11>3.0.CO;2-W.

Murphy, S. B., Ganz, R., and Müller, M. E. (1995). The prognosis in untreated dysplasia of the hip. a study of radiographic factors that predict the outcome. *The Journal of Bone & Joint Surgery*, 77(7):985--989. http://europepmc.org/abstract/MED/7608241.

Murray, D., Crown, R., Dickersin, K., and et al (1995). Total hip replacement. *JAMA*, 273(24):1950--1956, DOI:10.1001/jama.1995.03520480070043. http://dx.doi.org/10.1001/jama.1995.03520480070043.

Müller-Gerbl, M., Putz, R., and Kenn, R. (1992). Demonstration of subchondral bone density patterns by three-dimensional ct osteoabsorptiometry as a noninvasive method for in vivo assessment of individual long-term stresses in joints. *Journal of Bone and Mineral Research*, 7(S2):S411--S418, DOI:10.1002/jbmr.5650071409. http://dx.doi.org/10.1002/jbmr.5650071409.

Naish, J., Xanthopoulos, E., Hutchinson, C., Waterton, J., and Taylor, C. (2006). MR measurement of articular cartilage thickness distribution in the hip. *Osteoarthritis and cartilage*, 14(10):967--973, DOI:10.1016/j.joca.2006.03.017. http://dx.doi.org/10.1016/j.joca.2006.03.017.

Nakanishi, K., Tanaka, H., Sugano, N., Sato, Y., Ueguchi, T., Kubota, T., Tamura, S., and Nakamura, H. (2001). MR-based three-dimensional presentation of cartilage thickness in the femoral head. *European Radiology*, 11(11):2178--2183, DOI:10.1007/s003300100842. http://dx.doi.org/10.1007/s003300100842.

Naraghi, A. and White, L. M. (2012). Three-dimensional MRI of the musculoskeletal system. *AJR. American journal of roentgenology*, 199(3):W283--93, DOI:10.2214/ajr.12.9099. http://dx.doi.org/10.2214/AJR.12.9099.

Neubert, A., Fripp, J., Engstrom, C., Schwarz, R., Lauer, L., Salvado, O., and Crozier, S. (2012). Automated detection, 3D segmentation and analysis of high resolution spine MR images using statistical shape models. *Physics in Medicine and Biology*, 57(24):8357. http://stacks.iop.org/0031-9155/57/i=24/a=8357.

Nishii, T., Nakanishi, K., Sugano, N., Masuhara, K., Ohzono, K., and Ochi, T. (1998). Articular cartilage evaluation in osteoarthritis of the hip with MR imaging under continuous leg traction. *Magnetic Resonance Imaging*, 16(8):871--875, DOI:10.1016/S0730-725X(98)00009-5. http://www.sciencedirect.com/science/article/pii/S0730725X98000095.

Nishii, T., Shiomi, T., Tanaka, H., Yamazaki, Y., Murase, K., and Sugano, N. (2010). Loaded cartilage T2 mapping in patients with hip dysplasia. *Radiology*, 256(3):955--965, DOI:10.1148/radiol.10091928. http://pubs.rsna.org/doi/abs/10.1148/radiol.10091928.

Nishii, T., Sugano, N., Sato, Y., Tanaka, H., Miki, H., and Yoshikawa, H. (2004). Three-dimensional distribution of acetabular cartilage thickness in patients with hip dysplasia: a fully automated computational analysis of MR imaging. *Osteoarthritis and Cartilage*, 12(8):650--657, DOI:10.1016/j.joca.2004.04.009. http://www.sciencedirect.com/science/article/pii/S1063458404000846.

Nishii, T., Tanaka, H., Sugano, N., Sakai, T., Hananouchi, T., and Yoshikawa, H. (2008). Evaluation of cartilage matrix disorders by T2 relaxation time in patients with hip dysplasia. *Osteoarthritis and cartilage / OARS, Osteoarthritis Research Society*, 16(2):227--233, DOI:10.1016/j.joca.2007.06.003. http://dx.doi.org/10.1016/j.joca.2007.06.003.

Notohamiprodjo, M., Horng, A., Pietschmann, M. F., Müller, P. E., Horger, W., Park, J., Crispin, A., del Olmo, J. R. G., Weckbach, S., Herrmann, K. A., Reiser, M. F., and Glaser, C. (2009). Mri of the knee at 3t: first clinical results with an isotropic pdfs-weighted 3d-tse-sequence. *Investigative radiology*, 44(9):585--597, DOI:10.1097/rli.0b013e3181b4c1a1. http://dx.doi.org/10.1097/RLI.0b013e3181b4c1a1.

Nouh, M. R., Schweitzer, M. E., Rybak, L., and Cohen, J. (2008). Femoroacetabular impingement: can the alpha angle be estimated? *American Journal of Roentgenology*, 190(5):1260--1262.

Nötzli, H. P., Wyss, T. F., Stoecklin, C. H., Schmid, M. R., Treiber, K., and Hodler, J. (2002). The contour of the femoral head-neck junction as a predictor for the risk of anterior impingement. *Journal of Bone & Joint Surgery, British Volume*, 84-B(4):556--560, DOI:10.1302/0301-620X.84B4.12014. http://www.bjj.boneandjoint.org.uk/content/84-B/4/556.abstract.

Palmer, A. J. R., Brown, C. P., McNally, E. G., Price, A. J., Tracey, I., Jezzard, P., Carr, A. J., and Glyn-Jones, S. (2013). Non-invasive imaging of cartilage in early osteoarthritis. *Bone & Joint Journal*, 95-B(6):738--746, DOI:10.1302/0301-620X.95B6.31414. http://www.bjj.boneandjoint.org.uk/content/95-B/6/738.abstract.

Park, S. H., Lee, S., Yun, I. D., and Lee, S. U. (2013). Hierarchical MRF of globally consistent localized classifiers for 3D medical image segmentation. *Pattern Recognition*, 46(9):2408--2419, DOI:10.1016/j.patcog.2013.02.014. http://www.sciencedirect.com/science/article/pii/S0031320313001076.

Paulsen, F. and Waschke, J. (2013). *Sobotta atlas of human anatomy*, volume 1. Elsevier Health Science.

Perepezko, E., Kalscheur, V., Checovich, M., Rho, J.-Y., Vanderby, R., and Heiner, J. (2002). Osteoarthritic changes in cartilage and subchondral bone. In *Engineering in Medicine and Biology,*

2002. 24th Annual Conference and the Annual Fall Meeting of the Biomedical Engineering Society EMBS/BMES Conference, 2002. Proceedings of the Second Joint, volume 3, pages 2589--2590. http://dx.doi.org/10.1109/IEMBS.2002.1053440.

Peterfy, C., Schneider, E., and Nevitt, M. (2008). The osteoarthritis initiative: report on the design rationale for the magnetic resonance imaging protocol for the knee. *Osteoarthritis and Cartilage*, 16(12):1433--1441, DOI:10.1016/j.joca.2008.06.016. http://www.sciencedirect.com/science/article/pii/S1063458408002239.

Pfirrmann, C. W. A., Mengiardi, B., Dora, C., Kalberer, F., Zanetti, M., and Hodler, J. (2006). Cam and pincer femoroacetabular impingement: Characteristic MR arthrographic findings in 50 patients. *Radiology*, 240(3):778--785, DOI:10.1148/radiol.2403050767. PMID: 16857978. http://dx.doi.org/10.1148/radiol.2403050767.

Philippon, M., Maxwell, R., Johnston, T., Schenker, M., and Briggs, K. (2007). Clinical presentation of femoroacetabular impingement. *Knee Surgery, Sports Traumatology, Arthroscopy*, 15(8):1041--1047, DOI:10.1007/s00167-007-0348-2. http://dx.doi.org/10.1007/s00167-007-0348-2.

Pollard, T. (2011). A perspective on femoroacetabular impingement. *Skeletal Radiology*, 40(7):815--818, DOI:10.1007/s00256-011-1137-z. http://dx.doi.org/10.1007/s00256-011-1137-z.

Potter, H. G., Black, B. R., and Chong, L. R. (2009). New techniques in articular cartilage imaging. *Clinics in Sports Medicine*, 28(1):77--94, DOI:10.1016/j.csm.2008.08.004. Future Trends in Sports Medicine. http://www.sciencedirect.com/science/article/pii/S0278591908000720.

Pritzker, K., Gay, S., Jimenez, S., Ostergaard, K., Pelletier, J.-P., Revell, P., Salter, D., and van den Berg, W. (2006). Osteoarthritis cartilage histopathology: grading and staging. *Osteoarthritis and Cartilage*, 14(1):13--29, DOI:10.1016/j.joca.2005.07.014. http://www.sciencedirect.com/science/article/pii/S1063458405001974.

Radin, E. L. and Rose, R. M. (1986). Role of subchondral bone in the initiation and progression of cartilage damage. *Clinical orthopaedics and related research*, 213:34--40. http://europepmc.org/abstract/MED/3780104.

Rakhra, K., Sheikh, A., Allen, D., and Beaulé, P. (2009). Comparison of mri alpha angle measurement planes in femoroacetabular impingement. *Clinical Orthopaedics and Related Research*, 467(3):660--665, DOI:10.1007/s11999-008-0627-3. http://dx.doi.org/10.1007/s11999-008-0627-3.

Rakhra, K. S., Lattanzio, P.-J., Cárdenas-Blanco, A., Cameron, I. G., and Beaulé, P. E. (2012). Can T1-rho MRI detect acetabular cartilage degeneration in femoroacetabular impingement?: A pilot study. *Journal of Bone & Joint Surgery, British Volume*, 94-B(9):1187--1192, DOI:10.1302/0301-620X.94B9.29981. http://dx.doi.org/10.1302/0301-620X.94B9.29981.

Ravaud, P. and Dougados, M. (1997). Radiographic assessment in osteoarthritis. *The Journal of rheumatology*, 24(4):786--791. http://europepmc.org/abstract/MED/9101519.

Roach, H. and Tilley, S. (2007). The pathogenesis of osteoarthritis. In Bronner, F. and Farach-Carson, M., editors, *Bone and Osteoarthritis*, volume 4 of *Topics in Bone Biology*, pages 1--18. Springer London. http://dx.doi.org/10.1007/978-1-84628-701-5_1.

Roemer, F., Hunter, D., Winterstein, A., Li, L., Kim, Y., Cibere, J., Mamisch, T., and Guermazi, A. (2011). Hip Osteoarthritis MRI Scoring System (HOAMS): reliability and associations with radiographic and clinical findings. *Osteoarthritis and Cartilage*, 19(8):946--962, DOI:10.1016/j.joca.2011.04.003. http://www.sciencedirect.com/science/article/pii/S1063458411001117.

Rogowska, J. (2000). Overview and fundamentals of medical image segmentation. In *Handbook of medical imaging*, pages 69--85. Academic Press, Inc.

Rohlfing, T., Brandt, R., Menzel, R., and Jr., C. R. M. (2004). Evaluation of atlas selection strategies for atlas-based image segmentation with application to confocal microscopy images of bee brains. *NeuroImage*, 21(4):1428--1442, DOI:10.1016/j.neuroimage.2003.11.010. http://www.sciencedirect.com/science/article/pii/S1053811903007316.

Sato, Y., Nakanishi, K., Tanaka, H., Sugano, N., Nishii, T., Nakamura, H., Ochi, T., and Tamura, S. (2001). A fully automated method for segmentation and thickness determination of hip joint cartilage from 3D MR data. *International Congress Series*, 1230(0):352--358, DOI:10.1016/S0531-5131(01)00029-2. Computer Assisted Radiology and Surgery. http://www.sciencedirect.com/science/article/pii/S0531513101000292.

Schmid, J., Kim, J., and Magnenat-Thalmann, N. (2011). Robust statistical shape models for MRI bone segmentation in presence of small field of view. *Medical Image Analysis*, 15(1):155--168, DOI:10.1016/j.media.2010.09.001. http://www.sciencedirect.com/science/article/pii/S1361841510001118.

Seim, H., Kainmueller, D., Lamecker, H., Bindernagel, M., Malinowski, J., and Zachow, S. (2010). Model-based auto-segmentation of knee bones and cartilage in MRI data. *Proc. Medical Image Analysis for the Clinic: A Grand Challenge. Bejing, China*, pages 215--223.

Shan, L., Charles, C., and Niethammer, M. (2012). Automatic multi-atlas-based cartilage segmentation from knee MR images. In *Biomedical Imaging (ISBI), 2012 9th IEEE International Symposium on*, pages 1028--1031. http://dx.doi.org/10.1109/ISBI.2012.6235733.

Sholukha, V., Chapman, T., Salvia, P., Moiseev, F., Euran, F., Rooze, M., and Jan, S. V. S. (2011). Femur shape prediction by multiple regression based on quadric surface fitting. *Journal of Biomechanics*, 44(4):712--718, DOI:10.1016/j.jbiomech.2010.10.039. http://dx.doi.org/10.1016/j.jbiomech.2010.10.039.

Siebenrock, K. and Henle, P. (2012). X-ray examination in FAI. In *Femoroacetabular Impingement*, pages 31--39. Springer Berlin Heidelberg. http://dx.doi.org/10.1007/978-3-642-22769-1_4.

Siebenrock, K., Wahab, K. A., Werlen, S., Kalhor, M., Leunig, M., and Ganz, R. (2004). Abnormal extension of the femoral head epiphysis as a cause of cam impingement. *Clinical orthopaedics and related research*, 418:54--60. http://europepmc.org/abstract/MED/15043093.

Siversson, C., Akhondi-Asl, A., Bixby, S., Kim, Y.-J., and Warfield, S. (2014). Three-dimensional hip cartilage quality assessment of morphology and dGEMRIC by planar maps and automated segmentation. *Osteoarthritis and Cartilage*, 22(10):1511--1515, DOI:http://dx.doi.org/10.1016/j.joca.2014.08.012. Special Themed Issue - Imaging in Osteoarthritis. http://www.sciencedirect.com/science/article/pii/S1063458414012424.

Siversson, C., Akhondi-Asl, A., Kim, Y.-J., and Warfield, S. K. (2013). Planar hip cartilage quality maps - a novel approach to 3D cartilage assessment by combining dGEMRIC with automated segmentation. In *International Society for Magnetic Resonance in Medicine (ISMRM) 21st Scientific Meeting and Exhibition*, page 3535.

Skripkus, U. and Gentili, A. (2006). Radiographic evaluation. In Davies, A., Johnson, K., and Whitehouse, R., editors, *Imaging of the Hip & Bony Pelvis*, Medical Radiology, pages 3--14. Springer Berlin Heidelberg. http://dx.doi.org/10.1007/3-540-30000-7_1.

Song, Q., Bai, J., Garvin, M., Sonka, M., Buatti, J., and Wu, X. (2013). Optimal Multiple Surface Segmentation With Shape and Context Priors. *Medical Imaging, IEEE Transactions on*, 32(2):376--386, DOI:10.1109/TMI.2012.2227120. http://dx.doi.org/10.1109/TMI.2012.2227120.

Song, Q., Liu, Y., Liu, Y., Saha, P., Sonka, M., and Wu, X. (2010). Graph search with appearance and shape information for 3-D prostate and bladder segmentation. In Jiang, T., Navab, N., Pluim, J., and Viergever, M., editors, *Medical Image Computing and Computer-Assisted Intervention – MICCAI 2010*, volume 6363 of *Lecture Notes in Computer Science*, pages 172--180. Springer Berlin Heidelberg. http://dx.doi.org/10.1007/978-3-642-15711-0_22.

Sophia Fox, A. J., Bedi, A., and Rodeo, S. A. (2009). The basic science of articular cartilage: Structure, composition, and function. *Sports Health: A Multidisciplinary Approach*, 1(6):461--468, DOI:10.1177/1941738109350438. http://sph.sagepub.com/content/1/6/461.short.

Standring, S. (2008). *Grayś Anatomy: The Anatomical Basis of Clinical Practice*. Elsevier.

Standring, S., Ellis, H., Healy, J., Johnson, D., Williams, A., Collins, P., and Wigley, C. (2005). Grayś anatomy: the anatomical basis of clinical practice. *American Journal of Neuroradiology*, 26(10):2703.

Subburaj, K., Valentinitsch, A., Dillon, A. B., Joseph, G. B., Li, X., Link, T. M., Vail, T. P., and Majumdar, S. (2013). Regional variations in MR relaxation of hip joint cartilage in subjects with and without femoralacetabular impingement. *Magnetic Resonance Imaging*, 31(7):1129--1136, DOI:10.1016/j.mri.2013.01.009. http://dx.doi.org/10.1016/j.mri.2013.01.009.

Sur, S., Mamisch, T. C., Hughes, T., and Kim, Y.-J. (2009). High resolution fast T1 mapping technique for dGEMRIC. *Journal of Magnetic Resonance Imaging*, 30(4):896--900, DOI:10.1002/jmri.21869. http://dx.doi.org/10.1002/jmri.21869.

Sutter, R., Dietrich, T. J., Zingg, P. O., and Pfirrmann, C. W. (2012). How useful is the alpha angle for discriminating between symptomatic patients with cam-type femoroacetabular impingement and asymptomatic volunteers? *Radiology*, 264(2):514--521, DOI:10.1148/radiol.12112479. PMID: 22653190. http://dx.doi.org/10.1148/radiol.12112479.

Tamez-Pena, J., Farber, J., Gonzalez, P., Schreyer, E., Schneider, E., and Totterman, S. (2012). Unsupervised segmentation and quantification of anatomical knee features: Data from the osteoarthritis initiative. *Biomedical Engineering, IEEE Transactions on*, 59(4):1177--1186, DOI:10.1109/TBME.2012.2186612. http://dx.doi.org/10.1109/TBME.2012.2186612.

Tannast, M., Goricki, D., Beck, M., Murphy, S., and Siebenrock, K. (2008). Hip damage occurs at the zone of femoroacetabular impingement. *Clinical Orthopaedics and Related Research*, 466(2):273--280, DOI:10.1007/s11999-007-0061-y. http://dx.doi.org/10.1007/s11999-007-0061-y.

Tannast, M., Siebenrock, K. A., and Anderson, S. E. (2007). Femoroacetabular impingement: radiographic diagnosis—what the radiologist should know. *American Journal of Roentgenology*, 188(6):1540--1552. http://intl.ajronline.org/cgi/reprint/188/6/1540.pdf.

Tanzer, M. and Noiseux, N. (2004). Osseous abnormalities and early osteoarthritis: the role of hip impingement. *Clinical orthopaedics and related research*, 429:170--177. http://europepmc.org/abstract/MED/15577483.

Toogood, P., Skalak, A., and Cooperman, D. (2009). Proximal femoral anatomy in the normal human population. *Clinical Orthopaedics and Related Research*, 467(4):876--885, DOI:10.1007/s11999-008-0473-3. http://dx.doi.org/10.1007/s11999-008-0473-3.

Tuan, R. S. and Chen, F. H. (2006). Cartilage. In *Stem Cell and Gene-Based Therapy*, pages 179--193. Springer.

Tustison, N., Avants, B., Cook, P., Zheng, Y., Egan, A., Yushkevich, P., and Gee, J. (2010). N4ITK: Improved N3 bias correction. *Medical Imaging, IEEE Transactions on*, 29(6):1310--1320, DOI:10.1109/TMI.2010.2046908. http://dx.doi.org/10.1109/TMI.2010.2046908.

Van Dyck, P., Gielen, J. L., Vanhoenacker, F. M., De Smet, E., Wouters, K., Dossche, L., and Parizel, P. M. (2012). Diagnostic performance of 3d space for comprehensive knee joint assessment at 3 t. *Insights into imaging*, 3(6):603--610, DOI:10.1007/s13244-012-0197-5. http://europepmc.org/articles/PMC3505565.

Van Ginneken, B., Heimann, T., and Styner, M. (2007). 3D segmentation in the clinic: A grand challenge. *3D segmentation in the clinic: a grand challenge*, pages 7--15.

Van Reeth, E., Tham, I. W. K., Tan, C. H., and Poh, C. L. (2012). Super-resolution in magnetic resonance imaging: A review. *Concepts in Magnetic Resonance Part A*, 40A(6):306--325, DOI:10.1002/cmr.a.21249. http://dx.doi.org/10.1002/cmr.a.21249.

Vasanawala, S. S., Hargreaves, B. A., Pauly, J. M., Nishimura, D. G., Beaulieu, C. F., and Gold, G. E. (2005). Rapid musculoskeletal mri with phase-sensitive steady-state free precession: comparison with routine knee mri. *AJR. American journal of roentgenology*, 184(5):1450--1455, DOI:10.2214/ajr.184.5.01841450. http://intl.ajronline.org/cgi/content/full/184/5/1450.

Vercauteren, T., Pennec, X., Perchant, A., and Ayache, N. (2009). Diffeomorphic demons: Efficient non-parametric image registration. *NeuroImage*, 45(1, Supplement 1):S61--S72, DOI:10.1016/j.neuroimage.2008.10.040. Mathematics in Brain Imaging. http://www.sciencedirect.com/science/article/pii/S1053811908011683.

Wagner, S., Hofstetter, W., Chiquet, M., Mainil-Varlet, P., Stauffer, E., Ganz, R., and Siebenrock, K. (2003). Early osteoarthritic changes of human femoral head cartilage subsequent to femoro-acetabular impingement. *Osteoarthritis and Cartilage*, 11(7):508--518, DOI:10.1016/S1063-4584(03)00075-X. http://dx.doi.org/10.1016/S1063-4584(03)00075-X.

Wang, H., Suh, J., Das, S., Pluta, J., Craige, C., and Yushkevich, P. (2013). Multi-atlas segmentation with joint label fusion. *Pattern Analysis and Machine Intelligence, IEEE Transactions on*, 35(3):611--623, DOI:10.1109/TPAMI.2012.143. http://dx.doi.org/10.1109/TPAMI.2012.143.

Watanabe, A., Boesch, C., Siebenrock, K., Obata, T., and Anderson, S. E. (2007). T2 mapping of hip articular cartilage in healthy volunteers at 3T: A study of topographic variation. *Journal of Magnetic Resonance Imaging*, 26(1):165--171, DOI:10.1002/jmri.21014. http://dx.doi.org/10.1002/jmri.21014.

Waterton, J. C., Solloway, S., Foster, J. E., Keen, M. C., Gandy, S., Middleton, B. J., Maciewicz, R. A., Watt, I., Dieppe, P. A., and Taylor, C. J. (2000). Diurnal variation in the femoral articular cartilage of the knee in young adult humans. *Magnetic Resonance in Medicine*, 43(1):126--132, DOI:10.1002/(SICI)1522-2594(200001)43:1<126::AID-MRM15>3.0.CO;2-#. http://dx.doi.org/10.1002/(SICI)1522-2594(200001)43:1<126::AID-MRM15>3.0.CO;2-#.

Wiberg, G. (1939). Studies on dysplastic acetabula and congenital subluxation of the hip joint: with special reference to the complication of osteoarthritis. *Acta Chir Scand*, 83(58):53--68.

Williams, T., Taylor, C., Gao, Z., and Waterton, J. (2003). Corresponding articular cartilage thickness measurements in the knee joint by modelling the underlying bone. In Ellis, R. and Peters, T., editors, *Medical Image Computing and Computer-Assisted Intervention - MICCAI 2003*, volume 2879 of *Lecture Notes in Computer Science*, pages 480--487. Springer Berlin Heidelberg. http://dx.doi.org/10.1007/978-3-540-39903-2_59.

Wolfe, F., Smythe, H. A., Yunus, M. B., Bennett, R. M., Bombardier, C., Goldenberg, D. L., Tugwell, P., Campbell, S. M., Abeles, M., Clark, P., Fam, A. G., Farber, S. J., Fiechtner, J. J., Michael Franklin, C., Gatter, R. A., Hamaty, D., Lessard, J., Lichtbroun, A. S., Masi, A. T., Mccain, G. A., John Reynolds, W., Romano, T. J., Jon Russell, I., and Sheon, R. P. (1990). The american college of rheumatology 1990 criteria for the classification of fibromyalgia. *Arthritis & Rheumatism*, 33(2):160--172, DOI:10.1002/art.1780330203. http://dx.doi.org/10.1002/art.1780330203.

Wu, X. and Chen, D. (2002). Optimal net surface problems with applications. In Widmayer, P., Eidenbenz, S., Triguero, F., Morales, R., Conejo, R., and Hennessy, M., editors, *Automata, Languages and Programming*, volume 2380 of *Lecture Notes in Computer Science*, pages 1029--1042. Springer Berlin Heidelberg. http://dx.doi.org/10.1007/3-540-45465-9_88.

Wyler, A., Bousson, V., Bergot, C., Polivka, M., Leveque, E., Vicaut, E., and Laredo, J.-D. (2009). Comparison of MR-arthrography and CT-arthrography in hyaline cartilage-thickness measurement in radiographically normal cadaver hips with anatomy as gold standard. *Osteoarthritis and Cartilage*, 17(1):19--25, DOI:http://dx.doi.org/10.1016/j.joca.2008.05.015. http://www.sciencedirect.com/science/article/pii/S1063458408001684.

Xia, Y., Chandra, S., Salvado, O., Fripp, J., Schwartz, R., Lauer, L., Engstrom, C., and Crozier, S. (2012). Automated bone segmentation and bone-cartilage interface extraction from MR images of the hip. In *International Society for Magnetic Resonance in Medicine (ISMRM) 20th Annual Meeting & Exhibition: Adapting MRI in a Changing World*.

Xia, Y., Chandra, S. S., Engstrom, C., Strudwick, M. W., Crozier, S., and Fripp, J. (2014). Automatic hip cartilage segmentation from 3D MR images using arc-weighted graph searching. *Physics in Medicine and Biology*, 59(23):7245. http://stacks.iop.org/0031-9155/59/i=23/a=7245.

Xia, Y., Chandra, S. S., Salvado, O., Fripp, J., Schwarz, R., Lauer, L., Engstrom, C., and Crozier, S. (2011). Automated MR hip bone segmentation. In *Digital Image Computing Techniques and Applications (DICTA), 2011 International Conference on*, pages 25--30. http://dx.doi.org/10.1109/DICTA.2011.13.

Xia, Y., Fripp, J., Chandra, S. S., Schwarz, R., Engstrom, C., and Crozier, S. (2013). Automated bone segmentation from large field of view 3D MR images of the hip joint. *Physics in Medicine and Biology*, 58(20):7375. http://iopscience.iop.org/0031-9155/58/20/7375/.

Xia, Y., Fripp, J., Chandra, S. S., Walker, D., Crozier, S., and Engstrom, C. (2015). Automated 3D quantitative assessment and measurement of alpha angles from the femoral head-neck junction using MR imaging. *Physics in Medicine and Biology*. (Submitted).

Yang, Z., Crozier, S., Engstrom, C., Xia, Y., Neubert, A., Brancato, T., Schwarz, R., Lauer, L., Fripp, J., Chandra, S. S., and Salvado, O. (2012). Morphology-based interslice interpolation on manual segmentations of joint bones and muscles in MRI. In *Digital Image Computing Techniques and*

Applications (DICTA), 2012 International Conference on, pages 1--8. http://dx.doi.org/10.1109/DICTA.2012.6411678.

Yang, Z., Fripp, J., Chandra, S. S., Neubert, A., Xia, Y., Strudwick, M. W., Paproki, A., Engstrom, C., and Crozier, S. (2015). Automatic bone segmentation and bone-cartilage interface extraction for the shoulder joint from magnetic resonance images. *Physics in Medicine and Biology*, 60(4):1441. http://stacks.iop.org/0031-9155/60/i=4/a=1441.

Yen, Y.-M. and Kocher, M. S. (2013). Clinical and radiographic diagnosis of femoroacetabular impingement. *Journal of Pediatric Orthopaedics*, 33:S112--S120, DOI:10.1097/bpo.0b013e318288b450. http://dx.doi.org/10.1097/BPO.0b013e318288b450.

Yin, Y., Zhang, X., Williams, R., Wu, X., Anderson, D., and Sonka, M. (2010). LOGISMOS-Layered Optimal Graph Image Segmentation of Multiple Objects and Surfaces: Cartilage segmentation in the knee joint. *Medical Imaging, IEEE Transactions on*, 29(12):2023--2037, DOI:10.1109/TMI.2010.2058861. http://dx.doi.org/10.1109/TMI.2010.2058861.

Yokota, F., Okada, T., Takao, M., Sugano, N., Tada, Y., and Sato, Y. (2009). Automated segmentation of the femur and pelvis from 3D CT data of diseased hip using hierarchical statistical shape model of joint structure. In Yang, G.-Z., Hawkes, D., Rueckert, D., Noble, A., and Taylor, C., editors, *Medical Image Computing and Computer-Assisted Intervention – MICCAI 2009*, volume 5762 of *Lecture Notes in Computer Science*, pages 811--818. Springer Berlin Heidelberg. http://dx.doi.org/10.1007/978-3-642-04271-3_98.

Yushkevich, P. A., Piven, J., Cody Hazlett, H., Gimpel Smith, R., Ho, S., Gee, J. C., and Gerig, G. (2006). User-guided 3D active contour segmentation of anatomical structures: Significantly improved efficiency and reliability. *Neuroimage*, 31(3):1116--1128, DOI:10.1016/j.neuroimage.2006.01.015. http://dx.doi.org/10.1016/j.neuroimage.2006.01.015.

Zbýň, S., Mlynárik, V., Juras, V., Szomolanyi, P., and Trattnig, S. (2014). Sodium mr imaging of articular cartilage pathologies. *Current Radiology Reports*, 2(4), DOI:10.1007/s40134-014-0041-4. http://dx.doi.org/10.1007/s40134-014-0041-4.

Zhai, G., Cicuttini, F., Srikanth, V., Cooley, H., Ding, C., and Jones, G. (2005). Factors associated with hip cartilage volume measured by magnetic resonance imaging: The Tasmanian Older Adult Cohort Study. *Arthritis & Rheumatism*, 52(4):1069--1076, DOI:10.1002/art.20964. http://dx.doi.org/10.1002/art.20964.

Zhang, J., Yan, C.-H., Chui, C.-K., and Ong, S.-H. (2010). Fast segmentation of bone in CT images using 3d adaptive thresholding. *Computers in Biology and Medicine*, 40(2):231--236, DOI:10.1016/j.compbiomed.2009.11.020. http://www.sciencedirect.com/science/article/pii/S0010482509002157.

Zheng, Z.-Z., Shan, H., and Li, X. (2010). Fat-suppressed 3D T1-weighted gradient-echo imaging of the cartilage with a volumetric interpolated breath-hold examination. *AJR. American journal of roentgenology*, 194(5):W414--9, DOI:10.2214/ajr.09.2423. http://intl.ajronline.org/cgi/reprint/194/5/W414.pdf.

Zilkens, C., Miese, F., Krauspe, R., and Bittersohl, B. (2013). Symptomatic femoroacetabular impingement: Does the offset decrease correlate with cartilage damage? a pilot study. *Clinical Orthopaedics and Related Research®*, 471(7):2173--2182, DOI:10.1007/s11999-013-2812-2. http://dx.doi.org/10.1007/s11999-013-2812-2.

Zoroofi, R., Sato, Y., Sasama, T., Nishii, T., Sugano, N., Yonenobu, K., Yoshikawa, H., Ochi, T., and Tamura, S. (2003). Automated segmentation of acetabulum and femoral head from 3-d CT images. *Information Technology in Biomedicine, IEEE Transactions on*, 7(4):329--343, DOI:10.1109/TITB.2003.813791. http://dx.doi.org/10.1109/TITB.2003.813791.